



Udson Cabral Mendes

**Electronic and optical properties of diluted magnetic
semiconductors quantum wells and quantum dots**

*Propriedades eletrônicas e ópticas de poços quânticos e pontos
quânticos de semicondutores magnéticos diluídos*

Campinas

2014



UNIVERSIDADE ESTADUAL DE CAMPINAS
INSTITUTO DE FÍSICA “GLEB WATAGHIN”

Udson Cabral Mendes

Electronic and optical properties of diluted magnetic semiconductors quantum wells and quantum dots

*Propriedades eletrônicas e ópticas de poços quânticos e pontos
quânticos de semicondutores magnéticos diluídos*

Thesis presented to the Institute of
Physics “Gleb Wataghin” of the Univer-
sity of Campinas in partial fulfillment
of the requirements for the degree of
Doctor in Science.

*Tese apresentada ao Instituto de Física
“Gleb Wataghin” da Universidade Estad-
ual de Campinas para obtenção do título
de Doutor em Ciências.*

SUPERVISOR: Prof. Dr. José Antônio Brum

ESTE EXEMPLAR CORRESPONDE À VERSÃO FINAL
DA TESE DE DOUTORADO DEFENDIDA PELO ALUNO
UDSON CABRAL MENDES, E ORIENTADO PELO
PROF. DR. JOSÉ ANTÔNIO BRUM.

A handwritten signature in blue ink, appearing to read "JAB", is written over a horizontal line.

Campinas
2014

Ficha catalográfica
Universidade Estadual de Campinas
Biblioteca do Instituto de Física Gleb Wataghin
Valkíria Succi Vicente - CRB 8/5398

M522e Mendes, Udson Cabral, 1984-
Electronic and optical properties of diluted magnetic semiconductors quantum wells and quantum dots / Udson Cabral Mendes. – Campinas, SP : [s.n.], 2014.

Orientador: José Antônio Brum.
Tese (doutorado) – Universidade Estadual de Campinas, Instituto de Física Gleb Wataghin.

1. Semicondutores magnéticos diluídos - Propriedades óticas. 2. Estrutura eletrônica. 3. Interações magnéticas. 4. Efeitos de muitos-corpos. I. Brum, José Antônio, 1959-. II. Universidade Estadual de Campinas. Instituto de Física Gleb Wataghin. III. Título.

Informações para Biblioteca Digital

Título em outro idioma: Propriedades eletrônicas e óticas de poços quânticos e pontos quânticos de semicondutores magnéticos diluídos

Palavras-chave em inglês:

Diluted magnetic semiconductors - Optical properties

Electronic structure

Magnetic interactions

Many-body effects

Área de concentração: Física

Titulação: Doutor em Ciências

Banca examinadora:

José Antônio Brum [Orientador]

Pawel Hawrylak

Harry Westfahl Junior

Ricardo Luís Doretto

Eduardo Miranda

Data de defesa: 21-03-2014

Programa de Pós-Graduação: Física

MEMBROS DA COMISSÃO JULGADORA DA TESE DE DOUTORADO DE **UDSON MENDES CABRAL – RA: 100770** APRESENTADA E APROVADA AO INSTITUTO DE FÍSICA “GLEB WATAGHIN”, DA UNIVERSIDADE ESTADUAL DE CAMPINAS, EM 21 / 03 / 2014.

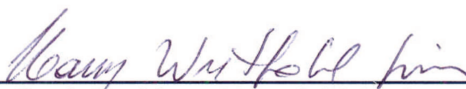
COMISSÃO JULGADORA:



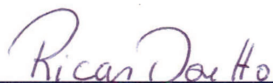
Prof. Dr. José Antonio Brum
Orientador do Candidato - DFMC/IFGW/UNICAMP



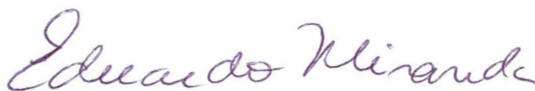
Prof. Dr. Pawel Hawrylak – National Research Council of Canada



Prof. Dr. Harry Westfahl Junior – CNPEM



Prof. Dr. Ricardo Luís Doretto – DFMC/IFGW/UNICAMP



Prof. Dr. Eduardo Miranda – DFMC/IFGW/UNICAMP

Abstract

In this thesis, we theoretically investigate the electronic and optical properties of diluted magnetic semiconductors quantum wells and quantum dots. This is strongly motivated by many experimental results on the optical properties of these materials. Using spin-density functional theory we described the electronic states as a function of the external magnetic field for quantum wells which have barriers doped with magnetic impurities. Our model takes into account the many-body effects of the two-dimensional hole gas and the interaction between carriers and the magnetic ions. We compare our findings with the available experimental data, which shows strong oscillations in the circularly polarized light as a function of the magnetic field. Our results show excellent qualitative and quantitative agreement with the experimental data. We show that the hole gas exchange effects are responsible for the strong oscillations observed in the photoluminescence. We perform a systematic investigation of the heterostructure parameters in order to enhance the carriers-Mn exchange interaction. With our model we understand the different regime of the electron's spin relaxation in quantum wells with barriers doped with Mn impurities.

We also investigate the electronic and optical properties of charged quantum dots doped with a single magnetic impurity in its center. Using an exact diagonalization method we show that the electrons that are not directly coupled with Mn do so via an indirect coupling mediated by electron-electron interaction. This indirect electron-Mn coupling can be either ferromagnetic or antiferromagnetic depending on both quantum dot confinement and the number of electronic confined shells. We also demonstrate that the indirect electron-Mn coupling is an important effect even when Mn is off-center. This coupling exists independently of the type of the direct interaction between carriers and Mn impurity. We also extend the theory of photoluminescence for charged quantum dots containing a single magnetic impurity. We show that the indirect interaction between carriers and magnetic ion generates a fine structure in both initial and final states of the emission, which allows us to determinate the number of confined shells in the quantum dots and the electronic spins. With this exact diagonalization

method, we explain the origin of the fine structure of a biexciton confined in quantum dot containing a single Mn impurity.

Resumo

Nesta tese, investigamos teoricamente as propriedades eletrônicas e ópticas de poços quânticos e pontos quânticos de semicondutores magnéticos diluídos. Este estudo é fortemente motivado por muitos resultados experimentais sobre as propriedades ópticas desse materiais. Usando a teoria do funcional da densidade dependente de spin descrevemos os estados eletrônicos como função do campo magnético externo para poços quânticos que possuem barreiras dopadas com impurezas magnéticas. Nosso modelo leva em conta os efeitos de muitos-corpos do gás de buracos e as interações entre portadores e os íons magnéticos. Comparamos nossos resultados com os dados experimentais disponíveis, que apresentam forte oscilações da luz polarizada circularmente como função do campo magnético. Nossos resultados apresentam excelente concordância qualitativa e quantitativa com os resultados experimentais. Mostramos que os efeitos de troca do gás de buraco são responsáveis pela forte oscilação observada na fotoluminescência. Também realizamos uma investigação sistemática dos parâmetros da heteroestrutura afim de aumentar a interação de troca entre portadores e íons de Mn. Com o nosso modelo entendemos os diferentes regimes de relaxação de spin do elétron em poços quânticos com barreiras dopadas com impurezas magnéticas.

Nós também investigamos as propriedades eletrônicas e ópticas de pontos quânticos carregados dopados com uma única impureza magnética em seu centro. Usando métodos de diagonalização exata mostramos que os elétrons que não estão diretamente acoplados com o íon de Mn acoplam-se via uma interação indireta que é mediada pela interação elétron-elétron. Este acoplamento indireto entre elétrons e Mn pode ser tanto ferromagnético quanto antiferromagnético dependendo de ambos confinamento e número de camadas eletrônicas confinadas no ponto quântico. Demonstramos que este acoplamento indireto é um efeito importante mesmo quando o íon de Mn não está no centro do ponto quântico. O acoplamento indireto existe independentemente do tipo de interação direta entre portadores e a impureza magnética. Também extendemos a teoria de fotoluminescência para essa heteroestrutura. Observamos que a interação indireta entre portadores e íon magnético gera uma estrutura fina em ambos

os estados iniciais e finais da emissão, o que nos permite determinar o número de camadas confinadas no ponto quântico e o spin eletrônico. Com esse método de diagonalização exata, explicamos a origem da estrutura fina do biexciton confinado em um ponto quântico dopado com uma única impureza magnética.

Contents

Abstract	ix
Resumo	xi
Contents	xiii
List of figures	xxiii
List of tables	xxiii
1 Introduction	1
2 Methodology	9
2.1 Density Functional Theory	11
2.1.1 The Kohn-Sham self-consistent equations	13
2.1.2 Spin-density functional theory	15
2.2 Configuration interaction method	19
2.3 Magnetic interaction	28
2.3.1 Magnetic impurities in III-V semiconductors	29
2.3.2 Single magnetic impurity in a quantum dot	34
2.4 Schrödinger's equation solution	36
2.4.1 Wave-function time evolution	37
2.4.2 Imaginary time wave function propagation	39
3 Electronic and optical properties of quantum wells with Mn-δ-doped barriers	42
3.1 Introduction	42
3.2 Model	46

3.3	Results	62
3.3.1	Role of interactions	63
3.3.2	$x_{Mn} = 0.13$ and $x_{Mn} = 0.2$ monolayers	73
3.4	Increasing p - d interaction	76
3.4.1	Mn position	76
3.4.2	Gate Voltage	81
3.5	Concluding Remarks	88
4	Electronic properties of charged quantum dots doped with a single magnetic impurity	92
4.1	Introduction	92
4.2	Model	94
4.3	Spin singlet closed shells coupled with the magnetic ion	96
4.4	Electrons in finite angular momentum channels	99
4.4.1	One electron on the p shell	100
4.4.2	Two spin-polarized electrons on the p shell	103
4.5	Conclusion	109
5	Optical properties of charged quantum dots doped with a single magnetic impurity	110
5.1	Introduction	110
5.2	Model	112
5.3	Electronic structure and emission spectra of charged magnetic dots	115
5.3.1	Emission from a nonmagnetic charged quantum dot	116
5.3.2	X -Mn and X^- -Mn complexes	117
5.3.3	X^{-2} -Mn complex	118
5.3.4	X^{3-} -Mn complex	126
5.3.5	Comparison between emission spectra of different complexes	134
5.3.6	Effects of Mn in an off-center position	135
5.4	Summary	137
6	Results form collaborative work	139
6.1	Biexciton-Mn complex photoluminescence	139
6.2	Electron spin dynamics in quantum wells with barriers doped with magnetic impurities	145

7 Final Remarks and Perspectives	148
Appendix	150
A Two-dimensional Harmonic Oscillator	151
B Electron-electron Coulomb matrix elements	155
C Magnetization of (III,Mn)V semiconductors	161
D Imaginary time wave-function evolution	165
Bibliography	179

To my mother Cleusa Helena Cabral Mendes.

“... If you work hard enough and assert yourself, and use your mind and imagination, you can shape the world to your desires.”

Malcolm Gladwell

Acknowledgments

I would like to thank my advisor José A. Brum for the opportunity to work with him, for his support, our vivid discussions, and above all for his patience and friendship during all these years.

I would like to thank Pawel Hawrylak for the opportunity to work in his group in Ottawa, but also to allow me to live in such an amazing country as Canada. I am grateful that he tried to teach me how to ski.

I would like to thank the State University of Campinas and the National Research Council of Canada for the learning opportunities they offered me and hospitality during my PhD.

To all my professors that contributed to my formation. In special Salviano and Caparica.

My special thank to Maria José Brasil, Fernando Iikawa, Odilon Couto, Miguel Balanta and everyone from the group of optical properties, with whom I have had many discussions about experimental physics.

To all that I have collaborated and discussed my research and physics over all the last ten years. Márcio Adriano, Gerson, Rosano....

To the ones that became my friends once I started to study physics and with whom I shared many moments in these last ten years. Rafael, David, Anderson, Sebastião, Larissa, José Carlos and Lilian. Thanks a lot guys!!!!

To my friends in Campinas: Zenner, Marcelo, Domingos, Ranyere, Braulio, Luis Henrique and Pedro, with whom I had the opportunity to discuss physics, and share the essential activity to drink beer.

To Anna Trojnar, Isil Ozfidan, Devrim Guclu, Marek Korkusinski, Charles Bamber and Chris Hall. Thanks a lot guys for welcoming me in Ottawa.

To my friends from Jataí: Juliano, Ivalci, and João Henrique. Thanks for everything.

To my brothers Udenys, Wendel, Weder and my mother Cleusa, who always supported me in my endeavor.

Finally, I would like to thank my lovely girlfriend Josée for everything, moving to a foreign land, being understanding.... Thank you so much mon Amour!!!

I would like to acknowledge the support from FAPESP (Project Number 2010/11393-5) and CAPES (Project Number 5860/11-3).

List of Figures

1.1	Investigated Quantum well and experimental results	5
1.2	Measured Mn-doped QD emission for exciton, charged exciton, and biexciton.	6
2.1	Three electrons GS and excited state configurations, and the GS energy as function of number of shells.	27
2.2	GaMnAs unit cell	30
2.3	Electron-Mn matrix elements as function of Mn position.	36
3.1	Schematic representation of the investigate quantum well and its profile potential.	48
3.2	Self-consistent profile potential, hole LLs, 2D hole density and LLs density, for sample $x_{Mn} = 0.4$ MLs.	65
3.3	Electron LLs and transition energies for $x_{Mn} = 0.4$ MLs	69
3.4	Holes LLs and transition energies for $x_{Mn} = 0.4$ MLs considering $v_{XC} = 0$	71
3.5	Landau fan diagram for holes and transition energies for $V_{pd} = 0$ and $v_{XC} \neq 0$	72
3.6	Holes Landau levels and transition energies for samples with $x_{Mn} = 0.13$ and $x_{Mn} = 0.2$ MLs	74
3.7	LLs for holes and electrons. Transition energy for heterostructure with $L_s = 1$ nm in absence of h-Mn and e-Mn interactions.	78
3.8	LLs for holes and electrons, and transition energies in absence of Zener exchange interaction for $L_s = 1$ nm	79
3.9	Landau fan diagram for electrons and holes, and transition energies considering all interaction in a sample with $L_s = 1$ nm.	81
3.10	Self-consistent potential, wave functions for $B = 0$ T and $B = 10$ T. Landau levels fan diagram and occupation for $x_{Mn} = 0.4$ MLs, $V_g = 0.71$ eV and $L_s = 3$ nm.	83
3.11	Electrons LLs and transition energies and non-linear shift considering $x_{Mn} = 0.4$ MLs, $V_g = 0.71$ eV and $L_s = 3$ nm.	85
3.12	Self-consistent potential, wave functions for $B = 0$ T and $B = 10$ T. Landau levels fan diagram and occupation for $x_{Mn} = 0.4$ MLs, $V_g = 0.71$ eV and $L_s = 1$ nm.	87
3.13	Electrons LLs and transition energies and non-linear shift considering $x_{Mn} = 0.4$ MLs, $V_g = 0.71$ eV and $L_s = 1$ nm.	89
4.1	Two-electrons-Mn configurations and energies	98
4.2	Three electrons GS properties.	101
4.3	Three electrons GS energy as function of QD shell spacing, and e-Mn coupling.	104
4.4	Four electrons GS properties.	106
4.5	Four electron GS energy as function of QD shell spacing, and e-Mn coupling.	108
5.1	X^{2-} initial and final states, and emission spectrum of a nonmagnetic QD	116
5.2	X^{2-} -Mn GS energy as a function of interactions, and its indirect coupling scheme	119
5.3	X^{2-} final states as function of interactions, and its indirect coupling scheme	122
5.4	X^{2-} -Mn emission	125

5.5	X^{3-} -Mn initial state energy as function of interaction, and e-Mn indirect coupling scheme.	127
5.6	Indirect coupling scheme for three electrons configurations, and final-state as a function of interactions.	130
5.7	Low-energy X^{3-} -Mn emission spectrum in σ_+	132
5.8	High-energy part of the X^{3-} -Mn emission spectrum	133
5.9	X -Mn, X^- -Mn, X^{2-} -Mn and X^{3-} -Mn emission spectra.	135
5.10	Mn position dependence of X^{2-} -Mn emission spectrum and two electrons final state for $J_{pp} \neq 0$ (left) and absence $J_{pp} = 0$	136
6.1	Biexciton-Mn luminescence	141
6.2	Biexciton-Mn calculated and measured photoluminescence	143
6.3	Average distance between XX-Mn and \bar{X} -Mn emission peaks	144
6.4	Hanle curves and PL-RT measurements for different samples with distinct Mn concentration.	146
6.5	Electron-Mn overlap for different Mn concentrations.	147
A.1	Two-dimensional harmonic oscillator single particle states	154

List of Tables

3.1	InAs and GaAs parameters	61
3.2	Manganese effective parameters	62

Chapter 1

Introduction

Semiconductor materials have been investigated for almost two centuries now [1]. Since the discovery of the transistor effect in 1947 and the improvement of the growth conditions, in the 1980's, they became the basis of today's electronic and opto-electronic commercial devices. The fundamental characteristic of semiconductors is that carriers concentration can be manipulated by external fields. Due to the high quality of the semiconductors samples, they are often used as proof of concept materials [2]. Therefore, semiconductors are of great interest to the scientific community. They are widely used for investigation of basic physics, such as Kondo and Majorana fermion physics [3–6].

In the last decades spin-related phenomena have attracted much attention, in metals with the discovery of the giant magneto-resistance [7, 8], and more recently, in diluted magnetic semiconductors [9–12], and in materials with strong spin-orbit interaction [13–16]. All this is part of the research field identified as spintronics [17, 18]. The context of this thesis is part of the semiconductor spintronics field.

In this thesis we investigate both semiconductor quantum wells (QWs) and quantum dots (QDs). QWs are obtained by growing two different materials. The growing sequence is ABA where, in general, B is the lower energy band gap material. Depending on the band alignment, there are three types of semiconductor QWs: type-I where both electron and holes are confined

in the same material, for example, GaAs quantum wells grown in AlGaAs. Type-II QW occurs when one of the carriers is confined in one material, and the other carrier in the other layer. As an example we have the InAs/GaSb heterostructures [19]. Finally, the type-III occurs when the Γ_6 band* of one material have smaller energy than the Γ_8 bands of the other material. The most known type-III semiconductor QW is the HgTe grown on CdTe [15]. In this thesis we investigate type-I systems.

Doped QW show a two-dimensional electron gas (2DEG) located at the QW layer. The physics of 2DEG is fascinating. It started with the invention of modulation doping, followed by the discovery of both integer quantum Hall effect and fractional quantum Hall effect in the 80's [20–22]. More recently, it was demonstrated and observed in type-III semiconductors the so called quantum spin Hall effect [15, 16], which is an emergence of the topological insulator phase [23–25]. In type-I semiconductors, the persistent spin helix phase was demonstrated [26]. The integer and fractional Hall phases emerge due to the presence of an external magnetic field, while the last two effects are due to spin-orbit interaction.

It is also possible to dope QWs with magnetic impurities. We can then investigate the interplay between the rich 2DG physics and magnetism [27–29]. Recently, it was proposed that InAs/GaSb QWs doped with Mn can show the quantum anomalous Hall effect [30]. In this phase, a Hall conductance is observed without an external magnetic field. Also, strong oscillations of the circularly polarized photoluminescence was observed in InGaAs quantum wells with barriers doped with magnetic impurity [31]. These oscillations are stronger than the ones observed in a non-magnetic *p*-doped quantum well [32].

Quantum dots are heterostructures in which the carrier is confined in all three dimensions. It shows a shell structure [33] and when the electronic shells are filled with carriers they obey the Hund's rule [34, 35]. If the electron-electron interaction dominates over the kinetic energy,

*In GaAs Γ_6 is the conduction band, and Γ_8 is the valence band.

a Wigner molecule phase may be formed [36]. Because of the many similarities that QDs have with atoms, they are often called *artificial atoms*. Quantum dots have a wide spectrum of applications, for example, lasers, amplifiers, detectors, single-photon sources, in quantum computation and quantum information processing [37–42].

Quantum dots can be created electrostatically or via structural induced confinement. In the first case, a gate voltage is applied to the 2DG in order to confine the carriers in three dimensions [43]. The problem here is that only one type of carrier is confined. The second method consists in growing different materials, for example, InAs grown on GaAs where its layers are strained. The formation of the islands minimizes both elastic, surface and interface energies of the strained layers [44]. The carrier confinement in these QDs depends on the band alignment between the QD material and the barriers. These QDs are identified as self-assembled QDs. Other type of QDs are obtained via chemical process [45, 46]. In this thesis we investigate the properties of self-assembled QDs.

Quantum dots with an odd number of electrons may behave like a magnetic impurity. If the QD is strongly coupled to fermionic reservoirs, we can observe the emergence of the Kondo physics [47, 48]. The Kondo effect in semiconductor nanostructures was first observed in transport experiments in electrostatically defined quantum dots [47] and more recently it was observed in both absorption and photoluminescence experiments on self-assembled quantum dots [4, 49]. Quantum dots in the Coulomb blockade regime, weakly coupled to electronic reservoirs, can work as a spin filter in the presence of an external magnetic field, and as a spin memory if the reservoirs are spin-polarized [50].

The introduction of magnetic impurities in semiconductors quantum dots opens the possibility to investigating the physics of quasi-3D localized electrons interacting with localized spins [51]. Today, it is possible to manipulate the localized spin states by using light [42] or by adding electrons into the QD [52, 53]. For Mn-doped QD coupled to an electronic reservoir,

it was shown theoretically that, depending on the rate J/T_K , with J being the electron-Mn interaction and T_K the Kondo temperature, it is possible to observe the underscreened Kondo state [54]. The emergence of an indirect electron-Mn interaction mediated by electron-electron interaction was also demonstrated [53, 55].

Doping quasi-2D and -0D systems with magnetic impurities gives rise to new phenomena or the enhancement of certain effects that were already observed in nonmagnetic semiconductors. Because of the rich physics that these systems present, they motivated our choice for this thesis. In this PhD thesis, we investigate both quantum wells and quantum dots doped with magnetic impurities.

We aim here to study the electronic and optical properties of quantum wells and quantum dots doped with magnetic impurities. In both cases, we expect to clarify the effects of the interaction between carriers and magnetic ions and its signature on the photoluminescence spectra.

Concerning QW systems, one of our motivations was to understand the origin of the strong magneto-oscillations of the circularly polarized photoluminescence (CPPL) as a function of the magnetic field observed by Gazoto *et al.* [31]. They investigated InGaAs QWs with barriers δ -doped on one side with carbon and the other side with Mn. Both C and Mn are acceptors and therefore, they provide holes to the heterostructure, with the Mn ion acting also as a magnetic impurity. Figure 1.1(a) illustrates the investigated heterostructure.

Figure 1.1(b) shows the observed magneto-oscillations of the CPPL for two samples, one that contains both Mn and C, and the other doped only with C. In the magnetically doped sample, strong oscillations of the luminescence as the magnetic field is increased were observed. For the nonmagnetic QW, the photoluminescence is practically linear with the magnetic field. Another difference between these two samples is the hole density. While in the Mn-doped heterostructure the hole density is of the order of 10^{11} cm^{-2} , in the non-magnetic sample it is

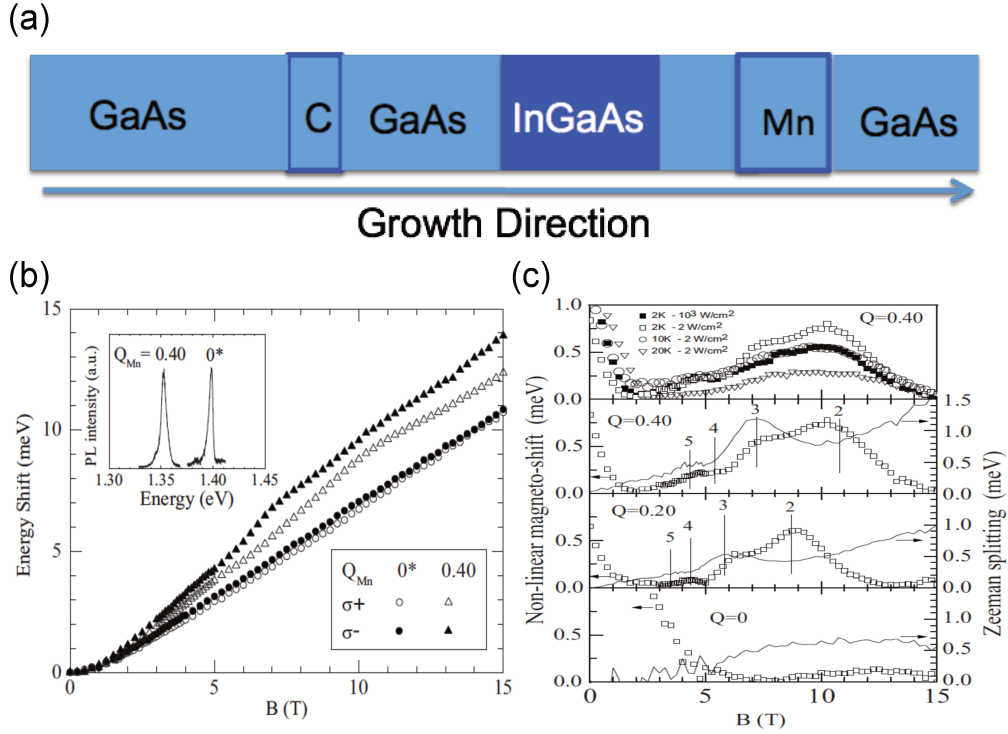


Figure 1.1: (a) Scheme of the investigated quantum well. Carbon and Mn are δ -doped. (b) Photoluminescence as function of the magnetic field for samples with both C and Mn, and one without Mn. (c) Non-linear and Zeeman splitting energy as a function of the magnetic field for samples with different Mn concentration. Upper figure shows the temperature dependence of the non-linear energy for the sample doped with 0.4 monolayers of Mn. Figure (b) and (c) were extracted from [31].

one order of magnitude smaller.

Motivated by these experimental results, we developed a theoretical model that captures most of the qualitative and quantitative physics behind the observed behavior of the photoluminescence. In our model, the strong oscillations of the PL are caused by the exchange energy of the hole gas, which tends to spin-polarize the hole gas, having a maximum at odd filling factors and minimum at even filling factors. This agrees with the experimental results shown in Fig. 1.1(c). We also show that the hole-Mn spin interaction has no major effect on the magneto-photoluminescence when we consider the same parameters of the samples studied in ref. [31]. This is related with the fact that the overlap between holes and Mn is small. As a consequence, we discuss the sample parameters that may enhance these effects.

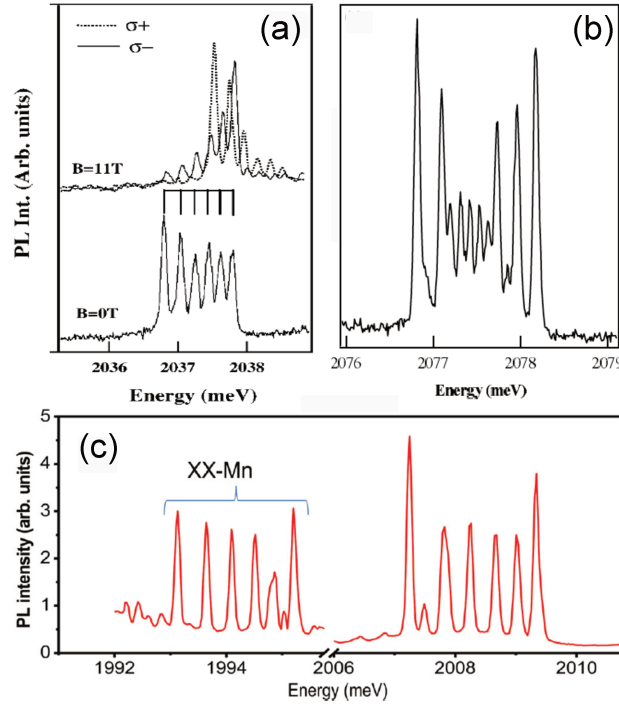


Figure 1.2: Continuous wave emission of a Mn-doped QD as a function of the photon energy, for (a) an exciton (one electron-hole pair) (b) negatively charged exciton (two-electrons and one hole), and (c) biexciton (two-electrons and two-holes). Figures. (a), (b) and (c) were extracted from [56–58], respectively.

The quantum dot project has a goal to extend the theory of optical emission to charged Mn-doped QDs. In previous works, both theoretical and experimental, the photoluminescence of Mn-doped QDs with a maximum number of four confined carriers it was investigated [56–62]. Also, in all the investigated cases, the carriers occupied only the QD s -shell. Electronic configurations where electrons occupy the p -shell had not yet been investigated. Figures 1.2(a), (b) and (c) show the measured emission spectra of a QD doped with a single Mn spin for an exciton, negatively charged exciton, and the biexciton, respectively.

The emission of nonmagnetic doped charged quantum dots show peculiar features, such as the formation of an emission plateau and the splitting of the emission line when there are more than two electrons in the initial states emission process [63, 64]. Here we developed a

microscopic model to investigate the optical properties of Mn-doped QDs as a function of number of electrons in the QD. This provides the emission theory for magnetically doped charged QDs. As a consequence, we observed that electron-electron interaction mediates indirect exchange interaction between electron and Mn and predict how to detect electron spin on half filled electronic shells [53, 55].

The quantum well project was developed in collaboration with the optical properties group (GPO - *grupo de propiedades ópticas*) at UNICAMP. They provided useful comments on the experimental findings and clarified many of ours doubts. The quantum dot project was conducted in Pawel Hawrylak's group at the National Research Council of Canada.

The content of this PhD thesis is build upon the following articles:

1. U. C. Mendes and J. A. Brum, in preparation.
2. U. C. Mendes, M. Korkusinski and P. Hawrylak, submitted to Phys. Rev. B.
3. U. C. Mendes, M. Korkusinski, A. H. Trojnar and P. Hawrylak, Phys. Rev. B **88**, 115306 (2013).
4. A. H. Trojnar, M. Korkusinski, U. C. Mendes, M. Goryca, M. Koperski, T. Smolenski, P. Kossacki, P. Wojnar and P. Hawrylak, Phys. Rev. B **87**, 205311 (2013).
5. M. A. G. Balanta, M. J. S. P. Brasil, F. Iikawa, U. C. Mendes, J. A. Brum, M. Z. Maialle, Yu A. Danilov, O. V. Vikhrova and B. N. Zvonkov, J. Phys. D: Appl. Phys. **46**, 215103 (2013).

This thesis is organized as follows. In chapter 2 we present a theory and methods employed to investigate the electronic and optical properties of diluted magnetic semiconductors quantum wells and quantum dots. The results are presented in Chapters 3, 4, 5 and 6. The quantum well project results are presented in Chapter 3. The quantum dot project results are

presented in both Chapters 4 and 5. In Chapter 6, we present a concise description of two other projects that we have participated. They are related with the results discussed in the previous chapters. Final remarks and perspectives are presented in Chapter 7.

Chapter 2

Methodology

In order to describe the electronic properties of carriers interacting with magnetic impurities we have to solve a many-body Hamiltonian, which is given by

$$\mathcal{H} = \sum_{i=1}^N \left[\frac{\mathbf{p}_i^2}{2m^*} + V(\mathbf{r}_i) \right] + \frac{1}{2} \sum_{i \neq j=1}^N \frac{e^2}{\epsilon |\mathbf{r}_i - \mathbf{r}_j|} + \sum_{i=1}^N \sum_j J(\mathbf{r}_i - \mathbf{R}_j) M_j \cdot s_i, \quad (2.1)$$

where the first term is kinetic energy and m^* is the electron effective mass. The second term is the external potential, which includes the confinement potential and the external fields, if present. The third term is the electron-electron (e-e) Coulomb interaction, with e being the electron charge, and ϵ the dielectric constant of the material. The last term is the spin interaction between carriers and the magnetic impurities. $J(\mathbf{r}_i - \mathbf{R}_j)$ is the exchange constant, R_j , M_j and s_i are the position of the Mn spin, the Mn spin, and the electron spin, respectively. For the quantum well system considered in this work there is a very large amount of Mn spins, while for the quantum dot problem there is only a single Mn impurity. To be able to write the above Hamiltonian we have performed the following approximations:

- *Born-Oppenheimer approximation*: It allows us to separate the electron's Hamiltonian from the nucleus' Hamiltonian, i.e, the motion of the nucleus does not affect the electron and therefore, the electron interacts with the nucleus via electron-nucleus Coulomb interaction, where the position of the nucleus is fixed at its average position. A more detailed view of this approximation can be found on the appendix C of ref. [65].

- *Effective mass approximation*: It is a continuum approximation for the crystal potential. It allows us to describe the band structure near a high symmetric point in the reciprocal space. In our case, we considered the Γ point of zincblend symmetry. For relative large gaps, as in our case, for both GaAs and CdTe, the conduction band can be described by a parabolic dispersion with an effective mass. The valence band structure is described by the Luttinger-Kohn (LK) Hamiltonian. Simple approximations for the valence band can start with only the diagonal terms of LK Hamiltonian, that is, a parabolic dispersion with respective effective mass for the holes.

In order to obtain the electronic states of the above Hamiltonian we have to solve a N -body problem which is not an easy task. We used two different methods to solve Eq. (2.1) depending on the system investigated. The electronic structure of the quantum wells were obtained via density functional theory (DFT) [66, 67]. For quantum dots we use the configuration interaction (CI) method [68].

The DFT allows us to map the many-body problem into an effective single particle one, which gives the exact ground state density and total energy of the interacting system [67, 69, 70]. The DFT fundamental basis is presented in section 2.1. We extend the formalism to include spin-dependent phenomena, i.e, we outline the spin-density functional theory (SDFT) [69, 71, 72]. This extension of the DFT is more suitable for our problem, since we have an external magnetic field and magnetic impurities that breaks the spin degeneracy.

The CI method is a many-body treatment of the problem, where the many particle wave function is expanded in a basis of configurations which allows us to diagonalize the Hamiltonian exactly. Without loss of generality we present the CI method in section 2.2 for a two-dimensional harmonic oscillator (2DHO). The 2DHO describes very well many important features of both electronic and optical properties of quantum dots [68]. It allows us to calculate the e-e matrix elements in an analytic way, as showed in Appendix B.

2.1 Density Functional Theory

The solution of Eq. (2.1) is very difficult for systems with a large number of interacting particles. One approach to solve this problem is to use a mean-field theory, where the electron moves in the effective field of all the other electrons. This kind of approach has been used for almost a century by now. Many methods were developed based on the mean-field theory, such as Hartree, Hartree-Fock (HF), and the Kohn-Sham (KS) equations of the DFT [65,66,69,73]. The Hartree method treats only the direct e-e interaction, leaving aside the fact that the electrons are indistinguishable particles. An improvement comes with the HF method where it considers an antisymmetric wave function, a consequence of the indistinguishability of the electrons, and it naturally leads to a new contribution of the e-e interaction, which is the exchange e-e interaction. The HF method still lacks the correlation energy, which in the HF method is defined as $E_c = E - E_{HF}$ [73], where E and E_{HF} are the total energies of the many-body problem and the HF energy, respectively. One way of including correlation is by expanding the the many-body wave function in Slater determinants. This is the basis of the CI method presented in section 2.2. This method goes beyond the mean-field approximation, and hence, it is very difficult to apply for system with large number of electrons.

A new improvement in the problem arises from the understanding that not only the wave function, but also the electronic density of the many-body system contains all the relevant information about it. This is the heart of the so-called *Density Functional Theory* [66,69,70], which is today one of the most used electronic structure methods. It is applied to a large variety of systems such as molecules, solids and quantum spin chains [65,73,74]. Due to its importance to quantum chemistry, and also for its very large number of applications, Walter Kohn, one of the DFT creators, received the chemistry *Nobel Prize* in 1998 [75].

The DFT is formulated on the basis of the Hohenberg-Kohn (HK) theorem [66,69,75], which states that:

- The ground state electronic density,

$$n(\mathbf{r}) = \int d\mathbf{r}_2 d\mathbf{r}_3 \dots d\mathbf{r}_N \Psi^*(\mathbf{r}, \mathbf{r}_2, \dots, \mathbf{r}_N) \Psi(\mathbf{r}, \mathbf{r}_2, \dots, \mathbf{r}_N), \quad (2.2)$$

fully characterizes the many-body system, i.e, it uniquely defines the external potential $v_e(\mathbf{r})^*$, which in turn specifies the Hamiltonian, and consequently, the many-body ground state wave function $\Psi(\mathbf{r}, \mathbf{r}_2, \dots, \mathbf{r}_N)$. Therefore, there exist one-to-one correspondence between all of those quantities, which ensures that the density has all information,

$$n(\mathbf{r}) \iff v_e(\mathbf{r}) \iff \mathcal{H} \iff \Psi(\mathbf{r}, \mathbf{r}_2, \dots, \mathbf{r}_N). \quad (2.3)$$

This means that one can invert Eq. (2.2) and write the wave function as a functional of the density [66, 70]. From the HK theorem we have that all the observable are a functional of the density,

$$O[n] = \langle \Psi[n] | \hat{O} | \Psi[n] \rangle. \quad (2.4)$$

An important aspect of the DFT, is that the ground state density is the one that minimizes the total energy [66, 69, 70, 75], which is written as

$$E[n] = \langle \Psi[n] | \mathcal{H} | \Psi[n] \rangle = F[n] + \int v_e(\mathbf{r}) n(\mathbf{r}) d\mathbf{r}, \quad (2.5)$$

where $F[n]$ is an universal functional of the density, i.e, it does not depend on v_e [66]. The second term is the functional of density of the external potential $V_e[n]$. $F[n]$ is the sum of the kinetic (T) and electron-electron Coulomb energy (U), that is

$$F[n] = T[n] + U[n]. \quad (2.6)$$

The kinetic energy can be separated into two contributions, one that arises from the kinetic energy of the noninteracting electrons, T_s , and the other is the correlation contribution of the kinetic energy T_c . The Coulomb energy is separated into three terms: the Hartree energy U_H ,

*The external potential can be the interaction between electrons with atoms or an external field.

the exchange energy U_X , and the correlation contribution of the e-e interaction U_c . The first two terms are present in the HF theory. Therefore, we can rewrite the total energy as

$$E[n] = T_s[n] + V_e[n] + U_H + E_{XC}[n], \quad (2.7)$$

where $E_{XC}[n] = T_c + U_X + U_c = U_X + E_c$ is the exchange-correlation (XC) energy. Therefore, by minimizing the above equation with respect to the density, one obtain the ground state density, and from that we can calculate all ground-state properties of the many-body system. One of the problems of Eq. (2.7) is that its functional form is not known [70], and hence, we need to find a scheme to determine it.

2.1.1 The Kohn-Sham self-consistent equations

One way to minimize the total energy [Eq. (2.7)] was proposed by Kohn and Sham [67]. They realized that one can obtain the ground-state density by solving an effective single-particle Schrödinger equation in the presence of an effective potential that contains the many-body effects. Let us now show how this mapping is done. We start by writing the total energy of the non-interacting electrons in the presence of the potential, that is:

$$E_s[n] = T_s[n] + V_{KS}[n]. \quad (2.8)$$

We now minimize it with respect to the noninteracting density n_s , and obtain

$$\frac{\delta E_s[n]}{\delta n_s(\mathbf{r})} = \frac{\delta T_s[n]}{\delta n_s(\mathbf{r})} + v_{KS}(\mathbf{r}) = 0, \quad (2.9)$$

where $v_{KS}(\mathbf{r}) = \delta V_{KS}[n]/\delta n_s(\mathbf{r})$ is the KS potential. Now we minimize the many-particle total energy [Eq. (2.7)] with respect to $n(\mathbf{r})$. That produces

$$\frac{\delta E[n]}{\delta n(\mathbf{r})} = \frac{\delta T_s[n]}{\delta n(\mathbf{r})} + v_e + v_H + v_{XC} = 0, \quad (2.10)$$

where $v_e(\mathbf{r}) = \delta V_e[n]/\delta n(\mathbf{r})$, $v_H(\mathbf{r}) = \delta U_H/\delta n(\mathbf{r})$, $v_{XC}(\mathbf{r}) = \delta E_{XC}[n]/\delta n(\mathbf{r})$, are the external, Hartree and XC potentials, respectively. Comparing Eqs. (2.9) and (2.10) we conclude that if

$$v_{KS}(\mathbf{r}) = v_e(\mathbf{r}) + v_H(\mathbf{r}) + v_{XC}(\mathbf{r}), \quad (2.11)$$

the noninteracting density must be equal to the interacting many-body density, i.e.,

$$n_s(\mathbf{r}) \equiv n(\mathbf{r}). \quad (2.12)$$

This implies that the minimization of the density can be obtained by solving the single-particle Schrödinger equation of the auxiliary system in the presence of an effective potential, $v_{KS}(\mathbf{r})$, defined in Eq. (2.11). The auxiliary Schrödinger equation is

$$\left[-\frac{\mathbf{p}^2}{2m^*} + v_{KS}(\mathbf{r}) \right] \phi_i(\mathbf{r}) = \varepsilon_i \phi_i(\mathbf{r}) \quad (2.13)$$

where $\phi_i(\mathbf{r})$ and ε_i are the KS orbitals and eigenvalues, respectively. The density is given by

$$n(\mathbf{r}) \equiv n_s(\mathbf{r}) = \sum_i^{\text{occup}} |\phi_i(\mathbf{r})|^2 \quad (2.14)$$

in which the sum is realized over all the occupied states. The electronic density above is calculated considering zero temperature. The Eqs. (2.11), (2.13) and (2.14) are known as the KS equations [67]. By solving the KS equations, one replaces the problem of minimizing the total energy [Eq. (2.7)] by a set of three single particle self-consistent equations. The KS equations are self-consistent because the effective potential v_{KS} depends on the density, as we can see from the Hartree potential

$$v_H(\mathbf{r}) = \int d\mathbf{r}' \frac{n(\mathbf{r}')}{|\mathbf{r} - \mathbf{r}'|}, \quad (2.15)$$

and from the XC potential

$$v_{XC}(\mathbf{r}) = \frac{\delta E_{XC}[n]}{\delta n(\mathbf{r})}. \quad (2.16)$$

Hence, to solve the Schrödinger equation, we start the self-consistent cycle with a guess density, which defines the potential, and then obtain the eigenstates that define a new density. This new density produces a new effective potential, and the cycle is repeated until the density converges, i.e., the new density has to be equal to the input density. Once the convergence

of the density is reached, we have obtained the true electronic ground state density that minimizes the total energy, which is written as

$$E = \sum_i^{\text{occup}} \varepsilon_i - \frac{1}{2} \int d\mathbf{r}d\mathbf{r}' \frac{n(\mathbf{r})n(\mathbf{r}')}{|\mathbf{r} - \mathbf{r}'|} - \int d\mathbf{r}v_{XC}(\mathbf{r})n(\mathbf{r}) + E_{XC}[n] \quad (2.17)$$

Let us now make some comments on the KS scheme.

- i) So far we have not done any approximation, i.e, the KS procedure is exact. The only problem is that the exchange and the correlation energies are not known. Therefore, we need to find an approximate expression for them. We present in the next sections the parametrization that is used in this thesis.
- ii) Only the density obtained from the KS equations and its functionals have a physical meaning.
- iii) The KS eigenvalues and eigenstates have, until today, no clear physical meaning [70, 75]. Nevertheless, the KS eigenvalues provide a semiquantitative description of the electronic structure of the investigated system, and because of that, the KS scheme is very useful [70].
- iv) If the the XC potential is not considered we recover the Hartree self-consistent scheme.
- v) The KS scheme is a mean-field theory, which provides a very good description of the many-body system.

In this section we have provided the basis of the DFT and the self-consistent KS procedure considering a non-relativistic and spin- and time independent system. It can be extended to consider these cases [69, 70]. We now extend the DFT for spin-dependent system, and present the XC parametrization used in this thesis.

2.1.2 Spin-density functional theory

Here we present an extension of the DFT to spin-dependent systems, which is called spin-density functional theory (SDFT) [69, 71, 72]. The SDFT can be easily extended from the

spin-independent DFT presented above. In order to introduce the basic aspect of the SDFT, let us consider an external magnetic field $\mathbf{B}(\mathbf{r})$ applied to the many-body system. Its total energy can be written as

$$E[n_\uparrow, n_\downarrow] = F[n_\uparrow, n_\downarrow] + \sum_{\sigma} \int d\mathbf{r} [v_e^{\sigma}(\mathbf{r})n_{\sigma}(\mathbf{r}) + \mathbf{B}(\mathbf{r}) \cdot \mathbf{n}_{\sigma}(\mathbf{r})] \quad (2.18)$$

where n_{σ} is the electron's spin density, with $\sigma = \uparrow, \downarrow$ or $\sigma = \pm 1$. In the SDFT the wave function is determined by both spin densities $n_{\uparrow}(\mathbf{r})$ and $n_{\downarrow}(\mathbf{r})$ [69]. Therefore, the total energy must be minimized by these two new variables, which gives us

$$\frac{\delta E[n_\uparrow, n_\downarrow]}{\delta n_{\sigma}(\mathbf{r})} = \frac{\delta T_s[n_\uparrow, n_\downarrow]}{\delta n_{\sigma}(\mathbf{r})} + v_e^{\sigma}(\mathbf{r}) + v_H(\mathbf{r}) + v_{XC}^{\sigma}(\mathbf{r}) = 0, \quad \sigma = \uparrow, \downarrow. \quad (2.19)$$

The potentials in the above equation are spin-dependent, with the exception of the Hartree potential. Eq. (2.19) has the same functional form as the spin-independent total energy [Eq. 2.10], therefore, the minimization process is done via spin-dependent KS equations,

$$\left[\frac{\mathbf{p}^2}{2m^*} + v_{KS}^{\sigma}(\mathbf{r}) \right] \phi_{i,\sigma}(\mathbf{r}) = \varepsilon_{i,\sigma} \phi_{i,\sigma}(\mathbf{r}) \quad (2.20)$$

where the effective single-particle spin-dependent potential is

$$v_{KS}^{\sigma}(\mathbf{r}) = v_e^{\sigma}(\mathbf{r}) + v_H + v_{XC}^{\sigma}(\mathbf{r}) + g\mu_B \mathbf{s} \cdot \mathbf{B}(\mathbf{r}), \quad (2.21)$$

in which the last term is the Zeeman interaction between electron spin, \mathbf{s} , and the magnetic field. The density is

$$n(\mathbf{r}) = n_{\uparrow}(\mathbf{r}) + n_{\downarrow}(\mathbf{r}), \quad (2.22)$$

where the spin density is $n_{\sigma} = \sum_i |\phi_{i,\sigma}(\mathbf{r})|^2$. The Eqs. (2.20), (2.21) and (2.22) are the self-consistent spin-dependent Kohn-Sham equations.

In order to solve Eq. (2.20) we need all the potentials. In principle the only unknown is the XC potentials, since the functional form of the XC energy is only known by parametrizations.

Exchange-correlation parametrization

The only approximation in the DFT is the parametrization of the XC energy. There are many different types of parametrizations available in the literature, such as the local-density approximation (LDA), gradient-dependent functional (GGE and GGA), hybrid functionals, and many others [70]. In this thesis we used a local-spin-density approximation (LSDA) functional. The LDA consist of approximating the XC energy of each element of volume of the electron liquid with density $n(\mathbf{r})$ by the value of the XC energy of a homogeneous electron gas with the same density. Therefore, the XC energy is written as

$$E_{XC}[n_{\uparrow}, n_{\downarrow}] \approx E_{XC}^{LDA}[n_{\uparrow}, n_{\downarrow}] = \int d\mathbf{r} n(\mathbf{r}) \varepsilon_{XC}^{\text{hom}}([n_{\uparrow}, n_{\downarrow}]; \mathbf{r}), \quad (2.23)$$

where $\varepsilon_{XC}^{\text{hom}}([n_{\uparrow}, n_{\downarrow}]; \mathbf{r})$ is the XC energy per particle of the homogeneous electron gas. The parametrizations are for $\varepsilon_{XC}^{\text{hom}}([n_{\uparrow}, n_{\downarrow}]; \mathbf{r})$ instead of $E_{XC}^{LDA}[n_{\uparrow}, n_{\downarrow}]$, and we utilized the LSDA parametrization provide by Vosko, Wilk and Nusair (VWN) [76]. It is convenient to write

$$\varepsilon_{XC}(n, \zeta) = \varepsilon_X(n, \zeta) + \varepsilon_C(n, \zeta), \quad (2.24)$$

that is, to separate the exchange from the correlation energy, with $\zeta = (n_{\uparrow} - n_{\downarrow})/n$ being the spin-polarization degree. We also dropped the index (hom) in the energies. Let us now look to the parametrization for the exchange energy. $\varepsilon_X(n, \zeta)$ has an analytic form, since its value for the unpolarized and polarized electron gas are known. The exchange energy is given by an interpolation of this two known energies [71, 72, 76] and is given by.

$$\varepsilon_X(n, \zeta) = \varepsilon_X(n, 0) + f(\zeta) [\varepsilon_X(n, 1) - \varepsilon_X(n, 0)] \quad (2.25)$$

where

$$\varepsilon_X(n, 0) = -\frac{3}{4\pi} (3\pi^2)^{1/3} n^{1/3}, \quad (2.26)$$

is the exchange energy of the non-polarized homogeneous electron gas, and

$$\varepsilon_X(n, 1) = 2^{1/3} \varepsilon_X(n, 0), \quad (2.27)$$

is the exchange energy of the spin-polarized homogeneous electron liquid. $f(\zeta)$ is given by

$$f(\zeta) = \frac{(1 + \zeta)^{4/3} + (1 - \zeta)^{4/3} - 2}{2(2^{1/3} - 1)}. \quad (2.28)$$

The correlation energy is also given by the interpolation between the non-polarized [$\varepsilon_C(n, \zeta = 0)$] and spin-polarized [$\varepsilon_C(n, \zeta = 1)$] cases, and has the following form

$$\varepsilon_C(n, \zeta) = \varepsilon_C(n, 0) + \alpha_c(n) \frac{f(\zeta)}{f''(0)} (1 - \zeta^4) + [\varepsilon_C(n, 1) - \varepsilon_C(n, 0)] f(\zeta) \zeta^4 \quad (2.29)$$

where $\alpha_c(n)$ is the spin stiffness. Its value is fitted by VWN. The functional form of the correlation energy above was also investigated by Perdew and Wang (PW) [77]. They proposed different values for the $\varepsilon_C(n, \zeta = 0)$, $\varepsilon_C(n, \zeta = 1)$, and $\alpha_c(n)$, but in the end, both parametrizations [VWN and PW] give almost the same behavior for the correlation energy for all of spin-polarization degree ζ .

The XC potential $v_{XC}^\sigma(\mathbf{r})$ is given by

$$\begin{aligned} v_{XC}^\sigma([n_\uparrow, n_\downarrow]; \mathbf{r}) &= \frac{\delta E_{XC}([n_\uparrow, n_\downarrow]; \mathbf{r})}{\delta n_\sigma(\mathbf{r})} = \frac{\partial [n(\mathbf{r}) \varepsilon_{XC}([n_\uparrow, n_\downarrow]; \mathbf{r})]}{\partial n_\sigma(\mathbf{r})} \\ &= \varepsilon_{XC}([n_\uparrow, n_\downarrow]; \mathbf{r}) + n(\mathbf{r}) \frac{\partial [\varepsilon_{XC}([n_\uparrow, n_\downarrow]; \mathbf{r})]}{\partial n_\sigma(\mathbf{r})} \end{aligned} \quad (2.30)$$

where the XC energies are defined in the Eqs. (2.25) and (2.29).

The total energy in the SDFT is

$$E[n_\uparrow, n_\downarrow] = \sum_{i,\sigma} \varepsilon_{i,\sigma} - \frac{1}{2} \int d\mathbf{r} d\mathbf{r}' \frac{n(\mathbf{r})n(\mathbf{r}')}{|\mathbf{r} - \mathbf{r}'|} - \sum_\sigma \int d\mathbf{r} v_{XC}^\sigma(\mathbf{r}) n_\sigma(\mathbf{r}) + E_{XC}[n_\uparrow, n_\downarrow]. \quad (2.31)$$

It is important to mention here that in our investigated system, a quantum well, we assume that the electronic density is homogeneous in the x - y plane, and inhomogeneous along the growth direction. Therefore, from now the electronic density depends only on the z -coordinate, i.e, $n(\mathbf{r}) \equiv n(z)$.

2.2 Configuration interaction method

Here we present a detailed description of the CI method. We use it to describe the electronic and optical properties of CdTe quantum dots doped with an single magnetic impurity [53, 55, 58, 62, 78]. To describe the QD electronic states, we model it as a two-dimensional harmonic oscillator. With that, the confining potential of Eq. (2.1) is $V(\mathbf{r}_i) = (1/2)m^*\omega_0^2\mathbf{r}_i^2$, where $\mathbf{r}_i = x\hat{i} + y\hat{j}$, and ω_0 is the characteristic frequency of the 2DHO confining potential. For simplicity we consider that there is no magnetic impurity, which will be introduced later. In order to demonstrate the CI method, it is more convenient to write the Hamiltonian [Eq. (2.1)] in second quantization, that is

$$\mathcal{H} = T + H_{ee} = \sum_{i,\sigma} E_{i,\sigma} c_{i,\sigma}^\dagger c_{i,\sigma} + \frac{1}{2} \sum_{\substack{i,j,k,l \\ \sigma,\sigma'}} \langle i\sigma, j\sigma' | V_{ee} | k\sigma', l\sigma \rangle c_{i,\sigma}^\dagger c_{j,\sigma'}^\dagger c_{k,\sigma'} c_{l,\sigma}, \quad (2.32)$$

in which $i = \{n, m\}$ are the 2DHO quantum states, $\sigma = \pm 1$ or \uparrow, \downarrow is the electron's spin z -component, $E_{i,\sigma}$ is the single particle energy of the 2DHO. The derivation of $E_{i,\sigma}$ and its single particle states ($|i\rangle = |n, m\rangle$) are given in the Appendix A. $c_{i,\sigma}^\dagger$ and $c_{i,\sigma}$ are the annihilation and creation operators. The last term is the e-e interaction term. Its matrix elements have an analytic closed form for 2DHO which is derived in Appendix B. The matrix elements take into account both direct and exchange e-e interaction.

To solve the Hamiltonian [Eq. 2.32] we expand the many-body eigenstate $|\Psi\rangle$ in a linear combination of the Slater determinants [73]. This is written as

$$|\Psi\rangle = \sum_{i=1}^{N_c} a_i |\nu_i\rangle, \quad (2.33)$$

where N_c is the total number of configurations, a_i are the expansion coefficient, and $|\nu_i\rangle$ is the i -th configuration, which is written as

$$|\nu_i\rangle = |i_{1\uparrow}, i_{2\uparrow}, \dots, i_{N_\uparrow}\rangle |i_{1\downarrow}, i_{2\downarrow}, \dots, i_{N_\downarrow}\rangle = c_{i_{1\uparrow}}^\dagger c_{i_{2\uparrow}}^\dagger \dots c_{i_{N_\uparrow}}^\dagger c_{i_{1\downarrow}}^\dagger c_{i_{2\downarrow}}^\dagger \dots c_{i_{N_\downarrow}}^\dagger |0\rangle \quad (2.34)$$

where N_\uparrow and N_\downarrow are the number of spin up and spin down electrons, respectively. $|0\rangle$ is the vacuum state.

The CI method consist in writing the Slater determinants with both occupied and unoccupied single particle states [73]. That means that not only the ground state (GS) single particle but also the excited states are included in the expansion of the many-body eigenstates. Therefore, we built our basis by distributing the N -electrons in all possible ways in the 2DHO single particle states. The only restriction is the Pauli exclusion principle. The correlations effects are included by the Hamiltonian matrix elements among two distinct configurations, i.e, $\langle \nu_j | \mathcal{H} | \nu_i \rangle \neq 0$. We obtain better results for larger N_c , but this increases the difficulty to diagonalize the Hamiltonian, due to the large size of the matrix. The total number of configurations is given by

$$N_c = \sum_{N_\downarrow=0}^N \frac{N_{sp}!}{N_\uparrow(N_{sp} - N_\uparrow)!} \frac{N_{sp}!}{N_\downarrow(N_{sp} - N_\downarrow)!} = \sum_{N_\downarrow=0}^N \binom{N_{sp}}{N_\uparrow} \binom{N_{sp}}{N_\downarrow}, \quad (2.35)$$

with N_{sp} being the number of single particle states. From Eq. (2.35) the number of configurations increases with the number of single particle states. For example, for three electrons distributed in three HO shells, i.e, six single particle states, we have $N_c = 220$. Now we distribute three electrons in four shells, $N_{sp} = 10$ and this gives $N_c = 1140$. In five shells there are fifteen single particle states, and the total number of configurations is $N_c = 4060$. Therefore, the number of configurations increases rapidly with increasing the number of single particle states. This makes the CI a very demanding computationally method. To circumvent this problem we can use the symmetries of the problem to reduce the size of the Hilbert space. The first symmetry that we use is the circular symmetry of the QD. The confining potential is circular and the angular momentum is a good quantum number. The total angular momentum of the i -th configuration is given by $L_i = \sum_{j=1}^N L_e$, where $L_e = n - m$ is the angular momentum of an electron in the single particle state $|n, m\rangle$. In the Hamiltonian, Eq. (2.32), both kinetic energy and e-e interaction conserves the total angular momentum. Therefore, we

can diagonalize the Hamiltonian in the subspace of fixed total angular momentum.

As an example, we chose three electrons. Its GS have total angular momentum equal to $L = 1$ or $L = -1$, i.e, two electrons in the s -shell and one electron in the p -shell. Using the fact that the Hamiltonian conserves total angular momentum we can obtain the three electrons GS properties by diagonalizing it in the $L = 1$ or $L = -1$ subspace. This reduce drastically the size of the matrix that has to be diagonalized numerically. For three, four and five shells the total number of configurations in the subspace $L = 1$ is 38, 142 and 420, respectively. One may note that using this symmetry the subspace that has to be diagonalized is reduced in more than 80% for three shells, and almost 90% for five shells.

To reduce even more the size of the Hamiltonian we can apply other conservation rules. The Hamiltonian described at Eq. (2.32) conserves also the spin z -component s_z , and the total spin S^2 . The operator s_z and S are written as

$$\hat{s}_z = \sum_{i,\sigma} \sigma c_{i,\sigma}^\dagger c_{i,\sigma} \quad (2.36)$$

and

$$\hat{S}^2 = \frac{N}{2} + \hat{s}_z^2 - \sum_{ij} c_{j,\uparrow}^\dagger c_{i,\downarrow}^\dagger c_{j,\downarrow} c_{i,\uparrow}. \quad (2.37)$$

For three electrons $s_z = \pm 1/2$ or $s_z = \pm 3/2$, and $S = 1/2$ or $S = 3/2$. Therefore, we reduce the $L = 1$ subspace employing these conservation rules. Since the numerical implementation of the S conservation is difficult and very demanding, we use only the conservation of s_z to reduce the size of our $L = 1$ subspace. As we know, the three electron GS is spin degenerate, i.e, the configurations with both $s_z = 1/2$ and $s_z = -1/2$ are the same. In order to obtain the three electrons GS we chose the $L = 1$ and $s_z = 1/2$ subspace. In this subspace the number of configurations are 15, 56, and 161 for three, four and five shells, respectively. Again, a very large reduction of the matrix size. Other advantage of reducing the size of the Hamiltonian matrix using the symmetries is that it allows us to use LAPACK [79]. This numerical linear

algebra package contains subroutines to solve the eigenvalue and eigenstate problem. With that we have access to all the excited states. For some systems containing many-electrons and many-shells, the matrix size sometimes is too large, which in turn makes the use of LAPACK impossible. To diagonalize this large matrix, we use the fact that it is sparse, i.e, many of the matrix elements are zero. That allows us to use, *e. g.*, the Lanczos method. Fortunately, we deal with $N = 1$ up to 6, in maximum five shells. For these cases LAPACK is sufficient to solve the eigenvalue problem.

We now discuss how to build the Hamiltonian matrix. For that purpose we chose a quantum dot containing three electrons and two shells. Also, we look to the subspace of $L = 1$ and $s_z = 1/2$. In this case there are only two configurations. They have the eigenstates

$$\begin{aligned} |\nu_1\rangle &= c_{00\uparrow}^\dagger c_{10\uparrow}^\dagger c_{00\downarrow}^\dagger |0\rangle \\ |\nu_2\rangle &= c_{10\uparrow}^\dagger c_{01\uparrow}^\dagger c_{10\downarrow}^\dagger |0\rangle. \end{aligned} \quad (2.38)$$

To write these eigenstates we follow two rules: first, we create the spin down electrons. After we have included all of them, we create the spin up electrons. Second, for each spin specie we order the creation operators following the ascending energy, i.e, the first operator at the left has spin up and it is in the lowest single particle energy of this configuration, while the last spin up creation operator is for the higher single particle energy. The same is true for the spin down specie.

We consider now the calculation of the Hamiltonian matrix elements $[\langle \nu_j | H | \nu_j \rangle]$. From Eq. (2.32) we know that the kinetic energy term produces only diagonal terms in the Hamiltonian, and hence, the configurations $|\nu_1\rangle$ and $|\nu_2\rangle$ are not mixed. However, the second term, the e-e interaction, can create off-diagonal terms in the Hamiltonian matrix. First, we calculate the

kinetic energy of the Hamiltonian:

$$\begin{aligned}
T_1 &= \langle \nu_1 | T | \nu_1 \rangle = \sum_{nm\sigma} E_{n,m,\sigma} \langle \nu_1 | c_{nm\sigma}^\dagger c_{nm\sigma} | \nu_1 \rangle = \sum_{nm\sigma} E_{n,m,\sigma} \langle 0 | c_{00\downarrow} c_{10\uparrow} c_{00\uparrow} c_{nm\sigma}^\dagger c_{nm\sigma} c_{00\uparrow}^\dagger c_{10\uparrow}^\dagger c_{00\downarrow}^\dagger | 0 \rangle \\
&= E_{0,0,\uparrow} + E_{1,0,\uparrow} + E_{0,0,\downarrow} = 4\omega_0.
\end{aligned} \tag{2.39}$$

where $E_{n,m,\sigma} = \omega_0(n + m + 1)$ is the single particle energy as demonstrated in Appendix A.

The kinetic energy of $|\nu_2\rangle$ eigenstate is

$$T_2 = \langle \nu_2 | T | \nu_2 \rangle = E_{1,0,\uparrow} + E_{0,1,\uparrow} + E_{1,0,\downarrow} = 6\omega_0. \tag{2.40}$$

Next we calculate the e-e matrix elements. First we work out the H_{ee} term to obtain an easier way to calculate it. For that, we rewrite it in a more compact way, by redefining the composite index as $i = \{n, m, \sigma\}$. The Coulomb term is now written as

$$H_{ee} = \frac{1}{2} \sum_{i,j,k,l} \langle i, j | V_{ee} | k, l \rangle c_i^\dagger c_j^\dagger c_k c_l, \tag{2.41}$$

where the sum over the composite index is for all the possible single particle states. Therefore, we need to take into account all the possibilities, for example, with $k > l$ and $k < l$. There is no $k = l$, otherwise the annihilation operator will act twice in the same orbital. Therefore, we can write H_{ee} as the sum of two terms, one for $k > l$ and the other for $k < l$, which gives

$$H_{ee} = \frac{1}{2} \left(\sum_{i,j,k<l} \langle i, j | V_{ee} | k, l \rangle c_i^\dagger c_j^\dagger c_k c_l + \sum_{i,j,k>l} \langle i, j | V_{ee} | k, l \rangle c_i^\dagger c_j^\dagger c_k c_l \right). \tag{2.42}$$

In the second term of Eq. 2.42 we can use the fact that $c_k c_l = -c_l c_k$. We exchange the indexes k and l by doing $k \rightarrow l$ and $l \rightarrow k$. Thus, we rewrite the second term of the above equation as

$$\begin{aligned}
H_{ee} &= \frac{1}{2} \left(\sum_{i,j,k<l} \langle i, j | V_{ee} | k, l \rangle c_i^\dagger c_j^\dagger c_k c_l - \sum_{i,j,l>k} \langle i, j | V_{ee} | l, k \rangle c_i^\dagger c_j^\dagger c_k c_l \right) \\
&= \frac{1}{2} \sum_{i,j,k<l} (\langle i, j | V_{ee} | k, l \rangle - \langle i, j | V_{ee} | l, k \rangle) c_i^\dagger c_j^\dagger c_k c_l.
\end{aligned} \tag{2.43}$$

We perform a similar manipulation for the indexes i and j . This generates four matrix elements, that can be grouped into two, which generates a factor of two that cancels with the factor $1/2$. The final form of the e-e Hamiltonian is

$$H_{ee} = \sum_{i>j,k<l} (\langle i, j | V_{ee} | k, l \rangle - \langle i, j | V_{ee} | l, k \rangle) c_i^\dagger c_j^\dagger c_k c_l, \quad (2.44)$$

where in the first term the spin of the particle in the state i must be equal to the particle in l , and the same is true for the particles in j and k . This is the well known direct e-e interaction. In the second term we have the same situation, but here the spin of the particle in i and j also must be equal to the particle in k and l , respectively. Therefore, the spin of all electrons in those orbitals must be the same. This term is the exchange e-e interaction. The equation above helps to reduce the number of terms in the sum we have to carry out to obtain the Coulomb matrix elements.

We are able now to evaluate the e-e interaction in the configurations $|\nu_1\rangle$ and $|\nu_2\rangle$. We have to calculate three elements: $\langle \nu_1 | H_{ee} | \nu_1 \rangle$, $\langle \nu_2 | H_{ee} | \nu_2 \rangle$, and $\langle \nu_1 | H_{ee} | \nu_2 \rangle$. Here we used the fact that our matrix is Hermitian, and $\langle \nu_2 | H_{ee} | \nu_1 \rangle = \langle \nu_1 | H_{ee} | \nu_2 \rangle$. Let us begin by calculating the matrix elements between the same states,

$$\langle \nu_1 | H_{ee} | \nu_1 \rangle = \sum_{i>j,k<l} (\langle i, j | V_{ee} | k, l \rangle - \langle i, j | V_{ee} | l, k \rangle) \langle 0 | c_{00\downarrow} c_{10\uparrow} c_{00\uparrow} c_i^\dagger c_j^\dagger c_k c_l c_{00\uparrow}^\dagger c_{10\uparrow}^\dagger c_{00\downarrow}^\dagger | 0 \rangle. \quad (2.45)$$

The expected value of the creation and annihilation operators can be viewed as a scalar product between the two states, that are defined as:

$$|a_{ji}\rangle = c_j c_i c_{00\uparrow}^\dagger c_{10\uparrow}^\dagger c_{00\downarrow}^\dagger | 0 \rangle \quad \text{and} \quad |b_{kl}\rangle = c_k c_l c_{00\uparrow}^\dagger c_{10\uparrow}^\dagger c_{00\downarrow}^\dagger | 0 \rangle. \quad (2.46)$$

The e-e matrix is,

$$\langle \nu_1 | H_{ee} | \nu_1 \rangle = \sum_{i>j,k<l} (\langle i, j | V_{ee} | k, l \rangle - \langle i, j | V_{ee} | l, k \rangle) \langle a_{ji} | b_{kl} \rangle. \quad (2.47)$$

As $i > j$ and $k < l$, we can easily compute the matrix elements. We now evaluate the ket states, starting with the $|b_{kl}\rangle$ state. As we know that $k < l$, there are only three possibilities of non-zero matrix elements: i) $k = \{0, 0, \uparrow\}$ and $l = \{1, 0, \uparrow\}$, ii) $k = \{0, 0, \uparrow\}$ and $l = \{0, 0, \downarrow\}$, and iii) $k = \{1, 0, \uparrow\}$ and $l = \{0, 0, \downarrow\}$. They generate three new ket states,

$$\begin{aligned}
\text{i)} \quad |b_{00\uparrow,10\uparrow}\rangle &= c_{00\uparrow}c_{10\uparrow}c_{00\uparrow}^\dagger c_{10\uparrow}^\dagger c_{00\downarrow}^\dagger |0\rangle = -c_{00\downarrow}^\dagger |0\rangle \\
\text{ii)} \quad |b_{00\uparrow,00\downarrow}\rangle &= c_{00\uparrow}c_{00\downarrow}c_{00\uparrow}^\dagger c_{10\uparrow}^\dagger c_{00\downarrow}^\dagger |0\rangle = c_{10\uparrow}^\dagger |0\rangle \\
\text{iii)} \quad |b_{10\uparrow,00\downarrow}\rangle &= c_{10\uparrow}c_{00\downarrow}c_{00\uparrow}^\dagger c_{10\uparrow}^\dagger c_{00\downarrow}^\dagger |0\rangle = -c_{00\uparrow}^\dagger |0\rangle,
\end{aligned} \tag{2.48}$$

where we have used the fermionic commutation rules to evaluate the ket states. Next, we obtain $|a_{ji}\rangle$, since the creation operators are the same as in the $|b_{kl}\rangle$, the result will be same as presented in Eq. (2.48). By replacing Eq. (2.48) in Eq. (2.47) we obtain the value of the e-e Coulomb matrix of $\langle\nu_1|H_{ee}|\nu_1\rangle$, that is

$$\begin{aligned}
\langle\nu_1|H_{ee}|\nu_1\rangle &= \langle 10 \uparrow, 00 \uparrow |V_{ee}|00 \uparrow, 10 \uparrow\rangle - \langle 10 \uparrow, 00 \uparrow |V_{ee}|10 \uparrow, 00 \uparrow\rangle \\
&+ \langle 00 \downarrow, 00 \uparrow |V_{ee}|00 \uparrow, 00 \downarrow\rangle + \langle 00 \downarrow, 10 \uparrow |V_{ee}|10 \uparrow, 00 \downarrow\rangle \\
&= 2.25\sqrt{\pi\omega_0}.
\end{aligned} \tag{2.49}$$

In Eq. (2.49) there are four terms, the first and the second are due to the direct and exchange e-e interaction of the state configuration listed in i), the exchange is nonzero since all particles have same spin. The third and the fourth terms are due the direct e-e interaction of the configurations in ii) and iii).

In a similar way, we calculate the matrix element $\langle\nu_2|H_{ee}|\nu_2\rangle$. The ket states of the e-e matrix element is $|d_{kl}\rangle = c_k c_l c_{10\uparrow}^\dagger c_{01\uparrow}^\dagger c_{10\downarrow}^\dagger |0\rangle$. The allowed values of k and l are: iv) $k = \{1, 0, \uparrow\}$ and $l = \{0, 1, \uparrow\}$, v) $k = \{1, 0, \uparrow\}$ and $l = \{1, 0, \downarrow\}$, and vi) $k = \{0, 1, \uparrow\}$ and $l = \{1, 0, \downarrow\}$,

which generates the following configurations

$$\begin{aligned}
\text{iv)} \quad |d_{10\uparrow,01\uparrow}\rangle &= c_{10\uparrow}c_{10\uparrow}c_{10\uparrow}^\dagger c_{01\uparrow}^\dagger c_{10\downarrow}^\dagger |0\rangle = -c_{10\downarrow}^\dagger |0\rangle \\
\text{v)} \quad |d_{10\uparrow,10\downarrow}\rangle &= c_{10\uparrow}c_{10\downarrow}c_{10\uparrow}^\dagger c_{01\uparrow}^\dagger c_{10\downarrow}^\dagger |0\rangle = c_{01\uparrow}^\dagger |0\rangle \\
\text{vi)} \quad |d_{01\uparrow,10\downarrow}\rangle &= c_{01\uparrow}c_{10\downarrow}c_{10\uparrow}^\dagger c_{01\uparrow}^\dagger c_{10\downarrow}^\dagger |0\rangle = -c_{10\uparrow}^\dagger |0\rangle
\end{aligned} \tag{2.50}$$

The matrix element is

$$\langle \nu_2 | H_{ee} | \nu_2 \rangle = \langle 01 \uparrow, 10 \uparrow | V_{ee} | 10 \uparrow, 01 \uparrow \rangle - \langle 01 \uparrow, 10 \uparrow | V_{ee} | 01 \uparrow, 10 \uparrow \rangle \tag{2.51}$$

$$\begin{aligned}
&+ \langle 10 \downarrow, 10 \uparrow | V_{ee} | 10 \uparrow, 10 \downarrow \rangle + \langle 10 \downarrow, 01 \uparrow | V_{ee} | 01 \uparrow, 10 \downarrow \rangle \\
&= 1.875\sqrt{\pi\omega_0}.
\end{aligned} \tag{2.52}$$

Lastly, we calculate the e-e matrix element between the configurations, $|\nu_1\rangle$ and $|\nu_2\rangle$. To obtain $\langle \nu_1 | H_{ee} | \nu_2 \rangle$, we just need to calculate the overlap $\langle b_{i,j} | d_{k,l} \rangle$. By looking at Eqs. (2.48) and (2.50) we observe that there is only one non-zero element, which is for $j = \{0, 0, \uparrow\}$, $i = \{0, 0, \downarrow\}$, $k = \{0, 1, \uparrow\}$ and $l = \{1, 0, \downarrow\}$. Therefore, we have

$$\langle \nu_1 | H_{ee} | \nu_2 \rangle = -\langle 00 \downarrow, 00 \uparrow | V_{ee} | 01 \uparrow, 10 \downarrow \rangle = -0.25\sqrt{\pi\omega_0} \tag{2.53}$$

We are now able to diagonalize the Hamiltonian [Eq. (2.32)] in the subspace of the configurations $|\nu_1\rangle$ and $|\nu_2\rangle$. Using Eqs. (2.39), (2.40), (2.49), (2.51), and (2.53), we built the Hamiltonian matrix

$$\mathcal{H} = \begin{bmatrix} \langle \nu_1 | \mathcal{H} | \nu_1 \rangle & \langle \nu_1 | \mathcal{H} | \nu_2 \rangle \\ \langle \nu_2 | \mathcal{H} | \nu_1 \rangle & \langle \nu_2 | \mathcal{H} | \nu_2 \rangle \end{bmatrix} = \begin{bmatrix} 4\omega_0 + 2.25\sqrt{\pi\omega_0} & -0.25\sqrt{\pi\omega_0} \\ -0.25\sqrt{\pi\omega_0} & 6\omega_0 + 1.875\sqrt{\pi\omega_0} \end{bmatrix}. \tag{2.54}$$

The eigenvalues of the Hamiltonian are

$$E_{1,2} = 5\omega_0 + 2.0625\sqrt{\pi\omega_0} \pm \frac{1}{2}\sqrt{(2\omega_0 - 0.375\sqrt{\pi\omega_0})^2 + 0.25\pi\omega_0},$$

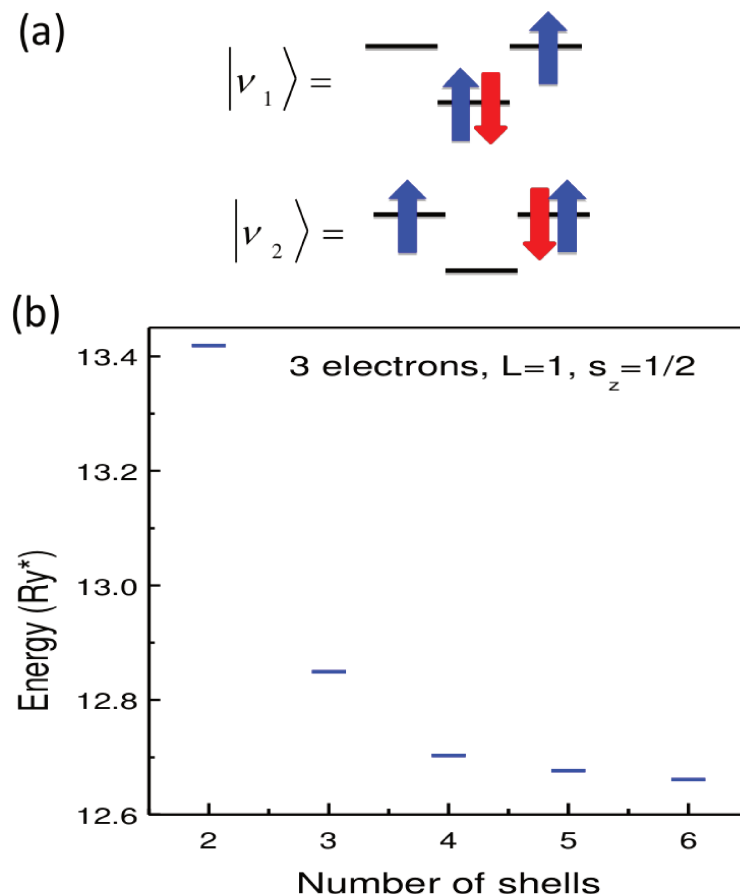


Figure 2.1: (a) Three electrons configurations for a quantum dot containing two shells, in the subspace of $L = 1$ and $s_z = 1/2$. The top figure is the GS, and bottom is the first excited state. (b) Evolution of the three electrons GS as a function of the number of quantum dot shells. We note that increasing the number of shells the GS energy converges. To calculate the GS energy we chose $\omega_0 = 1.98Ry^*$, and $Ry^* = 12.11$ meV.

This result is exact within this subspace, and represents the energy of three electrons confined in a QD containing two shells. To obtain this result, we have considered only two shells, which contains only one more configuration than the GS. A better result is obtained when more excited states are included in the subspace. This is done by including more shells, i.e., increase the number of configurations, and thus adding more correlation. Fig. 2.1 shows the evolution of the three electrons GS as a function of the number of shells for the subspace $L = 1$ and $s_z = 1/2$. As the number of shells is increased, the e-e correlation contribution

lowers the GS energy. We should remember that the three electrons GS is fourfold degenerate due angular momentum and spin ($L = \pm 1$ and $s_z = \pm 1/2$). To calculate the three electrons GS energy, we chose the CdTe QD parameters. The effective mass is $m^* = 0.1m_0$, dielectric constant $\epsilon = 10.6$, the effective Rydberg is $Ry^* = m^*e^4/2\epsilon^2\hbar^2 = 12.11$ meV.

We have presented the CI method. We applied it for many-electrons confined in a two-dimensional parabolic QD. The method can be extended for different potential forms, and systems. To get a better result, one can first proceed with a Hartree-Fock calculation, to obtain the single particle states in the presence of interactions, and then perform exact diagonalization [52,73,80]. All this makes the CI a very powerful method to investigate the many-body effects.

2.3 Magnetic interaction

So far we have neglected interactions between carriers and magnetic impurities. In this thesis, we instigated two different low-dimensional semiconductor materials doped with manganese atoms. The first one is a III-V quantum well with one of the barriers δ -doped with Mn. The second investigated semiconductor is a II-VI quantum dot doped with a single Mn impurity. In these materials Mn is a substitutional impurity, i.e, replaces the cation, and provides a localized spin $M = 5/2$ [12, 81]. Furthermore, in III-V materials, Mn is also an acceptor, which introduces holes into the system.

The Hamiltonian that describes the interaction between carriers and Mn spins is,

$$\mathcal{H}_{mag} = - \sum_{i,j} J(\mathbf{r}_i - \mathbf{R}_j) \mathbf{s}_i \cdot \mathbf{M}_j, \quad (2.55)$$

where $J(\mathbf{r}_i - \mathbf{R}_j)$ is the exchange coupling between the spins of carriers and Mn. \mathbf{s}_i is the spin of the i -th carrier. \mathbf{M}_j is the spin of the j -th Mn ion localized at \mathbf{R}_j . In the investigated QWs, the amount of Mn can be as large as 0.4 monolayers (MLs), and the QD is doped with a single magnetic impurity. Therefore, the above Hamiltonian is treated differently in each case.

2.3.1 Magnetic impurities in III-V semiconductors

In III-V semiconductors the substitutional Mn acts as both localized spin and acceptor impurity, and therefore, by doping these materials with Mn one introduces holes into the system [12]. The exchange interaction between holes and Mn mediates ferromagnetic interaction between Mn spins [11]. In the most studied ferromagnetic semiconductor, GaMnAs, the Curie temperature can reach more than 190 K in samples with $\approx 10\%$ of Mn ions [82, 83]. As ferromagnetism in these materials is mediated by delocalized holes, one can control its magnetic properties with electric fields [84] or even light [85, 86].

Mn in III-V semiconductors tends to replace Ga, but it also can enter in an interstitial position (Mn_I), as illustrated in Fig. 2.2. At that position Mn is a double donor, i.e, provides two electrons to the material, that compensate holes created by substitutional Mn (Mn_S). Due to charge effects, Mn_I tends to be close to the Mn_S and couple antiferromagnetically [12]. The presence of interstitial Mn tends to suppress the ferromagnetism of the GaMnAs. The amount of Mn_I increases with the Mn concentration [87]. One way to reduce the amount of Mn_I is by annealing the sample. In this case the interstitial impurities move to the surface of the sample [12, 88, 89].

Doping GaAs, at first, with Mn, is only possible for concentrations $x_{\text{Mn}} \ll 1\%$. In such case, the holes are binding to Mn, and the sample is a paramagnetic insulator. The binding energy of Mn in GaAs is 112.4 meV, in which 86.15 meV is due the Coulomb interaction and central cell correction, and the remaining 26.25 meV comes from the hybridization between Mn d -orbitals with the host valence band [12, 90]. It was only possible to beat the solubility limit of doping GaAs with Mn by the use of very optimized growth and post-growth conditions, such as low-temperature growth mode and annealing [12]. That allows to dope GaMnAs with Mn concentrations of more than 10% [83]. For concentrations of the order of 1%, GaMnAs is still in the insulating phase. However, there exists an overlap between holes and Mn that

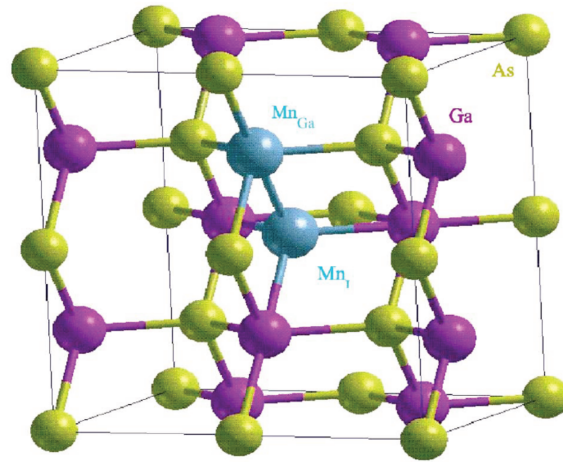


Figure 2.2: GaMnAs unit cell. It illustrates both substitutional and interstitial Mn position in the zincblende lattice. Figure extracted from reference [12].

mediates the ferromagnetic interaction between Mn spins [91]. At this concentration, the GaMnAs is close to the metal-to-insulator (MIT) transition, and the mechanism that induces the ferromagnetic phase is not clear, since the correlations play a crucial role close to the MIT. One of the proposals is that the double exchange mechanism mediates the ferromagnetic phase close to MIT [12]. In the metallic samples with $x_{Mn} > 1.5\%$, the holes are delocalized and occupy the valence- and impurity band that had merged [12,91]. The ferromagnetism in metallic samples is mediated by $p-d$ exchange interaction between holes and Mn. The Zener kinetic exchange theory [11,12,92], which describes the interaction between localized spin and band carriers, has been used to explain ferromagnetism in GaMnAs [93]. This picture explains many of the experimental results observed in metallic samples [94,95].

Regardless of the success of the Zener kinetic exchange theory, the picture that describes ferromagnetism in GaMnAs is still under debate [96]. Another point of view is that holes remain in a localized impurity band, which is detached from the valence band [97]. This model is usually referred as impurity band picture. It also describes some experimental results

[29, 97, 98]. There is a claim in the literature that when GaMnAs is perfectly optimized (excellent growth and annealed conditions), the samples are Mn_I free [88, 89]. In the impurity band picture, Mn_I has a crucial role in its formation, and therefore, in samples where interstitial Mn is not present this picture must fail [12, 96]. Therefore, Zener kinetic exchange is the only theory that explains many of the observed features in the metallic GaMnAs with low hole and Mn compensation [94, 95]. In this thesis we used the Zener kinetic exchange model to describe the magnetic properties of the investigated system.

Since the role of the interstitial Mn is to compensate the number of holes and the Mn_S spins, we define effective parameters to take into account only the uncompensated spins and holes that are used in our model. They are defined as

$$\begin{aligned} x_{eff} &= x_{Mn_S} - x_{Mn_I} \\ p_{Mn} &= x_{Mn_S} - 2x_{Mn_I}, \end{aligned} \tag{2.56}$$

where x_{eff} and p_{Mn} are the uncompensated Mn spin concentration and hole density, respectively. x_{Mn_S} and x_{Mn_I} are the concentration of substitutional and interstitial Mn, respectively. These effective parameters are used to describe the electronic and magnetic properties of GaMnAs [12].

To solve Eq. (2.55) it is necessary to make certain approximations. The many-particle problem is solved in the context of the SDFT. We need then to consider only one electron in H_{mag} . Since the carrier wave function is delocalized, the carrier interacts with a large number of Mn spins, suggesting to use the mean-field approximation. Basically, we replace the spin operator \mathbf{M}_j by its average $\langle M \rangle$ and neglect all the spin correlations [99]. We also make use of the virtual crystal approximation, which consists of replacing the sum over all Mn positions by the sum over all the cation sites weighted by Mn concentration. The exchange constant $J(\mathbf{r}_i - \mathbf{R}_j)$ is then replaced by a constant value J , independent of the position. The virtual crystal approximation restores the periodicity of the material, and therefore, we can

use GaAs Bloch wave functions to describe the electronic properties of GaMnAs[†]. Within these approximations, Eq. (2.55) takes the following form

$$H_{mag} = -JN_0x_{eff}\langle M \rangle \mathbf{e} \cdot \mathbf{s}, \quad (2.57)$$

where N_0 is the number of unit cells per unit of volume, and \mathbf{e} is the magnetization vector direction. As we are interested in the effects along of the growth directions, i.e, z -direction, we now restrict the above Hamiltonian to the z -direction.

$$H_{mag} = -JN_0x_{eff}\langle M_z \rangle s_z, \quad (2.58)$$

in which s_z is the z -component of the carrier spin. So far, we have not specified which carriers interact with Mn spin, i.e, valence band or conduction band electrons. In GaMnAs, there are three main electronic bands[‡], in order of ascending energy, we have, the heavy- (hh) and the light-hole (lh), and the conduction band (e). In a Luttinger-Kohn $\mathbf{k} \cdot \mathbf{p}$ description of the GaMnAs [92,100], the expected value of the above Hamiltonian with respect to the heavy-hole ($|3/2, \pm 3/2\rangle$), the light-hole ($|3/2, \pm 1/2\rangle$), and the conduction band ($|1/2, \pm 1/2\rangle$) Bloch wavefunctions, which are defined by the total spin and its projection in the z -direction ($|J, J_z\rangle$), defines the interaction between Mn and the carriers [12, 81, 92, 95, 101]. This gives us the potential that a carrier spin “feels” due the presence of Mn spins. They are written as

$$\begin{aligned} V_{sd}^e &= -\frac{1}{2}N_0\alpha x_{eff}\sigma_z\langle M_z \rangle \\ V_{pd}^{hh(lh)} &= -\frac{1}{3}N_0\beta x_{eff}\tau_z^{hh(lh)}\langle M_z \rangle \end{aligned} \quad (2.59)$$

in which $V_{b-d}^c = \langle J_z^b, J_b | H_{mag} | J_b, J_z^b \rangle$, where b defines the band and c the carrier. The conduction band s - d exchange constant is

$$\alpha = \langle 1/2, \pm 1/2 | J | 1/2, \pm 1/2 \rangle, \quad (2.60)$$

[†]Doping GaAs with Mn does not alter its crystal lattice, i.e, the GaMnAs remains a zincblende semiconductor.

[‡]To describe properly the electronic structure of GaMnAs the split-off band should be considered, but as it is split from the heavy-hole band by more than 0.3 eV, we neglect this band.

and the valence band p - d exchange constant is

$$\beta = \langle 3/2, \pm 3/2 | J | 1/2, \pm 3/2 \rangle = \langle 3/2, \pm 1/2 | J | 1/2, \pm 1/2 \rangle. \quad (2.61)$$

Their values are fitted from experiments [12], and the accepted values for GaMnAs are $N_0\beta = 1.2$ eV, and $N_0\alpha = 0.2$ eV. The electron spin is $\sigma_z = \pm 1$, and $\tau_z^{hh(lh)} = \pm 3/2(\pm 1/2)$ is the heavy-hole (light-hole) spin. $V_{pd}^{hh(lh)}$ was written in the hole picture, and that basically inverts the valence band and the spin ($\tau_z^{hh(lh)} \rightarrow -\tau_z^{hh(lh)}$). The average of the Mn spin $\langle M_z \rangle$ is related with the magnetization of the Mn spin system [11, 92] and is defined as

$$\langle M_z \rangle = M \mathcal{B}_M(y), \quad (2.62)$$

with $M = 5/2$ being the Mn spin, and $\mathcal{B}_M(y)$ it is the Brillouin function [102], with argument

$$y = \frac{g_{Mn}\mu_B MB}{k_B T} + \frac{J_{pd}M}{2k_B T} \int \xi(z) f(z - L_s) dz \quad (2.63)$$

in which g_{Mn} is the Mn g-factor, μ_B the Bohr magneton, B is the external magnetic field, k_B the Boltzmann constant, and T the temperature. $J_{pd} = 54$ meV nm³ is the exchange constant. $\xi(z) = p_\uparrow - p_\downarrow$ is the magnetization of the hole gas. $f(z - L_s)$ is the distribution function that describes the Mn distribution in the sample, and L_s is center of Mn doping.

The first term of the Eq. (2.63) describes the alignment of the Mn spin with the external magnetic field, and the second is the interaction between holes spin and Mn spins, which originates from the Zener kinetic exchange theory [12] and is responsible for mediating the ferromagnetic interaction in the GaMnAs. In Appendix C, we derive the magnetization of the GaMnAs.

The expression we developed here is justified in the presence of an external magnetic field and for valence bands described in the uncoupled approximations, that is, parabolic dispersion. In this situation, the Mn ions align along the direction of the external magnetic field already at very low values of the field [101]. In the absence of external magnetic field the magnetization has to be described by the full Luttinger-Kohn Hamiltonian with the split-off band included.

2.3.2 Single magnetic impurity in a quantum dot

In this section, we discuss the effects of the interaction between the carriers and the magnetic impurity in two-dimensional quantum dots. We considered only a single magnetic impurity inside the quantum dot. This system has been investigated theoretically [55, 58–60, 78] and experimentally [56, 57, 61, 103]. We consider the same system as before, and we just include the interaction between electrons and the magnetic impurity on Eq. (2.32). The magnetic impurity is a Mn atom, with spin $M = 5/2$. We assume Mn as an isoelectronic impurity, i.e., there is no charge effect associated with it. This is the case for Mn doping in II-VI materials, e.g., CdTe. If the QD is composed by a III-V semiconductor, e.g., InAs, the Mn atom is not isoelectronic, but rather an acceptor impurity. The interaction between electron's and Mn's spins is described via a Heisenberg-like interaction. The Hamiltonian that describes the electron-Mn (e-Mn) interaction is

$$H_{eMn} = -J_c^{2D} \sum_{i=1}^N \mathbf{M} \cdot \mathbf{s}_i \delta(\mathbf{r}_i - \mathbf{R}) \quad (2.64)$$

The e-Mn Hamiltonian is written in the contact interaction model, where $J_c^{2D} = 2J_{bulk}/d$ is the exchange constant. J_{bulk} is the bulk exchange contact interaction parameter, while d is the height of the QD. N is the number of electrons, \mathbf{M} and \mathbf{s}_i are the Mn and electron spins, respectively. \mathbf{r}_i and \mathbf{R} are the position of the i -th electron and the Mn impurity. It is more convenient to write the e-Mn Hamiltonian in the second quantization formalism, which is given by

$$H_{eMn} = - \sum_{i,j} \frac{J_{i,j}(R)}{2} \left[(c_{i\uparrow}^\dagger c_{j\uparrow} - c_{i\downarrow}^\dagger c_{j\downarrow}) M_z + c_{i\downarrow}^\dagger c_{j\uparrow} M^+ + c_{i\uparrow}^\dagger c_{j\downarrow} M^- \right] \quad (2.65)$$

with $J_{i,j}(R) = J_c^{2D} \phi_i(R) \phi_j^*(R)$ being the e-Mn exchange matrix, and $\phi_j(R)$ is the value of the single particle wave function of the i -th orbital at the Mn position (R). Therefore, the strength of this interaction can be modified by changing the Mn position [78]. M_z is the z -component of the Mn spin, and $M^{+(-)}$ is the Mn raising (lowering) spin operator.

This interaction does not conserve orbital angular momentum, except when the Mn is in the quantum dot center. Besides, we need to consider all six possible configurations of the Mn spin: $M_z = -5/2, \dots, 5/2$. The e-Mn interaction also does not conserve s_z and S . It conserves, however, the total spin $J = M + S$ and its z -projection $J_z = s_z + M_z$. Including e-Mn interaction, the number of configurations is now given by $N_c = (2M + 1)N_c^e$, where N_c^e is the number of electron configurations. The ket state configuration described in Eq. (2.34), is now generalized to include the Mn spin configurations and is written as

$$|\nu_i\rangle = |i_{1\uparrow}, i_{2\uparrow}, \dots, i_{N\uparrow}\rangle |i_{1\downarrow}, i_{2\downarrow}, \dots, i_{N\downarrow}\rangle |M_z\rangle \quad (2.66)$$

Figure 2.3 shows the scattering exchange matrix elements $[J_{i,j}(R)]$ as a function of the Mn position. From the top left to the bottom right of the Fig. 2.3 we have $J_{s,s}$, $J_{p,p}$, $J_{d,d}$, and $J_{s,d}$, where s, p, d are the electronic shells of the QD. In the s -shell there is only one orbital, which has $L = 0$, the p -shell has two orbitals, and their angular momentum are ± 1 . The d -shell has three orbitals, one with $L = 0$ and the others with $L = \pm 2$. We choose $L = 0$ orbital of the d -shell to calculate $J_{d,d}$ and $J_{s,d}$.

We observe that the matrix elements between two orbitals with $L = 0$ have a finite value at $R = 0$, while between any orbital and one with $L \neq 0$, its value at $R = 0$ is zero as can be seen in Fig. 2.3(b). We note that at $R = 0$, $J_{ss} = J_{dd} = -J_{sd}$, i.e, the same absolute value, but the scattering of an electron from the s - to the d -shell, or vice versa, changes the sign of the interaction. When we move Mn away from the center, the value of the $L = 0$ e-Mn matrix elements (in absolute value) decreases, while the matrix J_{pp} increases.

In general the e-Mn interaction breaks the cylindrical symmetry, and consequently, the angular momentum is not conserved. However, if Mn is at the QD center, only electrons in the $L = 0$ orbitals are coupled with Mn, and thus, the conservation of the angular momentum is restored. We investigate here only QDs with Mn at its center. The other consequence of the Mn in this position is that electrons in orbitals with finite angular momentum do not

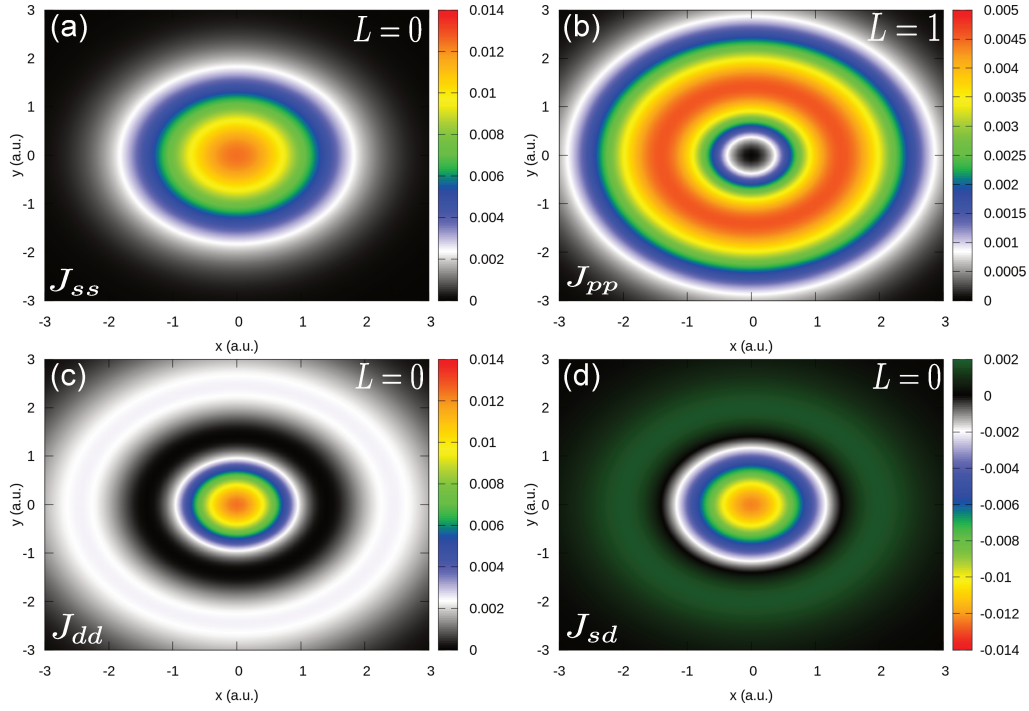


Figure 2.3: Electron-Mn matrix elements as a function of the Mn position. (a) J_{ss} , (b) J_{pp} , (c) J_{dd} , and (d) J_{sd} . For (c) and (d) we chose the $L = 0$ d -orbital to calculate the matrix element. For $R = 0$ only the matrix elements involving scattering between two $L = 0$ orbitals have a finite value, for all the other the other its value is zero as shown in (b). Also at $R = 0$, $J_{ss} = J_{dd} = -J_{sd}$. We used $\omega_0 = 1.98Ry^*$, and the units of the e-Mn matrix elements are in Ry^* .

interact with Mn. We explored the physical consequences of this interaction on the electronic structure and optical properties of QDs doped with a single Mn spin. The results are presented in Chapters 4 and 5.

2.4 Schrödinger's equation solution

In this section we present the split-operator method used to solve the Schrödinger's equation of the quantum well system [104]. This method is based on the time-dependent Schrödinger's equation, and hence, it allows us to investigate the temporal evolution of the wave function. We can also propagate the wave function in the imaginary time domain to obtain eigenstates of the system [104–106]. First, we show how to evolve the wave function in real time. After

that, by changing t by $-i\tau$, we obtain the ground and excited states of the quantum well.

2.4.1 Wave-function time evolution

To present the split-operator method we chose a one-dimensional Schrödinger equation, but it can be easily extended to the three-dimensional case [104]. The time-dependent Schrödinger equation is

$$i\hbar \frac{\partial \psi(z, t)}{\partial t} = \mathcal{H} \psi(z, t) \quad (2.67)$$

in which $\Psi(z, t)$ is the wave function, \mathcal{H} is the Hamiltonian, defined as

$$\mathcal{H} = -\frac{\hbar^2}{2m^*} \frac{d^2}{dz^2} + v_{KS}(z) = T + v_{KS}(z), \quad (2.68)$$

with T being the kinetic energy and $v_{KS}(z)$ the KS potential. Eq. (2.68) has the following formal solution

$$\psi(z, t) = \exp\left(-\frac{i}{\hbar} \int_0^t \mathcal{H} dt\right) \psi(z, 0).$$

For a time $t + \Delta t$ we have

$$\psi(z, t + \Delta t) = \exp\left(-\frac{i}{\hbar} \int_t^{t+\Delta t} \mathcal{H} dt\right) \psi(z, t). \quad (2.69)$$

Since the Hamiltonian is time independent, the wave function evolution can be written as

$$\psi(z, t + \Delta t) = \exp\left(-\frac{i}{\hbar} \mathcal{H} \Delta t\right) \psi(z, t). \quad (2.70)$$

Replacing Eq. (2.68) in (2.70), we obtain

$$\psi(z, t + \Delta t) = \exp\left[-\frac{i\Delta t}{\hbar} \left(\frac{v_{KS}(z)}{2} + T + \frac{v_{KS}(z)}{2}\right)\right] \psi(z, t). \quad (2.71)$$

Defining new operators

$$A = -\frac{i\Delta t}{\hbar} \frac{v_{KS}(z)}{2}$$

$$B = -\frac{i\Delta t}{\hbar} T,$$

using the relation, $e^{A+B+A} = e^A e^B e^A$, we can rewrite Eq. (2.71) as

$$\psi(z, t + \Delta t) = \exp \left[-\frac{iv_{KS}(z)\Delta t}{2\hbar} \right] \exp \left[-\frac{i\Delta t}{\hbar} T \right] \exp \left[-\frac{iv_{KS}(z)\Delta t}{2\hbar} \right] \psi(z, t), \quad (2.72)$$

which is valid only if $[A, [A, B]] = [B, [A, B]] = 0$. This is not true for the kinetic energy and potential operators, since they do not commute. Within this approximation, we introduce an error of the order of $(\Delta t)^3$, as can be seen by

$$\begin{aligned} [A, [A, B]] &= \frac{1}{4} \left(\frac{i\Delta t}{\hbar} \right)^3 [v_{KS}(z), [v_{KS}(z), T]] \cong 0; \\ [B, [A, B]] &= \frac{1}{4} \left(\frac{i\Delta t}{\hbar} \right)^3 [T, [v_{KS}(z), T]] \cong 0. \end{aligned} \quad (2.73)$$

Therefore, we chose Δt small enough, so that we can use Eq. (2.72) to obtain the wave function time evolution. It is important to notice that the operators are unitary, and hence, the wave function norm is preserved at each time steps, which ensures the conservation of the probability [104].

The time evolution of Eq. (2.72) is obtained numerically. We show now the necessary steps to obtain the time evolved wave function. We first discretize the space in a grid of points, which can be either uniform or non-uniform. Next we calculate the initial wave-function $\Psi(z, t)$, and the potential $v_{KS}(z)$. We obtain

$$\xi(z, t + \Delta t) = \exp \left[-\frac{iv_{KS}(z)\Delta t}{2\hbar} \right] \psi(z, t). \quad (2.74)$$

In the following, we act with the operator that contains the kinetic energy, which gives

$$\eta(z, t + \Delta t) = \exp \left[-\frac{i\Delta t}{\hbar} T \right] \xi(z, t + \Delta t). \quad (2.75)$$

Since the kinetic energy operator is a second derivative, we need to approximate it to be able

to calculate $\eta(z, t + \Delta t)$. The exponential is approximated by

$$\begin{aligned}
\exp\left[-\frac{i\Delta t}{\hbar}T\right] &= \exp(\alpha\Delta t) \\
&\approx 1 + \alpha\Delta t + \frac{(\alpha\Delta t)^2}{2!} + \frac{(\alpha\Delta t)^3}{3!} + \dots \\
&= 1 + \frac{\alpha\Delta t}{2} + \frac{\alpha\Delta t}{2} + \frac{(\alpha\Delta t)^2}{4} + \frac{(\alpha\Delta t)^2}{4} + O(\Delta t^3) \\
&= \left[1 + \frac{\alpha\Delta t}{2} + \frac{(\alpha\Delta t)^2}{4} + O(\Delta t^3)\right] \left[1 + \frac{\alpha\Delta t}{2}\right] \\
&\approx \left[1 - \frac{i\Delta t}{2\hbar}T\right]^{-1} \cdot \left[1 + \frac{i\Delta t}{2\hbar}T\right] + O(\Delta t^3). \tag{2.76}
\end{aligned}$$

Again, the error in this approximation is of order of $(\Delta t)^3$. The operator defined in Eq. (2.76) is unitary. Replacing Eq. (2.76) in (2.75), we obtain

$$\left[1 + i\frac{\hbar\Delta t}{4m}\frac{d^2}{dz^2}\right] \cdot \eta(z, t + \Delta t) = \left[1 - i\frac{\hbar\Delta t}{4m}\frac{d^2}{dz^2}\right] \cdot \xi(z, t + \Delta t). \tag{2.77}$$

To solve the above equation, i.e, to obtain $\eta(z, t + \Delta t)$, we use the finite difference method [107] to calculate the position derivatives in each point of the mesh. This transform Eq. (2.77) in a tridiagonal matrix whose solution can be found by inverting the matrix [Eq. (2.77)]. This give us $\eta(z, t + \Delta t)$ at each point of the grid. Therefore, the time evolved wave function is given by

$$\psi(z, t + \Delta t) = \exp\left(-i\frac{v_{KS}(z)\Delta t}{2\hbar}\right) \eta(z, t + \Delta t). \tag{2.78}$$

This solution is obtained for real time propagation. To extend it for imaginary time we replace Δt by $-i\Delta\tau$. In the next section we discuss the imaginary time wave function evolution.

2.4.2 Imaginary time wave function propagation

The eigenfunctions of a Hamiltonian system are obtained via the procedure described in the last section but changing Δt by $-i\Delta\tau$. This implies that we propagate the wave function in the imaginary time domain. In this case, the wave function evolve for the ground state

of the system (see Appendix D for proof). The excited states are obtained imposing the orthogonality condition between the wave functions at each step by the use of the Gram-Schmidt orthogonalization method.

$$|\psi_i(\tau)\rangle = \frac{|\varphi_i(\tau)\rangle - \sum_{j<i} \langle\psi_j(\tau)|\varphi_i(\tau)\rangle |\psi_j(\tau)\rangle}{\sqrt{\langle\varphi_i(\tau)|\varphi_i(\tau)\rangle - \sum_{j<i} |\langle\psi_j(\tau)|\varphi_i(\tau)\rangle|^2}}.$$

The indexes i and j represent the eigenstates of the heterostructure. In the real time propagation the wave functions are always normalized, but in the imaginary time evolution, the wave functions must be normalized at each time step $-i\Delta\tau$. This process has to be repeated, in ascending order of energy to all eigenvalues, until the energies converge.

The convergence process depends on Δt . It must be small so the approximations made in the previous section remain valid. However, if it is too small the convergence process is too slow. One can determine the best Δt by propagating the wave functions in real time, and observing if the energies are conserved during the process. We chose $\Delta t = 0.1$ fs, which produced good results and is not too slow for practical purposes.

To propagate the wave function, we need an initial guess wave function. In this work, we used Hermite polynomials. This method has the following characteristics.

- Very stable.
- A weakly dependence on the initially guessed wave function.
- It can be applied to a wide range of potentials.
- It allows the investigation of real time evolution of the wave function.

Since we realize a self-consistent calculation, by solving simultaneously both Schrödinger's and Poisson's equations, we define the convergence criteria as

$$|E_i^{t+\Delta t} - E_i^t| \leq 10^{-8} \text{ meV}, \quad i = 1, \dots, n \quad (2.79)$$

where n is the number of occupied subbands.

Chapter 3

Electronic and optical properties of quantum wells with Mn- δ -doped barriers

In this Chapter, we present our results for the electronic and optical properties of quantum wells with barriers doped with magnetic impurities. We first introduce (III,Mn)V ferromagnetic semiconductors, and the current interest in the properties of semiconductors heterostructure in which carriers and magnetic impurities are spatially separated. Second, we develop the model used to investigate the QW electronic states. After that, we present our results. As our goal is to understand the role of magnetic interactions on the two-dimensional hole gas, we investigate its properties for many structural parameters, such as the distance between QW interface and Mn-doping, Mn concentration, and Fermi level position. Finally, we present a summary and the conclusions of our findings. The content of this Chapter is an integral part of the final version of a paper by U. C. Mendes and J. A. Brum (2014) in process of submission.

3.1 Introduction

The research field of magnetic semiconductors has attracted much attention for more than two decades [11, 94, 108]. The most investigated material is the (Ga,Mn)As system, where a ferromagnetic phase with Curie temperatures (T_c) reaching 190 K has been observed for samples with Mn concentration of $\sim 10\%$ [82, 83]. Other (III,Mn)V materials have also shown

ferromagnetic phase such as (In,Mn)As, (Ga,Mn)Sb, (In,Mn)Sb [95]. In these materials, Mn acts both as an acceptor and a magnetic impurity. The ferromagnetism in these materials is mediated by the interaction between hole's and Mn's spins [11, 12]. As the magnetic interactions are mediated by the charged carriers, the control of the magnetic properties can be achieved by electrical and optical means. For example, in (Ga,Mn)As that many magnetic properties can be controlled, such as the manipulation of the magnetization vector by an external electric field [84], optical spin transfer torque [85], optical spin-orbit torque [86], and many others effects it was demonstrated [94].

The hole gas that is responsible in the (III,Mn)V semiconductors for the ferromagnetic interaction in these materials is provided by the Mn ions although there is not a one-by-one correspondence between the amount of doping and the hole concentration [12]. To act as an acceptor, the Mn atom has to replace the cation, i.e, become a substitutional Mn impurity. However, it also can occupy an interstitial position, where it is a double-donor [12]. Thus, the holes are self-compensated by the electrons provided by the interstitial Mn. Also, the interstitial Mn tends to be nearby the substitutional Mn due to Coulomb attraction with their spins coupling antiferromagnetically. Therefore, the presence of interstitial Mn reduces both hole density and the Mn effective spin concentration, decreasing the possible values of T_c [12, 95].

Ferromagnetism in (Ga,Mn)As occurs in the metallic phase, i.e, for $x_{\text{Mn}} \geq 0.015$. It also occurs in the insulator regime with $x_{\text{Mn}} \sim 0.01$, but T_c rapidly goes to zero for lower concentrations [95]. The origin of ferromagnetism in these materials is still controversial [96]. Two different mechanism have been proposed to explain the ferromagnetic interaction in (Ga,Mn)As. The first one is that the delocalized holes in the valence band mediate the ferromagnetism, which is described by the Zener kinetic exchange theory [11, 12, 92]. The other theory proposed is that the Fermi level is located in an impurity band, induced by the Mn

states, detached from the valence band [29, 97]. Some authors claim that when (Ga,Mn)As is perfectly optimized, that is, excellent growth and annealed conditions, the samples are Mn_I free [88, 89]. In the impurity band picture, the Mn_I has a crucial role in its formation and therefore, in samples where Mn_I is absent this picture fails [96]. The Zener kinetic exchange mechanism is the only one that explains many of the observed features in metallic (Ga,Mn)As with low hole compensation [94, 95].

Much of the research on GaMnAs is on bulk materials or in heterostructures where both Mn and holes are in the same spatial region. These systems allow a high ferromagnetic Curie temperature due to the strong interaction between the hole gas and the Mn ions. The negative side is the low quality of the material with the hole gas strongly perturbed by the Mn ions, reducing its mobility and the optical quality of the samples. To overcome this difficulty, the (Ga,Mn)As layers were grown in the presence of a quantum well, as for example in a GaAs-(In,Ga)As-(Ga,Mn)As sequence. In this situation, the hole gas is located in the quantum well, separated from the Mn ions. This separation, however, has to be controlled in order to maintain a certain level of overlap between the holes and the Mn ions to assure the magnetic properties. Recently, heterostructure where holes are in a quantum well (QW) and Mn is in the barrier have been investigated by means of transport [28, 109] and optical experiments [31, 110–112]. Their results suggest that the interaction between holes and Mn can not be neglected.

Gazoto *et al.* ref. [31] investigated (In,Ga)As QWs with GaAs barriers δ -doped with both carbon and Mn in alternate sides of the QW. The samples were δ -doped with Mn in order to increase the Mn doping concentration beyond the solubility limit. The presence of the δ -doped C layer on the other side of the QW aimed to increase the hole gas concentration and, with that, to increase the magnetic effects. They observed that the circularly polarized photoluminescence peak as a function of the magnetic field has strong oscillations. It was observed that the magneto-oscillations are more pronounced in the samples with higher Mn

concentration. These oscillations were related with the filling factor of the Landau levels. Magneto-oscillations of the circularly polarized emission peak were also observed in both two-dimensional electron (2DEG) and hole gas (2DHG) [32, 113], The origin of these oscillations are the many-body effects of both the two-dimensional gas [114, 115] and in the optical recombination process [116, 117]. The oscillations of the transition energies observed in ref. [31] are much stronger than those observed in other high quality 2DHG [32, 118]. It was suggested that this difference should be associated with the presence of Mn spins in the heterostructure.

Zaitsev *et al.* ref. [110] performed similar experiment as Gazoto *et al.* ref. [31], namely, circularly polarized photoluminescence in the presence of an external field, but they focused on the low-magnetic-field regime. Their samples are quite similar to those of Gazoto *et al.* [31]. They observed a non-linear behavior in the transition energy as a function of an external magnetic field for field values larger than 1 T. They interpreted their results as the spin-dependent charge transfer between the hole gas confined in the QW and the one confined in a ferromagnetic QW formed from the Mn doping. The same set of samples investigated in ref. [31] was used to study the electron-Mn interaction [112]. For that, the time-resolved photoluminescence and the magneto-Hanle effect were measured. It was observed that both electron lifetime and spin-relaxation time depend strongly on the Mn concentration for samples with high Mn doping. For low Mn doping, both electron lifetime and spin-relaxation time showed almost constant value. These results were interpreted by the increasing of the electron's wave function overlap with the Mn-doping layer [112]. In a similar experiment, Korenev *et al.* [111] observed hysteresis behavior of the circular-polarization degree, and electron spin-relaxation time between 2 ns and 45 ps, depending on the distance between the QW and the ferromagnetic layer. They concluded that the spin-dependent transfer of electrons between the GaMnAs ferromagnetic layer and the QW is responsible for the effects observed.

Aronzon *et al.* ref. [119] performed transport measurements in similar samples to those

investigated in the optical experiments above. They measured Curie temperature of $T_c \sim 30$ K for the ferromagnetic phase. This high temperature was interpreted by the formation of a ferromagnetic phase in the Mn- δ -doped layer. In another transport experiment, Wurstbauer *et. al* [28] showed that for InAs QWs the position of Mn doping strongly affects the results. When the Mn-doped layer is grown after the QW, they observed well-defined Hall plateaus, but when it is grown before the QW the Hall plateaus are not as pronounced as before, showing also a peak in the resistance at zero magnetic field. They attributed this difference to the Mn diffusion in the growing direction and, therefore, into the QW when the Mn was grown before the QW layer [28, 120].

For all these experiments, a clear dependence with the structural parameters, in particular the Mn concentration, doping position was observed. There was, however, no quantitative analysis of these structures. Here, we present the results of a calculation of the electronic structure of (In,Ga)As QWs with GaAs barriers δ -doped with Mn and C. The electronic states of the heterostructure are calculated using the spin-density function theory [66, 67, 72, 121] within the envelope function approximation [100].

This Chapter is organized as follows. In Section 3.2 we present the model used to obtain the electronic states of the structure and the estimate of the emission energies. In Section 3.3, we discuss in detail the theoretical results focusing on the samples used by Gazoto *et al.* [31]. In Section 3.4, we investigate the sample parameters to optimize the magnetic effects. Finally, in Sec. 7 we present our concluding remarks.

3.2 Model

Here we describe the theoretical model used to investigate the electronic structure and optical properties of (In,Ga)As QWs. The heterostructure investigated is illustrated in Fig. 3.1. It is composed of a 500 nm GaAs buffer layer, a carbon (C) δ -doping layer, followed by 10

nm GaAs spacer, a 10 nm $\text{In}_{0.17}\text{Ga}_{0.83}\text{As}$ layer, a GaAs spacer L_s , a Mn δ -doping layer with a concentration x_{Mn} given in percentage of monolayers (MLs), and finally a 60 nm GaAs top layer. The distance L_s between the QW and the Mn doping layer will be considered as a flexible parameter in our model. All the others parameters will be fixed. In the samples studied in ref. [31] we have $L_s = 3$ nm. As a consequence of the Mn and C δ -doping and the thermodynamic equilibrium, the QW presents a 2DHG. We consider the system under an external magnetic field applied along the growth direction, here the z -direction.

We used the envelope function and effective mass approximations to describe the electronic states of the QW. In order to obtain the valence band (VB) states it is necessary to use the six-band Luttinger-Kohn Hamiltonian [122], that describes the heavy-hole (hh), light-hole (lh) and split-off (so) bands and the coupling among them as well as the spin-orbit effects [12]. The presence of the hole gas in a non-parabolic dispersion heterostructure gives origin to non-linear Landau Levels (LLs) [123–125]. Exchange and correlation (XC) contribution of the hole gas has been considered in the framework of the spin-density-functional theory (SDFT) [71, 72]. Our system in particular favors a simplified approach. We are particularly interested in the electronic and optical properties associated with the levels confined in the QW. In our system, the $\text{In}_{0.17}\text{Ga}_{0.83}\text{As}$ is a compressed layer, since the dominant lattice parameter will be that of the GaAs layers (see discussion below). The net consequence is that the hh and lh bands are split by a value of the order of 50 meV. The lh is actually a type-II or marginally type-I heterostructure, depending on the parameters chosen to describe the structure. The hh and lh coupling among the $\text{In}_{0.17}\text{Ga}_{0.83}\text{As}$ QW states is weak for the energies of interest. This is not the case for the states associated with the δ -C region. However, as we will see, the main contribution of these states is in the charge transfer between the δ -C region and the QW. Although the hh and lh coupling may change the quantitative results regarding the charge transfer, it should not give a significant contribution to the properties related to the QW states.

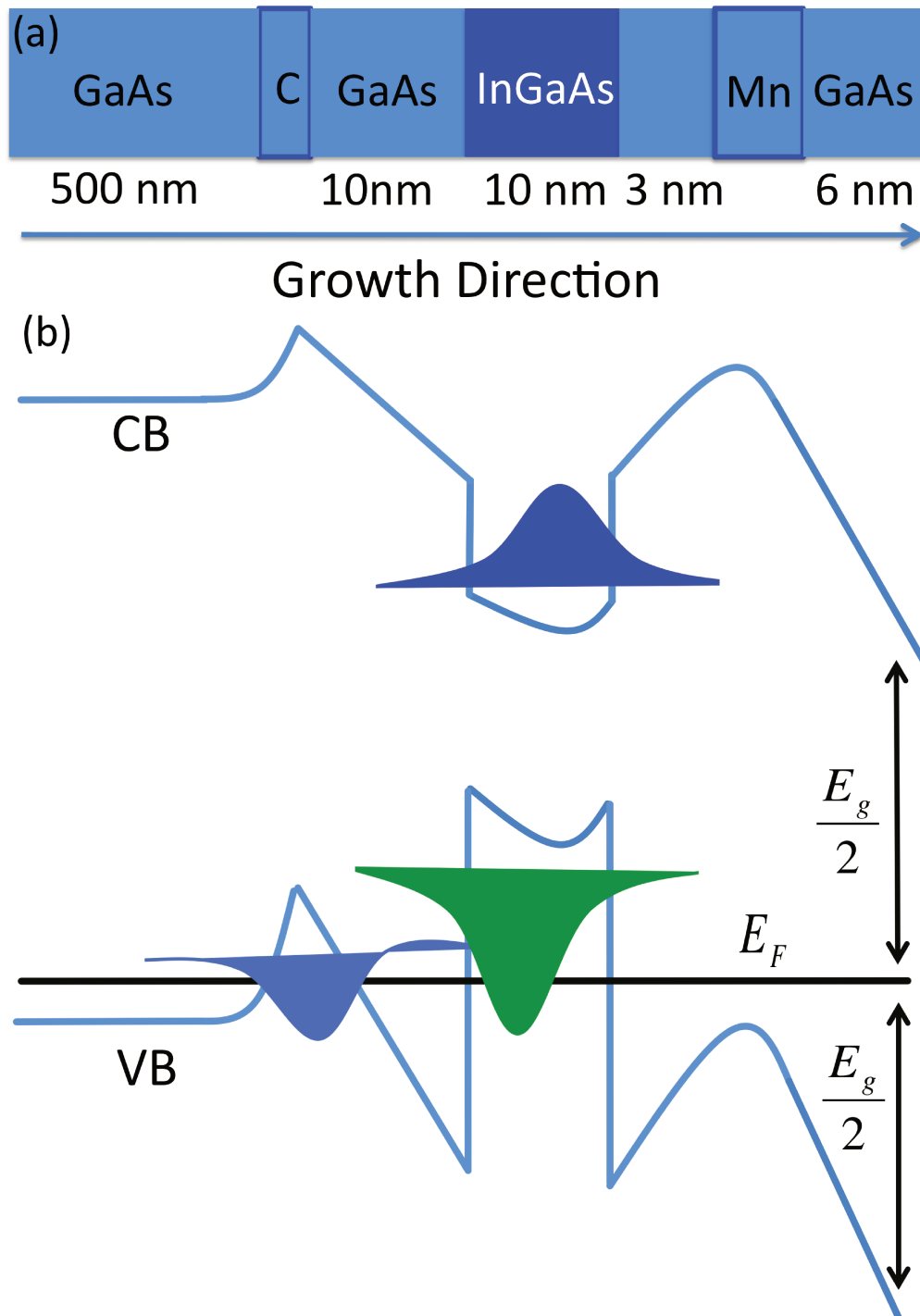


Figure 3.1: (Color online) (a) Schematic representation of the investigated heterostructure. (b) Self-consistent potential and wave functions.

The coupling among the states at the δ -C layer and the states located at the QW is weak due to the 10 nm spacer between the δ -C doping and the QW interface. We therefore use a simple parabolic approximation to describe the VB in our system. To verify this approximation, we calculated the VB structure for our system at zero magnetic field including the presence of the hole gas (see below for the details) for the highest Mn doped sample. We considered both the parabolic approximation and a calculation including the hh and lh coupling (4×4 Luttinger Hamiltonian). The results confirmed that the QW hole states do not show significant coupling and are well described by the parabolic approximation. The main quantitative difference is on the Fermi level, which is lower once the coupling is included. This is a consequence of the non-parabolic dispersion of the hole states in the δ -C region as it should be expected. A better result may be obtained with an effective in-plane mass that takes into account the coupling in a parabolic approximation [126].

The many-body effects of the 2DHG are considered within the SDFT [71, 72]. This allows us to calculate the ground states of our system including XC effects in the presence of an external magnetic field. To obtain the electronic structure we employ the Kohn-Sham (KS) minimization scheme [67], which maps the many-body problem in a set of non-interacting equations, which are solved self-consistently. We obtain the ground-state hole density and the KS eigenvalues. These are not, in principle, associated with the true energy spectrum. However, in practice, they do offer a reasonable first approximation to the actual energy levels [65, 70].

We considered an external magnetic field B applied along of the growth direction (z -direction). We approximate the sample as being homogeneous in the x - y plane. The z -direction and the in-plane (x, y) directions are therefore not coupled. The Hamiltonian can be written as

$$H^{hh(lh)} = H_z^{hh(lh)} + H_{xy}^{hh(lh)}, \quad (3.1)$$

where the first term is the z -part of the Hamiltonian and the second term is the in-plane Hamiltonian. The solution can be written as

$$\Psi^h(\mathbf{r}) = \psi^h(z)\phi^h(x, y). \quad (3.2)$$

Using the Landau gauge, we have

$$\phi_{nk_y}(x, y) = \frac{1}{\sqrt{S}} e^{ik_y y} \varphi_n(x - x_c)$$

with $n = 0, 1, \dots$

where $\varphi(x - x_c)$ are the harmonic oscillator eigenstates centered at $x_c(k_y)$. The in-plane Hamiltonian is written as

$$H_{xy}^{hh(lh)} = -\frac{\hbar^2}{2m_p^{hh(lh)}} \frac{d^2}{dx^2} + \frac{1}{2} m_p^{hh(lh)} [\omega_c^{hh(lh)}]^2 (x - x_c)^2, \quad (3.3)$$

in which \hbar is the reduced Planck constant, $m_p^{hh(lh)}$ is the in-plane hh (lh) effective mass, $\omega_c^{hh(lh)} = eB/m_p^{hh(lh)}$ is the respective cyclotron frequency, and $x_c = -\hbar k_y/eB$ is the orbit center. e is the electron charge, and k_y is the wave-vector in the y -direction. The solution of the in-plane Hamiltonian gives rise to the LLs [127],

$$E_n^{hh(lh)} = \hbar \omega_c^{hh(lh)} (n + 1/2). \quad (3.4)$$

The Hamiltonian in the z -direction is

$$H_z^{hh(lh)} = -\frac{\hbar^2}{2m_{hh(lh)}} \frac{d^2}{dz^2} + v_{het}^{hh(lh)}(z) + v_H(z) + v_{XC}(z) + g^* \mu_B \tau_z^{hh(lh)} B + V_{pd}^{hh(lh)}(z). \quad (3.5)$$

The first term is the kinetic energy, the second term is the heterostructure potential, the third and fourth terms are the Hartree and XC potentials. The fifth term is the Zeeman contribution, and lastly, the hole-Mn (h-Mn) coupling. We now describe each of the Hamiltonian terms in details.

Heterostructure potential - $v_{het}^{hh(lh)}(z)$ is the structural potential which is built up from the band gap difference and band alignment between $\text{Ga}_{0.83}\text{In}_{0.17}\text{As}$ and GaAs layers plus the

strain effects. The energy gaps, at low-temperature, are 1.264 eV [128] and 1.519 eV [129] for $\text{Ga}_{0.83}\text{In}_{0.17}\text{As}$ and GaAs, respectively. The band alignment between them makes that the InGaAs layer be a QW in both conduction band (CB) and VB, i.e, type-I alignment as illustrated in Fig. 3.1(b). As the QW is strained, its band offset contains both the band gap alignment and strain contributions. We can define a band offset without strain [128]. In this case, the VB offset (Δ_V) is given by 15% of the energy gap difference. The remaining energy gap difference, 85%, goes to the CB offset (Δ_C) [128].

Our system is dominated by the GaAs layers and we assume that the whole structure presents the GaAs lattice parameter. The $\text{Ga}_{0.83}\text{In}_{0.17}\text{As}$ layer has a larger lattice parameter than GaAs. This generates a compressive biaxial strain, which alters the QW band offset [130, 131]. If we neglect the *so* band, Γ_7 , the effect of the compressive biaxial strain is manifested in an hydrostatic term, which increases the gap, and a shear deformation, which splits the *hh* and *lh* bands [131]. The deformation potential for the hydrostatic term can be split in a contribution to the conduction band, a_{CB} and one to the valence band, a_{VB} . In this description, the bottom of the CB is lowered by an amount equal to

$$\delta E_c = \delta E_h^{CB} = a_{CB}(\epsilon_{xx} + \epsilon_{yy} + \epsilon_{zz}), \quad (3.6)$$

and the top of the *hh* VB is raised by

$$\delta E_{hh} = -\delta E_h^{VB} + \delta E_s, \quad (3.7)$$

where

$$\delta E_h^{VB} = a_{VB}(\epsilon_{xx} + \epsilon_{yy} + \epsilon_{zz})$$

$$\delta E_s = b_v(\epsilon_{xx} + \epsilon_{yy} - 2\epsilon_{zz})$$

The top of the *lh* VB is lowered by the amount

$$\delta E_{lh} = -\delta E_h^{VB} - \delta E_s. \quad (3.8)$$

For compressive biaxial strain, the strain components are given by $\epsilon_{xx} = \epsilon_{yy} = (a_{\text{GaAs}} - a_{\text{GaInAs}})/a_{\text{InGaAs}} < 0$, and $\epsilon_{zz} = -2C_{21}\epsilon_{xx}/C_{11}$, where a_{GaAs} and a_{GaInAs} are the GaAs and $\text{Ga}_{0.83}\text{In}_{0.17}\text{As}$ lattice parameters, respectively. $a_{VB(CB)}$ and b_v are the deformation potentials. C_{11} and C_{21} are elastic stiffness constants [129–131].

In a $\mathbf{k} \cdot \mathbf{p}$ description of the hh and lh bands, the compressive biaxial strain is described only by diagonal terms in the Hamiltonian, which in our model is included in $v_{het}^{hh(lh)}(z)$. This decouples the VB Hamiltonian into two scalar Hamiltonian.

The combined action of the hydrostatic term and the shear deformation increases the CB and hh VB band offset, while the lh VB decreases with respect to Δ_V . Therefore, the $\text{Ga}_{0.83}\text{In}_{0.17}\text{As}$ energy gap (energy difference between the CB and hh VB band), can be written as

$$E_g = 1.264 + \delta E_{hy}^{VB} + \delta E_{hy}^{CB} \mp \delta E_{sh}. \quad (3.9)$$

The insertion of the Mn in the GaAs is a complex situation [12]. As a first approximation, we assume that the Mn forms an alloy. The $\text{Ga}_{1-x_{Mn}}\text{Mn}_{x_{Mn}}\text{As}$ layer has a larger lattice parameter when compared to the GaAs and follows a similar analysis as for the $\text{In}_{0.17}\text{Ga}_{0.83}\text{As}$ layer regarding the strain effects. One additional difficulty is that the Mn is known to strongly diffuse towards the surface in the GaAs as it was shown from secondary ion mass spectroscopy (SIMS) [120, 132, 133]. Based on the SIMS results, instead of considering a Mn δ -doping layer, we assumed that the total Mn is distributed over many GaAs layers, forming a $\text{Ga}_{1-x_{Mn}}\text{Mn}_{x_{Mn}}\text{As}$ alloy. To take this effect into account, we assume that the system is homogeneous in the x - y directions and only variations of the Mn concentration in the z -direction are considered. We construct a distribution function that takes into account the Mn diffusion in GaAs [120, 132, 133]. The SIMS results show that the Mn diffuses gaussian-like in both sides of the heterostructure. However, it diffuses more strongly in the direction of the surface than in direction of the QW. We consider therefore a double-gaussian distribution function,

as defined below

$$f(z - L_s) = f_0 \exp\{ -[(z - L_s)/\Delta(z)]^2 \}, \quad (3.10)$$

where L_s is the gaussian center, that is, the nominally δ -Mn doping position. $\Delta(z)$ is the average width of the gaussian that describes the Mn diffusion

$$\Delta(z) = \begin{cases} d & \text{if } z < L_s, \\ D & \text{if } z \geq L_s, \end{cases} \quad (3.11)$$

and f_0 is the normalization constant, that is:

$$f_0 = \left[\int_{z_0}^{z_f} \exp\{ -[(z - L_s)/\Delta(z)]^2 \} dz \right]^{-1}, \quad (3.12)$$

where z_0 is the beginning of the GaAs buffer layer and z_f is the end of top-GaAs layer. To avoid many free parameters in our model, we established a relation between D and d , with $D/d = 2$ and $d = 1$ nm. These values are compatible with the SIMS results [120,132,133]. The $\text{Ga}_{1-x_{Mn}}\text{Mn}_{x_{Mn}}\text{As}$ layers also shows a different gap than GaAs, and an intrinsic band offset should be present. The main contribution for the $\text{Ga}_{1-x_{Mn}}\text{Mn}_{x_{Mn}}\text{As}$ band offset, however, has origin in the $sp-d$ interaction, which is discussed below. We will neglect the intrinsic band offset in the following.

Finally, we consider the δ -C layer. For the C concentrations considered here, the C is an acceptor and we assume that the δ -doping layer is actually homogeneously distributed in a 5 Å region. Its effect will be mainly due to the C ions charge effects just as in the usual δ -C layers in GaAs [134]. We do not have any structural potential contribution in this case.

We finally can assemble all the contributions and write the heterostructure potential as:

$$v_{het}^{hh}(z) = (\Delta_V - \delta E_{hy}^{VB} + \delta E_{sh})\Theta(z^2 - L_{Qw}^2/4) - (\delta E_{hyMn}^{VB} - \delta E_{shMn})a_{\text{GaMnAs}}f(z - L_s)$$

$$v_{het}^{lh}(z) = (\Delta_V - \delta E_{hy}^{VB} - \delta E_{sh})\Theta(z^2 - L_{Qw}^2/4) - (\delta E_{hyMn}^{VB} + \delta E_{shMn})a_{\text{GaMnAs}}f(z - L_s)$$

with $\Theta(x)$ being the Heaviside function, and L_{Qw} the QW width, that is, the $\text{In}_{0.17}\text{Ga}_{0.83}\text{As}$ layer.

Hartree potential - The third term of H_z is the Hartree potential, which is obtained by solving Poisson's equation

$$\frac{d^2 v_H(z)}{dz^2} = -\frac{4\pi e^2}{\epsilon} [p(z) - N_c \Theta(z - z_c^f) \Theta(z_c^0 - z) - p_{Mn} f(z - L_s)] \quad (3.13)$$

where ϵ is the GaAs dielectric constant. $p(z)$ is the total hole density, which at zero temperature ($T = 0$ K) is given by

$$p(z) = \begin{cases} \sum_{\substack{b,i \\ \tau_z}} \frac{m_p^b}{2\pi\hbar^2} |\psi_{i,\tau_z}^b(z)|^2 (E_F - E_{i,\tau_z}^b) \Theta(E_F - E_{i,\tau_z}^b) & \text{if } B = 0\text{T}, \\ \sum_{\substack{b,i \\ n,\tau_z}} \frac{m_p^b}{2\pi\hbar^2} |\psi_{i,\tau_z}^b(z)|^2 \int_{-\infty}^{E_F} g_{i,\tau_z}^{b,n}(\varepsilon) d\varepsilon & \text{if } B \neq 0\text{T}. \end{cases} \quad (3.14)$$

The first (second) line describes the hole density in absence (presence) of an external magnetic field. $\psi_{i,\tau_z}^b(z)$ are the KS eigenstates. E_F is the Fermi level and E_{i,τ_z}^b the KS eigenvalues,

$$H_z \psi_{i,\tau_z}^b(z) = E_{i,\tau_z}^b \psi_{i,\tau_z}^b(z) \quad (3.15)$$

The indices of summation b, i, τ_z, n are the hole-type, $b = hh, lh$. i is the level index for each hole, and τ_z is the z -component of the hole spin. n labels the LL as already mentioned. In the absence of a gate voltage, we assume that the Fermi level, E_F , is pinned at the surface states, that is, in the middle of the gap at the surface, $E_F = E_g^{GaAs}/2 - V_g$ [95, 134]. Here, we include the presence of an applied gate voltage, V_g , which allows us to change the Fermi level position. In the presence of an external magnetic field the density of states of the LLs [100, 135], is given by

$$g_{i,\tau_z}^{b,n}(\varepsilon) = \frac{eB}{2\pi\hbar} \frac{1}{\sqrt{2\pi}\Gamma} \exp\left[-\frac{(\varepsilon - E_{i,\tau_z}^{b,n})^2}{2\Gamma^2}\right] \quad (3.16)$$

where $\Gamma = \Gamma_0 \sqrt{B}$ is the LL broadening, and Γ_0 is related the 2DHG mobility. In our calculations, we considered Γ_0 as a parameter. $E_{i,\tau_z}^{b,n} = E_{i,\tau_z}^b + E_n^b$ is the total energy of the b -hole with spin τ_z in the n -th LL of the i -th subband.

Exchange-correlation potential - The fourth term of the Eq. (3.5) is the XC potential. Here we use the Vosko, Wilk, Nusair (VWN) parametrization [76] for the local-spin-density

approximation. $v_{XC}(z)$ depends on both the hole density $p(z) = p_{\uparrow}(z) + p_{\downarrow}(z)$ and the hole gas magnetization $\xi(z) = p_{\uparrow}(z) - p_{\downarrow}(z)$. Again, we consider that the density in the plane is homogeneous and hence, the hole density depends only on the z -coordinate.

Zeeman potential - The fifth term in H_z is the Zeeman interaction between hole spins and the external magnetic field. g^* is the hole g-factor defined as $g^* = g_0\kappa$, where $g_0 = 2$ is the free-electron g-factor. μ_B is the Bohr magneton. The hh and lh spins are $\tau_z^{hh} = \pm 3/2$ and $\tau_z^{lh} = \pm 1/2$, respectively. The actual hole effective g-factor depends on the magnetic field as a consequence of the coupling among the hole states [126]. The same arguments for our parabolic in-plane dispersion apply and a parabolic approximation [126] can be used to include the effects of the subband coupling in the InGaAs

p-d potential - The last term of the Hamiltonian is the p - d interaction between holes and Mn spins. This term has its origin in the interaction between VB states with the d -orbitals of the Mn impurity [136, 137]. The presence of the hole gas is described via Zener kinetic-exchange model [11, 12, 92]. The final expression is written as

$$V_{pd}^{hh(lh)}(z) = -\frac{1}{3}N_0\beta x_{eff}M\tau_z^{hh(lh)}\mathcal{B}_M(y)a_{Mn}f(z - L_s), \quad (3.17)$$

where $N_0\beta$ is the p - d exchange constant of the spin interaction between Mn's and holes, which is, mainly, due the hybridization between the VB (p -bands) and Mn d -orbitals [136, 137]. x_{eff} is the effective concentration of Mn spins (see below). $M = 5/2$ is the Mn spin. $\mathcal{B}_M(y)$ is the Brillouin function [102]. Its argument is given by

$$y = \frac{g_{Mn}\mu_B MB}{k_B T} + \frac{J_{pd}M}{2k_B T} \int \xi(z)f(z - L_s)dz, \quad (3.18)$$

the first term is due the interaction of Mn spin with the external magnetic field, where g_{Mn} is the Mn g-factor, k_B is the Boltzmann constant, and T is the temperature. The second term is the antiferromagnetic interaction between hole spins with Mn spins. This interaction is responsible for the ferromagnetic interaction of Mn's spins [11, 12, 92]. $J_{pd} = \beta/N_0$ is the

p - d exchange constant. N_0 is the cation concentration.

This antiferromagnetic interaction depends on the 2DHG magnetization and the overlap between hole and Mn ions. If Mn ions and holes are in the same spatial region, the distribution function $a_{Mn}f(z - L_s)$ is uniform and replaced by a unity constant. We then obtain the same results known from (Ga,Mn)As bulk [12]. As they are not in the same spatial region the second term in y depends strongly on the structural parameters, namely, the Mn position in the GaAs and the holes states. It is in general small since the holes are mainly located in the QW, which leads to very low Curie temperatures.

(Ga,Mn)As actually shows a magnetization in the xy -plane rather than in the z -direction (growth direction) [92, 101]. It is known, however, that already a small magnetic field along the z -direction aligns the magnetization vector [101]. We are interested in the magnetic effects when an external magnetic field is applied along the growth direction of the structure. Therefore, we assume the magnetization vector aligned along the z -direction in all the cases considered here. This is consistent with our parabolic valence band approximation. In fact, the circularly resolved photoluminescence measurements by Gazato *et.al.* [31] did not show any signature of ferromagnetic alignment at zero magnetic field.

Equations (3.5), (3.13), and (3.14) are the KS equations. They are solved self-consistently. The Schrödinger equation is solved via the split-operator method [104]. In the next section, we present results for the electronic structure of the 2DHG as a function of the external magnetic field for several parameters of the heterostructure. Our goal is to clarify how the Mn concentration, the Mn doping position (L_s), and the application of a gate voltage (V_g) alters the electronic states of the QW. With that we are able to determine the parameters that maximize the magnetic effects in these heterostructures, maintaining the central idea of a high-quality hole gas with the Mn ions and holes separated in different spatial regions.

Optical transitions - Our main interest is to understand the electronic structure and the

effect of the diluted magnetic layers in these structures. In particular, we want to study the efficiency in obtaining a high quality hole gas at the same time as preserving the magnetic effects. Recent work by Gazoto *et al.* [31] on polarized magneto-luminescence have shown oscillations in the energy of optical transitions as a function of the magnetic field. These oscillations are associated with the filling factor of the LLs. We extended our calculations to consider the optical transition for polarized photoluminescence in order to understand the origin of these effects. The calculation of the energy emission transition in the presence of a hole gas and an external magnetic field is a complex one. T. Uenoyama and L. J. Sham [114] and Katayama and Ando [115] consider a perturbative approach with the many-body effects being described by the electron and hole self-energies. They showed that the Coulomb self-energy in a 2DEG system gives origin to filling-factor dependent oscillations in the emission energy. More recently, Hawrylak and Potemski [116] calculated the interband recombination using exact diagonalization techniques. They observed oscillations related to the competition between the electron-electron and electron-valence hole interactions and the splitting of the recombination line for odd filling factors. Asano and Ando [138] also used numerical diagonalization method to obtain the photoluminescence spectra including spin effects. They observed a double peak structure for left-circularly polarized emission and a single peak for the right-circularly polarized emission. These effects are observed in high-quality QWs in the integer quantum Hall state [117]. Such detailed calculations is beyond the scope of the present work. We focus here on the effects of the Mn doping and the electronic structure on the emission energy. The many-body effects are described by the XC interaction [76] and the charge transfer obtained from the self-consistent calculations. The emission energy is extracted simply assuming the Kohn-Sham eigenstates as representing the actual energy spectra. This simple approach should help to understand the dependence of the charge effects with the magnetic field in the photoluminescence transition energies and should be seen

as complementary to the previous works [116, 138].

In order to obtain the energy transitions, it is necessary to calculate in the same framework the CB states. The in-plane Hamiltonian gives us the LLs for the CB, which is $E_m^e = \hbar\omega_c^e(m + 1/2)$. Here m is the electron LL index. The electron Hamiltonian in the z -direction is

$$H_z^e = -\frac{\hbar^2}{2m_e} \frac{d^2}{dz^2} + v_{het}^e(z) - v_H(z) + g_e\mu_B\sigma_z B + V_{sd}^e(z) + v_C(z)$$

where m_e is the effective electron mass in the CB. The second term is the CB heterostructure potential, which can be written as

$$v_{het}^e(z) = (\Delta_C - \delta E_{hy}^{CB})\Theta(z - L_{Qw}/2)\Theta(L_{Qw}/2 - z) - \delta E_{hyMn}^{CB} a_{GaMnAs} f(z - L_s). \quad (3.19)$$

The band offset is composed by 85% of the band gap discontinuity Δ_C , and the compressive biaxial strain for both InGaAs and GaMnAs layers. In the CB there is only the hydrostatic contribution (δE_{hy}^{CB}) for the strain. The third term is the Hartree potential defined at Eq. (3.13). The fourth term is the Zeeman interaction, in which g_e is the electron g-factor and $\sigma_z = \pm 1/2$ is the electron spin. In the fifth term we have s - d interaction between electron's and Mn's spins, which is written as

$$V_{sd}^e(z) = N_0\alpha x_{eff} M\sigma_z \mathcal{B}_M(y) a_{Mn} f(z - L_s), \quad (3.20)$$

where $N_0\alpha$ is the s - d exchange constant between electron and Mn spin. This term has origin in the Coulomb exchange interaction between electrons in the s -band and in the Mn d -orbital [136, 137]. In the last term, we have the effects of the correlation potential in the conduction band due to the presence of the hole gas. Since electrons and holes are treated as different particles, there is no exchange contribution for the CB. This potential was parametrized for the case of a non-polarized 2DHG [139, 140] and gives an important contribution for the band-gap renormalization observed in the optical spectrum of modulated-doped QWs [139]. There is no parametrization for the spin-dependent correlation potential for the CB in this case. Within

our description the electron-hole correlation potential should not present a dependence on the polarization of the hole gas, but only on the total hole gas density. Therefore, the main effect of this contribution will depend on the total charge transfer between the C and Mn acceptors and the QW states. We will neglect this term in our calculations. As it will be discussed in the next section, our results indicate that this simplification does not have a strong influence on the energy oscillations. The CB states are finally described by

$$H^e \Psi_{j,\sigma_z,m}^e(\mathbf{r}) = [H_z^e + H_{xy}^e] \Psi_{j,\sigma_z,m}^e = E_{j,\sigma_z,m}^e \Psi_{j,\sigma_z,m}^e(\mathbf{r}), \quad (3.21)$$

where the envelope function writes as

$$\Psi_{j,\sigma_z,m}^e(\mathbf{r}) = \psi_{j,\sigma_z}^e(z) \phi_m^e(x, y) \quad (3.22)$$

with the z -direction Schrödinger equation being

$$H_z^e \psi_{j,\sigma_z}^e(z) = E_{j,\sigma}^e \psi_{j,\sigma_z}^e(z), \quad (3.23)$$

and the in-plane part as

$$H_{xy}^e \phi_m^e(x, y) = E_m^e \phi_m^e(x, y). \quad (3.24)$$

The transition energy is obtained as the energy difference between the electron's and hole's eigenstates. Our focus is on the circularly polarized emission. The right circularly polarized (σ_+) light is given by the recombination of a spin-down electron with a spin-up hh , while the left circularly polarized (σ_-) light is the recombination of a spin-up electron with a spin-down hh . The recombination energies are given by

$$\begin{aligned} E_{Tot}^{\sigma_+} &= E_{j,\downarrow}^e + E_m^e + E_{i,\uparrow}^{hh} + E_n^{hh}, \text{ for } \sigma_+ \\ E_{Tot}^{\sigma_-} &= E_{j,\uparrow}^e + E_m^e + E_{i,\downarrow}^{hh} + E_n^{hh}, \text{ for } \sigma_-. \end{aligned}$$

The emission is allowed only if the LLs of electron and hole states are the same Landau Levels ($n = m$). To enhance the magnetic field effects on the transition energies, we subtract the

transition energy at zero magnetic field from $E_T^{\sigma_+(\sigma_-)}(B)$, redefining the transition energy as

$$E_T^{\sigma_+(\sigma_-)}(B) = E_{Tot}^{\sigma_+(\sigma_-)}(B) - E_{Tot}^{\sigma_+(\sigma_-)}(0). \quad (3.25)$$

To magnify the non-linear effects in the transition energy we further subtract from $E_T^{\sigma_+(\sigma_-)}(B)$ all terms that are linear in B , i.e, we subtract both Zeeman ($E_z^{\sigma_+(\sigma_-)}$) and Landau (E_L) energies. Therefore, we define the non-linear energy shift as

$$\Delta E_T^{\sigma_+(\sigma_-)}(B) = E_T^{\sigma_+(\sigma_-)}(B) - E_z^{\sigma_+(\sigma_-)}(B) - E_L(B) \quad (3.26)$$

Parameters - The holes in the heterostructure are provided by both the C and the Mn doping. The C concentration N_c is fixed for all systems we investigate here. We consider $N_c = 13.35 \times 10^{18} \text{ cm}^{-3}$ which is the value obtained by fitting the measured hole concentration in the QW for a sample without Mn and comparing with our calculations [31]. The nominal concentration of Mn, x_{Mn} , is known from the growth process. However, it does not provide the real hole density, since Mn can be either a substitutional impurity or an interstitial one [12]. In the first case Mn replaces Ga, and provides one hole to the system, while at the interstitial position it is a double donor, and gives two electrons. Therefore, there is a self-compensation of holes by the electrons, and the total density of holes provided by the Mn is given by $p_{Mn} = x_S - 2x_I$, where x_S and x_I are the concentration of substitutional and interstitial Mn, respectively [12]. Furthermore, because of the attractive Coulomb interaction, the interstitial Mn ions tend to be near to the substitutional ones presenting an antiferromagnetic coupling, which reduces the net Mn spins [12]. The effective Mn spin concentration is given by $x_{eff} = x_S - x_I$ [12,95]. In our model, we only describe the uncompensated substitutional Mn, p_{Mn} with the effective spin concentration x_{eff} . We do not have direct access to x_S and x_I . These values are strongly dependent on sample growing conditions. Gazoto *et al.* [31] estimate the hole concentration in the quantum well, p_{QW} , from Shubnikov-de-Hass and Stoke shift measurements. We extract p_{Mn} from our calculations by fitting the theoretical value p_{QW}

with the experimental data. This allows us to determine p_{Mn} for each sample which are used as fixed parameters for the remaining calculations. The other parameters are described in Table 3.1.

Table 3.1: Parameters used in the self-consistent calculation. The $\text{In}_{0.17}\text{Ga}_{0.83}\text{As}$ strain parameters used are linear interpolation between GaAs and InAs parameters. The parameters were extracted from the refs. [12, 126, 128–130, 141, 142].

Parameters	GaAs	InAs
γ_1 [129]	6.98	20.0
γ_2 [129]	2.06	8.5
C_{11} (10^{10} Pa) [129]	12.21	8.329
C_{21} (10^{10} Pa) [129]	5.66	4.526
a_L (\AA) [129]	5.65325	6.0583
a_{vb} (eV) [129]	-7.17	-5.08
a_{cb} (eV) [129]	-1.16	-1.0
b_v (eV) [129]	-2.0	-1.8
m_p^{hh} [126]	0.11	
g_e [126]	-2.9	
g^* [126]	-2.3	
$E_g(x_{In})$ (eV) [128]	$1.519 - 1.583x_{In} + 475x_{In}^2$	
Δ_{VB} (eV) [130]	$0.15E_g(x_{In})$	
$N_0\alpha$ (eV)	0.2	
$N_0\beta$ (eV) [12, 141]	1.2	
J_{pd} (meV nm^3) [12]	54	

We use a parabolic approximation for the valence band structure and a single set of parameters in the whole structure. Our focus is on the InGaAs layer. As already mentioned, a parabolic approximation is well justified for the in-plane mass as well as for the hole effective g-factor, g^* [126]. Furthermore, a parabolic contribution to these effective parameters is possible to include the hh - lh coupling effects in this case. Wimbauer *et al.* [126] performed a systematic study for this situation. They obtained $g^* \simeq 2.3$ and $m_p^{hh} \simeq 0.121$ for a 100 \AA InGaAs QW with In concentration of 18%. For the GaMnAs the parameters are not known and hence we used the same as GaAs. Table 3.1 shows the effective parameters used for the whole structure. This set of parameters gives values similar to those of ref. [126] for the InGaAs. At the same

time, they are compatible with a diagonal approximation for the GaAs Luttinger Hamiltonian. Observe that these parameters warrant the same m_{hh} effective mass for InGaAs as obtained from a linear interpolation of the GaAs and InAs Luttinger parameters. The $In_{0.17}Ga_{0.83}As$ strain parameters are a linear interpolation between GaAs and InAs parameters.

In the next section we present the results of our self-consistent calculations for the valence band structure and discuss the influence of several heterostructure parameters. We also compare the optical transition energies calculated in our simple model with the experimental results [31].

3.3 Results

We present here our results for the electronic structure and emission energies for different heterostructures. Our main interest is to understand the role of the structure to obtain simultaneously a good quality hole gas in the QW and magnetic effects in the hole gas. We therefore focus on the influence of the structural parameters and the effects of interactions on the electronic structure. The emission energies in our simple approximation are considered as an example of the manifestation of these effects. Initially we analyze the samples from Gazoto *et al.* [31]. The uncompensated Mn concentration is obtained from the measured QW hole gas as discussed in the previous section. Table 3.2 summarizes these values.

Table 3.2: Mn effective parameters used in the self-consistent calculation. They were obtained by fitting the experimental hole density given in ref. [31] with the first occupied QW subband.

x_{Mn}	x_{eff}	$p_{Mn} (10^{11} \text{ cm}^{-2})$	$p_{QW}^{1st} (10^{11} \text{ cm}^{-2})$
0.4	0.134	9.92	5.2
0.2	0.067	7.95	4.2
0.13	0.044	7.6	3.9

Figure 3.1(b) illustrates schematically the self-consistent profile potential for the hh VB and CB for $x_{Mn} = 0.4$ ML and $L_s = 3$ nm. The wave-functions in the VB represents the

first occupied hh -subband. We note that there is a 2DHG in the carbon doped layer. In the Mn layer there is no occupied state. Therefore, the only hole gas interacting with the Mn ions has its origin in the QW states. We also show the QW ground-state for the CB. We observe the strong anisotropy between the VB and CB. This is partially due to the different doping on both sides of the QW but also due to the proximity of the QW structure with the surface (63 nm). We assume that the Fermi level is pinned at the surface states which creates a high electric field between the surface and the QW as can be observed in Fig. 3.1(b). These features are common for most of the samples discussed here.

We now discuss the magnetic effects in the electronic structure. As a second step, we compare and discuss our results with the experimental results from Gazoto *et al.* [31]. Finally, we examine the structural parameters of the samples in order to enhance the magnetic effects in the hole gas.

3.3.1 Role of interactions

We consider the sample with $x_{Mn} = 0.4$ ML as our case study. This sample presents the largest magneto-oscillations observed in ref. [31] and also it shows the highest QW hole gas density. The other samples measured experimentally [31], with $x_{Mn} = 0.2$ and 0.13 MLs are considered in the following. The LLs broadening (Γ_0) is fixed for all investigated heterostructures independently of x_{Mn} . Γ_0 is related with the 2DHG mobility, which is approximately $\sim 2 \times 10^3$ cm²/Vs at 77 K in the QW for the samples investigated in ref. [31]. This implies in $\Gamma_0 \approx 1.8$ meV B^{-1/2}. The experimental photoluminescence is performed at 2 K. At lower temperatures the mobility increases and this leads to smaller values for the LL broadening. In our calculations we consider a value of $\Gamma_0 = 0.25$ meV B^{-1/2}.

We first perform a systematic study of the electronic structure as a function of the interactions. First, we present the results considering all interactions in the Hamiltonian. Second, we exclude the XC potential, i.e, $v_{XC} = 0$. This allows us to verify the role of Mn interactions in

the LL fan diagram and, consequently, in the transition energies. Finally, we investigate the effects of XC in the hole states assuming $v_{XC} \neq 0$ and $V_{pd} = 0$. We are then able to determine which contribution is more significant to the electronic structure and its consequences in the optical magneto-oscillations. It follows with a comparison with the experimental results [31].

All interactions

Here we consider the full Hamiltonian, Eq. (3.5), with all terms. At zero magnetic field, there are two hh and one lh occupied subbands. Fig. 3.2(a) shows the self-consistent potential profile for the hh and lh bands, and the wave functions of the hh occupied subbands at zero magnetic field. The first hh state is confined in the QW, while the second hh state is located mainly in the C layer. As the QW is compressed biaxially the lhs are confined in the C doped layer. The ground state lh is occupied but for clarity we did not show here its wave function. We observe that the overlap among the hh 's wave functions is small, which makes the 2DHG in the QW and the C layer almost independent from each other. Another feature of this heterostructure is that there is no hole gas in the Mn-doped layer as suggested in the refs. [110, 119]. The interaction between the hole gas and the Mn ions occurs only due to the penetration of the hh wave function in the barrier and the Mn diffusion. The absence of a hole gas in the Mn doped layer is a consequence of both its short distance from the surface (63 nm) and the Fermi level pinned at the surface states [95, 134]. This generates a strong electric field between the surface and the QW, inducing the transfer of the holes from the Mn to the QW. The presence of other acceptor doping, namely the C-doped layer, also contributes to the lack of holes in the Mn layer. It is well known that by doping with another acceptor before growing the GaMnAs layer the amount of interstitial Mn increases, decreasing the concentration of uncompensated Mn [143].

Figure 3.2(b) shows the holes LLs fan diagram. In order of increasing energy we have at zero magnetic field hh_{n,τ_z}^1 subband where the upper index refers to the state order, located at

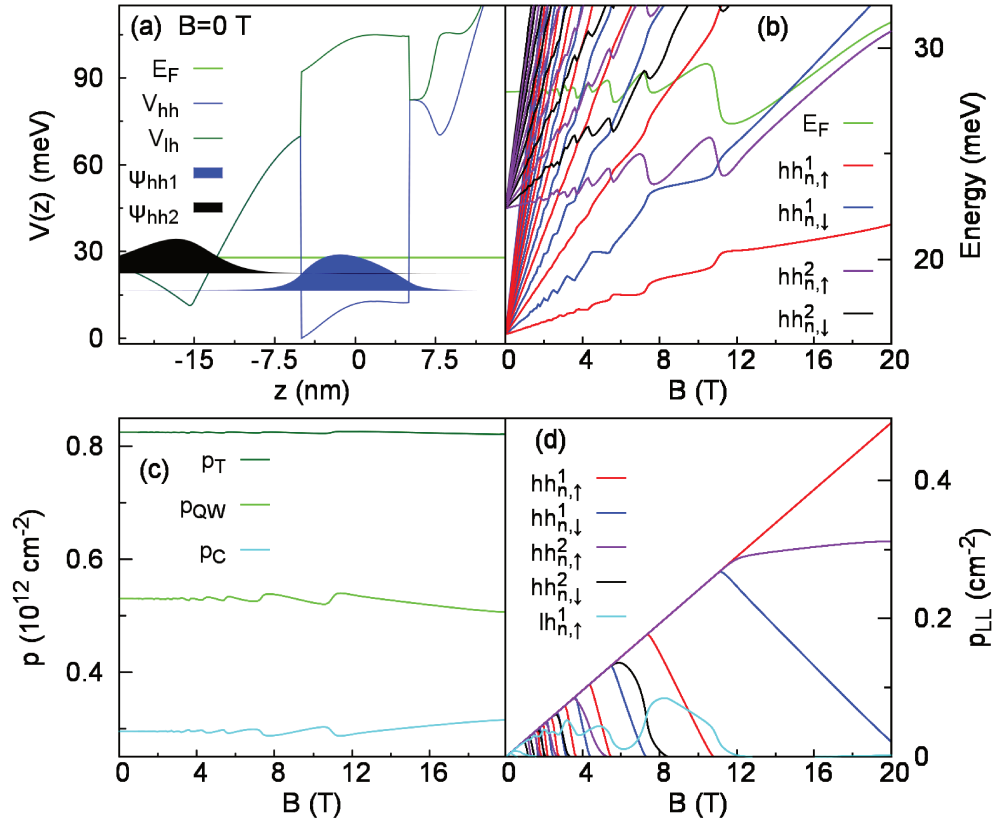


Figure 3.2: (Color online) (a) Profile of the self-consistent potential for hh and lh bands. The lh band in the QW and Mn-doped layer are type-II. The wave functions represented here are the two hh occupied subbands. There is also a lh occupied subband band, located at the C layer, which is not shown here. (b) Heavy-hole LL fan diagram. (c) Two-dimensional hole density in the quantum well (p_{QW}), C-layer (p_C) and their sum (p_T) as a function of the magnetic field. (d) LLs hole densities as a function of the magnetic field.

the QW, followed by hh_{n,τ_z}^2 state, located at the C-layer and the lh_{n,τ_z}^1 which is also located at the C-layer. Here the lower indices refer to the Landau Level, n , and the spin indices, τ_z . All these states are occupied although lh_{n,τ_z}^1 is only marginally occupied. We observe that all LLs and the Fermi level oscillate as a function of the magnetic field. These oscillations have origin in both the crossing of the LLs with E_F , and the charge transfer between the hole gas in the QW and the carbon layer. However, we observe that $hh_{1,\uparrow}^1$ and $hh_{1,\downarrow}^1$ oscillate in the same or opposite directions, depending on which spin hole level is crossing E_F . On the other hand, the $hh_{1,\uparrow}^2$ and $hh_{1,\downarrow}^2$ levels oscillate roughly following the E_F oscillations. We did not show the lh LL

fan diagram for the sake of clarity. Figure 3.2(c) shows the QW and the C hole concentration. This is possible to characterize here since the wave-functions are well separated spatially. It gives us a measure of the charge transfer between the QW and the C layer as a function of the LL filling factor. Figure 3.2(d) shows the LLs occupation as a function of the magnetic field. Most of the LLs show a similar behavior. They increase the hole concentration linearly with the magnetic field, as it should be expected from the LL degeneracy. As one LL crosses the Fermi level, it starts to be depopulated. If there was no broadening, this should be an abrupt decrease. In our case, the broadening makes the depopulation of the LL to last a finite range of magnetic field but with a nearly linear decrease. This behavior is consistent for all LLs associated to QW subbands. The C layer LLs show a different behavior. As they start to be depopulated, they do not follow a linear behavior. Actually, this behavior is associated with the LLs oscillation that roughly follows the Fermi level oscillation, as if they were partially pinned in the Fermi level.

Let us look now in more detail in the QW LLs oscillations and their correlation with the LL filling factor (ν). We focus on the effects on the lowest energy QW LLs, that is, $hh_{0,\uparrow}^1$ and $hh_{0,\downarrow}^1$ since they are responsible for most of the properties in transport and optical emission. We start our analysis at ~ 5 T since for lower magnetic fields the number of occupied LLs makes it difficult to obtain a clear picture. At this magnetic field, the states at the QW that are (fully) occupied are hh_{i,τ_z}^1 , $i = 0, 1$ and $\tau_z = \uparrow, \downarrow$. We have in this situation an unpolarized hole gas in the QW. Other LLs from states at the C layer are also occupied but they do not affect the results we discuss here. At ~ 5 T, as shown in 3.2(d) $hh_{1,\downarrow}^1$ starts to be depopulated, polarizing the QW hole gas. It depopulates entirely at ~ 7 T when the hole gas in the QW becomes spin-polarized. In this interval, $hh_{0,\uparrow}^1$ and $hh_{0,\downarrow}^1$ have a significant difference in their magnetic field dependence, with $hh_{0,\downarrow}^1$ energy increasing strongly with the magnetic field while $hh_{0,\uparrow}^1$ shows a weak dependence with it. At ~ 7 T $hh_{1,\uparrow}^1$ starts to be depopulated and the QW

hole gas starts to decrease its polarization until ~ 11 T when $hh_{1,\uparrow}^1$ is fully emptied and the QW hole gas is unpolarized. In this interval of magnetic field, both $hh_{0,\uparrow}^1$ and $hh_{0,\downarrow}^1$ states show similar weak magnetic field dependence. At ~ 11 T $hh_{0,\downarrow}^1$ starts to be depopulated and the hole gas is again polarized. The magnetic field dependence of $hh_{0,\uparrow}^1$ and $hh_{0,\downarrow}^1$ states again differ significantly, repeating the previous pattern. This behavior manifests itself by an oscillation in the LL dependence with the magnetic field. These oscillations take place each time a QW LL is emptied and a new one starts to be depopulated. It should be observed that during this range of magnetic fields hh and lh LLs associated to the C layer are also changing their occupation in relation to their maximum occupation but that does not affect the $hh_{0,\uparrow}^1$ and $hh_{0,\downarrow}^1$ magnetic field dependence. Actually, this picture is confirmed by the charge transfer between the C layer and the QW. Figure 3.2(c) shows the hole concentration in the hh^1 (p_{QW}) and the C layer (p_C) (more exactly, the hole concentration in the hh^2 and lh^1 states), and their sum (p_T). It shows that the charge transfer oscillates following the QW LL filling factor. This charge transfer has its origin in the thermodynamic equilibrium. The charges in the structure rearrange themselves in order to reach the same chemical potential in the whole structure. As the LLs are emptied, the local chemical potential changes abruptly inducing a charge transfer between the two hole gases. The charge transfer between the C layer and the QW, however, is not significant. Clearly, the most important effect is the spin-polarization of the hole gas in the QW, a consequence of the charge transfer between LLs within the QW. The oscillations observed in p_T are due the charge transfer between the QW and C holes with the surface states. The total density is constant.

We now turn our attention to the consequences of these results in the optical emission. For that, we first calculate the CB LLs. In Figure 3.3(a) we plot the LLs associated with the CB QW ground state, $e_{m,\sigma}^1$. We observe oscillations in the LLs associated to the crossing of the QW hole LLs. These oscillations, however, do not change the LLs dependence with the

magnetic field and they show the same behavior for both spins. The observed oscillations have their origin in the charge transfer between the C layer and the QW. We remind that we did not include here any effect due to the correlation potential. However, we should not expect a qualitative influence from this term. It certainly should lower the energy levels and enhance the oscillations since correlation potential should be dependent on the total hole density. Its effect is associated to the oscillations in the hh^1 hole concentration. As we observed, this is a minor effect [see Fig. 3.2(c)]. We therefore do not expect a qualitative effect in the oscillations coming from this contribution. It does, nevertheless, contribute to a lowering in the levels energy. The energy transitions calculated within this approximation should give a reliable behavior with the magnetic field but overestimate the total energy.

Figure 3.3(b) shows the fundamental energy transition shift, $E_T^{\sigma_+ (\sigma_-)}(B)$ and the non-linear energy shift $[\Delta E_T^{\sigma_+ (\sigma_-)}]$ as a function of the magnetic field. We observe a non-linear behavior in the emission energy shift as a function of the magnetic field. This effect is enhanced in the non-linear transition energy where the magnetic field linear dependent terms are extracted from the transition energies. This non-linear behavior is dominated by the QW holes LLs oscillations. We observe that the non-linear behavior for the σ_- transition increases as the QW hole gas starts to be polarized reaching a maximum value when the hole gas is spin-polarized. As this polarization starts to decrease, the non-linear behavior for σ_- decreases. The opposite behavior is observed for the σ_+ transition. It shows a negative non-linear behavior which roughly follows the same dependence. As a consequence, if we look at the transition energy shift, $E_T^{\sigma_+}$ shows a maximum oscillation at odd filling factor while $E_T^{\sigma_-}$ shows a maximum oscillation at even filling factor. Finally, the non-linear behavior reaches a maximum value near 1 meV. This value is weaker than the values observed experimentally but in the same order of magnitude.

From the results discussed here we verified that the oscillations in the electronic structure

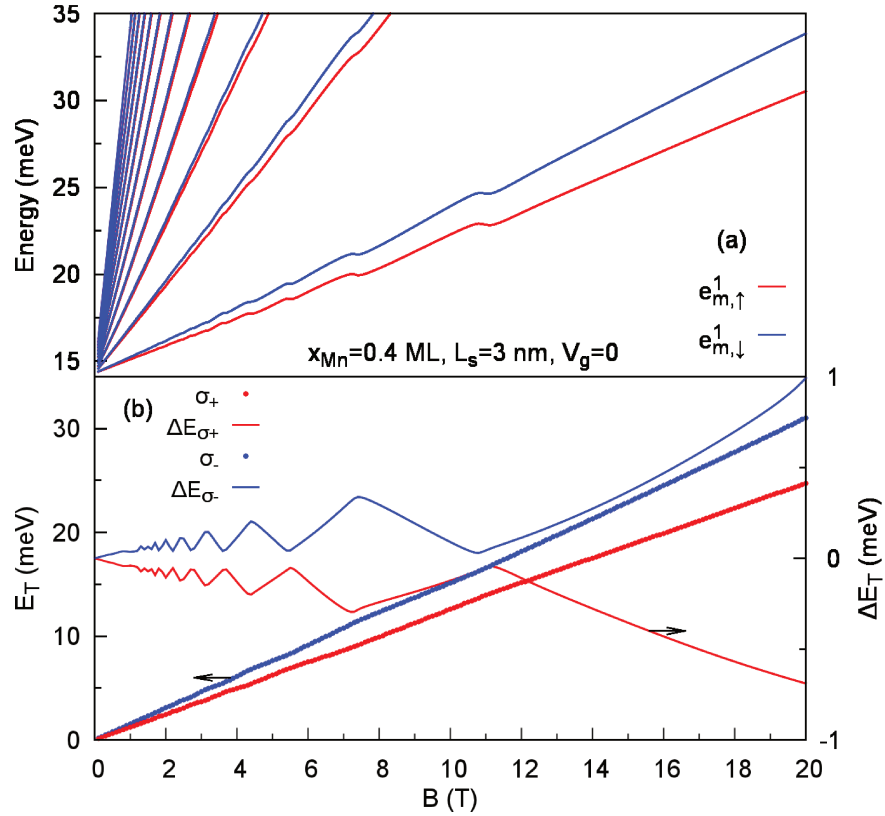


Figure 3.3: (Color online) (a) CB LL fan diagram. (b) Transition energy (right axis) and non-linear energy shift (left axis) as a function of the magnetic field.

and the optical transitions are related to the spin polarization of the QW 2DHG, which can have origin on the p - d exchange interaction between Mn and hole spins and in the exchange interaction due the Coulomb interaction. We will now investigate the physical origin of this behavior in more detail. For that, we discuss the results of our calculations when we turn off either the p - d interaction or the exchange-correlation potential v_{XC} .

Without exchange-correlation potential ($v_{XC} = 0$)

We aim now to understand the origin of the energy oscillations of the LLs. We first consider the case $v_{XC} = 0$ in the Hamiltonian, Eq. (3.5). With that the only effect that is spin-dependent is the sp - d exchange interaction. As it can be seen from Table 3.1, the main interaction is in the VB, p - d , while the s - d exchange contribution is one order of magnitude

smaller. All parameters are the same as discussed before.

Figure 3.4(a) shows the holes LL fan diagram of the $x_{Mn} = 0.4$ ML heterostructure in absence of the XC potential. Here, we again observe an oscillatory behavior in the hh_{n,τ_z}^1 LL with the magnetic field which are associated to the QW LL filling factor (ν). These oscillations, however, have a completely different qualitative and quantitative behavior. First of all, we do not observe a qualitative dependence with the spin in the oscillations. Both fundamental states, $hh_{0,\uparrow}^1$ and $hh_{0,\downarrow}^1$, oscillate following the same pattern with the magnetic field. Second, the value of these oscillations is significantly diminished. This can be better visualized in Fig. 3.4(b) where we plot the energy transition and the non-linear energy shift as a function of the magnetic field. The non-linear behavior is the same for both circularly polarized transitions, as expected from the hh LLs behavior. Furthermore, this is a tiny effect, ≈ 0.1 meV. There is, however, a small splitting between the two non-linear energies. This energy difference initially increases with the magnetic field and becomes practically the same for $B > 2$ T. We can separate, therefore, in two effects, one that is responsible for the spin-splitting and the other that is responsible for the near constant and spin-independent oscillations at $B > 2$ T. These effects have their origin exclusively in the hh levels since the CB levels are essentially the same as before [see Fig. 3.3(a)].

The origin of the oscillations can be associated with two contributions, the p - d exchange interaction and the charge transfer between the two hole gas reservoirs. The first contribution is spin-dependent while the second one is spin-independent. The spin-splitting between ΔE_{σ_+} and ΔE_{σ_-} is induced by the p - d interaction, which has a major effect up to $B \sim 2$ T, when the spin-splitting becomes nearly a constant. This occurs because the Brillouin function \mathcal{B}_M that describes the p - d exchange interaction saturates after a certain critical value of the magnetic field, B_c [102]. This means that the magnetic field already aligned all Mn spin. Its effect for $B > B_c$ is then a rigid splitting of the energies. This implies that for $B > 2$ T the

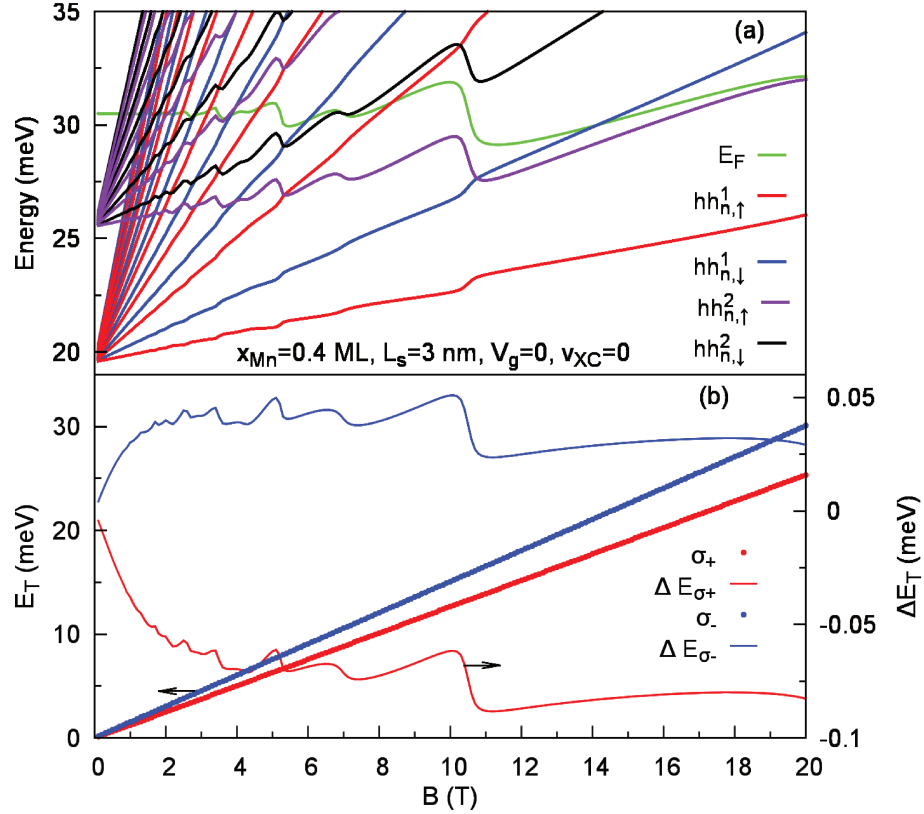


Figure 3.4: (Color online) (a) LL fan diagram for heavy-holes. (b) Transition energy (right y -axis) and non-linear energy shift (left y -axis) as function of the magnetic field. We considered $v_{XC} = 0$.

p - d interaction does not cause any oscillations in both hh LLs and the transition energies. The other effect responsible for the oscillations is the charge transfer of holes between the two 2DGH reservoirs situated at the QW and the C-doped layer. The Hartree potential gives origin to this effect and hence it is spin-independent. This effect dominates the spin-independent oscillations for $B > 2$ T. As already mentioned, this is a very weak contribution.

We conclude that the p - d interaction has a minor effect on the oscillations of the LLs and the transition energies. This is a consequence of the small overlap between the Mn ions and the QW hole gas. We will discuss how to enhance these effects in Section 3.4. Also, the charge transfer effect is very small when compared to the results obtained when the XC potential is present (see Fig. 3.3(b)). This occurs due to the separation between the C layer and the

QW (10 nm) and the hh effective mass that strongly confines the hh states in the attractive potentials (δ -doping potential and QW potential) decreasing the overlap between the different states.

For completeness, we consider the case when the $sp-d$ interaction is absent in the calculation but the XC potential is included. Figure 3.5 shows (a) the hh LL fan diagram and (b) the transition energies and the non-linear energy shift for this case. We observe that the results are very similar to those from Fig. 3.2(b) and 3.3(b). The only visible difference is the spin-splitting of the non-linear energy observed in Fig. 3.3(b), which originates from $sp-d$ interaction. Therefore, the XC potential is the dominant effective in the oscillatory nature of the LLs, and consequently, in the transition energies oscillations.

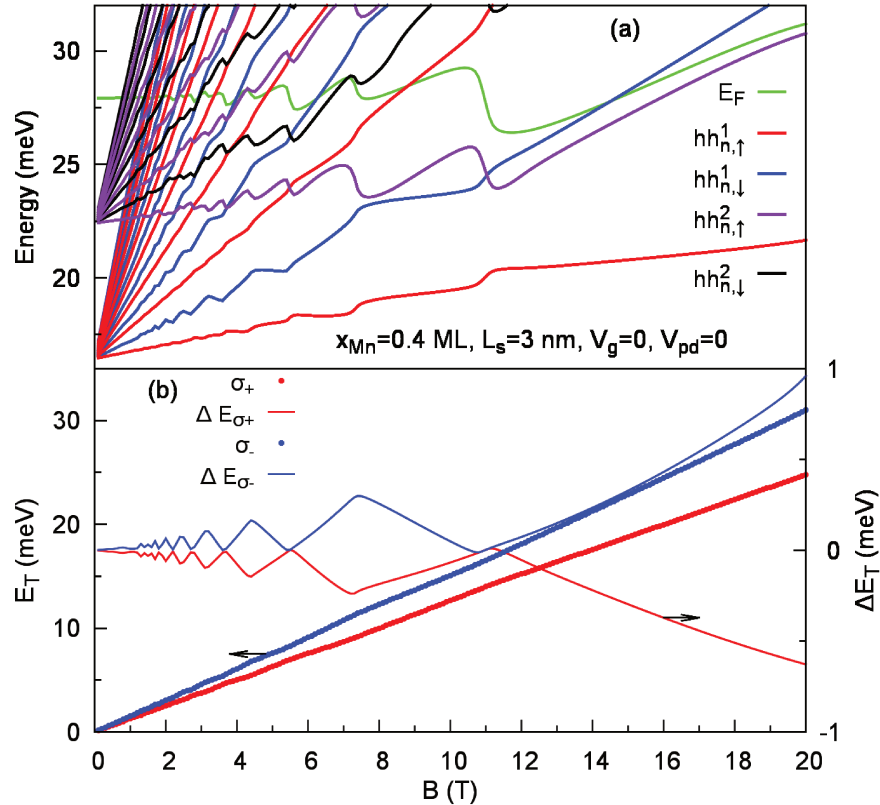


Figure 3.5: (Color online).(a) LL fan diagram for heavy-holes. (b) Transition energy (right y -axis) and non-linear energy shift (left y -axis) as a function of the magnetic field. We considered here $V_{pd} = 0$ and $v_{XC} \neq 0$.

3.3.2 $x_{Mn} = 0.13$ and $x_{Mn} = 0.2$ monolayers

We now compare the results of our calculations with the experimental results from Gazoto *et al.* ref. [31]. For that, we present the results for two others samples. All the parameters are the same except the nominal Mn doping layer which is now $x_{Mn} = 0.13$ MLs and $x_{Mn} = 0.2$ MLs. The experimental results [144] for the QW hole gas density decreases with the value of x_{Mn} as it should be expected for lower Mn concentrations. From Shubnikov-de-Haas and Stoke shift measurements they extracted 2D hole densities of $p_{2D} = 4 \times 10^{11} \text{ cm}^{-2}$ and $4.2 \times 10^{11} \text{ cm}^{-2}$ for $x_{Mn} = 0.13$ and $x_{Mn} = 0.2$ MLs, respectively. They showed lower 2D hole densities than the sample with $x_{Mn} = 0.4$ MLs but not in proportion to the Mn concentration. Furthermore, their 2D hole densities differ by just a slight margin in these two samples. The 2D hole concentration depends on the uncompensated Mn density which is dependent of the growth conditions. This set of samples were grown in the same conditions, nevertheless we observe that the amount of interstitial Mn may vary from sample to sample. Following our previous analysis, we obtain p_{Mn} and x_{eff} by fitting the 2D hole density with the QW hole density obtained in the calculations. The effective parameters are shown in Table 3.2.

Figures 3.6(a) and (b) show the hh LL fan diagram for the heterostructure with $x_{Mn} = 0.13$ and $x_{Mn} = 0.2$ MLs, respectively. We observe that the LLs cross E_F at smaller values of B in comparison with those from sample with $x_{Mn} = 0.4$ ML [see Fig. 3.2(b)]. This occurs because these QWs have lower hole density. All the other features are the same as those observed for sample $x_{Mn} = 0.4$ MLs. Essentially, the QW hh LLs oscillations are associated with the QW LLs filling factor with $hh_{0\uparrow}^1$ showing a qualitative difference from $hh_{0\downarrow}^1$ when the QW hole gas becomes spin-polarized.

Figure 3.6(c) and (d) exhibit the transition energies and the non-linear energy shifts as a function of the magnetic field for both samples with $x_{Mn} = 0.13$ and $x_{Mn} = 0.2$ MLs, respectively. We observe that the oscillations are slightly smoother than presented in Fig. 3.3(b)

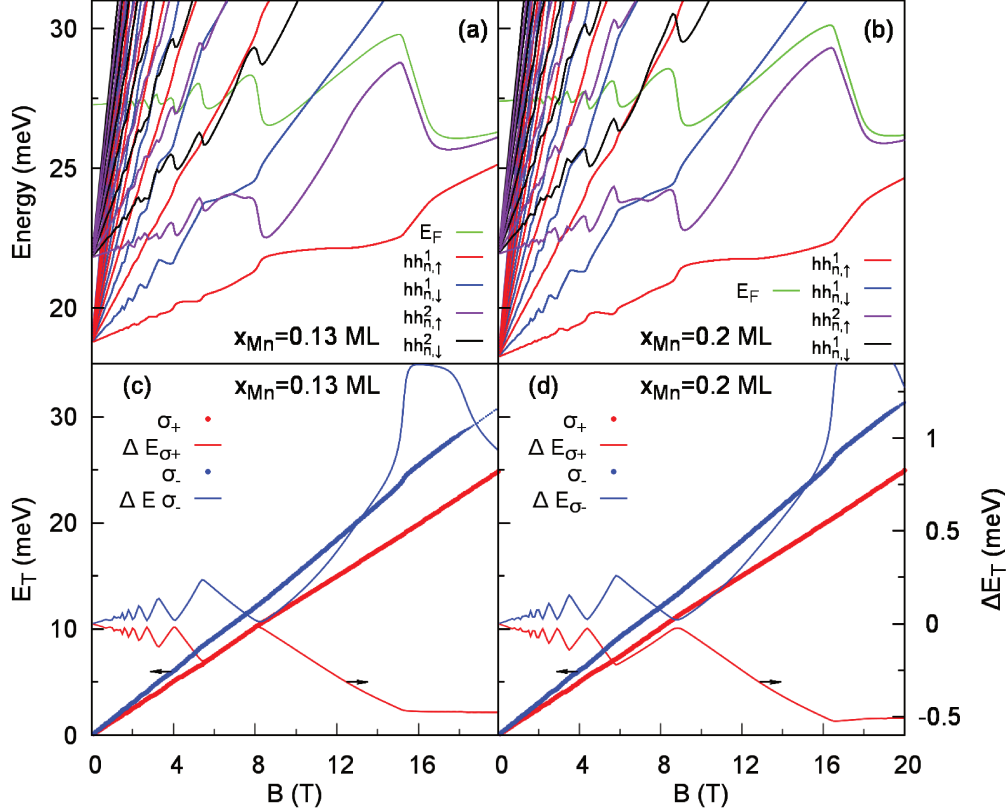


Figure 3.6: (Color online) Heavy-hole LL fan diagram for heterostructures with (a) $x_{Mn} = 0.13$ MLs and (b) $x_{Mn} = 0.2$ MLs. Transition energy (right y -axis) and non-linear energy shift (left y -axis) as a function of the magnetic field for samples (c) $x_{Mn} = 0.13$ MLs and (d) $x_{Mn} = 0.2$ MLs.

for sample $x_{Mn} = 0.40$ MLs. This should be expected since the oscillations are associated with the QW hole gas polarization which decreases for lower QW hole gas concentration. For $B < 15$ T the oscillations are practically the same in both cases. In all of them, the largest spin-splitting occurs when the hole gas is spin-polarized. For $B > 15$ T we observe that the ΔE_{σ_-} has a strong oscillation. This occurs because the QW hole gas is fully polarized, reaching its maximum value. This regime was not attained for sample $x_{Mn} = 0.40$ MLs for the magnetic fields considered here (up to 20 T).

We now compare with the results from Gazoto *et al.* ref. [31]. In their Fig. 2 they report the oscillatory behavior of the photoluminescence energy. For that, they subtracted a linear

energy dependence with the magnetic field. This was performed in a way that minimized the subtracted energies but remaining positive. In this analysis, the concave energy transition behavior with the magnetic field (see Fig. 1 in ref. [31]) translates into a peak in the non-linear behavior while the convex behavior shows an absence of peak. We extracted the linear terms with the magnetic field from the energy transitions. In our case, the concave (convex) behavior in the energy transition manifests itself as a positive (negative) peak in the non-linear shift. Once we make this correspondence between the two analysis we observe that our results are in perfect agreement with their results for sample $x_{Mn} = 0.40$ MLs. They observe a peak in the non-linear shift for the transition with higher energy transition for odd filling factor ($\nu = 3$) at $B \sim 7$ T and a peak in the non-linear shift for the lower energy transition for even filling factor ($\nu = 2$) at $B \sim 11$ T. This is the same oscillatory behavior we observe in our results as it can be observed by the peak in the non-linear shift for the higher energy transition at $\nu = 3$ at $B \sim 7$ T and the peak for the lower energy transition at $\nu = 2$ at $B \sim 11$ T [see Fig. 3.3(b)]. Furthermore, we obtain the peaks at the same magnetic field as in the experiment which shows that the self-consistent description of the structure describes well their samples. For the samples with lower values of x_{Mn} we have a similar behavior except that the filling factors occur for $B \sim 5.5$ T ($\nu = 3$) and $B \sim 8.5$ T ($\nu = 2$) while in the experiment they observe $\nu = 3$ at $B \sim 6$ T and $\nu = 2$ at $B \sim 9$ T for sample with $x_{Mn} = 0.20$ MLs and slightly lower values of the magnetic field for sample $x_{Mn} = 0.13$ MLs. These are again in excellent agreement with our results see Fig. 3.6(b). However, the experimental results are less conclusive about the nature of the oscillations in these cases. They do not show the case of filling factor $\nu = 1$ since they did not reach this regime for the magnetic fields employed. This is when we have the highest possible QW hole gas spin-polarization, and therefore the highest non-linear behavior in the energy shifts.

We did not consider the case $x_{Mn} = 0$ since in this case the experimental results showed

no hole gas in the QW. Our calculations would produce no oscillatory behavior in this case. This is what is also observed experimentally.

3.4 Increasing p - d interaction

The samples we analyzed in the last section showed that the hole-Mn interaction did not play an important role in the electronic structure and in the magneto-oscillations in the transition energies. This is a consequence of the weak overlap between holes and Mn for the sample parameters considered. The main goal of these structures is to obtain effects originated from this interaction maintaining a high-quality hole gas in the QW. In this section we discuss different venues to obtain a significant effect of the Mn ions on the hole gas. One way to enhance the magnetic effects is to increase the uncompensated Mn ions. This, however, depends on the samples growth conditions and some intrinsic conditions probably will hamper these attempts. We do not consider this case here. Another possibility is to grow the Mn layer closer to the QW. This may diminish the sample quality but it is a well controlled growing parameter. A third possibility is through the application of a gate voltage in order to redistribute the hole gas in the structure. This has the advantage to offer an external control parameter. We analyzed here the last two cases.

3.4.1 Mn position

In order to investigate the effects of Mn position on the 2DHG electronic structure, we start by changing the nominal position of the δ -Mn doping, L_S . All the others parameters are the same considered previously for sample $x_{Mn} = 0.4$ ML. We consider here a Mn layer closer to the QW, namely, with $L_S = 1$ nm. We assume the same Mn diffusion we considered before. To understand the details of these effects we consider three situations. First, we neglect the sp - d interaction, i.e, we do not consider $V_{pd}^{hh(lh)}$ and V_{sd}^e terms of the Eqs. (3.5) and (3.19), respectively. Second, we include this interaction, but we neglect the contribution due to Zener

effect, that is, the contribution of the direct coupling between the hole gas and the Mn ions. This is done by neglecting the second term of the Brillouin's function argument [Eq. (3.18)]. Finally, we consider the full Hamiltonian as described by equations Eqs. (3.5) and (3.19).

Without $sp-d$ interaction ($V_{sp-d} = 0$)

For $L_s = 1$ nm, the Mn ions are closer to QW, and the overlap between the VB states and the Mn ions starts to play an important role in the electronic structure. In order to map this interaction, we begin by showing the effects in the absence of Mn spin interactions. In other words, we consider the case where the $sp-d$ coupling is neglected. In this case the Mn ions act as a non-magnetic acceptor impurity. Figure 3.7(a) and (b) shows the LLs for holes and electrons, respectively. They both oscillate as a function of the magnetic field. These oscillations are very similar to those presented in the heterostructure with $L_s = 3$ nm including the full Hamiltonian [see Figs. 3.2(b) and 3.3(a)]. More precisely, the oscillations of the hole LLs depend on the filling factor. For odd filling factors the two hole spin species of LLs oscillate in the same direction, while for even filling factors the oscillations are in opposite directions. Therefore, the behavior of the LLs with the magnetic field depends on the QW hole-gas polarization and the effect is dominated by the hole gas exchange energy.

Figure 3.7(c) shows the transition energy and the non-linear energy shift as a function of the magnetic field. As it should be expected from the hh LLs, the results are very similar to those obtained with $L_s = 3$ nm and the full Hamiltonian [see Figs. 3.2(b) and 3.3]. These results confirm that when the Mn ions are sufficiently apart from the QW the $sp-d$ interaction does not play any role on the electronic structure of both electrons and holes QW states.

Without Zener interaction

We now consider the same heterostructure but in the presence of the $sp-d$ interaction. We do not consider, however, the contribution of the hole gas in this interaction (as described

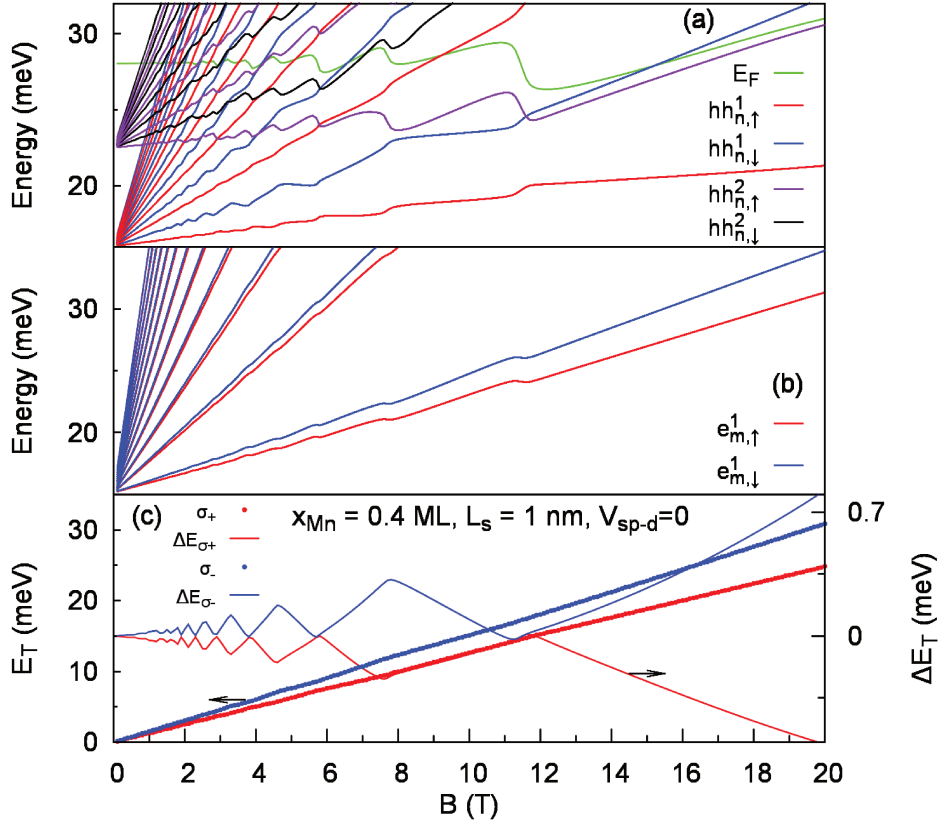


Figure 3.7: (Color online) LL fan diagram for heavy-holes (a) and CB (b). (c) Transition energy (right y -axis) and non-linear energy shift (left y -axis) as function of the magnetic field. In this case the distance between Mn-doping and QW interface is $L_s = 1$ nm, and we do not consider the interaction between carriers and Mn ions, $V_{pd}^{hh(lh)} = V_{sd}^e = 0$.

in this work by the Zener kinetic exchange approximation). Figure 3.8(a) shows the hh LL fan diagram. We clearly see that for low magnetic field the LLs behave differently from the previous results. For magnetic fields between zero and two Tesla, the spin-splitting between the fundamental spin-up and spin-down LLs is larger than the one induced by the Zeeman interaction [see Fig. 3.7(a)]. The $n = 0$ spin-down hh LL is practically degenerate with the $n = 1$ spin-up hh LL, and the $n = 0$ spin-up hh LL is approximately constant over this range of B . This behavior is induced by the competition between the Zeeman effect and the p - d interaction. For low magnetic field, the spin exchange interaction term dependent on the spin polarization is weak, since the spin-up and spin-down hole densities are nearly the same.

Therefore, the hole-Mn coupling is the dominant effect at low magnetic fields. For higher values of the magnetic field, the Mn spins are aligned and the Brillouin function saturates. The spin-splitting originated by the p - d coupling is constant for $B > 2$ T. Now the spin-splitting of the LLs is dominated by both the Zeeman and XC contributions. The behavior of the LLs at high magnetic field is the same as observed before, but with a larger spin-splitting which is a consequence of the enhancement of the hole-Mn interaction.

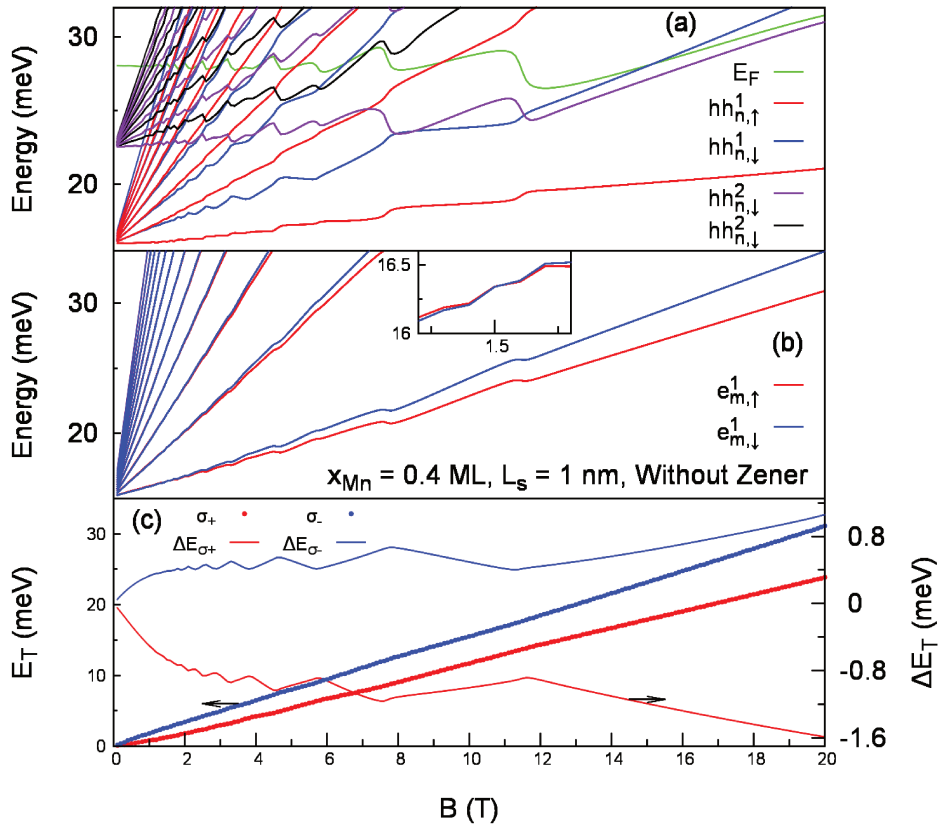


Figure 3.8: (Color online) LL fan diagram for (a) heavy-holes and for (b) electrons. Here we include the sp - d interaction but neglect the Zener kinetic exchange contribution. The inset in (b) shows a detail of the CB LLs to visualize the crossing between the $n = 0$ spin-up and spin-down electrons LLs. (c) Transition energy (left axis) and non-linear energy shift (right axis) as function of the magnetic field. Here $L_s = 1$ nm.

Figure 3.8(b) shows the CB LL fan diagram. We notice that there is a crossing of the $n = 0$ CB LLs at $B \sim 1.5$ T. The spin-down LL is the lowest state up to $B \sim 1.5$ T

when the spin-up LL becomes the ground-state. This is better visualized in the inset of the Fig. 3.8(b). This crossing is originated by the interplay between the Zeeman energy and the s - d interaction. Increasing the magnetic field, the Zeeman energy dominates and the oscillatory behavior induced by the Hartree interaction induced charge transfer is present. We observe here that the CB LLs oscillations are stronger than the ones showed in the absence of s - d interaction [see Fig. 3.7(b)].

Figure 3.8(c) shows the energy transition and the non-linear energy shift. The magneto-oscillations are now more pronounced. We do not observe here any signature of the electron's LLs crossing, since the dominant effect is the valence band p - d interaction. One way to probe this crossing is by measuring the degree of polarization of the circularly emitted light, since the intensity is dominated by the electron's population. The crossing of the CB LLs leads to an inversion of the electrons spin population, which in turn changes the sign of the degree of polarization. However, we should keep in mind that the energy scale of the effect is very small. In the non-linear energy shift we observe an antisymmetric behavior for the σ_- and σ_+ cases. For low fields the σ_- non-linear energy shift slightly increases with B , while σ_+ has a negative shift following the shape of the Brillouin function, that is, the sp - d interaction. For higher magnetic fields the oscillations are similar to those observed previously but with a finite splitting between the two polarizations, a consequence of the sizable sp - d interaction. Therefore, with increasing the overlap between the QW states and the Mn ions, we are able to modify the behavior at low magnetic fields and increase the spin-splitting of the transition energies at higher magnetic fields.

ALL interactions

We now include the direct coupling of the hole gas with the Mn ions via the Zener kinetic exchange term. In other words, we consider the full Hamiltonian of eqs. (3.5) and (3.19). Figure 3.9 shows the LLs fan diagram for (a) hh and (b) CB and (c) the transition energy

and the non-linear energy shift for this case. We do not observe a significant change in this case when compared to the previous one. Shortly, that means despite the proximity of the Mn layer, the coupling of the QW hole gas with the Mn ions (Zener kinetic exchange term) is still not significant. We conclude that by doping the Mn nearer the QW interface enhances the *sp-d* interaction through their coupling with the valence and conduction band states but it does not increase significantly the Zener kinetic exchange contribution.

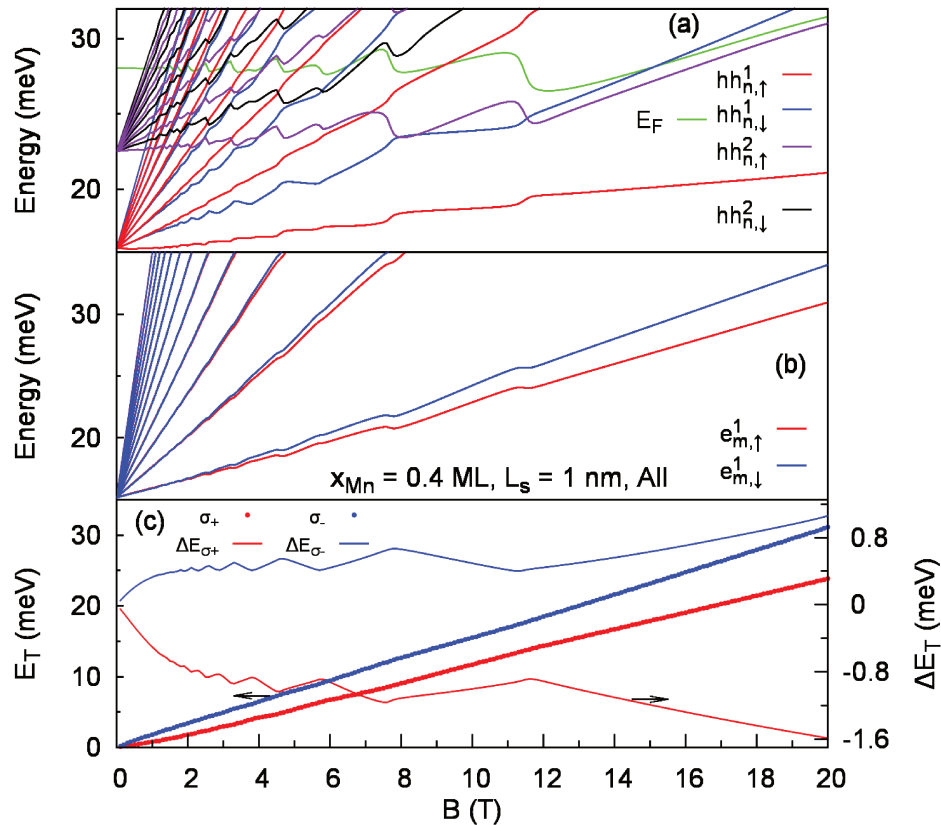


Figure 3.9: (Color online) LL fan diagram for *hh* (a) and CB (b) and (c) transition energy (right *y*-axis) and non-linear energy shift (left *y*-axis) as function of the magnetic field for the same case as in Fig. 3.8 but now including the contribution from the Zener kinetic exchange approximation.

3.4.2 Gate Voltage

The main reason the Mn layer has a weak participation in the electronic properties of the systems we studied here is that they have a weak overlap with the valence band states and the

hole gas. Besides the structural parameters already discussed, another reason for this situation is the proximity of the structure with the surface which induces a high electric field due to the pinning of the Fermi level at the surface states. We could change this situation either by increasing the GaAs cap layer or applying a gate voltage. A great advantage of using a gate voltage is that we can control electrically the magnetic properties of the heterostructure. It was demonstrated that by applying an electric field one can control the direction of the magnetization vector of the GaMnAs [84]. We consider now the same structure we have been analyzing, but assuming a gate voltage. Essentially, we will simply change the Fermi level at the surface by the expression $E_F \rightarrow E_g/2 - V_g$ and will consider the value $V_g = 0.71$ eV which leads to an almost flat band condition near the surface. This will induce a charge redistribution in the whole structure as we will see in the following. We consider two values for the Mn layer spacing, $L_S = 3$ nm and 1 nm. All the other parameters are the same as those used before for sample $x_{Mn} = 0.40$ MLs. With that, we are assuming that the growth conditions are similar to those considered before.

$V_g = 0.71$ eV and $L_s = 3$ nm

We first consider the case $L_S = 3$ nm, which is the same Mn spacing as the samples in the experiment of Gazoto *et al.* ref. [31]. The gate voltage changes the charge distribution. As a consequence, the hole gas density in the first occupied QW subband is now 9.2×10^{11} cm⁻². Figure 3.10 shows the hole potential profile and the wave-functions of the occupied hh levels at (a) $B = 0$ T and (c) at $B = 10$ T, (b) the hh Landau fan diagram and (d) the hh LLs charge concentration as a function of the magnetic field. We first observe that now we have three occupied hh subbands. The ground-state, hh^1 , is mainly located at the QW. There are then two other states, almost degenerate, which are extended in the whole structure. The second state, hh^2 , is mainly located at the Mn layer and the QW, while the third state, hh^3 , is located at the C layer and the QW. This situation changes completely the physics of the system. We

have now one state occupied which has a strong coupling with the Mn ions. Furthermore, all the states have a sizable presence in the QW, contributing to the QW hole gas. This situation becomes even more complex at higher magnetic fields. At $B = 10$ T, hh_{\uparrow}^1 is partially confined in the Mn region while hh_{\downarrow}^1 remains mainly in the QW. The same happens with hh_{\uparrow}^2 and hh_{\downarrow}^2 . This occurs due to the Mn ions polarization and the p - d interaction which makes the Mn rich region a strongly attractive potential for spin-up states while acting as a barrier for spin-down. hh^3 subbands are again mainly localized at the C layer and are not qualitatively affected by the magnetic field, except for the polarization dependence in the XC interaction which breaks their spin-degeneracy.

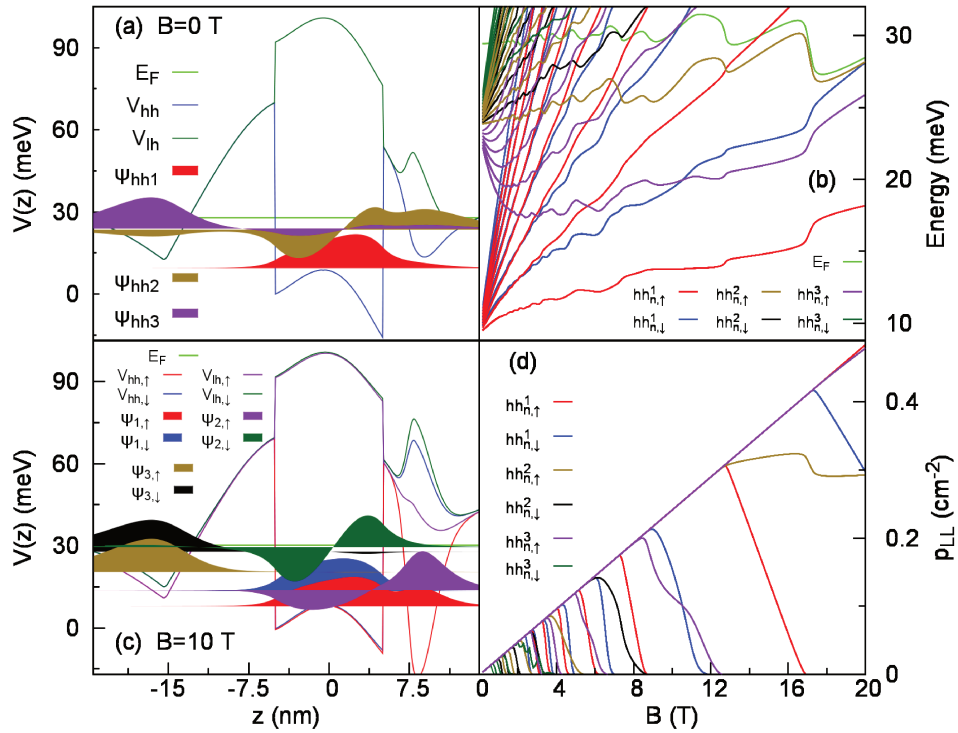


Figure 3.10: (Color online) (a) and (c) Self-consistent potential profile for the heavy-holes and occupied heavy-hole wave-functions for $B = 0$ T and $B = 10$ T, respectively. (b) Heavy-hole LLs and (d) two-dimensional density of the LLs. $x_{Mn} = 0.4$ MLs, $V_g = 0.71$ eV and $L_s = 3$ nm.

The hh LLs show in general a strong and non-linear dependence with the magnetic field. The most striking behavior is with the state hh^2 . Since it strongly overlaps with the Mn

layer, it shows a strong influence of the p - d interaction. As a consequence, the spin-down LLs rapidly become depopulated while the spin-up LLs, first decrease in energy and second, for $B > 3$ T, increase their energy. The behavior at lower magnetic field is dominated by the p - d interaction, while at larger magnetic fields this interaction is saturated and it recovers the usual LL behavior. The LLs associated with state hh^3 follows approximately the same behavior as in previous cases. The LLs associated to the hh ground-state, hh^1 , which is mainly confined in the QW, shows a different oscillatory behavior with the magnetic field when compared to the absence of the gate voltage [see Fig. 3.2(b)]. Since this subband is responsible for the optical emission, we will analyze its behavior in more detail. We remind that for transport properties, the occupation of the other levels should also directly influence the outcome of the experiments.

The $hh_{1,\uparrow}^1$ and $hh_{1,\downarrow}^1$ LLs show a non-linear behavior at weak magnetic field. For magnetic fields below ~ 3 T, the hole concentration in the QW is not significantly spin-polarized. At the same time, in this regime, the Mn spins start to be aligned by the magnetic field and the Zener kinetic exchange mechanism. Since the hh^1 wave-functions have a sizable overlap with the Mn ions, this effect is significant. As a consequence, the p - d interaction is more important and is responsible for these LLs behavior. As the magnetic field increases, this effect saturates while the QW hole gas becomes more polarized and the XC potential starts to be dominant. We recover then most of the features described in Fig. 3.2(b). A careful examination of the LLs, however, shows an oscillatory behavior super-imposed on the oscillations originated from the XC interaction. This occurs in particular for magnetic fields ~ 7 T and ~ 9 T and ~ 11 T. These oscillations have their origin in the crossing of the Fermi level by the LLs $hh_{2,\uparrow}^2$, $hh_{0,\downarrow}^3$ and $hh_{1,\uparrow}^2$, respectively [see Fig. 3.10(b) and (d)]. The partial presence of these levels in the QW induces an increase in the QW hole gas spin-polarization, adding to the exchange induced splitting.

Figure 3.11(a) illustrate the CB LL fan diagram. For $B < 2$ T we observe that fundamental electron LLs are practically independent of the magnetic field. This occurs due the interplay between Zeeman and s - d interactions. As mentioned before, these energies have difference sign which can lead to a LL crossing as showed in Fig. 3.8(b). For magnetic field $B > 2$ T the CB LLs show their typical oscillatory behavior induced by the Hartree energy of the hole gas.

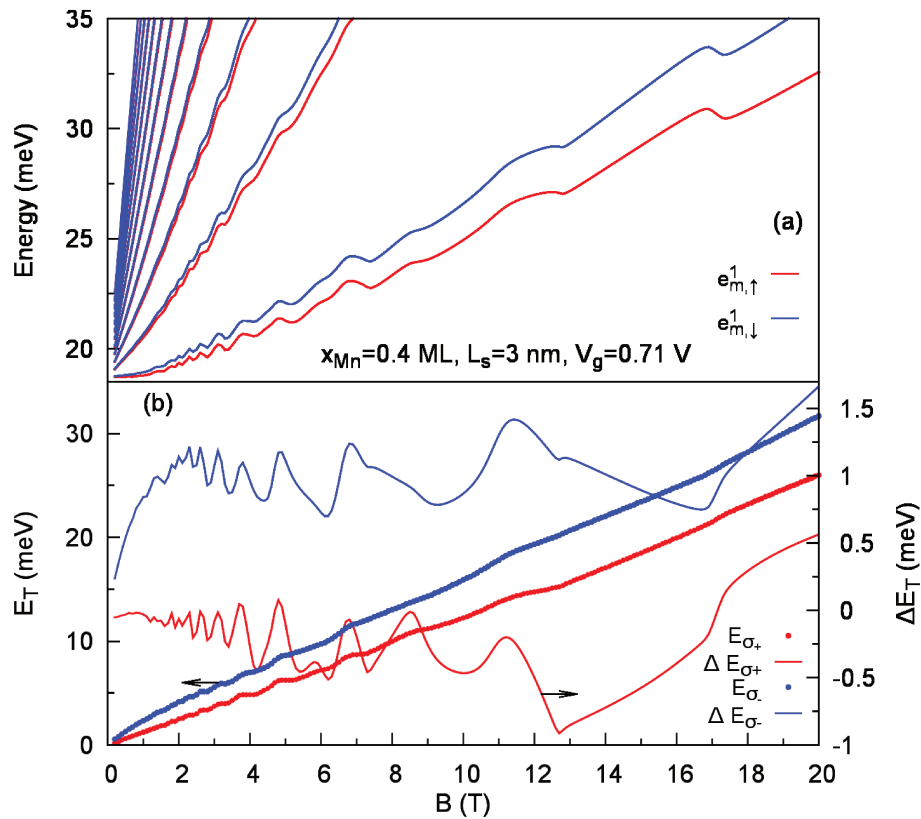


Figure 3.11: (Color online) (a) CB LL fan diagram. (b) Transition energy (right y -axis) and non-linear energy shift (left y -axis) as function of the magnetic field. $x_{Mn} = 0.4$ MLs, $V_g = 0.71$ eV and $L_s = 3$ nm.

Figure 3.11(b) shows the transition energies and the non-linear energy shift as a function of the magnetic field. The non-linear shift shows the combined effect of the two sets of oscillations presented in the hh LLs. Although we still can see some of the oscillations showing the different

behavior for σ_+ or σ_- circularly polarized transition according to an odd or even filling factor, just as in Fig. 3.3(b), the super-imposed oscillations break the antisymmetric pattern observed previously. Since the second set of oscillations has its origin in the $sp-d$ interaction, it does not have the antisymmetric behavior but rather a symmetric oscillation. As a consequence, the combination of the two sets produce a completely different pattern for the the right- and left-circularly polarized non-linear energy shift. We can see this in detail when we observe the break of the antisymmetric pattern at $B \sim 8$ T which lasts up to $B \sim 13$ T. In this interval of magnetic field $hh_{1\uparrow}^2$ is depopulated. This level strongly overlaps with the Mn ions and therefore enhances the participation of the $p-d$ interaction in the non-linear shift. Also, the full depopulation of the $hh_{n,\uparrow}^2$ LLs generates a spike in the non-linear energy shifts, as can be seen at $B \sim 7$ T and $B \sim 13$ T. This occurs due the redistribution of the spin-down holes from $hh_{n,\uparrow}^2$ into the other subbands LLs.

$V_g = 0.71$ eV and $L_s = 1$ nm

Here we consider the case $L_S = 1$ nm and $V_g = 0.71$ eV. This situation is the most favorable for the overlap between the hole gas and the Mn ions we are considering in this work. The Mn ions are close to the QW interface. Actually, due to the Mn diffusion we consider here, part of the Mn ions are in the QW. At the same time, the almost flat band condition at the surface leads to a redistribution of charge along the whole structure. Figure 5.1 shows the hh potential profile and the wave-functions of the occupied hh levels at (a) B=0 T and (c) for B=10 T, (b) the hh LLs fan diagram and (d) the LLs charge concentration as a function of the magnetic field. We first observe that again we have three occupied hh states except that now there is no state concentrated on the Mn layer. This happens because the proximity of the Mn layer to the QW prevents the formation of enough confinement in this region. On the other side, all the three states have a considerable overlap with the Mn ions. As the magnetic field increases, this picture changes completely. The Mn rich region is more attractive and the QW levels

are pushed towards this region. As a consequence, following the previous terminology, hh_{\uparrow}^1 strongly overlaps with the Mn region. The same happens for hh_{\downarrow}^1 although less pronounced. hh_{\uparrow}^2 also presents a significant overlap with the Mn region, while hh_{\downarrow}^2 is mainly confined in the QW. The states hh_{\uparrow}^3 and hh_{\downarrow}^3 become almost fully confined in the C layer. All this evolution in the state wave-functions produces a complex structure in the LLs fan diagram.

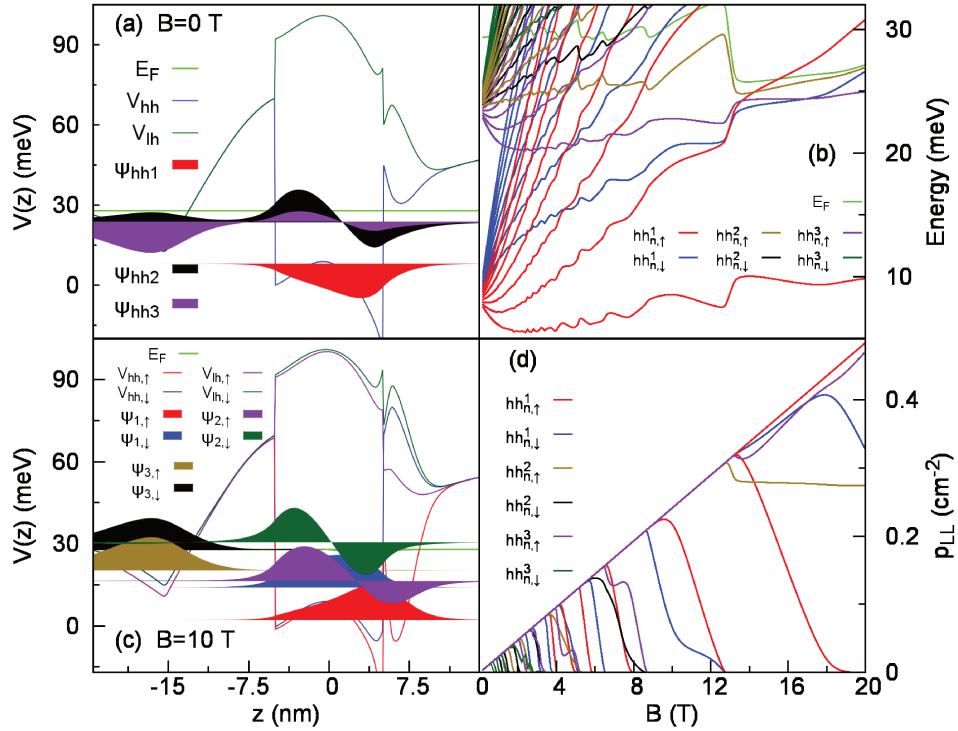


Figure 3.12: (Color online) (a) and (c) Self-consistent profile potential and heavy-hole wave-functions for $B = 0$ T and $B = 10$ T, respectively. (b) Heavy-hole LLs and (d) two-dimensional density of the LLs. For $x_{Mn} = 0.4$ MLs, $V_g = 0.71$ eV and $L_s = 1$ nm.

We focus here our analysis on the hh ground-state fundamental LL, that is, $hh_{0,\uparrow}^1$ and $hh_{0,\downarrow}^1$. At low magnetic fields, the two states show a strong non-linear behavior, with $hh_{0,\uparrow}^1$ showing a convex curvature while $hh_{0,\downarrow}^1$ shows a concave curvature with the magnetic field. This regime is entirely dominated by the p - d interaction. At higher magnetic fields, for $B > 6$ T, the oscillations with the LLs filling factors become more pronounced and dominate the features. However, in this case, we do not observe the difference in the magnetic field dependence from

spin up and spin down with the odd and even filling factors which originated in the hole gas exchange energy as a consequence of the its spin-polarization. Here, both states oscillate in a similar way. One of the reasons for this behavior is in the way that the LLs associated to the QW are depopulated. This can be observed in Fig. 5.1(d). In particular, for example, for $B \sim 13$ T, both LLs associated to spin up and down becomes depopulated almost at the same time. This prevents the spin-polarization of the QW hole gas. At the same time, the participation of the states hh_{\uparrow}^2 in the polarization of the QW hole gas prevents a clear oscillation in this polarization. On the other way, the states hh_{0,τ_z}^1 have a strong influence of the Mn ions which dominates the magnetic field dependence. The oscillations are therefore mainly dominated by the charge transfer among the QW levels but not in the polarization of the hole gas.

Figure 4.1(a) shows the CB LLs fan diagram and (b) the transition energies and the non-linear energy shift for this case. The CB LLs show the usual oscillation associated to the charge transfer between different hole gas reservoirs. The non-linear shift observes a rapid split at low magnetic fields due to the increasing of the $sp-d$ interaction with the magnetic field and for $B > 3$ T this splitting saturates and the oscillatory behavior dominates its features. These oscillations, as it was already manifest for the hh LLs, show symmetric oscillations for the two circularly polarized transitions and are associated to the LLs filling factor.

3.5 Concluding Remarks

We presented here the results of calculations of the electronic structure and optical emission energy for (In,Ga)As QWs with barriers doped with Mn and C acceptors. Our results show an excellent agreement with the circularly polarized photoluminescence experiments from Gazoto *et al.* [31]. We were able to explain the origin of the non-linear energy shift in their results both qualitatively as well as quantitatively. The origin of these non-linear behavior

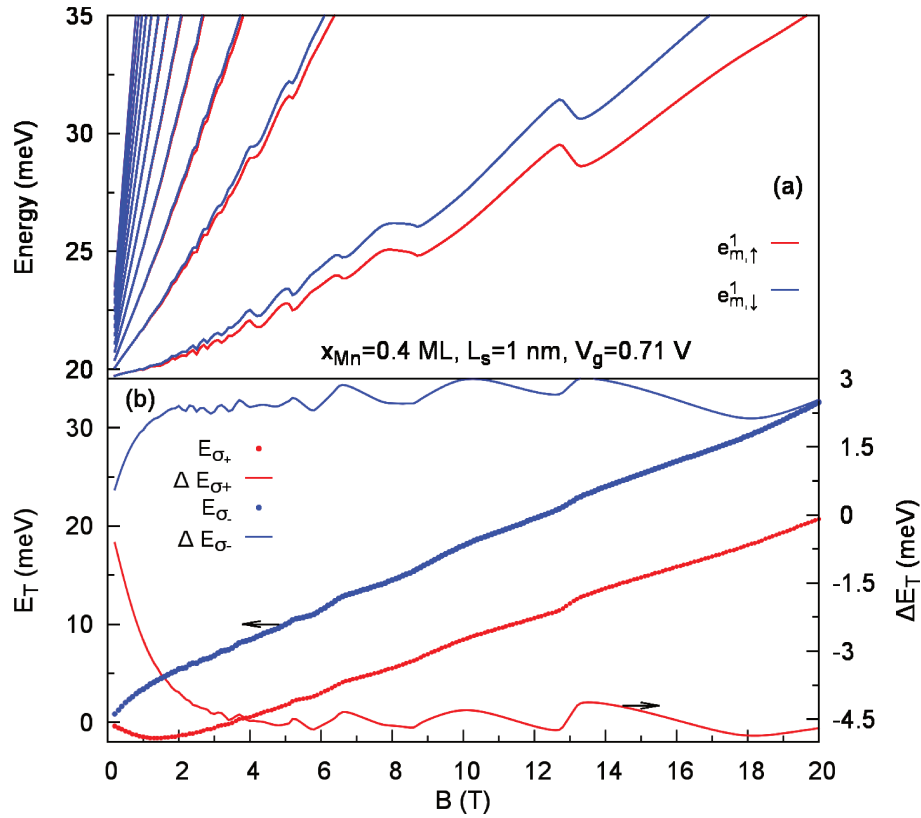


Figure 3.13: (Color online) (a) CB LL fan diagram . (b) Transition energy (right y -axis) and non-linear energy shift (left y -axis) as function of the magnetic field. $x_{Mn} = 0.4$ MLs, $V_g = 0.71$ eV and $L_s = 1$ nm.

was interpreted as an effect of the spin-polarization induced by the hole gas exchange energy. The different types of oscillations for the different spins was induced by the spin-polarization and depolarization of the QW hole gas with the odd and even LLs filling factors. These results demonstrated that the p - d interaction, including the Zener kinetic exchange contribution due to the antiferromagnetic interaction between hole spins and Mn ions, did not show to be relevant for these samples. We should not expect any significant ferromagnetic signature in the electronic properties for these cases. This result is disappointing in the sense that these samples were grown with the expectation of obtaining a high-quality hole gas and at the same time a sizable magnetic effect. We investigated the conditions to favor the combination of

these effects. We showed here that in order to have a dominant magnetic effect in the hole gas properties it is necessary to prevent the built up of a high electric field induced by the presence of the QW structure near the surface. This can be achieved by controlling the Fermi level with a gate voltage. Also, we showed that to enhance the p - d interaction influence in the hole gas it is necessary to grow the Mn layer closer to the QW interface. This has a drawback since Mn is known to diffuse and the growth conditions of the (Ga,Mn)As layer is not the optimal conditions to grow III-V materials. As a consequence, samples with lower value of L_s may present a low-mobility hole gas.

We also showed that, depending on the samples parameters, the fundamental spin-up and spin-down CB LLs exhibit crossing. This crossing is due to the opposite sign of s - d and Zeeman contributions. As the transition energy is dominated by the hole spin-splitting, this effect can not be visualized in the transition energy. Therefore, we suggest that this crossing can be observed in the degree of polarization of the circularly emitted light since the intensity is dominated by the electron population, and with the LLs crossing its population will invert causing a changing of sign in the degree of polarization.

Several approximations were used to obtain a simple and clear picture for this system. We used a parabolic approximation for both the effective hole g-factor and masses. These values are compatible with experimental data for a similar InGaAs QW [126] and the strain effects justify the parabolic approximation for this case. For the GaAs (and GaMnAs) regions, however, this is a less justified approximation. A complete 6×6 band description certainly would modify the self-consistent calculation and the charge transfer with the magnetic field. We obtained an excellent agreement with the experiment for the LLs filling factor, once the QW hole gas concentration was fitted with the experimental data at zero magnetic field. This suggest that our approximation was sufficient to describe the charge transfer in the structure for the magnetic fields considered here. One possible interpretation of this result is that the

VB complexity at the C doped layer states does not significantly modify the total density of states but mainly rearrange the occupation among the occupied states in that region.

We did not include in our calculations the effects described by Asano and Ando [138] and Hawrylak and Potemski [116], that is, the effects of the electron-electron and electron-hole interaction in the final states of the optical emission. The many-body effects here were limited to the VB spin-density functional theory. The excellent agreement we obtained with the experiments suggest that although the samples show a relative high mobility for this kind of structure, it is not enough to give the refined structures in the emission spectra predicted by those authors.

Finally, we did not include in our spin-density functional description the effects of the hole gas on the minority charge, that is, the CB states. First, due to the fact that they are of different species there is no exchange interaction between them. Second, the correlation interaction should be spin-independent, and therefore, it does not affect the origin of the oscillations associated to the different spin states, but rather causes a rigid energy shift in the transition energy, known as band-gap renormalization [139, 140]. For the experimental situation, we showed that this simplification is good enough for the description of the observed effects. For the other situations explored here, namely when the gate voltage is applied and we considered a Mn layer nearer to the QW this should be revised for a more quantitative analysis. We do not expect that the qualitative conclusions observed in this case will be modified.

Chapter 4

Electronic properties of charged quantum dots doped with a single magnetic impurity

We present here the electronic structure of charged quantum dots doped with a single magnetic impurity. This problem was already investigated by other authors [78, 145], for an off-center Mn impurity. Here we consider the Mn at the QD center. One of the consequences is that electrons that are in QD orbitals with nonzero angular momentum do not interact directly with Mn. We show that electron-electron interaction mediates an indirect interaction between those electrons and Mn. The indirect interaction depends on the number of confined shells, quantum dot confining energy, and electron-Mn coupling. This Chapter is the integral article by U. C. Mendes, M. Korkusinski and P. Hawrylak, submitted to Phys. Rev. B (2014).

4.1 Introduction

There is currently interest in understanding the coupling of a localized spin, either magnetic impurity or nuclear spin, with spins of interacting electrons [41, 51]. This includes the Kondo effect in metals [146–150] and quantum dots [3, 4, 47, 49], the impurity spin in diamond [151, 152], charged quantum dots with magnetic ions [55, 57, 59, 78, 153], and nuclear spins coupled to fractional quantum Hall states [154–156]. Here we focus on a highly tunable system of quantum dots with a single magnetic ion and a controlled number of electrons. Such system

is realised in CdTe quantum dots with a magnetic impurity at the center of the dot loaded with a controlled, small at present, number of electrons [57]. The interplay between electron-electron interactions and the electron-Mn exchange interaction has been studied using exact diagonalization techniques [78,153] and mean-field approaches [59,157]. Other studies focused on electron-electron interactions in excitonic complexes coupled with localized spins [55,57,58,60,62,157].

Here we focus on the indirect coupling of the electrons and magnetic/nuclear ion spins in self-assembled quantum dots (QDs) mediated by the electron-electron interaction. With a localized spin placed at the center of the dot only the spin of the electrons occupying the zero angular momentum states of the s , d , ... shells couples directly to the localized spin via contact exchange interaction. The situation is identical to the Kondo problem in metals where only zero angular momentum states of the Fermi sea are considered as interacting with the localized spin. The question arises as to the role of the electron-electron interaction. Here we show that, in quantum dots, when electron-electron interactions are included, the electrons occupying finite angular momentum orbitals (e.g., p shell) do interact with the localized spin. The effective interaction for p -shell electrons is obtained using exact diagonalization of the microscopic Hamiltonian as a function of the number of electronic shells, shell spacing and anisotropy of the exchange interaction. The anisotropy of exchange interpolates between interaction types characteristic for conduction band electrons (Heisenberg-like) and valence band holes (Ising-like). We show that the effective exchange interaction can be engineered to be either ferro- or antiferromagnetic by varying quantum dot parameters.

The Chapter is organized as follows: in section II we describe the model of a self-assembled quantum dot with a single Mn impurity at its center and a controlled number of electrons. Section III presents results of exact diagonalization calculations of the model Hamiltonian for quantum dots confining from two to six electrons and the emergence of the indirect electron-

Mn coupling for QDs with partially filled p -shell. Section IV summarizes our results.

4.2 Model

We consider a model system of N electrons ($N = 2, \dots, 6$) confined in a two-dimensional (2D) parabolic quantum dot with a single magnetic impurity at the center. For definiteness we consider an isoelectronic impurity, a Manganese ion with total spin $M = 5/2$ in a CdTe quantum dot [51]. In the effective mass and envelope function approximations, the single-particle states $|i, \sigma\rangle$ are those of a 2D harmonic oscillator (HO) with the characteristic frequency ω_0 . They are labeled by two orbital quantum numbers, $i = \{n, m\}$, and the electron spin $\sigma = \pm 1/2$. The single-particle states are characterized by energy $E_{n,m} = \omega_0(n + m + 1)$ and angular momentum $L_e = n - m$. We express all energies in the units of effective Rydberg, $Ry^* = m^*e^4/2\epsilon^2\hbar^2$, and all distances in units of the effective Bohr radius, $a_B^* = \epsilon\hbar^2/m^*e^4$, where m^* , e , ϵ , and \hbar are respectively the electron effective mass and charge, the dielectric constant, and the reduced Planck constant. For CdTe we take $m^* = 0.1m_0$ and $\epsilon = 10.6$, where m_0 is the free-electron mass, and $Ry^* = 12.11$ meV and $a_B^* = 5.61$ nm. Unless otherwise stated, we take the HO frequency $\omega_0 = 1.98Ry^*$, consistent with our previous work [58].

The Hamiltonian of N electrons confined in our QD and interacting with a single Mn spin is written as [78]:

$$\begin{aligned}
 H = & \sum_{i,\sigma} E_{i,\sigma} c_{i,\sigma}^\dagger c_{i,\sigma} + \frac{\gamma}{2} \sum_{\substack{i,j,k,l \\ \sigma,\sigma'}} \langle i,j | V_{ee} | k,l \rangle c_{i,\sigma}^\dagger c_{j,\sigma'}^\dagger c_{k,\sigma'} c_{l,\sigma} \\
 & - \sum_{i,j} \frac{J_{i,j}(R)}{2} \left[\left(c_{i,\uparrow}^\dagger c_{j,\uparrow} - c_{i,\downarrow}^\dagger c_{j,\downarrow} \right) M_z + \varepsilon \left(c_{i,\downarrow}^\dagger c_{j,\uparrow} M^+ + c_{i,\uparrow}^\dagger c_{j,\downarrow} M^- \right) \right], \quad (4.1)
 \end{aligned}$$

where $c_{i,\sigma}^\dagger$ ($c_{i,\sigma}$) creates (annihilates) an electron on the orbital $i = \{m, n\}$ with spin σ . In the above Hamiltonian, the first term is the single-particle energy and the second term is the electron-electron (e-e) interaction. The e-e term is scaled by a dimensionless parameter γ : $\gamma = 0$ describes the noninteracting electronic system and $\gamma = 1$ describes the interacting

system. The matrix elements $\langle i, j | V_{ee} | k, l \rangle$ of the Coulomb interaction are evaluated in the basis of 2D HO orbitals in the closed form [158]. The last term of the Hamiltonian describes the electron-Mn interaction (e-Mn). It is scaled by the exchange coupling matrix elements $J_{i,j}(R) = J_C^{2D} \phi_i^*(R) \phi_j(R)$, where $J_C^{2D} = 2J_{bulk}/d$, $J_{bulk} = 15 \text{ meV nm}^3$ is the s - d exchange constant for the CdTe bulk material, $d = 2 \text{ nm}$ is the QD height, and $\phi_i(R)$ is the amplitude of the HO wave function at the Mn position R . The e-Mn interaction consists of two terms. The first one is the Ising interaction between the electron and the Mn spin. The second term accounts for the e-Mn spin-flip interactions. The anisotropy of the exchange interaction is tuned by the factor ε . By setting $\varepsilon = 0$ we obtain the anisotropic Ising e-Mn exchange Hamiltonian and setting $\varepsilon = 1$ we obtain the isotropic, Heisenberg exchange Hamiltonian. In the former case, the spin projections s_z and M_z are separately good quantum numbers. The total spin projection of the electrons depends on the number and polarization of the particles. For the manganese spin, we have $M = 5/2$ and the six possible spin projections $M_z = -5/2, \dots, 5/2$. The isotropic Heisenberg Hamiltonian, in contrast, conserves the total angular momentum $\mathbf{J} = \mathbf{M} + \mathbf{S}$ and its projection $J_z = s_z + M_z$. Hence, for the case $\varepsilon = 1$ one can establish the total spin quantum number J of the given manifold of states by considering its degeneracy $g(J) = 2J + 1$.

Since the elements $J_{i,j}$ depend on the position R of the Mn spin, the e-Mn coupling can be engineered by choosing a specific R [78]. In this work we place the Mn spin at the center of the QD and the only nonzero matrix elements $J_{i,j}$ that appear are related with i and j orbitals with zero angular momentum states. The spin of an electron placed on any other HO orbital is not coupled directly to the Mn spin.

The eigenenergies and eigenstates of the Hamiltonian (4.1) are obtained in the configuration-interaction approach. In this approach, we construct the Hamiltonian matrix in the basis of configurations of N electrons and one Mn spin: $|\nu_i\rangle = |i_{1\uparrow}, i_{2\uparrow}, \dots, i_{N\uparrow}\rangle |i_{1\downarrow}, i_{2\downarrow}, \dots, i_{N\downarrow}\rangle |M_z\rangle$,

where $|i_{1\sigma}, i_{2\sigma}, \dots, i_{N\sigma}\rangle = c_{i_{1\sigma}}^\dagger c_{i_{2\sigma}}^\dagger \dots c_{i_{N\sigma}}^\dagger |0\rangle$, $|0\rangle$ is the vacuum state, $N = N_\uparrow + N_\downarrow$ is the number of electrons, in which N_\uparrow and N_\downarrow are the number of electron with spin up and spin down, respectively. The total number of configurations depends on the number of electrons and on the number of HO shells available in the QD. With Mn impurity at the center, the total orbital angular momentum of electrons $L = \sum_{i=1}^N L_e^i$ is conserved by the Hamiltonian (4.1). Moreover, depending on the anisotropy of e-Mn interactions, the Hamiltonian also conserves the total projections S_z and M_z of the electron and Mn spin separately (the Ising model) or the projection $J_z = s_z + M_z$ of the total spin (the Heisenberg model). Based on these conservation rules, we divide the basis of configurations into subspaces labeled by the numbers L , S_z , and M_z (for the Ising model) or L and J_z (for the Heisenberg model), and diagonalize the Hamiltonian in each subspace separately.

The computational procedure adopted in this work is as follows. For a chosen number of electrons $N = 2, \dots, 6$ and a chosen number of HO shells, we look for the ground and several excited states for the system with and without e-e interactions in the Ising and isotropic Heisenberg models. By analyzing the degeneracies of the states we find the total spin of the system. Further, from the ordering of different states with respect to their total spin we draw conclusions as to the ferromagnetic or antiferromagnetic character of the effective e-Mn interactions. By comparing the results for the system with and without the e-e interactions ($\gamma = 1$ or $\gamma = 0$, respectively) we establish that the e-e interactions mediated an effective e-Mn Hamiltonian for electrons not directly coupled to the central spin.

4.3 Spin singlet closed shells coupled with the magnetic ion

We start with a discussion of a filled s -shell with $N = 2$ electrons in the zero angular momentum channel. Each electron is directly coupled to the Mn impurity, but the singlet state couples only via e-e interactions [58]. Here we discuss the role of the anisotropy of the

exchange interaction on this indirect coupling. A similar discussion applies to other closed shells, e.g., $N=6$.

The lowest-energy s -shell spin singlet configuration with $S = 0$ and orbital angular momentum $L = 0$, $|s_z^{GS} = 0, M_z\rangle = c_{s,\uparrow}^\dagger c_{s,\downarrow}^\dagger |0, M_z\rangle$, is shown schematically in the top left panel of Fig. 4.1(a). The expectation value of the e-Mn Hamiltonian with respect to the configuration $|s_z^{GS} = 0, M_z\rangle$ is zero.

Increasing the number of confined shells to three adds one additional orbital $(1, 1)$ with zero angular momentum in the d -shell directly coupled to the Mn spin. Now the two-electron triplet states with total angular momentum $L = 0$ couple to the Mn spin. The triplet with $S_z = 0$, $|s_z^E = 0, M_z\rangle = (1/\sqrt{2}) (c_{d,\uparrow}^\dagger c_{s,\downarrow}^\dagger - c_{s,\uparrow}^\dagger c_{d,\downarrow}^\dagger) |0\rangle |M_z\rangle$. One of its components is shown schematically in the top right panel of Fig. 4.1(a), while the bottom left panel of that figure shows the spin-polarized triplet $|s_z = 1, M_z - 1\rangle = c_{s,\uparrow}^\dagger c_{d,\uparrow}^\dagger |0, M_z - 1\rangle$, and the bottom right panel shows the triplet $|s_z = -1, M_z + 1\rangle = c_{s,\downarrow}^\dagger c_{d,\downarrow}^\dagger |0, M_z + 1\rangle$. Applying the e-Mn Hamiltonian to the $|s_z^{GS} = 0, M_z\rangle$ state we obtain

$$\begin{aligned} H_{eMn} |s_z^{GS} = 0, M_z\rangle &= -\frac{J_{sd}}{\sqrt{2}} M_z |s_z^E, M_z\rangle \\ &- \frac{J_{sd}}{2} \varepsilon (\beta_- |s_z = 1, M_z - 1\rangle - \beta_+ |s_z = -1, M_z + 1\rangle), \end{aligned} \quad (4.2)$$

where J_{sd} is the exchange matrix element in which one electron is scattered from the s orbital to the d orbital and $\beta_\pm = \sqrt{(M \mp M_z)(M \pm M_z + 1)}$. We find that upon the inclusion of the d shell, the low-energy s -shell singlet two-electron configuration becomes coupled by e-Mn interactions to electron triplet configurations, with and without flip of the Mn spin.

We now diagonalize the two-electron-Mn Hamiltonian and compute the ground state energy E_{Mn} of the QD with a manganese ion, and the energy E_e of the system without Mn. Fig. 4.1(b) shows the effect of the Mn ion on the ground state energy, $\Delta = (E_{Mn} - E_e)/J_{ss}$, measured from the ground state energy without Mn ion, as a function of number of shells for the interacting system ($\gamma = 1$) and the isotropic exchange interaction ($\varepsilon = 1$). We find that,

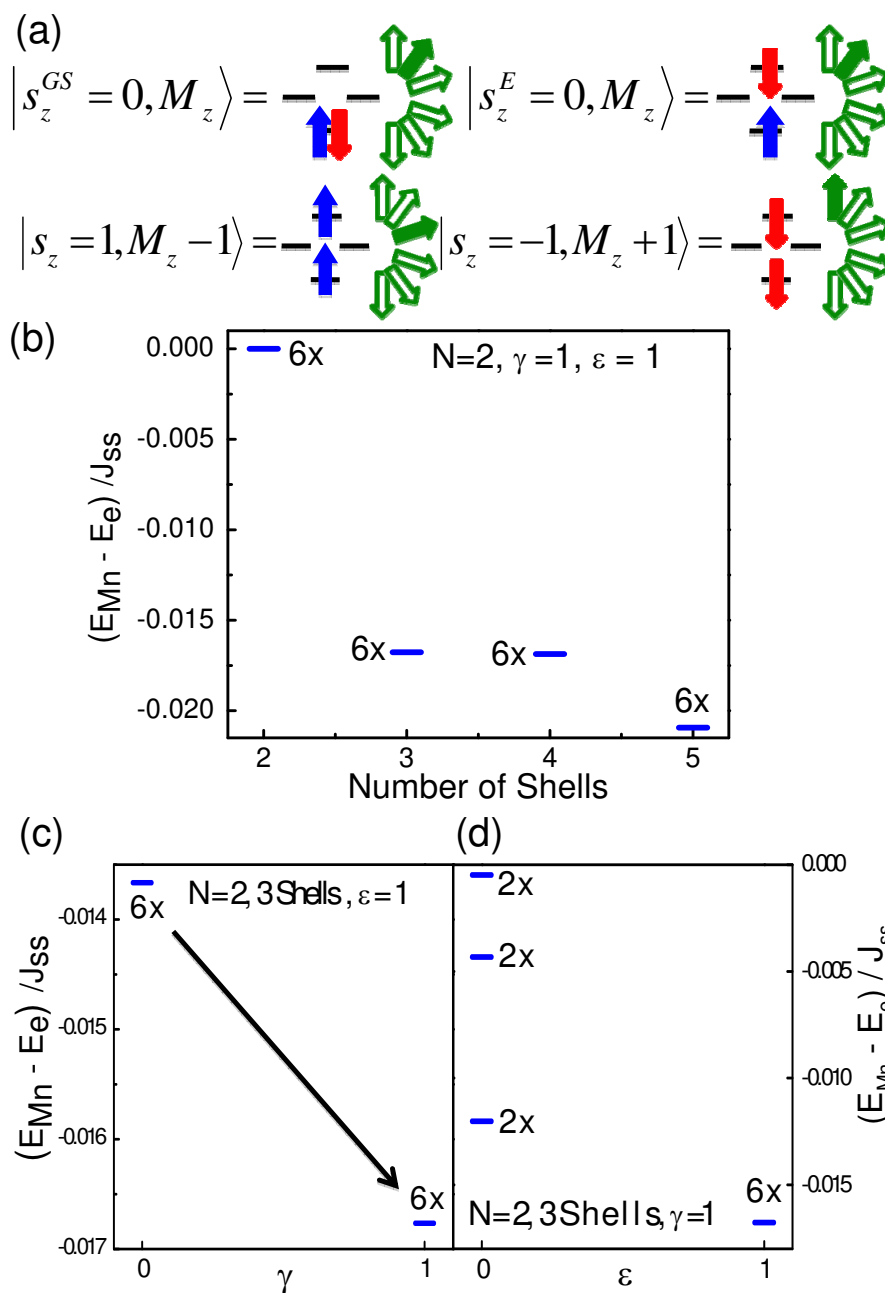


Figure 4.1: (a) Schematic pictures of two-electron-Mn configurations, GS and electronic triplet states, coupled by the e-Mn interactions. (b) Ground-state energy of the two-electrons-Mn system as a function of the number of quantum-dot shells. (c) and (d) Ground-state energies of the two-electron-Mn system for the quantum dot confining three shells plotted as a function of the strength of electron-electron interactions in the Heisenberg e-Mn model (c) and as a function of the isotropy of the e-Mn Hamiltonian for the fully interacting electron system (d). Numbers at the energy level bars represent the degeneracy of states.

irrespective of the number of confined shells, the GS is sixfold degenerate, with the total spin $J_{GS} = 5/2$. However, the energy of the GS markedly depends on the number of shells. For two confined shells we have $\Delta = 0$, because in this case we can generate only one configuration, $|s_z^{GS} = 0, M_z\rangle$, which is decoupled from the Mn spin. The inclusion of the d -shell adds an additional $L_e = 0$ orbital into the single-particle basis, resulting in the scattering of electrons by the localized spin and lowering of energy. A further lowering of the energy occurs when the fifth shell, containing another $L_e = 0$ single-particle state, becomes confined.

Now we fix the number of shells to three, set the Heisenberg form of e-Mn interactions and study the effect of e-e interactions. Fig. 4.1(c) shows the energy Δ without ($\gamma = 0$) and with full Coulomb interactions ($\gamma = 1$). We find that the ground state in both cases is sixfold degenerate but the e-e Coulomb interactions enhance the effects of the e-Mn coupling, lowering Δ . This is due to a larger contribution of triplet configurations to the GS.

We now compare the results for the isotropic coupling versus the anisotropic coupling. For the anisotropic coupling, $\varepsilon = 0$, we observe that the GS is split into three energy levels labeled by $|M_z|$, each of them twice degenerate, as shown in Fig. 4.1(d). For the Ising-like coupling, the total angular momentum J is not conserved, and the characteristic sixfold degeneracy of the ground state is broken. Comparing the isotropic and anisotropic coupling we observe that Δ is negative for both couplings and also that the Heisenberg-like interaction results in a lower energy than the Ising-like interaction [58].

4.4 Electrons in finite angular momentum channels

In this section, we discuss electrons populating finite angular momentum channels which are not directly coupled with Mn ion. For $N = 3$, we show the existence of an effective coupling mediated by e-e interactions. Similar results are obtained for $N = 5$.

4.4.1 One electron on the p shell

The lowest-energy configuration in the ground state of three electrons is formed by two electrons in the s -shell and one electron in the p -shell. With Mn in the QD center the total angular momentum L of the three electrons is conserved and we show the results for $L = 1$.

Figure 4.2(a) illustrates the degenerate three-electron configurations, $|s_z = 1/2, M_z\rangle$ and $|s_z = -1/2, M_z + 1\rangle$, with an electron with spin up and Mn in state M_z and electron with spin down on the p -orbital and Mn in state $M_z + 1$. As the electron-Mn exchange interaction in the p -shell vanishes, $J_{pp} = 0$, these configurations do not interact with each other. As a consequence, the GS is twelvefold degenerate, two electron spin configurations times six Mn spin orientations. In order to understand the effect of interactions we include configurations coupled with $|s_z = 1/2, M_z\rangle$ and $|s_z = -1/2, M_z + 1\rangle$ by both e-e and e-Mn interactions and diagonalize the Hamiltonian in the $L = 1$ subspace. The number of three-electron-Mn configurations depends on the number of electronic shells, with 24, 228, 852, 2520 for two, three, four and five shells, respectively.

Figure 4.2(b) shows the exact diagonalization results of the Hamiltonian for three confined shells in the QD and an isotropic e-Mn interaction ($\epsilon = 1$), for both non-interacting ($\gamma = 0$) and interacting ($\gamma = 1$) electron system. For the non-interacting case we observe that the GS is twelvefold degenerate, with the energy lowered by e-Mn interaction (negative Δ). This behavior is identical to the one observed for the two electrons (see previous section), i.e, the two electrons in s -shell are coupled with Mn, while the electron in the p -shell is only a spectator. However, in the strongly interacting regime, $\gamma = 1$, we observe a splitting of the degenerate GS into two degenerate shells. The splitting and the degeneracy of levels is consistent with an effective Hamiltonian $H_{eff} = -J_{eff}\vec{s} \cdot \vec{M}$ coupling the p -shell electron spin s with the Mn spin M [78]. The effective coupling J_{eff} is mediated by Coulomb interactions. In Fig. 4.2(c) we illustrate the processes which couple $|s_z = 1/2, M_z\rangle$ and $|s_z = -1/2, M_z + 1\rangle$

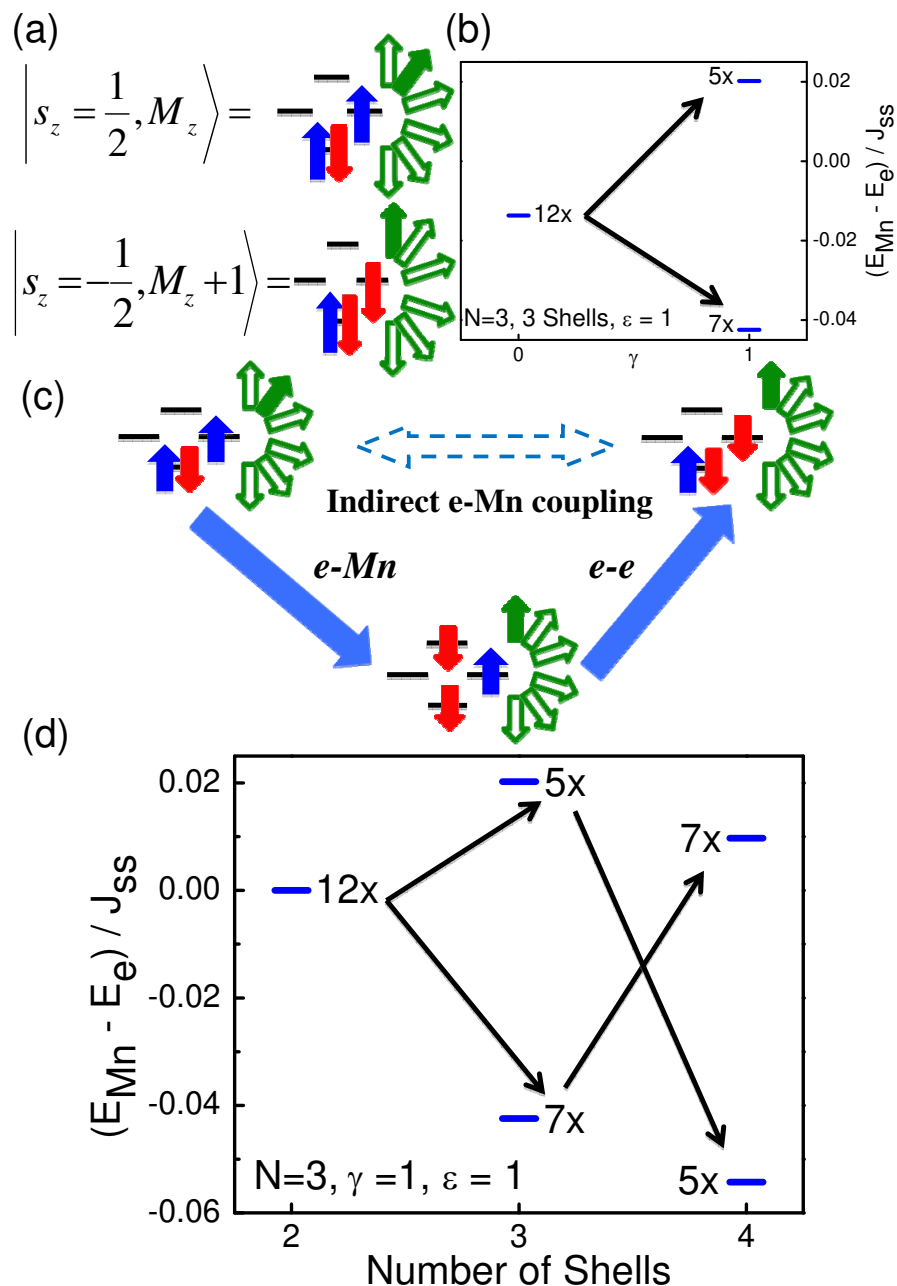


Figure 4.2: (a) Ground-state three-electron configurations with the p -shell electron spin up (top) and spin down (bottom). (b) Energy difference Δ between three-electron GS in the Mn-doped and undoped QD for both non-interacting ($\gamma = 0$) and interacting ($\gamma = 1$) electrons. The numbers indicate the degeneracy of each level. (c) Diagram of coupling between electrons in the p -shell and Mn. The filled arrow represents a direct coupling via e -Mn coupling or e - e Coulomb interaction, and the dashed arrow illustrates the indirect coupling. (d) The energy difference Δ as a function of number of shells for a QD containing three shells and $\gamma = 1$.

states. The e-Mn interaction acting on the $|s_z = 1/2, M_z\rangle$ state scatters the spin up (blue) electron from the s shell to the spin down (red) electron on the d shell with simultaneous transition of the Mn spin from M_z to $M_z + 1$. In the next step, the e-e interaction scatters the d -shell and p -shell electron pair into the s -shell and p -shell electron pair, with the spin down electron on the p shell and the spin up electron on the s shell. The net result is a spin flip of the p -shell electron and of the Mn spin. We see that the ground state is sevenfold degenerate implying that the electron spin is aligned with the Mn spin and J_{eff} is hence ferromagnetic.

Let us now investigate the dependence of the GS energy on the number of confined shells in the QD. Fig. 4.2(d) shows the evolution of the GS energy as function of the number of shells for $\gamma = 1$ and $\varepsilon = 1$. We observe that for two shells there is no splitting, i.e. $J_{eff} = 0$, while for three and four shells the GS is split into two shells. For two shells the GS is twelvefold degenerate, $\Delta = 0$, and there is no interaction between Mn and electrons. For three shells the GS is split into two shells as discussed above. For four shells the GS is also split into two, but there is an inversion of the degeneracy of the energy levels. This is a consequence of an antiferromagnetic interaction $J_{eff} < 0$ between electron and Mn spins. We have also observed that for QDs confining five or six shells the results are similar to what was obtained for QD with four shells, i.e, the antiferromagnetic coupling is stabilized for a QD containing more than three confined shells. This can be understood by looking at the way the GS is coupled to Mn. In Fig. 4.2(c) we show that there is an indirect coupling between configurations $|s_z = 1/2, M_z\rangle$ and $|s_z = -1/2, M_z + 1\rangle$ which is mediated via e-e Coulomb and e-Mn interactions between the GS and excited configurations. As the number of shells increases, more excited state configurations interact with the GS stabilizing the antiferromagnetic indirect coupling between the electrons and Mn.

If the indirect magnetic ordering shown above depends on the number of shells, it also should depend on the QD shell spacing ω_0 . Fig. 4.3(a) shows the dependence of GS energy

on ω_0 for three electrons confined in Mn-doped QD containing three shells, $\gamma = 1$ and $\varepsilon = 1$. We note that the exchange coupling changes from ferromagnetic to antiferromagnetic for $\omega_0 \approx 3.3Ry^*$. We observe the same behavior for QDs with four shells, but in this case the crossing occurs at $\omega_0 \approx 0.45Ry^*$.

Next we discuss the effect of anisotropy on the e-Mn exchange interaction. Fig. 4.3(b) shows the GS energy for three electrons in a QD containing three shells in the strongly interacting regime as a function of the e-Mn coupling. For $\epsilon = 0$ the electrons and Mn interact via an anisotropic Ising-like Hamiltonian, and for $\epsilon = 1$ the e-Mn interaction is isotropic, Heisenberg-like. For $\epsilon = 0$, s_z is a good quantum number, and therefore the electron spin degeneracy is preserved. In Fig. 4.3(b) we observe that for $\epsilon = 0$ the energy spectrum is split into six doubly-degenerate levels. This splitting is due to the e-e Coulomb interaction driving the indirect e-Mn interaction between the p -shell electron and Mn, as was observed in the $\epsilon = 1$ case. The double degeneracy for the anisotropic coupling arises due to the fact that the state $|s_z = 1/2, M_z\rangle$ has the same energy as the configuration of $|s_z = -1/2, -M_z\rangle$.

4.4.2 Two spin-polarized electrons on the p shell

Next we describe the electronic properties of a half-filled p -shell. The lowest-energy configuration of the four electron GS state is formed by two electrons in the s shell and two spin triplet electrons in the p shell. Fig. 4.4(a) illustrates the four-electron configurations, triplet $|S = 1, s_z = 1, M_z\rangle$ and one of the singlet components $|S = 0, s_z = 0, M_z + 1\rangle$ configuration. These two configurations have the same total spin projection J_z . In the presence of e-e Coulomb interaction the $S = 1$ triplet state is the GS and the singlet is an excited state. For Mn in the QD center the p electrons do not couple with Mn, the electron spin degeneracy is preserved, and the degeneracy of the triplet state in a Mn-doped QD is 18, while the singlet state is sixfold degenerate.

We shall now investigate how the GS of four electrons confined in a Mn-doped QD is

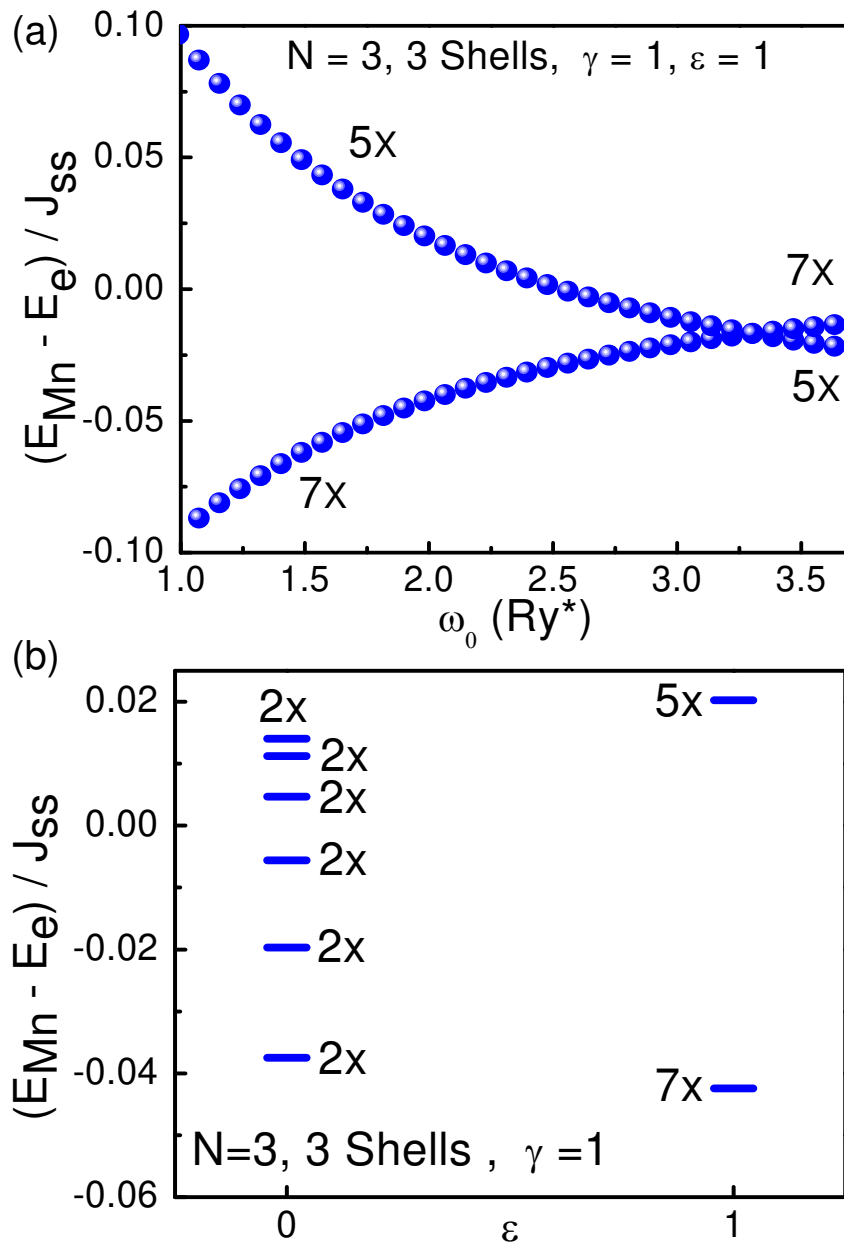


Figure 4.3: (a) Evolution of the energies of three-electron levels with $J = 3$ and $J = 2$ as a function of the QD shell spacing ω_0 . (b) Energy difference Δ for both anisotropic ($\epsilon = 0$) and isotropic ($\epsilon = 1$) e-Mn interaction in a three-shell QD with full interactions ($\gamma = 1$).

affected by the presence of the e-e Coulomb interaction, number of shells, shell spacing, and e-Mn coupling. We take advantage of the conservation of the total angular momentum and diagonalize our microscopic Hamiltonian in the $L = 0$ subspace. The number of configurations in this subspace is 30, 498, and 3498 for two, three and four shells, respectively.

The e-e mediated coupling of electronic and Mn spin is interpreted in terms of effective exchange Hamiltonian. Adding the electron and Mn spins results in total spin $J = 7/2, 5/2, 3/2$ and splitting of 18-fold degenerate ground state into 8-fold, 6-fold and 4-fold degenerate shells. Figure 4.4(b) shows the evolution of the low-energy part of the spectrum of four electrons in the magnetic dot as a function of the number of shells for full e-e interactions ($\gamma = 1$) and the isotropic e-Mn coupling ($\varepsilon = 1$). The energies of these states are shown relative to the energy of the ground-state triplet of the undoped QD. The triplet and singlet states split for any number of shells due to e-e exchange interaction. In a QD with only s and p shells, the effective exchange coupling for p -shell electrons is zero and the triplet and singlet states are 18 and 6 times degenerate, respectively. Increasing the number of shells leads to a finite and ferromagnetic exchange interaction with the triplet states coupled to Mn spin and the 18-fold degenerate shell split into 8-, 6- and 4-fold degenerate levels. The character of this exchange interaction depends on the number of shells. For three shells we have a ferromagnetic coupling but for four shells the coupling becomes antiferromagnetic.

Figure 4.4(c) illustrates the configurations involved in the indirect coupling of the electrons on the p -shell and the Mn spin. Here, the filled arrows represent the direct coupling between configurations, and the dashed arrow represents the indirect interaction between two configurations. Let us explain how this indirect coupling arises, starting from the configuration with two spin-up electrons in the p -shell, which is labeled as $|S = 1, s_z = 1, M_z\rangle$, Fig. 4.4(c) top left. This configuration is coupled with an excited state in which there are two spin-down electrons in both $L_e = 0$ orbitals, one in the s -shell and the other in the d -shell. This coupling occurs via

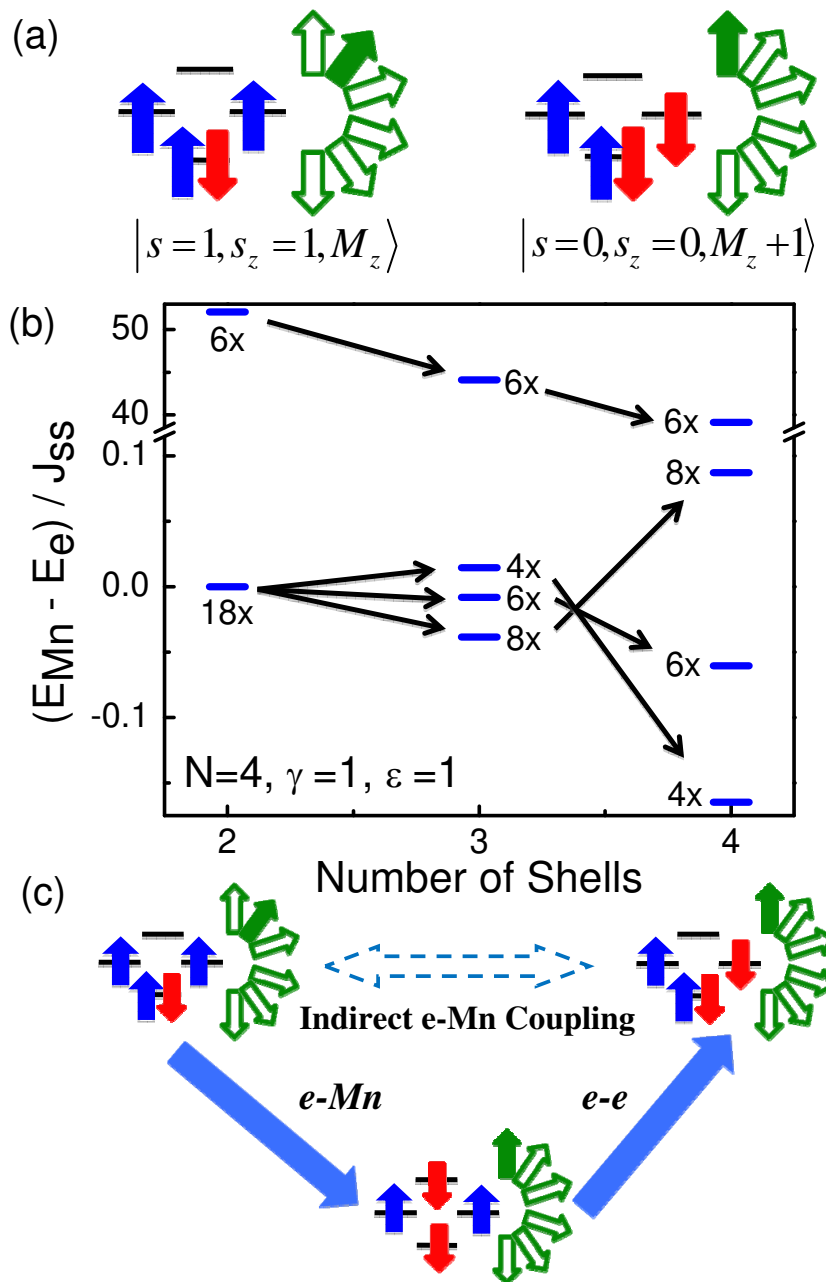


Figure 4.4: (a) Low-energy configurations of four electrons in a magnetic QD. (b) Low-energy spectrum of the system as a function of the number of shells for interacting ($\gamma = 1$) electrons, measured from the respective GS energy E_e of a nonmagnetic system. Here the QD shell spacing $\omega_0 = 1.98Ry^*$. (c) Indirect coupling diagram of two four-electron configurations. The filled arrows represent direct interaction between configurations and the dashed arrow represents the indirect e-Mn coupling.

e-Mn interaction, which scatters the spin-up electron in the s -shell of $|S = 1, s_z = 1, M_z\rangle$ to the d -shell, flipping the electron spin down, and the Mn spin up, i.e, $M_z + 1$. This excited state with $s_z = 0$ and $M_z + 1$ is coupled with one of the $|S = 0, s_z = 0, M_z + 1\rangle$ GS configuration via the e-e Coulomb interaction, in which the spin down electron in the d -shell is scattered to the $L_e = 1$ p orbital, and the spin up electrons in this orbital is scattered to the s -shell.

Figure 4.5(a) shows the GS energy for both noninteracting ($\gamma = 0$) and fully interacting ($\gamma = 1$) electrons. We considered a Mn-doped QD with three confined shells and the isotropic e-Mn interaction ($\varepsilon = 1$). For the noninteracting case there is no triplet-singlet splitting, and as e-e Coulomb interaction mediates the indirect interaction between Mn and p -shell electrons the triplet is not split either. Therefore, the four-electron GS is 24-fold degenerate. Even though the four noninteracting electron triplet states are not split by the indirect coupling, we see a negative Δ , which means that electrons lower their energy by exchange interaction with Mn. Turning the e-e Coulomb interaction on the singlet-triplet split and a further splitting of the triplet energy shell is observed. The triplet splitting is caused by the indirect interaction between Mn and electrons in the p -shell, which is mediated by the e-e Coulomb interaction.

In Fig. 4.5(a) we show the effect of the e-e interaction on the low-energy spectrum of the four-electron and Mn complex. We note the appearance of triplet and singlet energy shells, separated by the e-e exchange interaction. The splitting of the triplet shell is governed by the e-e and e-Mn exchange interactions.

Figure 4.5(b) presents the energy difference Δ , i.e., the effective exchange coupling, as a function of ω_0 for four interacting electrons ($\gamma = 1$) confined in the Mn-doped QD with three confined shells. Here we have also a ferromagnetic to antiferromagnetic crossing as a function of the QD shell spacing. For QDs with four shells the ferromagnetic to antiferromagnetic crossing occurs at $\omega_0 \approx 0.04Ry^*$.

Now we show the effect of the symmetry of the e-Mn coupling on the four electron GS. In

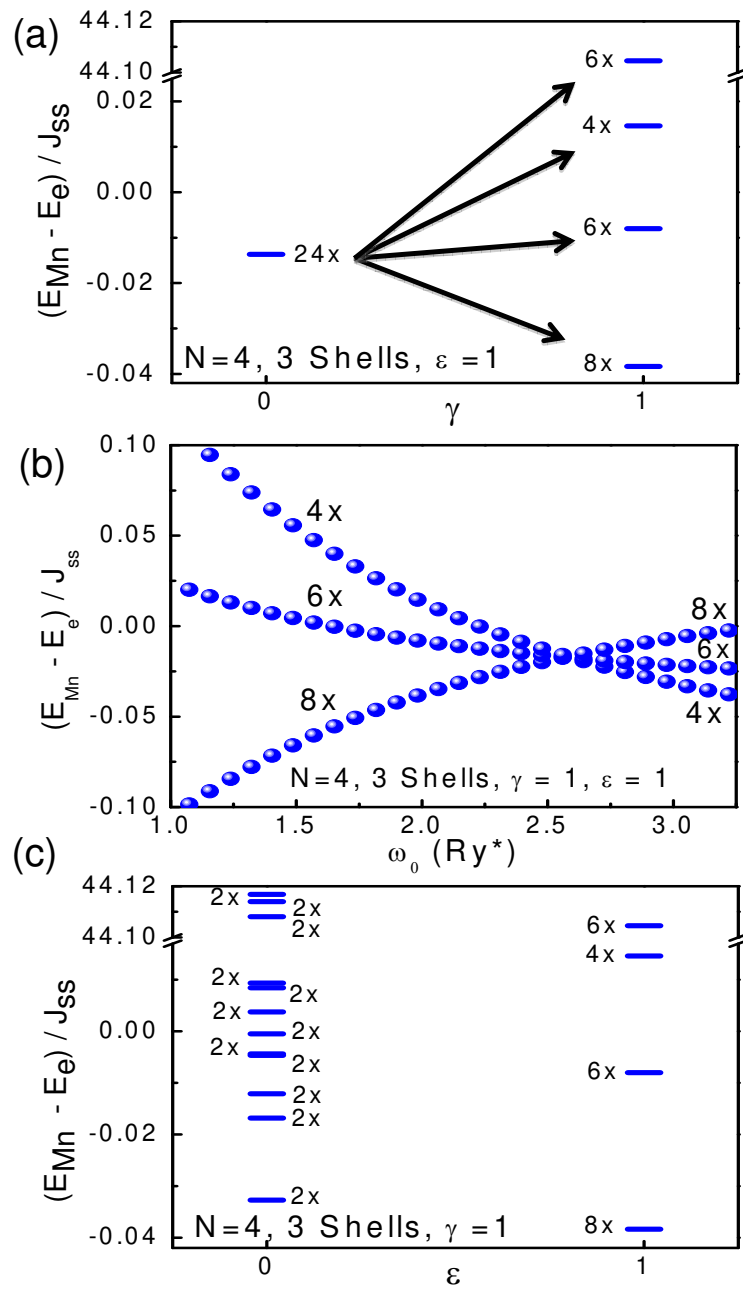


Figure 4.5: (a) Energy difference Δ for non-interacting ($\gamma = 0$) and interacting ($\gamma = 1$) electrons in the four-electron magnetic dot. (b) GS energy difference as function of the QD shell spacing ω_0 for three shells confined in the QD. (c) GS energy difference for the anisotropic ($\epsilon = 0$) and isotropic ($\epsilon = 1$) e-Mn coupling.

Fig. 4.5(c) we compare the effects of the anisotropic ($\varepsilon = 0$) and isotropic ($\varepsilon = 1$) coupling for a Mn-doped QD with three confined shells and in the presence of full e-e Coulomb interaction ($\gamma = 1$). For the anisotropic coupling, the triplet state is split into nine doubly degenerate levels. In this case, both s_z and M_z are good quantum numbers, and therefore, $s_z = 1$ and $s_z = -1$ breaks the Mn spin degeneracy into six. As the energy of state with $s_z = 1$ and M_z is equal to the energy of the state $s_z = -1$ and $-M_z$, these six states are double degenerate. The $s_z = 0$ configurations split into three, where the degeneracy is given by M_z , i.e, the $s_z = 0$ configurations are degenerate and labeled by $|M_z|$, as for the two electrons interacting with the Mn via an anisotropic e-Mn interaction. The singlet state is also split into three doubly-degenerate levels.

4.5 Conclusion

In conclusion, we presented a microscopic model of interacting electrons coupled with a magnetic ion spin localized at the center of a self-assembled quantum dot. We showed that the electrons occupying finite angular momentum orbitals interact with the localized spin through effective exchange interaction mediated by electron-electron interactions. The effective interaction for p -shell electrons is obtained using exact diagonalization of the microscopic Hamiltonian as a function of the number of electronic shells, shell spacing, and anisotropy of exchange interaction. It is shown that the effective interaction can be engineered to be either ferro- or antiferromagnetic, depending on quantum dot parameters.

Chapter 5

Optical properties of charged quantum dots doped with a single magnetic impurity

Here we present the optical properties of charged II-VI self-assembled quantum dots doped with a single magnetic impurity. Our primary goal is to extend the theory of charged quantum dots doped with Mn. Second, we discuss how the indirect electron-Mn interaction, which was demonstrated in the chapter 4, alters the photoluminescence spectra of quantum dots doped with Mn. This indirect interaction allows us to access the number of confined electronic shells, the number of electrons and their spin. We present results for $X^{2-} + \text{Mn}$ and $X^{3-} + \text{Mn}$ complex*. We also show that the indirect electron-Mn coupling is robust to modifications in the Mn position. This Chapter is based on the article “*Optical properties of charged quantum dots doped with a single magnetic impurity*” by U. C. Mendes, M. Korkusinski, A. H. Trojnar, and P. Hawrylak, Phys. Rev. B **88**, 115306 (2013).

5.1 Introduction

There is currently interest in developing means of controlling spin at the nanoscale [41, 45, 46, 51, 93, 159, 160]. This includes spin of electrons and holes in gated [161, 162] and self-assembled quantum dots [33, 163] as well as magnetic impurities in semiconductors [51, 93]. It

* X^{n-} represent the excitonic charged complex with n indicating that there are $n + 1$ electrons and 1 hole confined in the QD.

is now possible to place, optically detect, and manipulate a single magnetic impurity in a single self-assembled quantum dot (QD) [56, 61, 62, 103, 164–167]. The electrical control of the spin of manganese (Mn) ions in CdTe quantum dots with a small electron population controlled by the gate has been implemented [57]. The properties of CdTe quantum dots with magnetic impurities have been extensively investigated theoretically [59, 60, 62, 78, 153, 157, 159, 168–171], including the theory of Coulomb blockade and capacitance spectroscopy [78, 168, 172], cyclotron resonance [153], and photoluminescence (PL) [59, 60, 62, 173, 174]. The optical properties of carriers confined in III-V quantum wells [31] and quantum dots [61] containing Mn ions have also been investigated.

The electronic properties of quantum dots containing N_e electrons and a single localized spin have been investigated theoretically [59, 78]. It was shown that the electron spin can be controlled by controlling the number N_e (see Refs. [78, 173]). For closed electronic shells the total spin is zero and electrons are decoupled from the Mn spin, while for half-filled shells the electron spin is maximized and the coupling to the Mn spin is strongest [78, 173]. The spin-singlet N_e -electron droplet coupled to the Mn spin gives insight into the Kondo effect in the interacting electron system, and this coupling might potentially allow for direct detection of the electron spin. Simultaneously, the optical properties of charged QDs without magnetic ions have been studied both numerically and experimentally [63, 64, 175, 176].

Here we present a microscopic theory of the optical properties of charged self-assembled quantum dots doped with a single magnetic Mn ion as a function of number of electrons N_e . The single-particle electron and heavy-hole electronic shells are described by states of a two-dimensional harmonic oscillator. The electron-electron, electron-hole Coulomb interactions, as well as the short-range electron spin-Mn spin and hole spin-Mn spin contact exchange interactions are included. The electronic states of the photoexcited $N_e + 1$ electron- 1 hole- 1 Mn complex ($X^{N_e-} + \text{Mn}$) and of the final N_e electron-Mn complex ($N_e + \text{Mn}$) are expanded in

a finite number of configurations. The full interacting initial and final state Hamiltonians are diagonalized numerically. The emission spectra as a function of photon energy are obtained from Fermi's golden rule as a function of N_e . We show that the emission spectra depend on the number N_e , the position of Mn ion, the spin of the initial and final electronic states, and the size of the QD measured by the number of confined electronic shells. We demonstrate that the emission spectra allow to establish the number of electrons N_e populating electronic shells and, most importantly, to read the electronic spin through multiplets of energy levels manifested in the number of emission lines. If the Mn ion is placed in the center of the QD, the p -shell electrons do not interact with it directly. However, we show that in this case there exists an effective electron-Mn interaction mediated by electron-electron interactions. This mechanism allows to detect the spin polarization of a half-filled p shell.

The Chapter is organized as follows. Section II describes the microscopic model, electronic structure, total spin, and the emission spectrum of the system of many electrons and a hole in a QD doped with a single Mn atom. Section III summarizes the results of the calculations of the emission spectra from nonmagnetic QDs as a function of the number of initial-state electrons, and discusses in detail the emission from a magnetic QD containing p -shell electrons, i.e., X^{2-} and X^{3-} complexes. In this section, we also compare the emission spectra of X^- , X^{-} , X^{2-} and X^{3-} -Mn complexes and discuss the differences and similarities between them. At last we discuss the effects of Mn position on the X^{2-} -Mn PL spectrum. Summary of the work is presented in Sec. IV.

5.2 Model

We model the confining potential of the QD in the effective-mass approximation as a quasi-two-dimensional isotropic harmonic oscillator (HO) [34, 177]. Since the strain in the QDs results in the significant splitting between the light- ($\tau = \pm 1/2$) and heavy-hole ($\tau = \pm 3/2$)

subbands [178], we retain only heavy-holes in this calculations. We define the single-particle basis for electrons (hole) in terms of the eigenstates of the isotropic parabolic quantum dot with the characteristic frequency $\omega_{e(h)}$. The basis states are denoted by $|i\sigma\rangle$ for the electron and $|j\tau\rangle$ for the hole, where the complex index denotes a set of the HO quantum numbers $i = \{n, m\}$, while σ (τ) is a spin z -projection of the particle. Each single-particle state has an angular momentum of $L_e = m - n$ for the electron and $L_h = n - m$ for the hole. The energies of these single-particle states are given by $E_i^{e(h)} = \omega_{e(h)}(n + m + 1)$.

We measure energy in units of the effective Rydberg, $\text{Ry}^* = m^* e^4 / 2\epsilon^2 \hbar^2$, and length in the units of the effective Bohr radius, $a_0^* = \epsilon \hbar^2 / m^* e^4$, where e is the electron charge, \hbar is the reduced Planck constant, m^* is the effective mass of the electron, while ϵ is the dielectric constant of the material.

The Hamiltonian of the confined, interacting $N_e + 1$ electrons and a valence hole interacting with the spin of the magnetic impurity can be written in the second quantization language as [63, 173]

$$\begin{aligned}
H = & \sum_{i,\sigma} E_{i,\sigma}^e c_{i,\sigma}^\dagger c_{i,\sigma} + \frac{1}{2} \sum_{\substack{i,j,k,l \\ \sigma,\sigma'}} \langle i, j | V_{ee} | k, l \rangle c_{i,\sigma}^\dagger c_{j,\sigma'}^\dagger c_{k,\sigma'} c_{l,\sigma} + \sum_{i,\tau} E_{i,\tau}^h h_{i,\tau}^\dagger h_{i,\tau} \\
& - \sum_{\substack{i,j,k,l \\ \sigma,\tau}} \langle i, j | V_{eh} | k, l \rangle c_{i,\sigma}^\dagger h_{j,\tau}^\dagger h_{k,\tau} c_{l,\sigma} - \sum_{i,j} \frac{J_{i,j}^e(R)}{2} \left[\left(c_{i,\uparrow}^\dagger c_{j,\uparrow} - c_{i,\downarrow}^\dagger c_{j,\downarrow} \right) M_z + c_{i,\downarrow}^\dagger c_{j,\uparrow} M^+ \right. \\
& \left. + c_{i,\uparrow}^\dagger c_{j,\downarrow} M^- \right] + \sum_{i,j} \frac{3J_{i,j}^h(R)}{2} \left(h_{i,\uparrow}^\dagger h_{j,\uparrow} - h_{i,\downarrow}^\dagger h_{j,\downarrow} \right) M_z,
\end{aligned} \tag{5.1}$$

where $c_{i,\sigma}^\dagger$ ($h_{i,\tau}^\dagger$) creates an electron (hole) on the orbital i with spin σ (τ). The first two terms of the Hamiltonian are the electron kinetic energy and the electron-electron Coulomb interaction (e-e). The next two terms describe the hole kinetic energy and the Coulomb interaction between the hole and all electrons. The fifth term, describing the short-range electron-Mn (e-Mn) interaction [78], consist of two types of terms. The first one is the Ising interaction, which conserves the spin of both the electron and the Mn. The second and third

terms of the e-Mn Hamiltonian allow for the simultaneous flip of the electron and Mn spins in such a way as to conserve $M_z + \sigma$. The last term is the anisotropic heavy-hole-Mn spin interaction [59, 179], which describes a scattering of the hole from i to j single-particle states by a Mn ion at the position R . The e-Mn and hole-Mn (h-Mn) interaction is proportional to the $s(p)$ - d exchange matrix elements, $J_{i,j}^{e(h)}(R) = J_C^{e(h)} \phi_i^*(R) \phi_j(R)$, where $\phi_i(R)$ is the value of the HO wave-function at the position R , while $J_C^{e(h)} = 2J_{s(p)-d}/d$. $J_{s(p)-d}$ is the bulk exchange contact interaction parameter, while d is the height of the QD. As $J_{i,j}^{e(h)}(R)$ depends on the position R of the Mn ion in the QD, by changing R one can control the strength of the e-Mn interaction [78].

The many-particle wave function is expanded in the basis of the configurations of $N_e + 1$ electrons and a hole $|\nu_i\rangle = |i_{1\uparrow}, i_{2\uparrow}, \dots, i_{N\uparrow}\rangle |j_{1\downarrow}, j_{2\downarrow}, \dots, j_{N\downarrow}\rangle |k\rangle |M_z\rangle$, where $|j_{1\sigma}, j_{2\sigma}, \dots, j_{N\sigma}\rangle = c_{j_{1,\sigma}}^\dagger c_{j_{2,\sigma}}^\dagger \dots c_{j_{N\sigma}}^\dagger |0\rangle$ is a state of N_σ electrons, each with spin σ , while $|k\rangle = h_{k,\tau}^\dagger |0\rangle$ is the hole state. $|M_z\rangle$ denotes all possible spin states of the Mn ion, $M_z = -5/2, \dots, 5/2$, while $|0\rangle$ denotes the vacuum. The total number of electrons $N_e + 1 = N_\uparrow + N_\downarrow$, where N_\uparrow and N_\downarrow are the number of electrons with spin up and spin down, respectively. After recombination and emission of a photon, we are left with N_e electrons and the Mn ion. The final states of N_e electrons $|\nu_f\rangle$ are built in a similar way. The many-particle basis states are characterized by the total angular momentum $L = \sum_{i=1}^{N_e+1} L_e^i + L_h$ as well as an electron and hole spins $s_z = \sum_{i=1}^{N_e+1} \sigma_i$ and τ or $L = \sum_{i=1}^{N_e} L_e^i$ and $s_z = \sum_{i=1}^{N_e} \sigma_i$ for the initial and final states, respectively.

Having obtained the initial and final states, one can calculate the circularly polarized emission spectra from the Fermi's golden rule:

$$E(\omega) = \sum_f P_i |\langle \nu_f | \mathcal{P} | \nu_i \rangle|^2 \delta(\mathcal{E}_i - \mathcal{E}_f - \omega), \quad (5.2)$$

where ω is the photon energy, while \mathcal{E}_i and \mathcal{E}_f are the energies of the initial and final states, respectively. The coefficient P_i is the probability of thermal occupation of the initial state

$|\nu_i\rangle$, $P_i = \exp(-\mathcal{E}_i/kT) / P_{SUM}$, with $P_{SUM} = \sum_i \exp(-\mathcal{E}_i/kT)$. The interband polarization operator $\mathcal{P} = \sum_{kl} \langle k|l \rangle c_k h_l$ removes one electron-hole pair from the initial state. The optical selection rules [63] are defined by the overlap $\langle k|l \rangle$ between the electron and hole orbitals.

5.3 Electronic structure and emission spectra of charged magnetic dots

In this section, we present the results of numerical calculation of the emission spectra of multiply charged QDs doped with a single Mn ion. Recent experiments and theory [58, 62] indicate that in the CdTe quantum dots there are at least three confined single-particle shells, s , p , and d , and the presence of the d shell can give rise to new effects, such as the quantum interference (QI) [62]. When Mn is at the center of the QD ($R = 0$), only those electrons that occupy the zero angular momentum orbitals are coupled with it. In the presence of three shells in the QD, there are two zero angular momentum orbitals, one in the s and one in the d shell.

The calculations are carried out with the following parameters: $Ry^* = 12.11$ meV, $a_0^* = 5.61$ nm, for CdTe with the dielectric constant $\epsilon = 10.6$. The electron and hole effective masses are $m^* = 0.1m_0$ and $m_h = 4m^*$, respectively, with m_0 being the free-electron mass. The electron characteristic frequency $\omega_e = 1.98$ Ry * and $\omega_h = \omega_e/4$. The constant scaling the exchange contact interaction in the bulk CdTe for electrons is $J_{s-d} = 15$ meV·nm 3 , and for holes is $J_{p-d} = 60$ meV·nm 3 , while the height of the QD $d = 2$ nm.

As already mentioned, first we present the emission spectra for a nonmagnetic QD for $N_e = 0$ to 6. In the case of $N_e = 6$, both s and p shells of the QD are filled. After that we investigate in detail the PL of X^{2-} and X^{3-} complex for the QD doped with a single Mn atom at its center. Lastly, we compare the emission spectra from X , X^- , X^{2-} and X^{3-} complexes confined in a magnetic QD, and discuss their features.

5.3.1 Emission from a nonmagnetic charged quantum dot

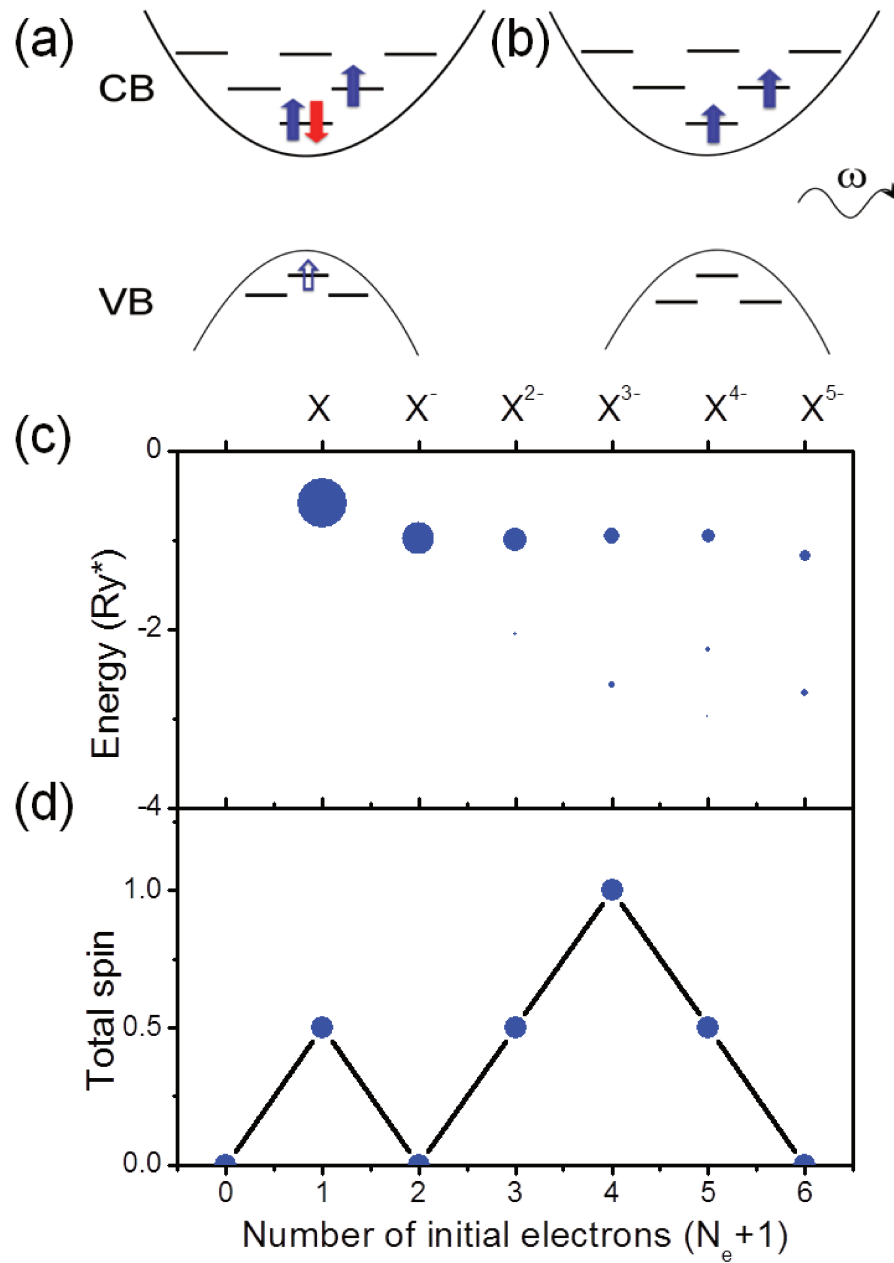


Figure 5.1: A schematic representation of (a) the ground state of an X^{2-} complex, formed by three electrons and a spin-up hole, and (b) the final state after recombination of electron-hole pair from the configuration (a). (c) Emission spectrum of a nonmagnetic QD calculated in the σ_+ polarization as a function of the number of electrons in the initial state. It is assumed that the probability P_i of occupation each of the degenerate initial states is equal. (d) Total spin of electrons in the ground state of the initial system as a function of the number of confined electrons.

Figure 5.1(a) schematically shows a ground state of the X^{2-} complex, composed of three electrons in the conduction band (CB) and a hole in the valence band (VB). Two electrons and the hole occupy the s shell, while the third electron is in the p shell. After the electron-hole recombination from the X^{2-} complex, the final state is formed by two electrons in the CB and a photon with energy ω , as shown in Fig. 5.1(b). The remaining two electrons can be either in a triplet or in a singlet spin configuration, which have the same kinetic energy but are split by the e-e exchange Coulomb interaction [63].

Figure 5.1(c) shows the evolution of the recombination spectrum in σ_+ polarization as a function of the number of electrons in the initial (photoexcited) state. The area of the circles is proportional to the intensity of individual transitions. The emission is symmetric with respect to the hole spin, so the σ_- polarization spectrum is exactly the same.

For doubly (X^{2-}) and higher-charged exciton states the emission peak splits into two or more. The splitting in the emission spectra originates from the splitting of the final state as discussed above and in ref. [63]. From the emission spectra of nonmagnetic QDs, one can not draw any conclusion about the spin of N_e electrons left after the electron-hole pair recombination.

Figure 5.1(d) illustrates the total electron spin of the initial ground state as a function of number of electron in this state. The QD is filled obeying the QD Hund's rule [63]. Until each shell is half-filled, subsequent electrons are added with the same spin, increasing the total spin of this shell. After the half-filling is reached, electrons are added with opposite spin, which results in the spin zero of a completely filled shell. As the p shell is being filled, the maximum spin is reached when there are four electrons in the QD, while in the presence of six electrons, both s and p shells are filled, and the spin of electrons is equal to zero.

5.3.2 X -Mn and X^- -Mn complexes

The emission spectra of both the exciton (X) and negatively charged exciton X^- inter-

acting with the spin of the Mn ion have been described previously [56, 57, 62]. Here we briefly summarize these results.

The ground state (GS) of the exciton-Mn system can be approximated by the configuration in which the electron and the hole occupy their respective s shell. The final states left after the electron-hole pair recombination are the degenerate states $|M_z\rangle$ of Mn. Thus, the emission spectrum from X -Mn complex consists of six emission lines (one for each M_z). The splitting between these lines corresponds directly to the splittings between X -Mn states, approximated by $1/2 (3J_{ss}^h + J_{ss}^e)$ in the symmetric QDs [56]. Since the h-Mn exchange constant J_{ss}^h is four times greater than the e-Mn exchange constant J_{ss}^e , the splittings are dominated by the h-Mn interaction [56, 62].

The GS of a negatively charged exciton X^- interacting with Mn consists of two electrons and one hole, all occupying the single-particle s shell. The two electrons are in the singlet state, which prevents them from interacting with Mn. X^- interacts with Mn only through the h-Mn Ising Hamiltonian, which splits the otherwise degenerate X^- -Mn into six levels similarly to the X -Mn case. However, in contrast to the X -Mn complex, there are two final states of the one e-Mn system with one electron on the s shell interacting with the Mn ion. These two e-Mn states have $J = S + M = 2$ or $J = 3$ and are split by the e -Mn interaction. Since the emission from the initial state with $M_z = 5/2$ to the final state with $J = 2$ is forbidden, the emission spectrum of the X^- -Mn has eleven lines arranged into six groups [57]. The emission spectra of the X -Mn and X^- -Mn complexes will be shown in greater detail later on.

5.3.3 X^{2-} -Mn complex

Here we present the emission spectra from X^{2-} -Mn complex confined in our magnetic QD with a single Mn ion in its center. We begin with a detailed description of the electronic structure of both initial and final states and then discuss the calculated emission spectrum.

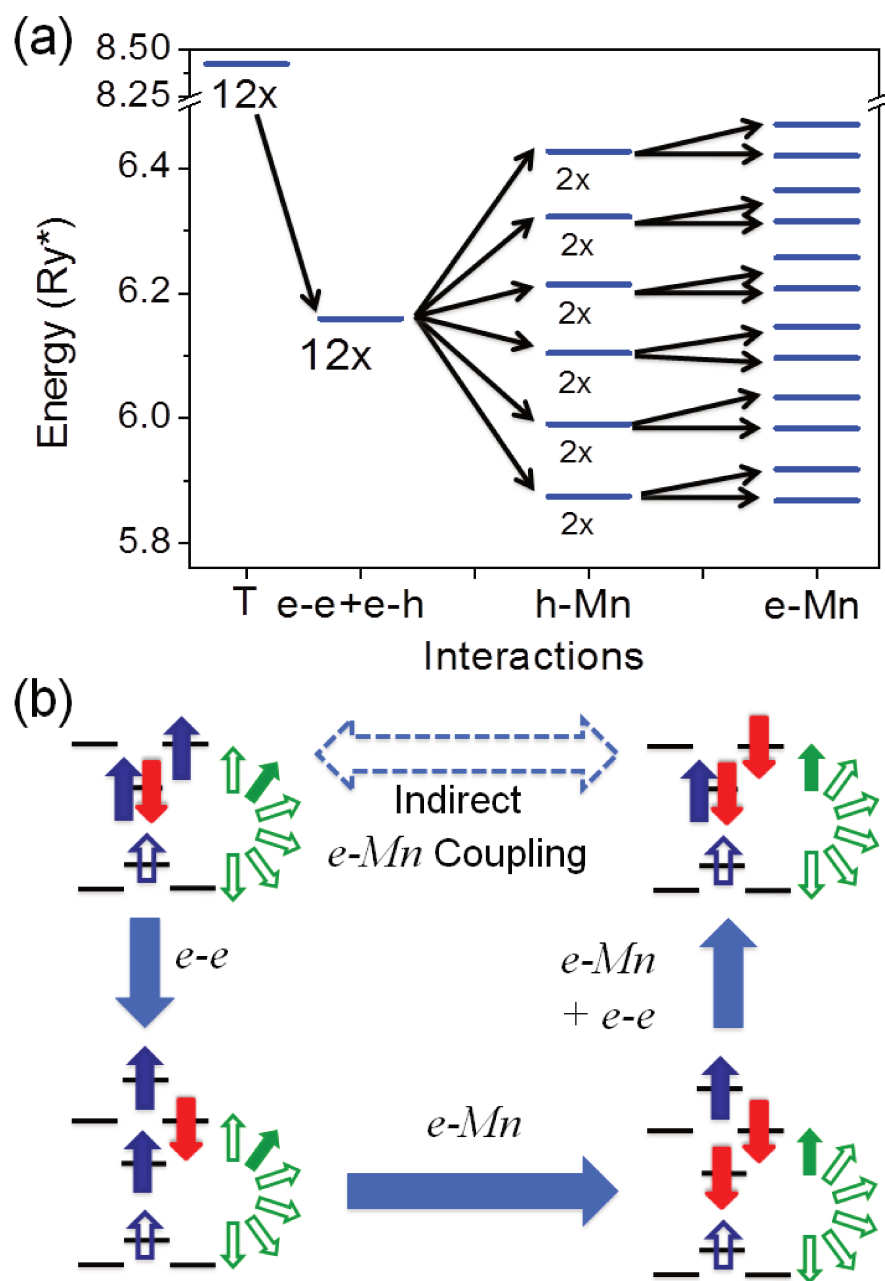


Figure 5.2: (a) The ground-state energy of the X^{2-} -Mn system as a function of interactions (subsequent terms added towards the right-hand side of the panel). The degeneracy of the energy levels is marked. The splitting in the ground state caused by e-Mn interaction is not to scale. (b) The coupling scheme between the $|X^{2-}, s_z = 1/2\rangle$ and $|X^{2-}, s_z = -1/2\rangle$ configurations. Filled arrows indicate the direct coupling, while the dashed arrow indicates an indirect coupling.

Initial state

The ground state of the X^{-2} complex confined in a nonmagnetic QD can be approximated by the lowest-energy configuration shown schematically in Fig. 5.1(a). The X^{-2} GS is fourfold degenerate: twice with respect to the spin of the electron in the p shell, and twice with respect to its angular momentum ($L = \pm 1$). Since the total angular momentum L is a good quantum number, the analysis will be carried out in the $L = 1$ subspace. The double degeneracy of the GS of X^{2-} complex due to the spin persists even in the presence of e-e and e-h interactions. The two main configurations of the X^{2-} complex are: $|X^{2-}, s_z = 1/2\rangle = c_{s\uparrow}^+ c_{p\uparrow}^+ c_{s\downarrow}^+ h_{s\uparrow}^+ |0\rangle$ and $|X^{2-}, s_z = -1/2\rangle = c_{s\uparrow}^+ c_{s\downarrow}^+ c_{p\downarrow}^+ h_{s\uparrow}^+ |0\rangle$. These two states do not interact with each other since they have different spin projections s_z . In a QD with three confined single-particle shells, one can construct 198 different configurations of X^{2-} complex with $L = 1$ which interact either with $|X^{2-}, s_z = 1/2\rangle$ or with $|X^{2-}, s_z = -1/2\rangle$ via e-e and e-h Coulomb interactions. In a magnetic QD with Mn in its center, the angular momentum is conserved, and the total number of the X^{2-} -Mn configurations increases $(2M + 1) = 6$ times, reaching 1188 configurations in the $L = 1$ subspace.

Figure 5.2(a) shows the evolution of the X^{2-} -Mn low-lying energy spectrum with inclusion of interactions. The first column shows calculations with only kinetic energy T , second after we include e-e and e-h Coulomb interactions, third with h-Mn interaction added, and finally fourth includes e-Mn interaction. In the absence of any interactions the GS is twelvefold degenerate, twice due to electron spin and six times due to Mn spin orientations. This degeneracy does not change after inclusion of the e-e and e-h Coulomb interactions, however the energy of the complex decreases. After addition of the h-Mn Ising-type interaction, Eq. (5.1), the ground state of the X^{2-} -Mn complex splits into six doubly degenerate levels. Since none of the $|X^{2-}, s_z = 1/2\rangle$ and $|X^{2-}, s_z = -1/2\rangle$ configurations interact directly with the Mn via e-Mn interaction, $\langle X^{2-}, s_z = 1/2 | H_{e-Mn} | X^{2-}, s_z = 1/2 \rangle = \langle X^{2-}, s_z = -1/2 | H_{e-Mn} | X^{2-}, s_z =$

$-1/2\rangle = 0$, one expects no change in the energy spectra of the X^{2-} -Mn complex after inclusion of the e-Mn interaction as in Eq. (5.1). However, addition of the e-Mn interaction leads to further splitting of the X^{2-} -Mn energy levels as shown in Fig. 5.2(a). Since the e-Mn coupling is smaller than the h-Mn coupling, the resulting splitting is magnified out of scale in order to visualize the effect. The origin of this splitting is in the indirect coupling between the p -shell electrons and Mn, mediated by e-e Coulomb interaction.

Figure 5.2(b) shows the coupling scheme among seemingly noninteracting configurations of X^{2-} complex and Mn ion. In order to simplify the discussion we focus only on the splitting caused by the e-Mn interaction. The filled arrows indicate a direct coupling between the X^{2-} -Mn configurations, while the dashed arrow represents an indirect coupling.

Let us start with the $|X^{2-}, s_z = 1/2\rangle \otimes |M_z\rangle$ configuration, see Fig. 5.2(b) top left. This configuration is coupled via e-e Coulomb interaction with an excited configuration (with the same s_z and M_z) with a spin-down electron in the p shell, and two unpaired electrons in the s and d shells. The e-Mn interaction can flip the spin of the spin-up electron in the s shell with simultaneous flip of the Mn spin to $M_z + 1$, as illustrated in the bottom of Fig. 5.2(b). This excited state with $s_z = -1/2$ and $M_z + 1$ is coupled with the $|X^{2-}, s_z = -1/2\rangle \otimes |M_z + 1\rangle$ via the e-e Coulomb interaction as well as the e-Mn interaction ($J_{sd}(0) \neq 0$).

One can replace the coupling scheme between $|X^{2-}, s_z = 1/2\rangle \otimes |M_z\rangle$ and $|X^{2-}, s_z = -1/2\rangle \otimes |M_z + 1\rangle$ configurations presented in Fig. 5.2(b) by filled arrows with a single dashed arrow, representing the indirect coupling. Effectively, one can look at this coupling as that of the p -shell electrons to a Mn ion, mediated by e-e and e-Mn interactions.

Final state

The final state left after the electron-hole recombination from the X^{2-} -Mn complex is composed of one electron in the s shell and one in the p shell, as illustrated in Fig. 5.1(b). This state has the same total angular momentum as the initial state, namely, $L = 1$. The

remaining electrons can be in a triplet state with total spin $S = 1$, or in a singlet state with $S = 0$. These states have the same kinetic energy, therefore in the absence of any interaction they are 24 times degenerate, four times due to electron spin and six times due to Mn spin.

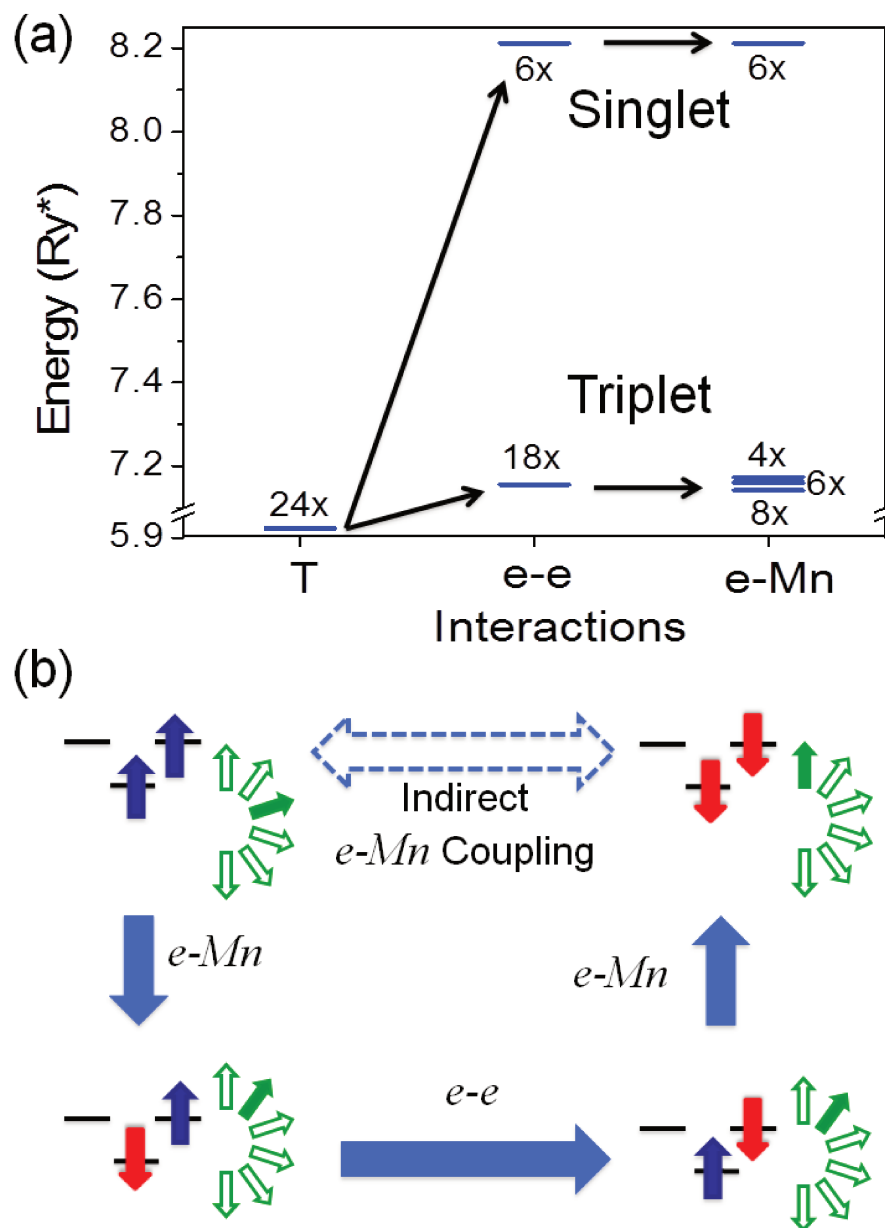


Figure 5.3: (a) Evolution of the final-state energy as a function of interactions, with marked degeneracy of the energy levels. (b) The coupling scheme between the final state configurations. Types of arrows have the same meaning as in Fig. 5.2(b).

Figure 5.3(a) shows the evolution of the energy of X^{2-} final states with the inclusion of different types of interactions. The e-e Coulomb interaction splits the triplet and the singlet states. The triplet is 18 times degenerate while the singlet is sixfold degenerate. Addition of the e-Mn interaction leads to the splitting of the triplet state into three levels with eight-, six- and fourfold degeneracy. The triplet state of the pair of electrons on the s and p shell experiences the same kind of splitting as a particle with $S = 1$ interacting with Mn via ferromagnetic interactions. At the same time, the singlet remains six times degenerate.

To understand the fine structure of the triplet state, let us analyze how the electrons interact with Mn. Figure 5.3(b) shows the coupling scheme between two pairs of s - p electrons: $|s_z = 1\rangle \otimes |M_z\rangle$ and $|s_z = -1\rangle \otimes |M_z + 2\rangle$ in the presence of the Mn ion. Again, the filled arrows indicate a direct coupling between the configurations, while the dashed arrow indicates an indirect coupling. Let us start from the configuration $|s_z = 1\rangle \otimes |M_z\rangle$, Fig. 5.3(b), top left. The e-Mn spin-flip interaction couples it with the configuration with $s_z = 0$ and $M_z + 1$, where the electron with the spin $s_z = -1/2$ is on the s shell. This configuration is coupled by the e-e Coulomb interaction with a configuration with $s_z = 0$ and $M_z + 1$, but the spin down electron occupying the p shell. Again, the e-Mn interaction couples the former configuration with the $|s_z = -1\rangle \otimes |M_z + 2\rangle$, through the e-Mn spin-flip process. Effectively, the coupling scheme shown by the filled arrows can be replaced by the dashed arrow, representing the indirect coupling between configurations $|s_z = 1\rangle \otimes |M_z\rangle$ and $|s_z = -1\rangle \otimes |M_z + 2\rangle$. From this coupling scheme, one can conclude that indeed a pair of s - p electrons interacts with Mn ion in the same way as a spin $S = 1$ particle, with three possible spin projections $S_z = -1, 0, 1$, changing the spin of Mn from $|M_z\rangle$ to $|M_z + 2\rangle$, with simultaneous change of its spin from $S_z = 1$ to $S_z = -1$. The difference is that in a spin Hamiltonian both spins ($S = 1$ and $M_z = 5/2$) interact directly, while in our model, the coupling with the p -shell electron is indirect.

Emission spectrum

Having obtained the X^{2-} initial and final eigenvalues and eigenstates, we calculate the emission spectrum of X^{2-} -Mn complex. The spectrum in the σ^+ polarization is calculated at temperature in which a thermal population of the twelve lowest X^{2-} -Mn states is equal [$P_i = 1$ in Eq. 5.2]. The σ^+ polarized light is emitted due to the recombination of the spin-up hole and a spin-down electron from the initial X^{2-} -Mn state. Both total angular momentum of the electronic state as well as M_z are conserved in the recombination process.

Figure 5.4(a) schematically shows the energy levels of both initial and final states. The dashed, solid, and dashed-dotted arrows indicate the optically active transition from all twelve initial states to the triplet final states, split into three levels with degeneracy eight, six, and four. The dashed-double-dotted arrows present six optically active transitions from the initial states with electron spin $s_z = -1/2$ to the sixfold degenerate singlet state.

The emission spectrum from the X^{2-} -Mn complex is shown in Fig. 5.4(b), with the colors and styles of lines corresponding to the styles of arrows in Fig. 5.4(a). The emission spectrum consists of two groups of transitions [as in a QD without Mn in Fig. 5.1(c)]: the lower lying transitions (six dashed-double-dotted lines) correspond to the transition to the final state with the two electrons in a singlet state ($S = 0$), while the higher-lying group corresponds to the transitions to their triplet state ($S = 1$).

Let us start the discussion by analyzing the lower-energy part of the spectrum presented by dashed-double-dotted peaks. Since the final state—in this case an electron singlet—is degenerate, the splitting between the emission lines corresponds to the splitting between the initial states due to the hole-Mn interaction. One could expect that each of the lines is in fact a doublet, with the small splitting between them due to the e-e and e-Mn interactions, however only one of them is bright: only states with $s_z = -1/2$ can have an electron singlet as a final state. The existence of the *six* lines in the emission confirms the previous hypothesis

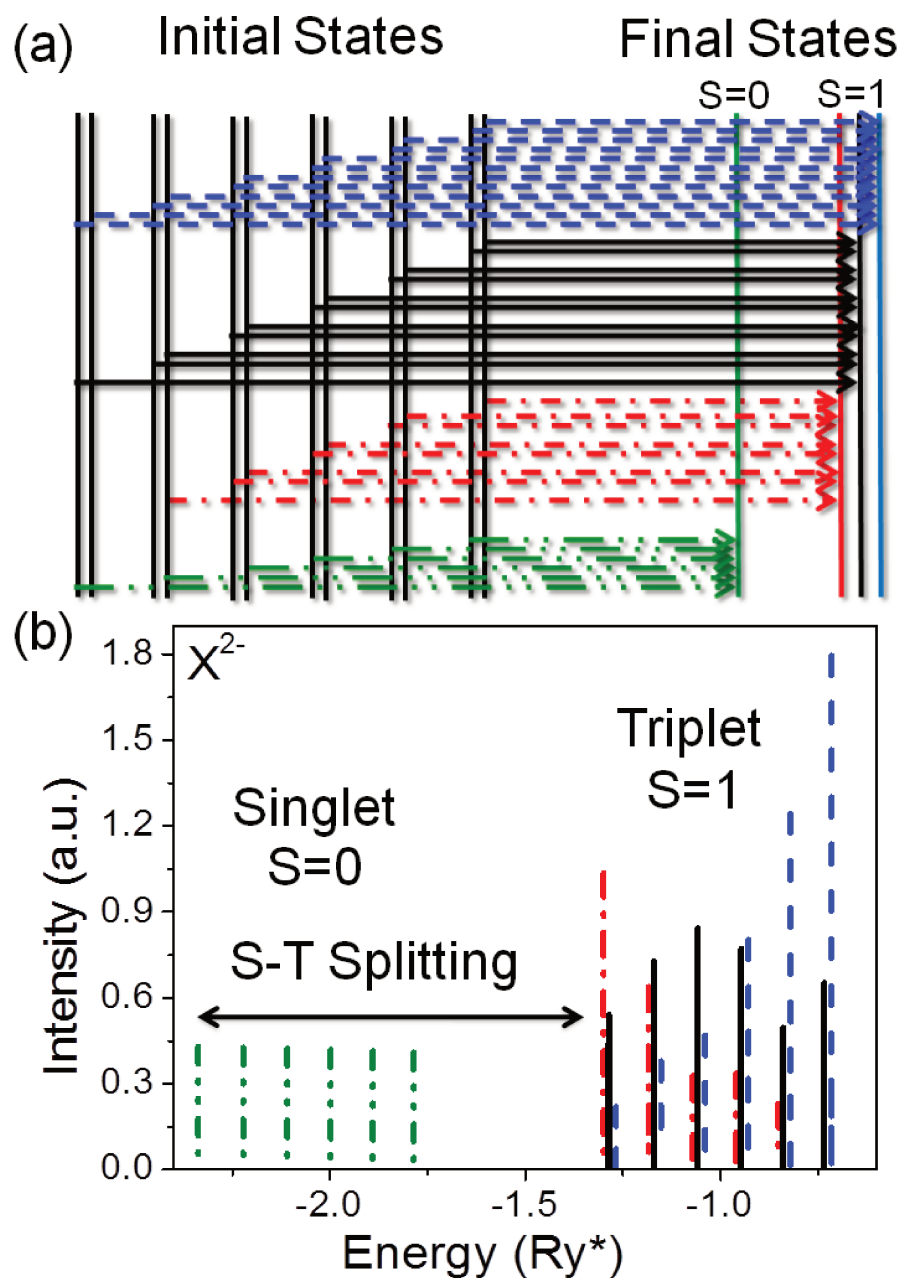


Figure 5.4: (a) The energy levels of initial and final states with allowed transitions between them indicated by the arrows. The dashed, solid, and dashed-dot arrows denote the transitions to the $S = 1$ electron states, while the dashed-double-dotted arrow denotes the transitions to the $S = 0$ final electron states. (b) Emission spectrum of X^{2-} -Mn complex calculated in the σ_+ polarization as a function of the photon energy.

of the s - p electron pair behavior as a $S = 0$ particle.

In the higher-energy part of the emission spectra [see Fig. 5.4(b)], the transitions to the final states of electrons in a triplet states are presented. This part of emission spectra consists of six groups of peaks split by the h-Mn interaction in the initial state. Five of the main peaks are then further split into three due to the e-e and e-Mn-induced splitting in the final state and correspond to different final states. The highest-energy main peak is split into two, since the transition from the highest energy state of the X^{2-} -Mn complex to the fourfold-degenerate final state is dark. Therefore, by looking at the energy difference between two consecutive peaks, within the same main peak, i.e., the solid and dashed-dot peaks, one can obtain the effective splitting of the final state, which depends on e-e and e-Mn interactions. Each of these peaks can be further split, reflecting the e-Mn induced splitting in the initial state giving total of 31 optically active transitions, however this splitting is not visible on the scale of Fig. 5.4(b).

5.3.4 X^{3-} -Mn complex

The simplest system allowing to study the behavior of electrons in a half-filled shell is the X^{3-} complex. In the GS of this complex, the two electrons in the p shell are in a triplet state $S = 1$, which makes them a good candidate to interact with the Mn spin. Indeed, as we have shown previously, there exists an effective interaction between the p -shell and the Mn spin mediated by the e-e Coulomb interactions. Here we describe the electronic properties of the initial and final states of the X^{3-} complex and its emission spectrum.

Initial state

The GS of the X^{3-} is composed of four electrons and one hole. As previously, we focus only on one subspace, with the hole spin projection $\tau = 3/2$. The lowest-energy configurations of the X^{3-} complex have total angular momentum equal to zero, and are fourfold degenerate in the absence of e-e Coulomb interactions. The degeneracy is due to the four possible spin

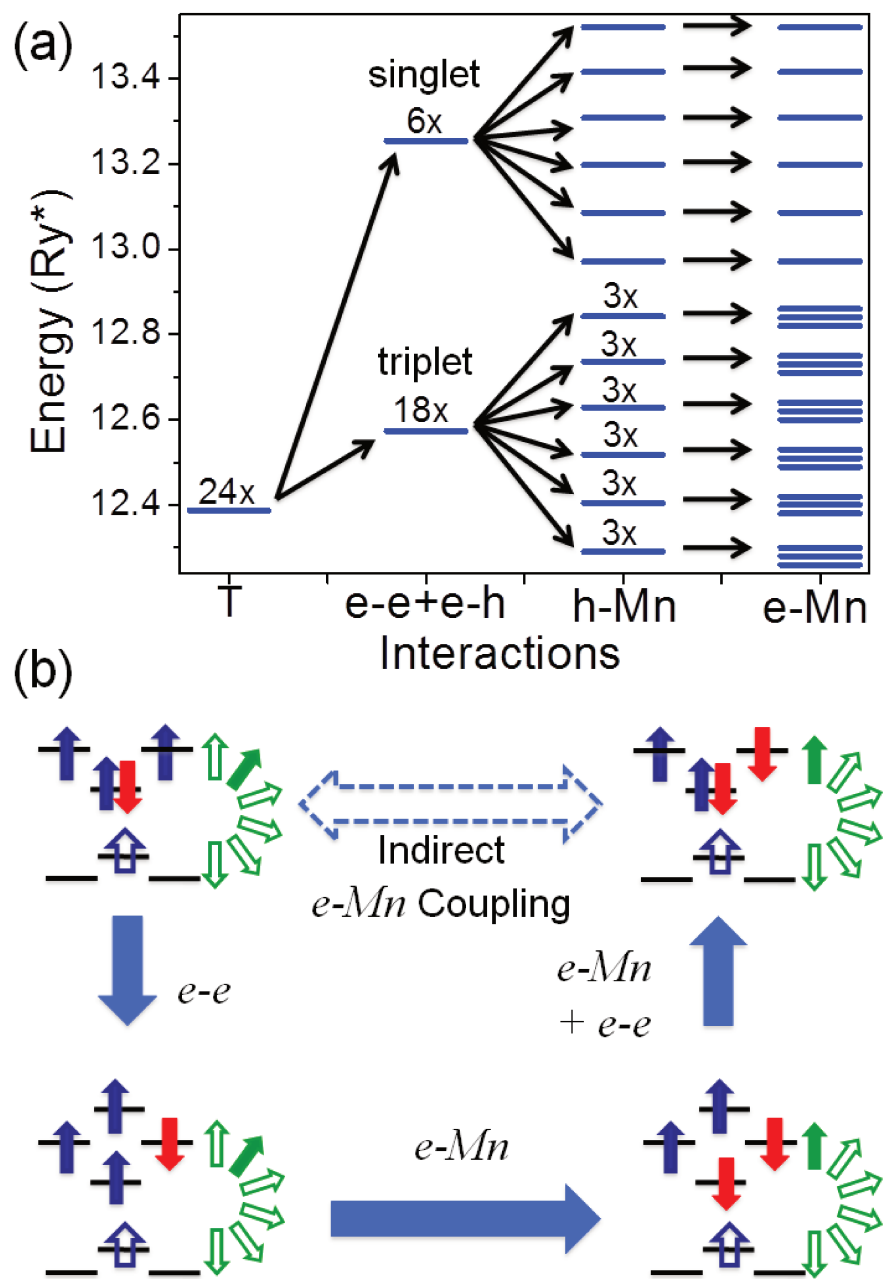


Figure 5.5: (a) The ground-state energy of X^{3-} -Mn complex as function of interactions, with marked degeneracy of the energy levels. The splitting in the GS caused by e-Mn interaction is out of scale. (b) The coupling scheme between X^{3-} -Mn configurations with different s_z . Types of arrows have the same meaning as in Fig. 5.2(b).

configurations of the two unpaired electrons in the p shell: they can be either spin polarized ($s_z = \pm 1$) or with $s_z = 0$, creating either a singlet or a triplet state.

The total number of the X^{3-} -Mn configurations with the angular momentum $L = 0$ and $\tau = 3/2$ in a QD confining three single-particle shells is 2664. The excited configurations of the X^{3-} -Mn complex play an important role in mediating the interactions between the p -shell electrons and Mn. Therefore, the X^{3-} complex allows us to study the behavior of $S = 1$ and $S = 0$ spins interacting indirectly with Mn.

Figure 5.5(a) shows the evolution of the GS energy as we add the interactions. With inclusion of the Coulomb interactions between the carriers, the 24-fold degenerate X^{3-} -Mn GS splits into two states: a lower-lying triplet-Mn (18-fold degenerate) and a singlet-Mn (sixfold degenerate). The h-Mn interaction breaks the Mn symmetry and splits both of these manifolds into six levels. Each of the six triplet-Mn levels is still threefold degenerate. This degeneracy is lifted by e-Mn interaction. This takes place only in the presence of the e-e Coulomb interaction in the QDs containing at least three shells and it is another proof that both of the p electrons are coupled indirectly with the Mn ion. The splitting of singlet-Mn state remains unchanged, but its energy is lowered in relation to the system without e-Mn interaction. As the e-Mn splitting is smaller than the h-Mn splitting, it is out of scale in Fig. 5.5(a).

Figure 5.5(b) shows the coupling scheme between X^{3-} -Mn configurations with different s_z . The configuration of X^{3-} -Mn with two spin-up electrons in the p shell and the Mn spin M_z is coupled by e-e Coulomb interactions with an excited configuration (with the same M_z) in which the spin-down electron is scattered to the p shell and the spin-up electron is scattered to the d shell [as shown in the bottom-left panel of Fig. 5.5(b)]. The e-Mn interaction can flip the spin of the electron occupying the s shell, with a simultaneous increase of the Mn spin by one (to the state with $M_z + 1$). Now, this configuration is coupled via e-e Coulomb interactions with a low-energy X^{3-} -Mn configuration in which there is a spin-up and spin-down electron in the p shell and the Mn spin is in the state $M_z + 1$. Therefore, all initial states forming

the GS manifold are indirectly coupled via e-e and e-Mn interactions, as shown by the dashed arrow. This coupling breaks the triplet degeneracy, and can be again treated as one induced by an indirect coupling between two p -shell electrons and the Mn ion.

Final state

The final state, left over after recombination of the spin down electron with the spin up hole from the X^{3-} complex, is an *excited state* of the three electrons system (with $L = 0$). It is formed by one electron in the s shell and two in the p shell. However, since the configurations with two electrons in the s shell and one in the d shell have the same kinetic energy as the configurations mentioned before, they are strongly coupled by the e-e Coulomb interaction.

Figure 5.6(a) shows the coupling scheme between four three-electron-Mn (3e-Mn) configurations with the same kinetic energy but with different s_z . The coupling mechanism between the configurations is the same as that explained in previous sections.

Figure 5.6(b) illustrates how the energies of the 3e-Mn system evolve as interaction terms are added. In the absence of any interactions, all of the considered configurations have the same energy. This energy level is 60-fold degenerate, ten due to electron configurations times six Mn spin orientation. Addition of the e-e Coulomb interaction splits the energy of the 3e-Mn complex into four levels, with degeneracy 24, 12, 12, 12, respectively. The lowest-energy electron state has total spin $S = 3/2$, while all higher energy levels correspond to $S = 1/2$. It is important to notice that the two intermediate $S = 1/2$ states are not final states of the X^{3-} complex recombination in a QD with or without Mn. It is so because they are built by the configurations with two electrons in the s shell and the third electron in the d shell mixed with the configurations with one electron on the s shell and a pair of electrons occupying the p shell in a singlet state. At the same time the lowest and higher energy states are formed mostly by configurations with only one electron in the s shell and two in the p shell, allowing them to be final states in the recombination of the X^{3-} (-Mn) complex.

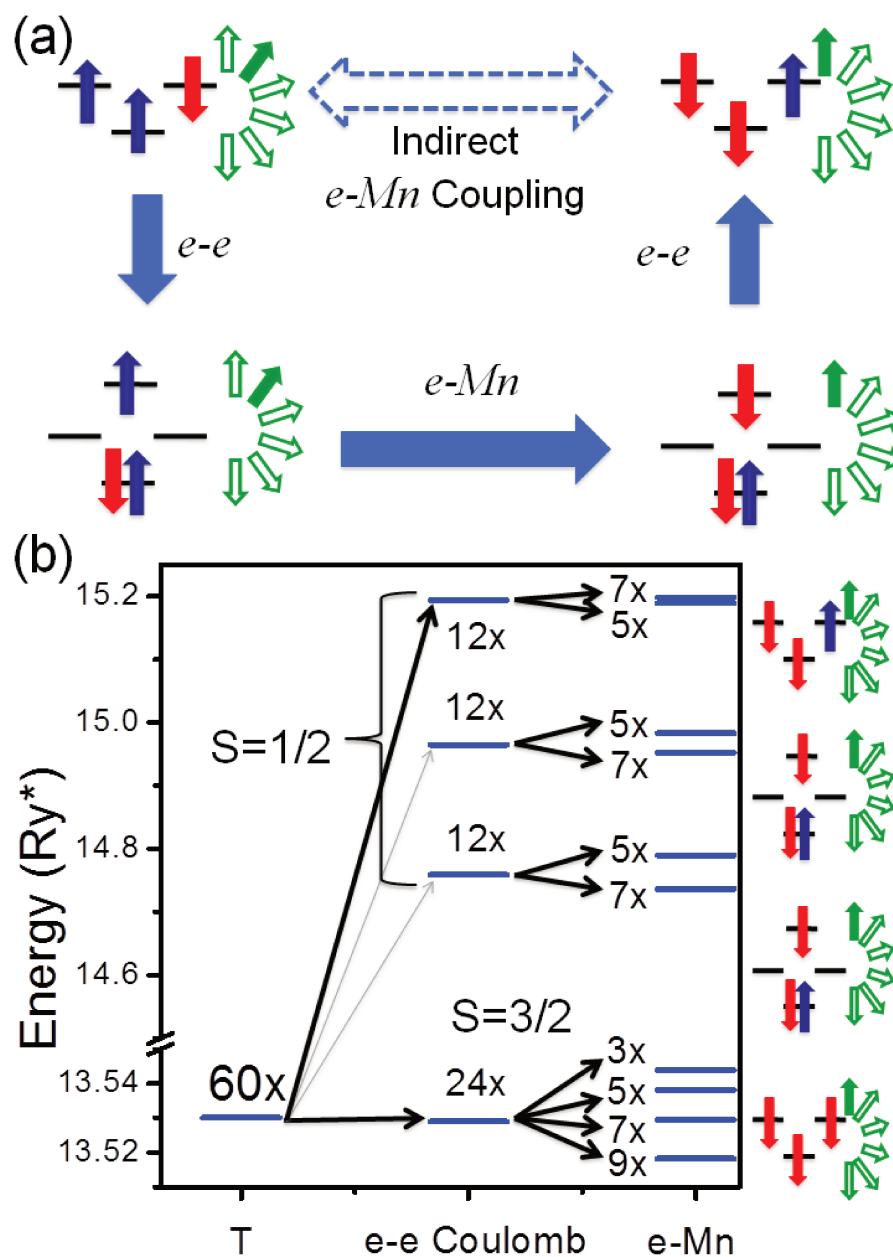


Figure 5.6: (a) The coupling scheme between the three-electron-Mn configurations with different s_z . Types of arrows have the same meaning as in Fig. 5.2(b). (b) Evolution of the final-state energy with various interaction terms, the numbers indicate the degeneracy of the energy levels.

In the presence of the e -Mn interaction, the $S = 3/2$ level splits into four states and each of the $S = 1/2$ levels into two. We observe that the $S = 3/2$ and two first $S = 1/2$ three-electron states are ferromagnetically coupled with Mn, since the degeneracy of levels (related to total

electron-Mn spin) decreases as a function of energy. The ordering of states is different in the case of highest $S = 1/2$ state which is antiferromagnetically coupled with Mn.

Emission spectrum

Here we investigate the emission from the equally populated initial states of the X^{3-} -Mn complex with $S = 1$ [18 lowest energy levels in Fig. 5.5(a)]. The emission spectra from the X^{3-} -Mn complex consist of two main groups of peaks corresponding to optical transitions from the initial states to the $S = 3/2$ and the highest of $S = 1/2$ final states, in the way resembling the emission from X^{3-} in nonmagnetic QD [see Fig. 5.1(b)]. These two types of transitions will be analyzed separately.

Figure 5.7(a) shows the X^{3-} -Mn initial and final energy levels, with the dashed arrows denoting the transitions to the highest two final states with $S = 1/2$. The emission spectrum from X^{3-} -Mn complex to these final states consists of six groups of peaks and it is shown in Fig. 5.7(b). The splitting into main six groups is caused by the h-Mn interaction in the initial state, while the splitting into two peaks in each group is due to the e-Mn interaction in the final state. The effects of the splitting of the initial state induced by the e-Mn interaction are not visible in this figure, but they cause further splittings of emission lines. Figure 5.8(a) shows the X^{3-} -Mn initial and final energy levels, with the solid arrows representing optical transitions from all initial states to four final states with $S = 3/2$ (differentiated by the color).

In the high-energy part of the X^{3-} -Mn emission spectrum, Fig. 5.8(b), there are also six main groups of peaks originating from the splitting of the initial states due to the h-Mn interaction. Each of these groups is further split by the e-Mn interaction in both the final and initial states. To observe these splittings, the details of the emission from the first three energy levels of the initial state to the four final states with $S = 3/2$ are shown in the inset. It consists of nine emission lines (three transitions are dark), arranged into four groups, each corresponding to a different final state. The splitting between these four groups corresponds

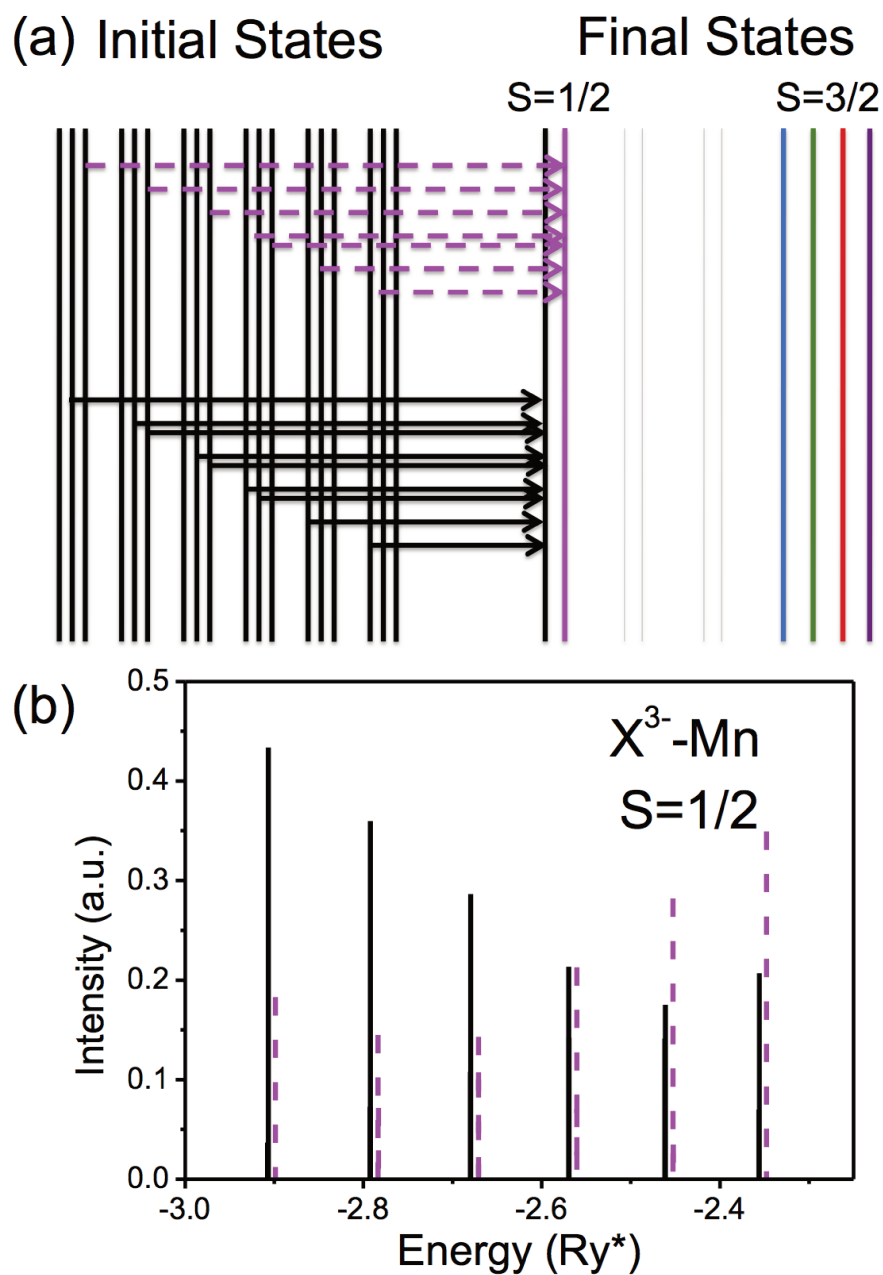


Figure 5.7: (a) Schematic representation of the X^{3-} -Mn initial and final states, with the allowed transitions to the final states with $S = 1/2$ indicated by the dashed arrows. (b) The low-energy X^{3-} -Mn emission spectrum in σ_+ polarization. The styles of emission lines correspond to the styles of arrows (a).

to the strength of e-Mn interaction in the final state, while the splitting within each group is due to the indirect e-Mn interaction in the initial state. The e-Mn-induced splitting in

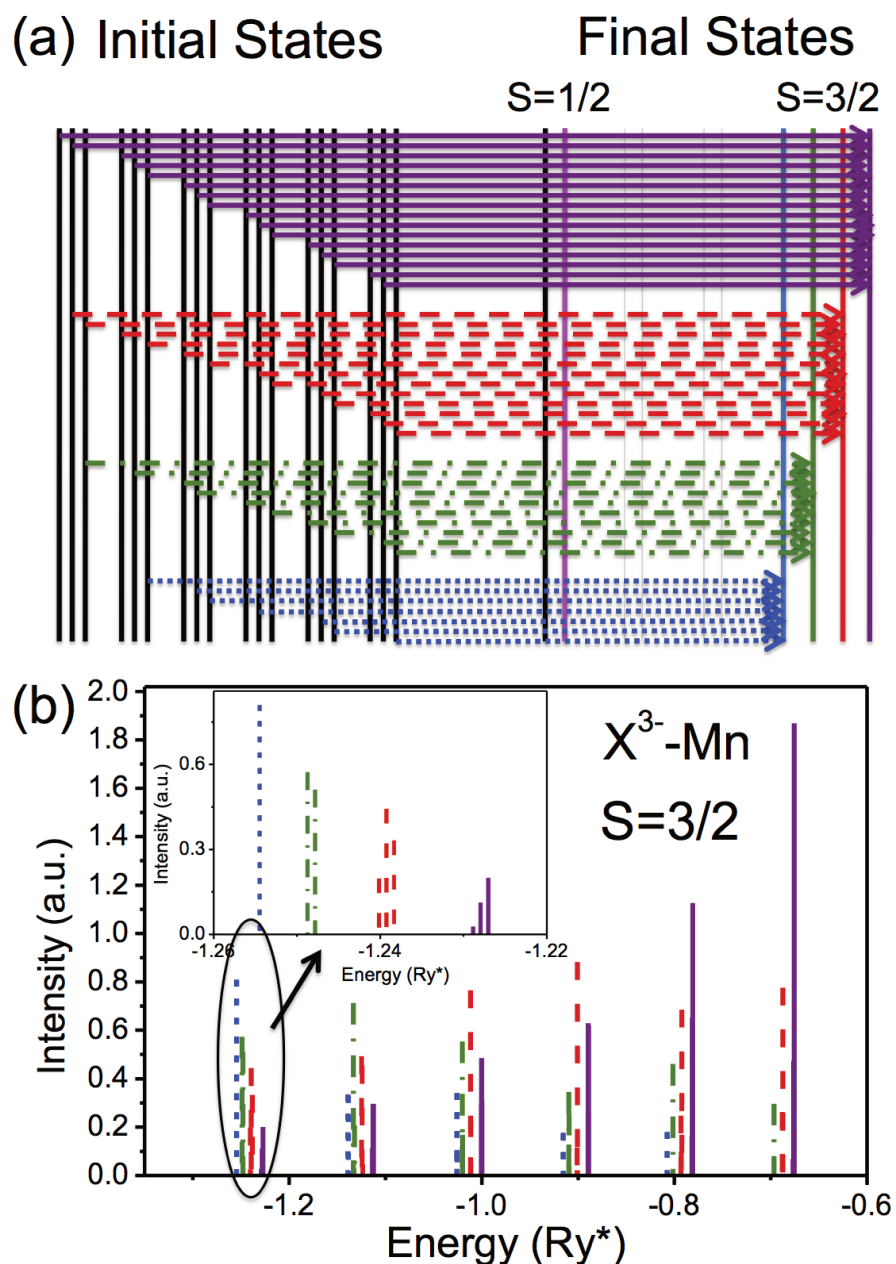


Figure 5.8: (a) Schematic representation of the X^{3-} -Mn initial and final states, and the allowed transitions from all initial states to the $S = 3/2$ final states indicated by the arrows. (b) High-energy part of the X^{3-} -Mn emission spectrum in σ_+ polarization. The styles of emission lines correspond to the styles of arrows in (a). The inset shows the emission from the first group of three initial states to all final states with $S = 3/2$.

the final state is larger than that in the initial state, because the final-state configuration has an electron in an open s shell directly interacting with Mn, while in the initial state, the interaction between p -shell electrons and Mn is mediated by e-e Coulomb interactions.

5.3.5 Comparison between emission spectra of different complexes

Now we analyze the evolution of the emission spectrum for the right circularly-polarized light as the number of excess electron N_e confined in the QD is increased. In Fig. 5.9(a), we show the comparison between the emission spectra of X -Mn, X^- -Mn, and the high-energy parts of the emission spectra of X^{2-} -Mn, and X^{3-} -Mn complexes. The emission spectra of these complexes are shown as a function of the number N_e of extra electrons in a QD in Fig. 5.9(b), where the low-energy peak is clearly marked in red. Its energy is almost the same for X^- , X^{2-} , and X^{3-} -Mn, and it is much lower than the low-energy peak for X -Mn. This corresponds to the similar plateau as is visible in the emission of a nonmagnetic charged QD [63, 64] [see Fig. 5.1(c)].

Figure 5.9(c) shows the evolution of the low-energy emission lines with the number of excess electrons N_e . For the X -Mn complex, there is only one emission line, since there is only one final state of the electron-hole recombination, being the state of Mn with $M_z = -5/2$. The emission from the lowest state of X^- -Mn complex consists of two lines with the splitting between them corresponding to the final-state splitting (electron-Mn complex creating state with total angular momentum $J = 2$ or $J = 3$). In the case of the X^{2-} -Mn complex with $S = 1$, there are three final states of the two-electron system, all of them triplets. Again, the splitting between the emission lines can be translated into the splitting between final states. The lowest-energy emission spectrum of the X^{3-} -Mn complex with $S = 3/2$ consists of four groups of levels, with the splitting between them reflecting the splitting of the four final states of three electrons with $S = 3/2$ as described in the previous section. Each of these groups exhibits a fine structure related to the fine structure of the initial state.

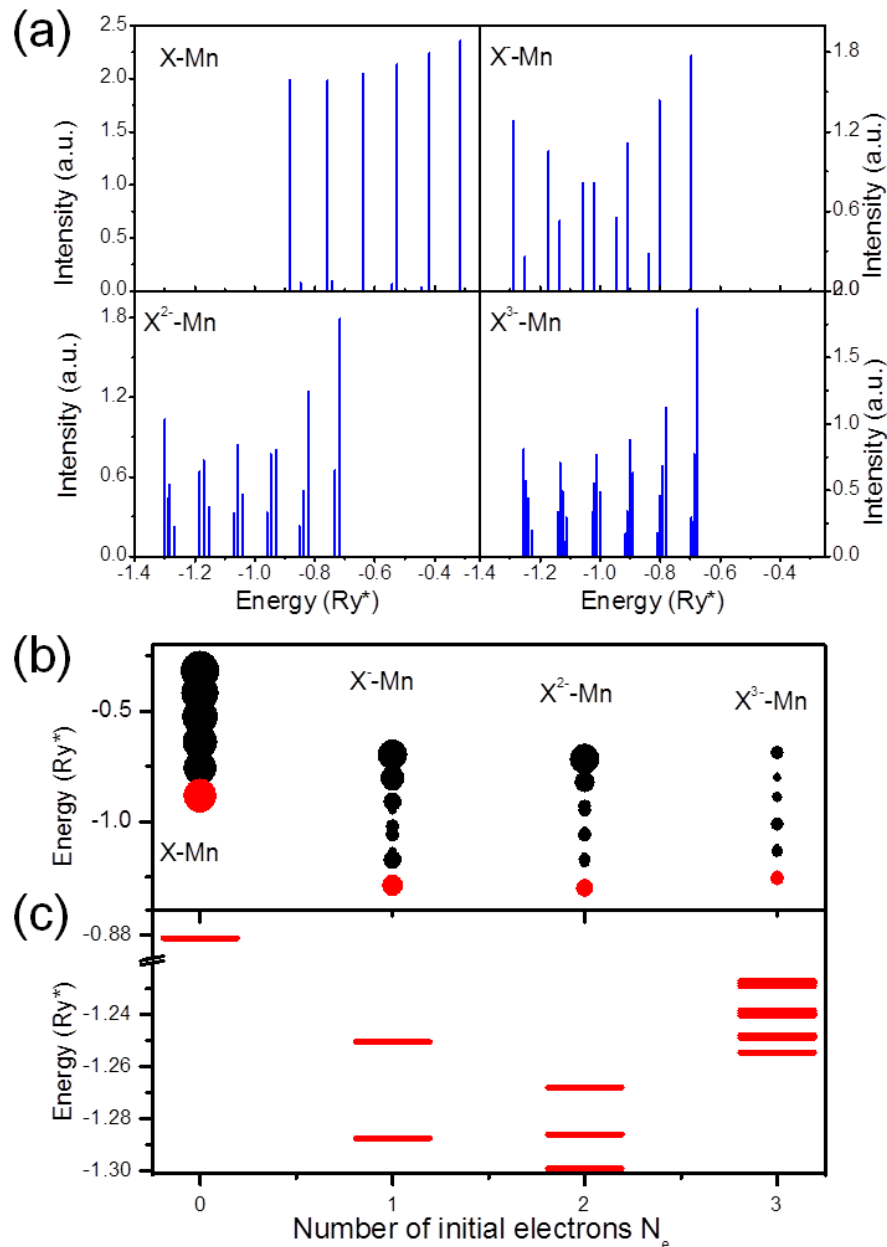


Figure 5.9: (a) Emission spectrum of X -Mn, X^{-} -Mn complexes and high-energy part of the spectrum of X^{2-} -Mn and X^{3-} -Mn complexes. (b) Emission spectra from (a) as a function of the number of electrons in the initial state. (c) Close-up of the lowest-energy emission lines as a function of the number of electrons in the initial state with clearly visible multiplicity of lines.

5.3.6 Effects of Mn in an off-center position

When Mn is positioned away from the dot center, the cylindrical symmetry of the dot

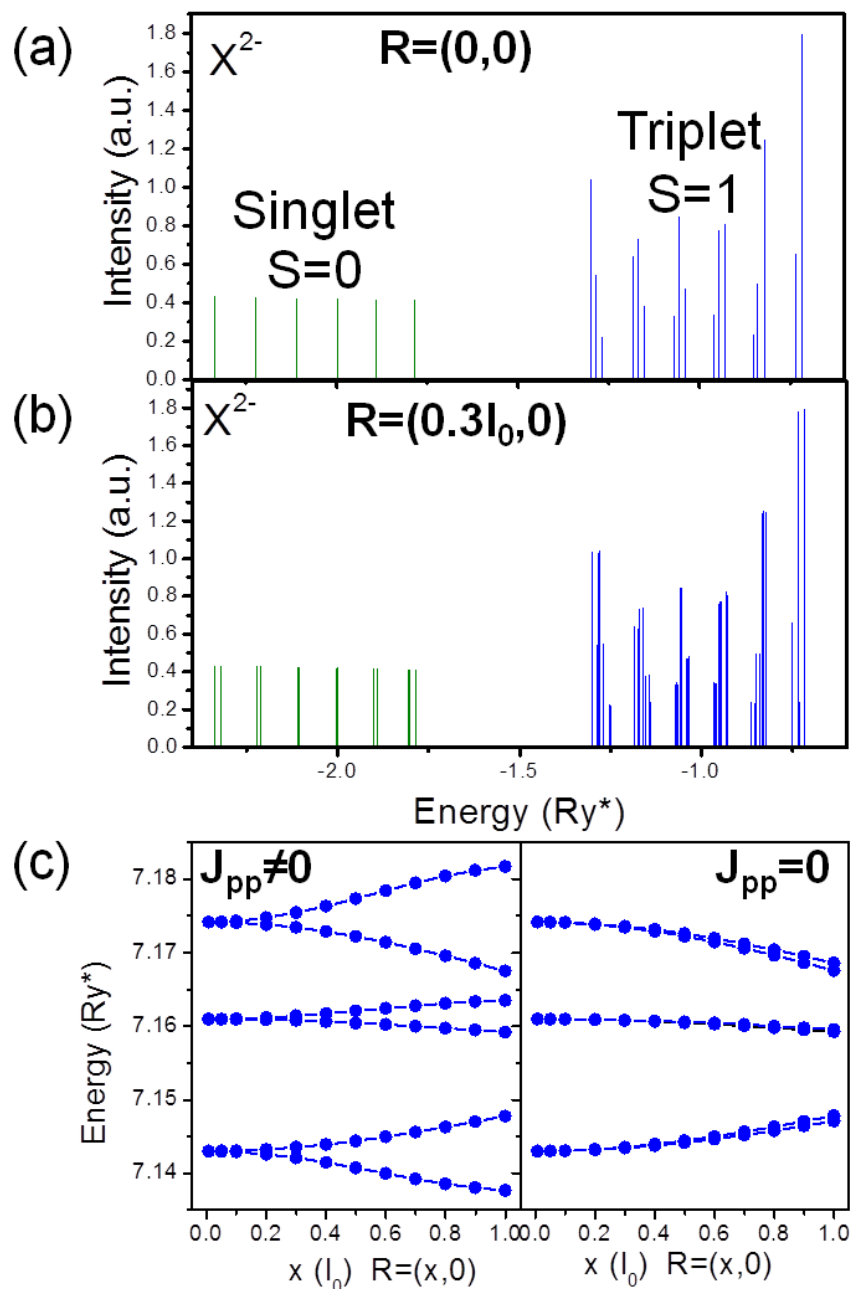


Figure 5.10: Emission spectrum of X^{2-} -Mn complex when Mn is in the center $R = (0, 0)$ (a) or at position $R = (0.3l_0, 0)$ (b). (c) Comparison between the splitting of $2e$ -Mn complex in the presence $J_{pp} \neq 0$ (left) and absence $J_{pp} = 0$ (right) of direct p -electron-Mn interaction.

is broken and the total angular momentum L is no longer a good quantum number. As a result, the states with finite angular momenta, e.g., $L = \pm 1$, are coupled by Mn-induced scattering of the carriers, which opens additional gaps in the spectrum. Moreover, carriers

occupying QD orbitals with non-zero angular momentum, e.g., p orbitals, interact directly with Mn. Figures 5.10(a) and (b) allows to compare the emission spectra from X^{2-} -Mn complex confined in the QD with Mn ion in the center $R = (0, 0)$ (a) and at position $R = (0.3l_0, 0)$ away from the center (b). Indeed, in Fig. 5.10(b), one can observe additional peaks that arise from the removal of degeneracy of energy levels, which for a rotationally symmetric dot were orbitally degenerate, in this case states with $L = \pm 1$. Shifting Mn to a more off-center position leads to significant changes in the emission spectrum, as discussed in refs. [60] and [180].

In previous sections, we have demonstrated that the measure of the strength of the indirect p -electron-Mn interactions is given by the splitting of the six groups of the emission lines in the X^{2-} -Mn spectrum, and this in turn is determined by the splitting of the final state of the emission. This allows to assess the relative importance of the indirect component of that interaction, which is the only coupling mechanism for the impurity in the center of the QD, compared to the direct p -electron-Mn interaction, which is present when the impurity is shifted off-center. In Fig. 5.10(c), the evolution of the energies of the 2e-Mn complex as the Mn is displaced is presented. Figure 5.10(c) (left), shows the evolution of the 2e-Mn spectrum as a function of Mn position capturing all direct and indirect terms, while in Figure 5.10(c) (right) the direct interactions is turned off, artificially setting $J_{pp} = 0$. In Fig. 5.10(c) (left) the three sets of lines split as the impurity is shifted as due to symmetry breaking. However, apart from that, the splitting of 2e-Mn complex (the large gaps) is of the same order in both cases until the position of Mn exceeds $R \approx (0.6l_0, 0)$. We conclude that the indirect interaction is dominating the direct one over very broad range of the Mn position in the QD, and as such should not be ignored.

5.4 Summary

In summary, we presented a microscopic theory of the optical properties of self-assembled

quantum dots doped with a single magnetic (Mn) impurity containing a controlled number of electrons N_e . The total spin of the electron complex is controlled by the population of electronic shells: it is zero for closed shells and maximal for half-filled shells. We show that even though electrons may occupy electronic states that are not coupled directly with Mn, there exists an indirect coupling mediated by electron-electron interactions. This coupling allows for the detection of electron spin and verification of Hund's rules in self-assembled quantum dots from emission spectra. We have shown that the indirect interaction between p electrons and Mn ion is an important effect even when Mn is shifted away from the center of the quantum dot, and dominates over the direct interaction over a broad range of Mn positions. The details and a complete analysis of this e-Mn coupling mediated by e-e Coulomb interaction is a subject of a further study [53].

Chapter 6

Results form collaborative work

Here we present the results of two other work that we have participated. First, we discuss the work “*Fine structure of a biexciton in a single quantum dot with a magnetic impurity*”, published in Phys. Rev. B **87**, 205311 (2013). Lastly, we comment the article “*Compensation effect on the CW spin-polarization degree of Mn-based structures*” published in J. Phys. D: Appl. Phys. **46**, 215103 (2013). In these papers we have collaborated with experimental groups. Our theoretical calculations agree qualitatively with the experimental results. Here we do not give any detail about the experimental setup, we only discuss the main results of the articles and our contribution.

6.1 Biexciton-Mn complex photoluminescence

In this section we present the calculated and measured photoluminescence spectra of a biexciton confined in a CdTe quantum dot doped with a single Mn impurity. To investigate the biexciton-Mn (XX-Mn) complex, we employed the same methodology described in chapters 4 and 5, i.e, we used the configuration interaction method to obtain both initial and final correlated states of the emission. The Fermi’s golden rule [Eq. (5.2)] was used to obtain the emission spectra as a function of the photon energy. Here we just point out the main findings of our calculations. For details see ref. [58]. We assume that the Mn is at the QD center.

Biexciton is a four particle state composed by two electrons and two holes. Its ground state (GS) is a singlet state where both electrons and holes occupy the QD s -shell orbital. It can be written as

$$|XX_{GS}, M_z\rangle = |E_{GS}\rangle \oplus |H_{GS}\rangle \oplus |M_z\rangle = c_{s,\uparrow}^\dagger c_{s,\downarrow}^\dagger h_{s,\uparrow}^\dagger h_{s,\downarrow}^\dagger |0, M_z\rangle \quad (6.1)$$

where $|E_{GS}\rangle$ and $|H_{GS}\rangle$ are the electron and hole state, respectively. $c_{i,\sigma}^\dagger$ and $h_{i,\tau}^\dagger$ are the electron and hole creation operators, i refers to the electronic shell, and σ and τ are the electron and hole spin state, respectively. M_z is the z -projection of Mn spin state. We are interested in the effects of XX coupling with Mn. We calculate the XX GS expected value with relation to the magnetic interactions terms of the Hamiltonian. As the hole-Mn (h-Mn) interaction is four times larger than the e-Mn, we take the expectation value of the XX GS with respect to the h-Mn interaction (last term of the Hamiltonian described at Eq. (5.1)), which is given by

$$\langle XX_{GS}, M_z | H_{hMn} | XX_{GS}, M_z \rangle = \langle H_{GS}, M_z | H_{hMn} | H_{GS}, M_z \rangle = 0. \quad (6.2)$$

The same is true for the e-Mn interaction acting on the XX-Mn GS. Therefore, considering only the s -shell, the XX-Mn GS is not affected by the presence of the Mn spin interaction. This is not surprising, since the XX GS is a singlet state. The XX-Mn GS is six-fold degenerate, one XX configuration times six Mn spin orientations. This is the initial state of the emission. We now examine the final state. The XX final state is a exciton (X), which consists in one electron-hole pair. As we consider a polarized photoluminescence, the spin-down electron recombines with the spin-up hole (σ_+ -light), and the spin-up electron with the spin-down hole (σ_- -light). The final state is composed by one electron-hole pair in the s -shell. The X σ_- ground state is

$$|X_{GS}, M_z\rangle = c_{s,\uparrow}^\dagger h_{s,\downarrow}^\dagger |0, M_z\rangle \quad (6.3)$$

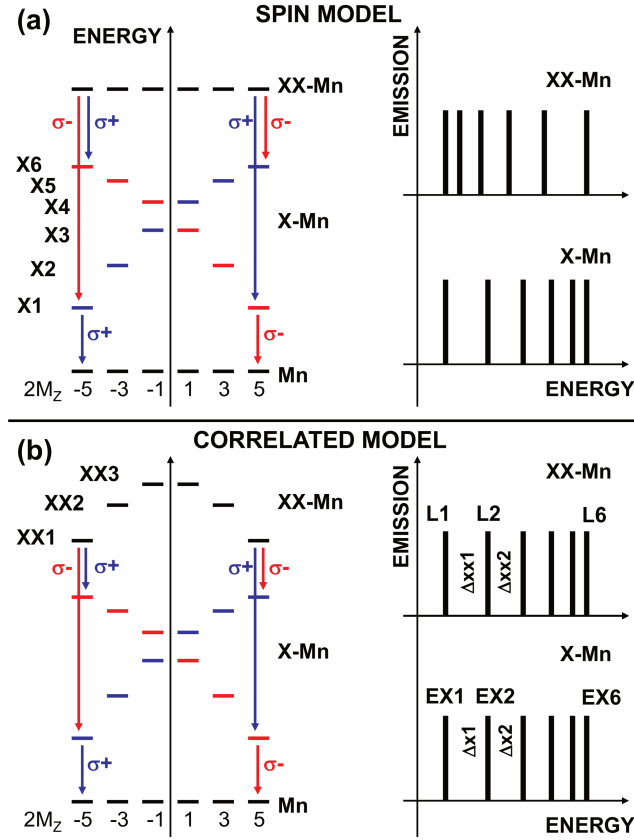


Figure 6.1: (a) Spin model for the biexciton-Mn complex luminescence, i.e, only s -shell is confined in the QD. (b) Correlated model of the biexciton-Mn complex luminescence, here we consider three confined shells, s -, p -, and d -shells. Figure was extracted from Ref. [58].

The expected value with respect to the h-Mn produces

$$\langle X_{GS}, M_z | H_{hMn} | X_{GS}, M_z \rangle = \frac{3}{2} J_{ss}^h M_z \quad (6.4)$$

where J_{ss}^h is the h-Mn exchange matrix element. We observe that the X-Mn complex splits into six states [56, 60, 62]. The X-Mn state decays to the vacuum state emitting light. The X-Mn is the only complex here that interacts with the Mn spin, if the QD contains only the s -shell. Therefore, the decay from XX-Mn to X-Mn, and X-Mn to vacuum produces the same spectrum form as illustrated in Fig. 6.1(a). Fig. 6.1(a) left shows the decay process, and the right side the luminescence.

Our single confined state model, produces the same emission pattern for both X-Mn and

XX-Mn emissions. Now we include more electronic shells, to create a correlated ground state. We consider three electronic shells, i.e, s -, p -, and d -shells. The reason to include the d -shell is that it contains one zero angular momentum orbital that is directly coupled with Mn, when it is in the QD center. This new zero angular momentum orbital allows the scattering of a carrier in the s -shell to the d -shell. We can create a triplet excited state by promoting one carrier from the s -shell to the d -shell. Here we focus only on the effects of h-Mn. The excited triplet hole state can be written as

$$|H_{ES}, M_z\rangle = \frac{-1}{\sqrt{2}}(h_{s,\downarrow}^\dagger h_{d,\uparrow}^\dagger - h_{d,\downarrow}^\dagger h_{s,\uparrow}^\dagger)|0, M_z\rangle. \quad (6.5)$$

The excited triplet state also does not couple with Mn, which can easily be seen by

$$\langle H_{ES}, M_z | H_{hMn} | H_{ES}, M_z \rangle = 0. \quad (6.6)$$

However, the matrix element, between the GS and the ES gives

$$\langle H_{ES}, M_z | H_{hMn} | H_{GS}, M_z \rangle = \frac{3J_{sd}^h}{\sqrt{2}} M_z \quad (6.7)$$

where J_{sd}^h is the matrix element of one electron scattered from the d -shell to the s -shell due to the h-Mn interaction. The energy of the XX-Mn correlated GS can be obtained by considering only two states, one with the holes and electrons in both s -shell, and one excited state with the electrons and one hole in the s -shell and other hole in the d -shell. We obtain the GS energy is proportional to $|M_z|^2$. For details see Ref. [58]. Therefore, the XX-Mn initial state is split into three states, with the $M_z = \pm 5/2$ configuration being the lowest energy states, and $M_z = \pm 1/2$ configuration the highest. The emission of the XX-Mn to X-Mn produces a different pattern now, as it is illustrated at Fig. 6.1(b) right. The emission lines are illustrated in Fig. 6.1(b) left.

We now compare our findings with the experimental results. Fig. 6.2(a) and (b) illustrate the calculated and measured emission spectrum, respectively. The computed emission was

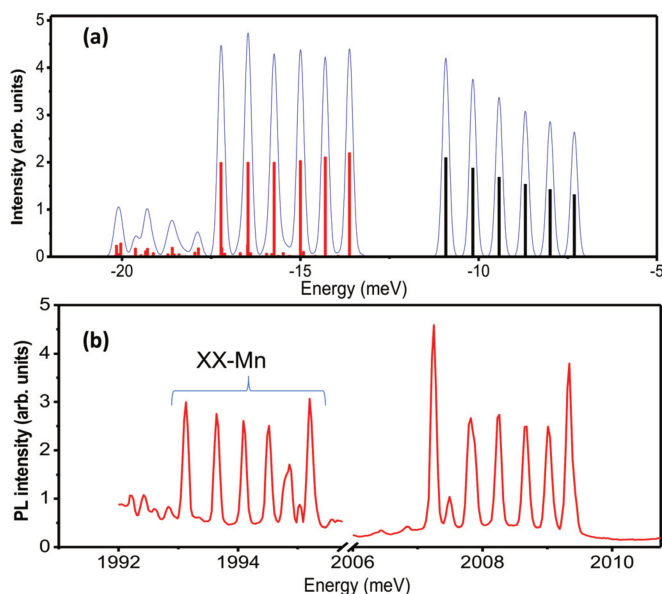


Figure 6.2: (a) Computed and (b) measured XX-Mn and X-Mn photoluminescence. To obtain the spectra we built our Hamiltonian considering all possible configurations for a QD containing three electronic shells. We considered thermal occupation, with a temperature of 75 K. Figure extracted from Ref. [58].

obtained via exact diagonalization, where we considered all possible configurations of the XX-Mn complex in the $L = 0$ subspace for a QD containing three shells. We also considered thermal occupation of the initial states, with a temperature of $T = 75$ K. We note that both experimental theoretical photoluminescence have a similar form. In order to get a better comparison between both spectra, we show in Fig. 6.3 the XX-Mn and X-Mn normalized spacing of the emission lines, i.e, the distance between two peaks divided by the average spacing. We observe that both theoretical and experimental averages have the same behavior. The deviations arise from the fact that the Mn impurity is not in the QD center. Also, the effects of light-heavy hole coupling must also affect the results.

Here we have shown the fine structure of a XX-Mn complex which arises due to the coupling of the singlet GS with excited triplet states. This also shows that one can use singlet state to probe the localized magnetic spins state.

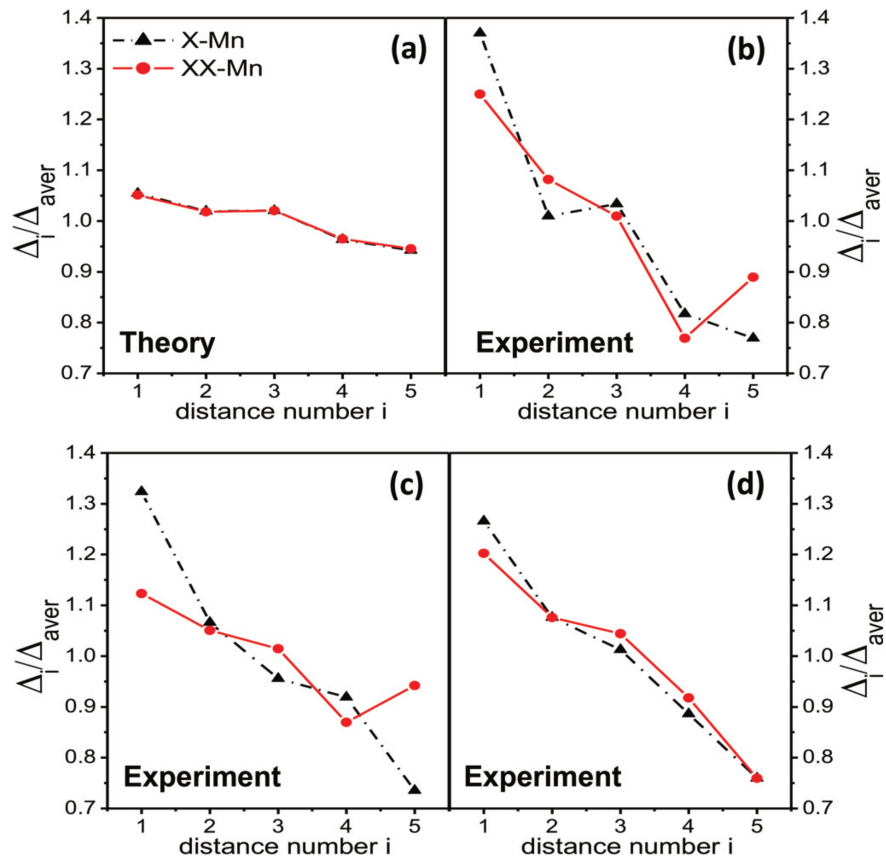


Figure 6.3: Average distance between XX-Mn and X-Mn emission peaks (a) calculated (b), (c) e (d) measured for different QDs. Figure extracted from Ref. [58].

6.2 Electron spin dynamics in quantum wells with barriers doped with magnetic impurities

In this section we comment on results of electron's spin dynamics that are confined in quantum wells with barriers δ -doped with a Mn layer [112]. The investigated heterostructures are the same as described in chapter 3. In this work we have collaborated with the optical properties group at UNICAMP to understand the effects of Mn on the electron's spins dynamics. They performed both time-resolved photoluminescence (RTPL) and circularly polarized Hanle measurements, which allowed to obtain two independent measurements of the total spin-relaxation time, T_s , which is given by $T_s^{-1} = \tau_s^{-1} + \tau^{-1}$, where τ_s and τ are the spin-relaxation time and the electron lifetime. The spin dynamics of electrons was obtained for five samples containing different concentration of Mn, that is, $Q_{Mn} = 0, 0.13, 0.2, 0.27$ and 0.4 monolayers*.

Figure 6.4(a) and (b) shows both Hanle and PL-RT measurements, respectively [112]. In both cases, we observe two different behaviors of both polarization and PL intensity, depending on the Mn concentration. In the Hanle curve [Fig. 6.4(a)], samples with higher Mn concentration ($Q_{Mn} = 0.27$ and 0.4) have a much broader curve than the lower Mn-content ones. In the PL-RT curves [Fig. 6.4(b)] we note the same kind of behavior, while the low Mn content samples have a slow intensity decay, the high concentration Mn samples have a faster decay. Therefore, heterostructures with $Q_{Mn} \leq 0.2$ have a similar electron dynamics, even for the sample with no Mn, which differs from what is observed in samples with $Q_{Mn} > 0.2$.

We interpreted the results by observing that, with the increase of the Mn-content, more Mn diffuses into the QW, increasing the overlap between electron and the Mn ions. Consequently, the scattering of the electron due the electron-Mn interaction becomes more effective. To verify this interpretation, we calculated the electron-Mn overlap for the different Mn concentration,

*Here we use Q_{Mn} to designate Mn concentration (Q_{Mn}). This is done to be in agreement with the figures showed here, which were extracted from ref. [112].

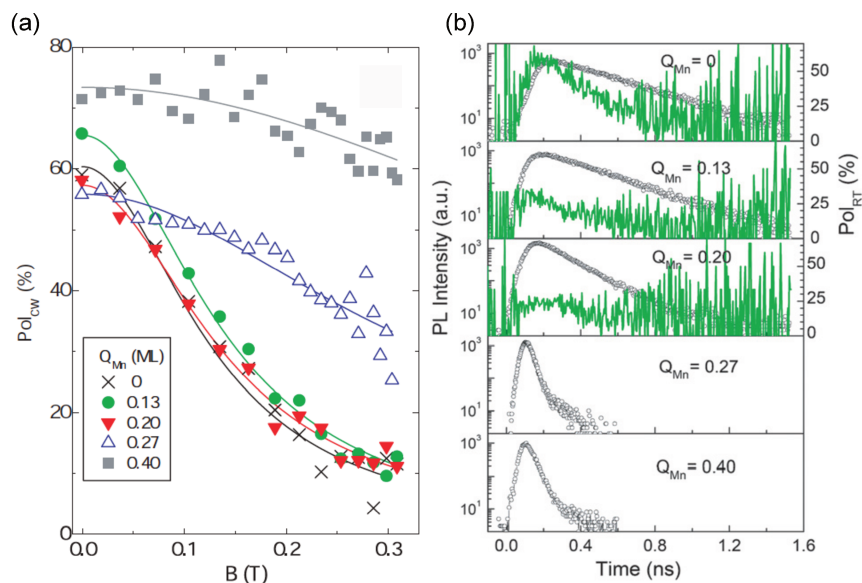


Figure 6.4: (a) Hanle curves and (b) Time-resolved photoluminescence for all set of samples. In both cases, samples with high Mn content have a different behavior from the low concentrations one. Figure extracted from Ref. [112].

using the self-consistent model presented in chapter 3. Figure 6.5 illustrated the calculated electron-Mn overlap for all samples. We note that the e-Mn overlap increases with the Mn content, except for sample $Q_{Mn} = 0.27$. This sample has the lowest hole concentration of all samples, and as we use this value to obtain the effective Mn concentration, we get a very small uncompensated Mn concentration, which is responsible for the small e-Mn overlap. The stronger enhancement of the overlap for higher Mn concentrations favors our interpretation. We should keep in mind that this overlap is a consequence of the self-consistent calculations, that is, the degree of asymmetry in the QW as well as the Mn concentration.

At the present moment, however, we still do not understand the exact scattering mechanism that dominates the electron spin relaxation. One possible mechanism may be related with the formation of inhomogeneous regions in the plane, which Mn-rich regions. Electrons will tend to be bound in these regions with its spin pinned by the effective magnetic field created by the Mn ions. This mechanism may explain the fast spin relaxation. At the same time, the high-

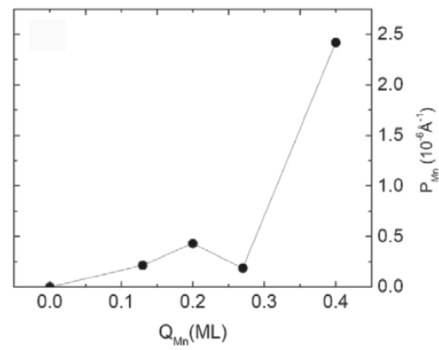


Figure 6.5: Electron-Mn overlap as a function of Mn concentration. Figure reprinted from Ref. [112].

density of non-radiative centers at this region justifies the decrease in the electron's lifetime. Both mechanism depend on the presence of the electron in the Mn region, that is, they should be enhanced by the increase in the e-Mn coupling.

Chapter 7

Final Remarks and Perspectives

This thesis investigates the electronic and optical properties of diluted magnetic semiconductors quantum wells and quantum dots. In order to study these systems we used spin-density functional theory and the configuration interaction method. In the QW heterostructure, the magnetic impurities were grown in the barrier. The transition energy as a function of the magnetic field were estimated, using the Kohn-Sham single particle eigenvalues to describe the electronic spectra. For quantum dots, we considered a two-dimensional harmonic oscillator confinement, with the magnetic impurity in the QD center. The emission spectra were calculated via Fermi's Golden Rule.

The QWs have barriers doped with carbon on one side and Mn on the other side. This system presents strong oscillations in the circularly polarized photoluminescence spectra as a function of the external magnetic field. Within our model, we showed that Mn-doped layer is depleted of holes. They are mainly transferred to the QW. We show that the strong oscillations observed in the circularly emission are mainly due to the exchange energy of the hole gas. As in the experiment, we observed that the oscillations are related with the Landau levels filling factors, and that the oscillations are maximum for odd filling factors, and it is a minimum for even filling factors.

Our model was able to capture the Mn concentration dependence of the PL spectrum. We

showed that by reducing the Mn content, and consequently the hole density, the oscillations are less pronounced, as a direct consequence of the reduction of the exchange energy of the hole gas. We also investigated the role of the sample parameters on the PL spectrum, in particular the Mn-doping position, and the application of a gate voltage to enhance the effects of the Mn ions. For very larger gate voltages, we observe the formation of a hole gas in the Mn-doped layer. The interaction between the two hole gas reservoir produces spike structures on the luminescence of the InGaAs QW. In our model, we verify that the carbon doping does not play any significant role in the PL spectrum, mainly due the distance between carbon and InGaAs QW.

We can also describe different regimes of the electron's spin dynamics in quantum wells with barriers doped with Mn. For low Mn-content the electron spin relaxation and lifetime are almost constants, but samples doped with more than 0.2 Mn monolayers show a very fast spin relaxation and electron lifetime. We interpreted that with the increase of scattering generated by the increasing of the overlap between electron and rich inhomogeneous Mn regions.

For quantum dots doped with a single magnetic impurity in its center, we investigated its electronic structure for systems containing from two to six electrons. We studied their electronic properties as a function of the number of shells, quantum dot confinement, electron-Mn coupling, and electron-electron interaction. We showed the emergence of an indirect coupling between electron and Mn, which are not directly coupled. This indirect coupling depends on the number of confined shells and the electron-electron interaction. The coupling does not exist if there are only two confined shells in the QDs. For three or more confined electronic shells, the indirect coupling can be either ferromagnetic or antiferromagnetic, depending on the QDs confining energy. We also demonstrated that the indirect coupling exists independently of the type of the direct electron-Mn interaction, the indirect interaction exists for either Ising- or Heisenberg-like direct e-Mn interaction.

We also extended the theory of optical properties for charged quantum dots doped with a single Mn impurity. We presented a detailed theory of the photoluminescence for both X^{2-} -Mn and X^{3-} -Mn complex. We demonstrated that the indirect e-Mn coupling gives rise to a fine structure in both initial and final states of the emission, which can in principle be observed experimentally. From the PL spectra, we deduce the number of confined shells in the QDs, and infer the electronic spin. These are quantities that are not accessible on the PL of nonmagnetic QDs. We also verify that the PL of Mn-doped QDs presents the emission plateaux which is observed in nonmagnetic QDs. Finally, we showed that even if Mn impurity is off-center, the indirect e-Mn interaction is important and dominant for a wide range of Mn positions. With our model, we also explained the origin of the biexciton-Mn fine structure.

As a perspective of future projects, we aim first to understand the role of the electron-hole correlation in the spin-polarized holes gas. This allows us to obtain a better understanding of the role of the electron on the circularly polarized photoluminescence. Second, we plan to study the Mn magnetization vectors dynamics via pump and probe experiments. This will be done in collaboration with the GPO of the IFGW.

For quantum dots, we aim to extend this theory for two, three and N -Mn impurities inside the QDs. We want to verify if the indirect e-Mn coupling is robust to the presence of many magnetic impurities. If this is the case, we aim to investigate the electron spin dynamics in this system. More precisely, we want to understanding how this indirect interaction affects the electron coherence time, which is an important quantity for quantum information processing.

Appendix A

Two-dimensional Harmonic Oscillator

We derive here the single particle states used in our exact diagonalization method. The quantum dot is described by a two-dimensional harmonic oscillator. Using the effective mass approximation, the Hamiltonian is

$$\mathcal{H} = -\frac{\hbar}{2m^*} \left(\frac{\partial^2}{\partial x^2} + \frac{\partial^2}{\partial y^2} \right) + \frac{1}{2} m^* \omega_0^2 (x^2 + y^2) \quad (\text{A.1})$$

where m^* is the electron effective mass, and ω_0 is the characteristic frequency of the confining potential. In order to simplify the Hamiltonian, we introduce new complex variables, that are:

$$\begin{aligned} z &= x - iy, \quad z^* = x + iy; \\ \frac{\partial}{\partial z} &= \frac{\partial}{\partial x} + i \frac{\partial}{\partial y}, \quad \frac{\partial}{\partial z^*} = \frac{\partial}{\partial x} - i \frac{\partial}{\partial y}. \end{aligned} \quad (\text{A.2})$$

Now we write the Hamiltonian variables in terms of the new set of complex variables, which implies that

$$\begin{aligned} x &= \frac{1}{2}(z + z^*), \quad y = \frac{1}{2i}(z^* - z); \\ \frac{\partial}{\partial x} &= \frac{1}{2} \left(\frac{\partial}{\partial z} + \frac{\partial}{\partial z^*} \right), \quad \frac{\partial}{\partial y} = \frac{1}{2i} \left(\frac{\partial}{\partial z} - \frac{\partial}{\partial z^*} \right). \end{aligned} \quad (\text{A.3})$$

Substituting Eq. (A.3) in Eq. (A.1), we have the Hamiltonian in terms of the new variables

$$\mathcal{H} = -\frac{\hbar}{2m^*} \frac{\partial^2}{\partial z \partial z^*} + \frac{1}{2} m^* \omega_0^2 z z^*. \quad (\text{A.4})$$

It is convenient to write the new operators in dimensionless units, defining $l_0 = \sqrt{\frac{\hbar}{2m^*\omega_0}}$. Making the following transformation $z = l_0z$ and $\partial/\partial z = (1/l_0)\partial/\partial z$. The Hamiltonian is now rewritten as

$$\begin{aligned}\mathcal{H} &= -\frac{\hbar}{2m^*l_0^2}\frac{\partial^2}{\partial z\partial z^*} + \frac{1}{2}m^*l_0^2\omega_0^2zz^* \\ &= -\hbar\omega_0\frac{\partial^2}{\partial z\partial z^*} + \frac{\hbar\omega_0}{4}zz^* = \hbar\omega_0\left(\frac{1}{4}zz^* - \frac{\partial^2}{\partial z\partial z^*}\right).\end{aligned}\tag{A.5}$$

We now define raising and lowering operators as

$$\begin{aligned}a &= \frac{1}{2}\left(\frac{z}{\sqrt{2}} + \sqrt{2}\frac{\partial}{\partial z^*}\right), \quad a^\dagger = \frac{1}{2}\left(\frac{z^*}{\sqrt{2}} - \sqrt{2}\frac{\partial}{\partial z}\right), \\ b &= \frac{1}{2}\left(\frac{z^*}{\sqrt{2}} + \sqrt{2}\frac{\partial}{\partial z}\right), \quad b^\dagger = \frac{1}{2}\left(\frac{z}{\sqrt{2}} - \sqrt{2}\frac{\partial}{\partial z^*}\right).\end{aligned}\tag{A.6}$$

In the next step, we rewrite the complex variables as a function of raising and lowering operators as

$$\begin{aligned}z &= \sqrt{2}(a + b^\dagger), \quad z^* = \sqrt{2}(a^\dagger + b), \\ \frac{\partial}{\partial z} &= \frac{1}{\sqrt{2}}(b - a^\dagger), \quad \frac{\partial}{\partial z^*} = \frac{1}{\sqrt{2}}(a - b^\dagger).\end{aligned}\tag{A.7}$$

It can easily be shown that the raising and lowering operators obey the following commutation relations: $[a, a^\dagger] = 1$, $[b, b^\dagger] = 1$, and $[a, b] = [a, b^\dagger] = [a^\dagger, b] = [a^\dagger, b^\dagger] = 0$. Inserting the relations described in Eq. (A.7) on Eq. (A.5) the Hamiltonian is written as

$$\mathcal{H} = \omega_0(a^\dagger a + b^\dagger b + 1),\tag{A.8}$$

we redefine $\omega_0 = \hbar\omega_0/Ry^*$, where Ry^* is the effective Rybderg. The Hamiltonian described in Eq. (A.8) is the two-dimensional harmonic oscillator Hamiltonian, whose eigenvalues are given by

$$E_{n,m} = \omega_0(n + m + 1),\tag{A.9}$$

where $n = 0, \pm 1, \dots$ and $m = 0, \pm 1, \dots$ are the Harmonic oscillator quantum numbers. The eigenstates are labelled by these quantum numbers. The lowering and raising operators have

the following properties

$$\begin{aligned} a|n, m\rangle &= \sqrt{n}|n-1, m\rangle, \quad a^\dagger|n, m\rangle = \sqrt{n+1}|n+1, m\rangle, \\ b|n, m\rangle &= \sqrt{m}|n, m-1\rangle, \quad b^\dagger|n, m\rangle = \sqrt{m+1}|n, m+1\rangle. \end{aligned} \quad (\text{A.10})$$

The eigenstates are defined as

$$|n, m\rangle = \frac{1}{\sqrt{n!m!}}(a^\dagger)^n(b^\dagger)^m|00\rangle, \quad (\text{A.11})$$

in which $|00\rangle$ is the vacuum state. The Hamiltonian conserves momentum angular. The z -component of the angular momentum operator is

$$\hat{l}_z = xp_y - yp_x = \frac{\hbar}{2} \left(z^* \frac{\partial}{\partial z^*} - z \frac{\partial}{\partial z} \right) = \hbar(a^\dagger a - b^\dagger b). \quad (\text{A.12})$$

The eigenvalue of the angular momentum operator is

$$\hat{l}_z|n, m\rangle = \hbar(n-m)|n, m\rangle = \hbar L_e|n, m\rangle, \quad (\text{A.13})$$

where we define $L_e = n - m$. The harmonic oscillator eigenvalues are plotted as a function of L_e in Fig. A.1. We note the existence of a shell structure as in an atom. This is one of the reason that quantum dots are known as an artificial atom.

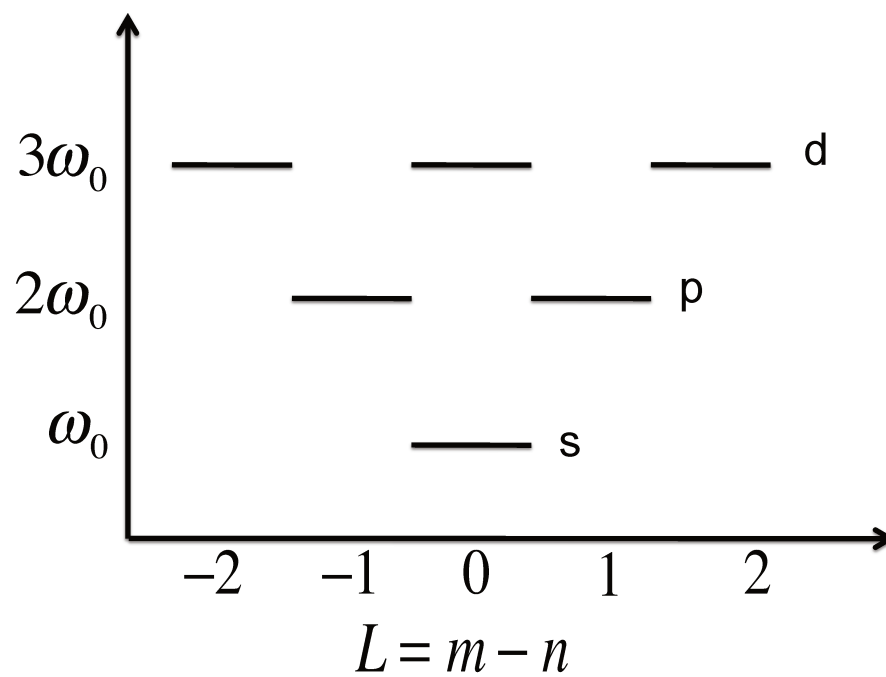


Figure A.1: Two-dimensional harmonic oscillator single particle states as a function of the angular momentum. The shell structure is observed and we use the same notation employed to define the shell of an atom, i.e, *s*-shell, *p*-shell, *d*-shell and so on.

Appendix B

Electron-electron Coulomb matrix elements

In this section we calculate the electron-electron (e-e) Coulomb matrix elements for the QD. For a two-dimensional parabolic quantum dot, the e-e matrix elements have an analytical expression. We measure the energy in effective Rydberg $Ry^* = m^*e^4/2\epsilon^2\hbar^2$ and length in Bohr radius $a_0^* = \epsilon\hbar^2/m^*e^2$. The e-e Hamiltonian is

$$\mathcal{H}_{ee} = \frac{1}{2} \sum_{i,j,k,l} \langle i, j | V_{ee} | k, l \rangle c_i^\dagger c_j^\dagger c_k c_l, \quad (\text{B.1})$$

where the composite indexes are $i = \{n'_1, m'_1\}$, $j = \{n'_2, m'_2\}$, $k = \{n_2, m_2\}$, and $l = \{n_1, m_1\}$. n_k and m_k are the 2D harmonic oscillator quantum numbers, as defined in the Appendix A. The e-e interaction is

$$V_{ee}(|\mathbf{r}_1 - \mathbf{r}_2|) = \frac{2}{|\mathbf{r}_1 - \mathbf{r}_2|}. \quad (\text{B.2})$$

In order to calculate the e-e Coulomb matrix element, we start writing it in the basis of plane waves as

$$\langle i, j | V_{ee} | k, l \rangle = \langle i, j | \sum_{\mathbf{q}} V_{\mathbf{q}} e^{i\mathbf{q}\cdot(\mathbf{r}_1 - \mathbf{r}_2)} | k, l \rangle = \sum_{\mathbf{q}} V_{\mathbf{q}} \langle i | e^{i\mathbf{q}\cdot\mathbf{r}_1} | l \rangle \langle j | e^{i\mathbf{q}\cdot\mathbf{r}_2} | k \rangle, \quad (\text{B.3})$$

where $V_{\mathbf{q}}$ is the Fourier transformation of Eq. (B.2), which is given by

$$\begin{aligned}
 V_{\mathbf{q}} &= 2 \int d\mathbf{r} \frac{e^{-i\mathbf{q}\cdot\mathbf{r}}}{\mathbf{r}} = 2 \int_0^\infty r dr \int_0^{2\pi} d\phi_r \frac{e^{iqr \cos(\phi_r - \phi_q)}}{r} \\
 &= 2 \int_0^\infty dr \int_0^{2\pi} d\phi_r \sum_{m=-\infty}^{\infty} (-i)^m e^{-im(\phi_r - \phi_q)} J_m(rq) \\
 &= 4\pi \int_0^\infty dr \sum_{m=-\infty}^{\infty} (-i)^m e^{im\phi_q} \delta_{m,0} J_m(rq) \\
 &= 4\pi \int_0^\infty dr J_0(rq) = \frac{4\pi}{q}.
 \end{aligned} \tag{B.4}$$

Therefore, inserting Eq. (B.4) in Eq. (B.2) we have

$$\langle i, j | V_{ee} | k, l \rangle = \sum_q \frac{4\pi}{q} \langle i | e^{i\mathbf{q}\cdot\mathbf{r}_1} | l \rangle \langle j | e^{i\mathbf{q}\cdot\mathbf{r}_2} | k \rangle. \tag{B.5}$$

The next step is to calculate the e-e matrix elements. In order to do that, we first write the electrons coordinate ($\mathbf{r} = x\mathbf{i} + y\mathbf{j}$) as a function of the lowering and raising operators*

$$x = \frac{l_c}{\sqrt{2}} (a + a^\dagger + b + b^\dagger) \tag{B.6}$$

and

$$y = \frac{il_c}{\sqrt{2}} (a - a^\dagger - b + b^\dagger), \tag{B.7}$$

which implies in

$$\begin{aligned}
 \exp(i\mathbf{q} \cdot \mathbf{r}_1) &= \exp \left\{ i \left[\frac{q_x l_c}{\sqrt{2}} (a_1 + a_1^\dagger + b_1 + b_1^\dagger) + i \frac{q_y l_c}{\sqrt{2}} (a_1 - a_1^\dagger - b_1 + b_1^\dagger) \right] \right\} \\
 &= \exp \left(iQ^* a_1^\dagger + iQ a_1 + iQ b_1^\dagger + iQ^* b_1 \right),
 \end{aligned} \tag{B.8}$$

where we defined $Q = \frac{l_c}{\sqrt{2}}(q_x + iq_y)$. The above equation can be simplified using the Trotter-Suzuki formula

$$e^{\hat{A} + \hat{B}} = e^{\hat{A}} e^{\hat{B}} e^{-[\hat{A}, \hat{B}]/2}, \tag{B.9}$$

which is true only if $[\hat{A}, [\hat{A}, \hat{B}]] = [\hat{B}, [\hat{A}, \hat{B}]] = 0$. Since the operators $a_1(a_1^\dagger)$ and $b_1(b_1^\dagger)$ commute, the above relation is satisfied in pairs, i.e, the operators a and b are decouple.

*They are defined in Appendix A

Now the commutator between the lowering and rising operators are $[iQ^*a_1^\dagger, iQa_1] = |Q|^2$ and $[iQb_1^\dagger, iQ^*b_1] = |Q|^2$. Eq. (B.8), is given by

$$e^{i\mathbf{q}\cdot\mathbf{r}_1} = e^{-|Q|^2} e^{iQ^*a_1^\dagger} e^{iQa_1} e^{iQb_1^\dagger} e^{iQ^*b_1}, \quad (\text{B.10})$$

and the eigenstates are written in terms of the raising operators as

$$|l\rangle = \frac{1}{\sqrt{n_1!m_1!}} (a_1^\dagger)^{n_1} (b_1^\dagger)^{m_1} |00\rangle. \quad (\text{B.11})$$

Finally, using Eqs. (B.10) and (B.11) we obtain the matrix element

$$\begin{aligned} \langle i|e^{i\mathbf{q}\cdot\mathbf{r}_1}|l\rangle &= \langle i|e^{-|Q|^2} e^{iQ^*a_1^\dagger} e^{iQa_1} e^{iQb_1^\dagger} e^{iQ^*b_1}|l\rangle \equiv M_1 \\ &= \frac{1}{\sqrt{n_1'!m_1'!n_1!m_1!}} \langle 00|b_1^{m_1'} a_1^{n_1'} e^{-|Q|^2} e^{iQ^*a_1^\dagger} e^{iQa_1} e^{iQb_1^\dagger} e^{iQ^*b_1} (a_1^\dagger)^{n_1} (b_1^\dagger)^{m_1} |00\rangle \\ &= \frac{1}{\sqrt{n_1'!m_1'!n_1!m_1!}} \langle 00|b_1^{m_1'} a_1^{n_1'} e^{-|Q|^2} e^{iQ^*a_1^\dagger} e^{iQb_1^\dagger} \hat{\mathbf{1}} e^{iQa_1} e^{iQ^*b_1} (a_1^\dagger)^{n_1} (b_1^\dagger)^{m_1} |00\rangle. \end{aligned} \quad (\text{B.12})$$

Note that we have rearranged the order of the operators and introduced the completeness relation ($\hat{\mathbf{1}}$) given by

$$\hat{\mathbf{1}} = \sum_{p_1=0}^{\infty} \sum_{p_2=0}^{\infty} |p_1p_2\rangle \langle p_2p_1| = \frac{1}{p_1!p_2!} \sum_{p_1=0}^{\infty} \sum_{p_2=0}^{\infty} (a_1^\dagger)^{p_1} (b_1^\dagger)^{p_2} |00\rangle \langle 00|b_1^{p_2} a_1^{p_1}. \quad (\text{B.13})$$

We now expand the exponential operators as

$$e^{iQb_1} = \sum_{s=0}^{\infty} \frac{(iQ)^s}{s!} b_1^s. \quad (\text{B.14})$$

Substituting Eqs. (B.13) and (B.14) in Eq. (B.12) we obtain

$$\begin{aligned} M_1 &= \frac{1}{\sqrt{n_1'!m_1'!n_1!m_1!}} \sum_{\substack{s_1, s_2 \\ s_3, s_4}} \sum_{p_1, p_2} \frac{e^{-|Q|^2}}{p_1!p_2!} \langle 00|b_1^{m_1'} a_1^{n_1'} \frac{(iQ^*)^{s_1}}{s_1!} (a_1^\dagger)^{s_1} \frac{(iQ)^{s_2}}{s_2!} (b_1^\dagger)^{s_2} (a_1^\dagger)^{p_1} (b_1^\dagger)^{p_2} |00\rangle \\ &\quad \times \langle 00|b_1^{p_2} a_1^{p_1} \frac{(iQ)^{s_3}}{s_3!} a_1^{s_3} \frac{(iQ^*)^{s_4}}{s_4!} b_1^{s_4} (a_1^\dagger)^{n_1} (b_1^\dagger)^{m_1} |00\rangle. \end{aligned} \quad (\text{B.15})$$

The above matrix element is only different from zero if $s_1 = n_1' - p_1$, $s_2 = m_1' - p_2$, $s_3 = n_1 - p_1$, and $s_4 = m_1 - p_1$. Also the maximum value of p_1 and p_2 must be $\min(n_1, n_1')$ and $\min(m_1, m_1')$,

respectively. Therefore, we have

$$\begin{aligned}
M_1 &= \frac{1}{\sqrt{n_1!m_1'n_1!m_1!}} \sum_{p_1=0}^{\min(n_1,n_1')} \sum_{p_2=0}^{\min(m_1,m_1')} \frac{e^{-|Q|^2}}{p_1!p_2!} \frac{(iQ^*)^{n_1-p_1}}{(n_1-p_1)!} \frac{(iQ)^{m_1-p_2}}{(m_1-p_2)!} \frac{(iQ)^{n_1-p_1}}{(n_1-p_1)!} \frac{(iQ^*)^{m_1-p_2}}{(m_1-p_2)!} \\
&\times \langle 00|b_1^{m_1'}a_1^{n_1'}(a_1^\dagger)^{n_1-p_1}(b_1^\dagger)^{m_1-p_2}(a_1^\dagger)^{p_1}(b_1^\dagger)^{p_2}|00\rangle \langle 00|b_1^{p_2}a_1^{p_1}a_1^{n_1-p_1}b_1^{m_1-p_2}(a_1^\dagger)^{n_1}(b_1^\dagger)^{m_1}|00\rangle \\
&= \frac{1}{\sqrt{n_1!m_1'n_1!m_1!}} \sum_{p_1=0}^{\min(n_1,n_1')} \sum_{p_2=0}^{\min(m_1,m_1')} \frac{e^{-|Q|^2}}{p_1!p_2!} \frac{n_1!}{(n_1-p_1)!} \frac{m_1!}{(m_1-p_2)!} \frac{n_1!}{(n_1-p_1)!} \frac{m_1!}{(m_1-p_2)!} \\
&(iQ^*)^{n_1-p_1}(iQ)^{m_1-p_2}(iQ)^{n_1-p_1}(iQ^*)^{m_1-p_2} \\
&= \frac{e^{-|Q|^2}}{\sqrt{n_1!m_1'n_1!m_1!}} \sum_{p_1=0}^{\min(n_1,n_1')} \sum_{p_2=0}^{\min(m_1,m_1')} p_1!p_2! \binom{n_1'}{p_1} \binom{m_1'}{p_2} \binom{n_1}{p_1} \binom{m_1}{p_2} \\
&(iQ^*)^{n_1-p_1}(iQ)^{m_1-p_2}(iQ)^{n_1-p_1}(iQ^*)^{m_1-p_2}. \tag{B.16}
\end{aligned}$$

The matrix element $M_2 = \langle j|e^{-i\mathbf{q}\cdot\mathbf{r}_2}|k\rangle$ is obtained in a similar way. It is given by

$$\begin{aligned}
M_2 &= \frac{e^{-|Q|^2}}{\sqrt{n_2!m_2'n_2!m_2!}} \sum_{p_3=0}^{\min(n_2,n_2')} \sum_{p_4=0}^{\min(m_2,m_2')} p_3!p_4! \binom{n_2'}{p_3} \binom{m_2'}{p_4} \binom{n_2}{p_3} \binom{m_2}{p_4} \\
&(-iQ^*)^{n_2-p_3}(-iQ)^{m_2-p_4}(-iQ)^{n_2-p_3}(-iQ^*)^{m_2-p_4}. \tag{B.17}
\end{aligned}$$

Replacing Eqs. (B.4), (B.16) and (B.17) on Eq. (B.3), the e-e Coulomb matrix elements is given by

$$\begin{aligned}
\langle i,j|V_{ee}|k,l\rangle &= \frac{1}{4\pi^2} \int_0^\infty qdq \int_0^{2\pi} d\phi_q \frac{4\pi}{q} M_1 M_2 \tag{B.18} \\
&= \frac{1}{\pi \sqrt{n_1!m_1'n_1!m_1'n_2!m_2'n_2!m_2!}} \sum_{p_1=0}^{\min(n_1,n_1')} p_1! \binom{n_1}{p_1} \binom{n_1'}{p_1} \sum_{p_2=0}^{\min(m_1,m_1')} p_2! \binom{m_1}{p_2} \binom{m_1'}{p_2} \\
&\sum_{p_3=0}^{\min(n_2,n_2')} p_3! \binom{n_2}{p_3} \binom{n_2'}{p_3} \sum_{p_4=0}^{\min(m_2,m_2')} p_4! \binom{m_2}{p_4} \binom{m_2'}{p_4} I_{p_1 p_2 p_3 p_4}
\end{aligned}$$

where

$$\begin{aligned}
I_{p_1 p_2 p_3 p_4} &= \int_0^\infty dq \int_0^{2\pi} d\phi_q e^{-2|Q|^2} (iQ^*)^{n_1-p_1} (iQ)^{m_1-p_2} (iQ)^{n_1-p_1} (iQ^*)^{m_1-p_2} (-iQ^*)^{n_2-p_3} \\
&\times (-iQ)^{m_2-p_4} (-iQ)^{n_2-p_3} (-iQ^*)^{m_2-p_4} \tag{B.19}
\end{aligned}$$

We shall now solve the integral. For that, we first change variables. It is more convenient to work in the polar representation of Q . We know that $Q = \frac{l_c}{\sqrt{2}}(q_x + iq_y) = |Q|e^{i\phi_q}$, where

$|Q| = \frac{l_c}{\sqrt{2}}q$. Therefore, we have that $dq = \frac{\sqrt{2}}{l_c}d|Q|$. Inserting the definitions in the integral above we can rewrite Eq. (B.19) as

$$\begin{aligned}
 I_{p_1 p_2 p_3 p_4} &= \frac{\sqrt{2}}{l_c} (-1)^{n'_2+m'_2+n_2+m_2} \left[i^{n'_1+m'_1+n_1+m_1+n'_2+m'_2+n_2+m_2-2p_1-2p_2-2p_3-2p_4} \right] \\
 &\times \int_0^{2\pi} d\phi_q e^{i\phi_q(-n'_1+m'_1+n_1-m_1-n'_2+m'_2+n_2-m_2)} \\
 &\times \int_0^\infty d|Q| e^{-2|Q|^2} |Q|^{n'_1+m'_1+n_1+m_1+n'_2+m'_2+n_2+m_2-2p_1-2p_2-2p_3-2p_4}
 \end{aligned} \tag{B.20}$$

We first solve the angular integral,

$$\int_0^{2\pi} d\phi_q e^{i\phi_q(-n'_1+m'_1+n_1-m_1-n'_2+m'_2+n_2-m_2)} = 2\pi \delta_{L_L, L_R} \tag{B.21}$$

where $L_L = (m'_1 + m'_2) - (n'_1 + n'_2)$ and $L_R = (m_1 + m_2) - (n_1 + n_2)$ are the angular momentum of the two electrons on the left and right side of the matrix element, respectively. The result of the above integral gives the angular momentum conservation of the e-e Coulomb interaction.

Now we solve the integral in $|Q|$. Using the conservation of the angular momentum. We simplify the integral such as

$$\begin{aligned}
 I_{p_1 p_2 p_3 p_4} &= \frac{2\pi\sqrt{2}}{l_c} (-1)^{n'_2+m'_2+n_2+m_2} i^{2(n'_1+n'_2+m_1+m_2-p_1-p_2-p_3-p_4)} \delta_{L_L, L_R} \\
 &\times \int_0^\infty d|Q| e^{-2|Q|^2} |Q|^{2(n'_1+n'_2+m_1+m_2-p_1-p_2-p_3-p_4)}.
 \end{aligned} \tag{B.22}$$

To solve the above integral we first define $p = n'_1 + n'_2 + m_1 + m_2 - p_1 - p_2 - p_3 - p_4$. Second we do the following changing of variable: $x = 2|Q|^2$. Lastly, we multiply and divide the integral by 2^{2p} , obtaining

$$\begin{aligned}
 I_{p_1 p_2 p_3 p_4} &= \frac{\pi}{l_c} (-1)^{n'_2+m'_2+n_2+m_2} \frac{i^{2p}}{2^p} \delta_{L_L, L_R} \int_0^\infty dx e^{-x} x^{p+1/2-1} \\
 &= \frac{\pi}{l_c} \left(\frac{-1}{2} \right)^p (-1)^{n'_2+m'_2+n_2+m_2} \Gamma\left(p + \frac{1}{2}\right) \delta_{L_L, L_R}.
 \end{aligned} \tag{B.23}$$

The final form of the e-e Coulomb matrix element is obtained by replacing Eq. (B.23) in Eq.

(B.24), which is given by

$$\begin{aligned} \langle i, j | V_{ee} | k, l \rangle = & \frac{\delta_{LL,LR} (-1)^{n'_2+m'_2+n_2+m_2}}{l_c \sqrt{n_1!m_1!n'_1!m'_1!n_2!m_2!n'_2!m'_2!}} \sum_{p_1=0}^{\min(n_1,n'_1)} p_1! \binom{n_1}{p_1} \binom{n'_1}{p_1} \sum_{p_2=0}^{\min(m_1,m'_1)} p_2! \binom{m_1}{p_2} \binom{m'_1}{p_2} \\ & \sum_{p_3=0}^{\min(n_2,n'_2)} p_3! \binom{n_2}{p_3} \binom{n'_2}{p_3} \sum_{p_4=0}^{\min(m_2,m'_2)} p_4! \binom{m_2}{p_4} \binom{m'_2}{p_4} \left(\frac{-1}{2}\right)^p \Gamma\left(p + \frac{1}{2}\right). \end{aligned} \quad (\text{B.24})$$

The above expression gives the e-e matrix elements for a 2D parabolic quantum dot. As an example, we calculate the e-e matrix elements of two electrons in the s -shell, which implies in, $i = j = k = l = \{0, 0\}$, and gives to us

$$\langle i, j | V_{ee} | k, l \rangle = \frac{1}{l_c} \Gamma\left(\frac{1}{2}\right) = \sqrt{\omega_0 \pi}. \quad (\text{B.25})$$

This is the largest possible value of the e-e matrix element. All the values of the e-e matrix elements are scaled with $\sqrt{\omega_0 \pi}$. Therefore, we need to calculate them only once and its correct value for a defined quantum confinement is given by multiplying this factor.

Appendix C

Magnetization of (III,Mn)V semiconductors

The introduction of substitutional Mn ions in GaAs provides both localized spin and holes [12]. Mn doping III-V or II-VI semiconductors has the 3*d*-shell half-filled, with spin $M = 5/2$. Therefore, Mn spins can couple with each other, and give origin to a magnetic phase. In metallic GaMnAs, it is known that the ferromagnetism is mediated by the delocalized holes in the valence band, and the Hamiltonian that describes the interaction between hole spin and Mn spin is given by the Zener kinetic exchange model. It is expressed as

$$\mathcal{H}_{pd} = -J_{pd} \sum_{i,j} \mathbf{s}_i \cdot \mathbf{M}_j f(\mathbf{r}_i - \mathbf{R}_j), \quad (\text{C.1})$$

where J_{pd} is the exchange interaction, \mathbf{s} and \mathbf{M} are the hole and manganese spins, respectively. $f(\mathbf{r}_i - \mathbf{R}_j)$ is the Mn distribution function and describes the overlap between holes and the Mn ions. That Hamiltonian is treated with both virtual crystal approximation (VCA) and mean field theory (MFT). The Hamiltonian of valence holes, in the presence of an external magnetic field, \mathbf{B} , and Mn ions, is given by

$$\mathcal{H} = \mathcal{H}_L - \mu_B g^* \sum_i \mathbf{s}_i \cdot \mathbf{B} - g \mu_B \sum_j \mathbf{M}_j \cdot \mathbf{B} - J_{pd} \sum_{i,j} \mathbf{s}_i \cdot \mathbf{M}_j f(\mathbf{r}_i - \mathbf{R}_j), \quad (\text{C.2})$$

where \mathcal{H}_L is the Hamiltonian that describes the valence band holes, e.g. the Luttinger-Kohn Hamiltonian [100]. μ_B is the Bohr magneton, g and g^* are the g -factor for Mn ions and holes, respectively. In order to solve this Hamiltonian we use thermal-spin-density functional theory

(TSDFT) [66, 72, 121, 181, 182], which includes thermal and spin effects. In the TSDFT the electronic density minimizes the grand potential, given by

$$\Omega = -K_B T \ln \left[\sum_{\alpha} \exp(-\langle \alpha | \mathcal{H} | \alpha \rangle / K_B T) \right] \quad (\text{C.3})$$

where $|\alpha\rangle = |a, s_{z_i}, m_j\rangle$, a is the hole state, defined by \mathcal{H}_L . s_{z_i} is the hole spin state and m_j defines the Mn spin state. With that, we have

$$\langle \alpha | \mathcal{H} | \alpha \rangle = - \sum_j \left(g \mu_B B + J_{pd} \sum_i s_{z_i} f(\mathbf{r}_i - \mathbf{R}_j) \right) m_j - \sum_i g^* \mu_B B s_{z_i} + \langle a | \mathcal{H}_L | a \rangle. \quad (\text{C.4})$$

the sum over the index i in the second term can be performed as follows

$$\sum_i s_{z_i} f(\mathbf{r}_i - \mathbf{R}_j) = \frac{1}{2} \left(\sum_{i=1}^{N_{\uparrow}} 1 - \sum_{i=1}^{N_{\downarrow}} 1 \right) f(\mathbf{r}_i - \mathbf{R}_j) \quad (\text{C.5})$$

$$= \frac{1}{2} \int \xi(\mathbf{r}) f(\mathbf{r}_i - \mathbf{R}_j) d\mathbf{r}, \quad (\text{C.6})$$

where $\xi(\mathbf{r}) = (n_{\uparrow}(\mathbf{r}) - n_{\downarrow}(\mathbf{r}))$ is the hole gas magnetization. As we consider the system is homogeneous in the x - y plane, only variations in the z direction of the electronic density are considered. Hence, we have $\xi(\mathbf{r}) \equiv \xi(z)$, and $f(\mathbf{r}_i - \mathbf{R}_j) = (1/A)f(z - z_{Mn})$, where A is the x - y plane area. Defining,

$$\sum_i s_{z_i} f(\mathbf{r}_i - \mathbf{R}_j) = \frac{1}{2} \int \xi(z) f(z - z_{Mn}) dz, \quad (\text{C.7})$$

the above equation describes the overlap between holes and Mn ions. With this in hand, Eq. (C.4) can be written as

$$\langle \alpha | \mathcal{H} | \alpha \rangle = - \sum_j b m_j - \sum_i g^* \mu_B B s_{z_i} + \langle a | \mathcal{H}_L | a \rangle, \quad (\text{C.8})$$

where $y = [g \mu_B B + J_{pd} \int m(z) f(z - z_{Mn}) dz / 2] / k_B T$. The sum over many-hole states ($|\alpha\rangle \equiv |a, s_{z_i}\rangle$) is performed in the SDFT developed in the section 2.1. Using Eq. (C.8), the grand

potential, defined in Eq. (C.3), is

$$\begin{aligned}\Omega[p(z), \xi(z)] &= -K_B T \ln \left[\sum_{\alpha} \exp(-\langle \alpha | \mathcal{H}_L | \alpha \rangle / K_B T) \right] - \frac{g^* \mu_B}{2} \int B(z) \xi(z) dz + \Omega_{m_j} \\ &= \Omega_f[p(z), \xi(z)] - \frac{g^* \mu_B}{2} \int B(z) \xi(z) dz + \Omega_{m_j}\end{aligned}\quad (\text{C.9})$$

where Ω_{m_j} is the grand potential of a collection of Mn spins. This is defined as

$$\begin{aligned}\Omega_{m_j} &= -k_B T \ln \left[\sum_{m_j=-M}^M \exp \left(\sum_j y m_j \right) \right] = -k_B T \ln \left[\sum_{m_j=-M}^M \Pi_j \exp(y m_j) \right] \\ &= -k_B T \sum_j \ln \left[\sum_{m_j=-M}^M \exp(y m_j) \right].\end{aligned}\quad (\text{C.10})$$

The sum over m_j is carried from $-M$ to M and produces

$$\begin{aligned}\sum_{m_j=-M}^M \exp(-y m_j) &= \sum_{m_j=-M}^M x^{m_j} = x^M (1 + x + x^2 + \dots + x^{2M}) \\ &= x^M \frac{x^{2M+1} - 1}{x^{1/2} - 1} = \frac{x^{M+1/2} - x^{-(M+1/2)}}{x^{1/2} - x^{-1/2}} \\ &= \frac{e^{(M+1/2)y} - e^{-(M+1/2)y}}{e^{y/2} - e^{-y/2}} \\ &= \frac{\sinh \left[\left(1 + \frac{1}{2M}\right) y \right]}{\sinh \left[\frac{y}{2M} \right]}.\end{aligned}\quad (\text{C.11})$$

Redefining $y = M [g\mu_B B + J_{pd} \int m(z) f(z - z_{Mn}) dz / 2] / k_B T$ and substituting Eq. (C.11) in

Eq. (C.10), we obtain

$$\Omega_{m_j}[p(z), \xi(z)] = -k_B T \sum_j \ln \left[\frac{\sinh \left[\left(1 + \frac{1}{2M}\right) y \right]}{\sinh \left(\frac{y}{2M} \right)} \right] = -k_B T V N_0 x_{eff} \ln \left[\frac{\sinh \left[\left(1 + \frac{1}{2M}\right) y \right]}{\sinh \left(\frac{y}{2M} \right)} \right]\quad (\text{C.12})$$

where $\sum_j \equiv V N_0 x_{eff}$ is the effective concentration of Mn that contributes to the magnetiza-

tion. V is the unit cell volume. The magnetization is defined as

$$\begin{aligned}
 M_T &= -\frac{1}{V} \frac{\partial \Omega_{m_j}[p(z), \xi(z)]}{\partial B} \\
 &= \frac{k_B T N_0 x_{eff} \sinh\left(\frac{y}{2M}\right)}{\sinh\left[\left(1 + \frac{1}{2M}\right)y\right]} \frac{\partial y}{\partial B} \left\{ \left(1 + \frac{1}{2M}\right) \cosh\left[\left(1 + \frac{1}{2M}\right)y\right] \sinh\left(\frac{y}{2M}\right) \right. \\
 &\quad \left. - \sinh\left[\left(1 + \frac{1}{2M}\right)y\right] \frac{1}{2m} \cosh\left(\frac{y}{2M}\right) \right\} / \sinh^2\left(\frac{y}{2M}\right) \\
 &= Mg\mu_B N_0 x_{eff} \left\{ \left(1 + \frac{1}{2M}\right) \frac{\cosh\left[\left(1 + \frac{1}{2M}\right)y\right]}{\sinh\left[\left(1 + \frac{1}{2M}\right)y\right]} - \frac{1}{2M} \frac{\cosh\left(\frac{y}{2M}\right)}{\sinh\left(\frac{y}{2M}\right)} \right\} \\
 &= Mg\mu_B N_0 x_{eff} \mathcal{B}_S(y) = g\mu_B N_0 \langle M_z \rangle = g\mu_B N_0 \langle M_z \rangle, \tag{C.13}
 \end{aligned}$$

where $\mathcal{B}_M(y)$ is the Brillouin's function. $\langle M_z \rangle = M\mathcal{B}_S(y)$ is the average of the z -component of the Mn spin per Mn site. The above equation is the magnetization of the Mn spin, in the presence of an effective magnetic field H_{eff} , which is defined by

$$H_{eff} = B + \frac{J_{pd}}{2g\mu_B} \int \xi(z) f(z - z_{Mn}) dz. \tag{C.14}$$

Equation (C.14) shows that even in absence of an external magnetic field $\xi(z)$ is non-zero. The Mn spin is then in a ferromagnetic phase due the spin polarization of the hole gas.

Appendix D

Imaginary time wave-function evolution

We demonstrate here that the wave function, defined by a time-independent Hamiltonian, evolves to the ground state when it is propagated in the imaginary time domain.

Consider that the eigenstates of the Hamiltonian are $|\phi_n\rangle$, with eigenvalues ε_n , such as, $\varepsilon_0 < \varepsilon_1 < \varepsilon_2 < \dots < \varepsilon_n$. Thus, the wave function $|\psi(t)\rangle$ can be expanded in the basis of the Hamiltonian

$$|\psi(t)\rangle = \sum_n a_n \exp\left(-i\frac{\varepsilon_n t}{\hbar}\right) |\phi_n\rangle. \quad (\text{D.1})$$

Replacing t by $-i\tau$, we have

$$|\psi(\tau)\rangle = \sum_n a_n \exp\left(-\frac{\varepsilon_n \tau}{\hbar}\right) |\phi_n\rangle. \quad (\text{D.2})$$

The above equation is not normalized. This can be seen from the normalization condition:

$$\langle\psi(t)|\psi(t)\rangle = \int |\psi(\mathbf{r}, \tau)|^2 d\mathbf{r} = \sum_n |a_n|^2 \exp\left(-\frac{2\varepsilon_n \tau}{\hbar}\right). \quad (\text{D.3})$$

We observe that the norm depends on τ and therefore the wave function has to be normalized at each time step of the propagation. The normalized eigenstate are

$$|\psi(\tau)\rangle^{norm} = \frac{\sum_n a_n \exp\left[-\frac{\varepsilon_n \tau}{\hbar}\right] |\phi_n\rangle}{\sqrt{\sum_n |a_n|^2 \exp\left[-\frac{2\varepsilon_n \tau}{\hbar}\right]}}. \quad (\text{D.4})$$

Since our basis is kept in ascending order of energy, the first term of Eq. (D.4) is the ground state eigenstate. We put it into evidence and rewrite Eq. (D.4) as

$$|\psi(\tau)\rangle^{norm} = \frac{|\phi_0\rangle + \sum_{i>0} \frac{a_i}{a_0} \exp\left[\frac{(\varepsilon_0 - \varepsilon_i)\tau}{\hbar}\right] |\phi_i\rangle}{\sqrt{1 + \sum_{i>0} \left|\frac{a_i}{a_0}\right|^2 \exp\left[\frac{(\varepsilon_0 - \varepsilon_i)\tau}{\hbar}\right]}}. \quad (\text{D.5})$$

Taking $\tau \rightarrow \infty$, we obtain

$$\lim_{\tau \rightarrow \infty} |\psi_{GS}(\tau)\rangle^{norm} = |\phi_0\rangle. \quad (\text{D.6})$$

The above results show that propagating the wave function for a long time in the imaginary time domain, the wave function converges to the ground state. Once we have the ground state, we can access all the excited states of the spectra through the Gram-Schmidt orthogonalization method.

As an example, we demonstrate how the first excited state is obtained. Consider that the ground state ($|\psi_{GS}(\tau)\rangle$) is known and the excited state can be written as a linear combination of $|\phi_n\rangle$, i.e.,

$$|\phi_1(\tau)\rangle = \sum_n b_n e^{-\varepsilon_n \tau / \hbar} |\phi_n\rangle. \quad (\text{D.7})$$

The Gram-Schmidt orthogonalization method gives the first excited state

$$|\psi_1(\tau)\rangle = \frac{|\phi_1(\tau)\rangle - \langle\psi_{GS}(\tau)|\phi_1(\tau)\rangle |\psi_{GS}(\tau)\rangle}{\sqrt{\langle\phi_1(\tau)|\phi_1(\tau)\rangle + |\langle\psi_{GS}(\tau)|\phi_1(\tau)\rangle|^2}}. \quad (\text{D.8})$$

This equation is already normalized. From Eqs. (D.7) and (D.6), we have

$$\langle\phi_1(\tau)|\phi_1(\tau)\rangle = \sum_n |b_n|^2 e^{-2\varepsilon_n \tau / \hbar} \quad (\text{D.9})$$

$$\langle\psi_{GS}(\tau)|\phi_1(\tau)\rangle = \langle\phi_0(\tau)|\phi_1(\tau)\rangle = b_0 e^{-\varepsilon_0 \tau / \hbar}. \quad (\text{D.10})$$

Replacing the relations above [Eq. (D.9)] in Eq. (D.8), we have

$$|\psi_1(\tau)\rangle = \frac{|\phi_1\rangle + \sum_{i>1} \frac{b_i}{b_1} \exp\left[\frac{(\varepsilon_1 - \varepsilon_i)\tau}{\hbar}\right] |\phi_i\rangle}{\sqrt{1 + \sum_{i>1} \left|\frac{b_i}{b_1}\right|^2 \exp\left[\frac{(\varepsilon_1 - \varepsilon_i)\tau}{\hbar}\right]}}. \quad (\text{D.11})$$

In the limit of $\tau \rightarrow \infty$, we obtain the first excited state,

$$\lim_{\tau \rightarrow \infty} |\psi_1(\tau)\rangle = |\phi_1\rangle. \quad (\text{D.12})$$

This process is repeated in order of increasing energy to all eigenfunctions. This gives the complete spectra of the Hamiltonian.

Bibliography

- [1] L. Lukasiak and A. Jakubowski, “History of semiconductors,” *Journal of Telecommunications and Information Technology*, vol. 1, p. 3, 2010.
- [2] A. H. MacDonald, P. Schiffer, and N. Samarth, “Ferromagnetic semiconductors: moving beyond (Ga,Mn)As,” *Nat. Mater.*, vol. 4, p. 195, 2005.
- [3] S. M. Cronenwett, T. H. Oosterkamp, and L. P. Kouwenhoven, “A tunable kondo effect in quantum dots,” *Science*, vol. 281, p. 540, 1998.
- [4] C. Latta, F. Haupt, M. Hanl, A. Weichselbaum, M. Claassen, W. Wuester, P. Fallahi, S. Faelt, L. Glazman, J. von Delft, H. E. Türeci, and A. Imamoglu, “Quantum quench of kondo correlations in optical absorption,” *Nature*, vol. 474, p. 627, 2011.
- [5] L. Fu and C. L. Kane, “Superconducting proximity effect and majorana fermions at the surface of a topological insulator,” *Phys. Rev. Lett.*, vol. 100, p. 096407, 2008.
- [6] V. Mourik, K. Zuo, S. M. Frolov, S. R. Plissard, E. P. A. M. Bakkers, and L. P. Kouwenhoven, “Signatures of majorana fermions in hybrid superconductor-semiconductor nanowire devices,” *Science*, vol. 336, p. 1003, 2012.
- [7] M. N. Baibich, J. M. Broto, A. Fert, F. N. V. Dau, F. Petroff, P. Etienne, G. Creuzet, A. Friederich, and J. Chazelas, “Giant magnetoresistance of (001)Fe/(001)Cr magnetic superlattices,” *Phys. Rev. Lett.*, vol. 61, p. 2472, 1988.
- [8] G. Binasch, P. Grünberg, F. Saurenbach, and W. Zinn, “Enhanced magnetoresistance in layered magnetic structures with antiferromagnetic interlayer exchange,” *Phys. Rev. B*, vol. 39, p. 4828, 1989.
- [9] J. K. Furdyna, “Diluted magnetic semiconductors,” *J. Appl. Phys.*, vol. 64, p. R29, 1988.
- [10] H. Ohno, A. Shen, F. Matsukura, A. Oiwa, A. Endo, S. Katsumoto, and Y. Iye, “(Ga,Mn)As: A new diluted magnetic semiconductor based on GaAs,” *Appl. Phys. Lett.*, vol. 69, p. 363, 1996.
- [11] T. Dietl, H. Ohno, F. Matsukura, J. Cibert, and D. Ferrand, “Zener model description of ferromagnetism in zinc-blende magnetic semiconductors,” *Science*, vol. 287, p. 1019, 2000.
- [12] T. Jungwirth, J. Sinova, J. Mašek, J. Kučera, and A. H. MacDonald, “Theory of ferromagnetic (III,Mn)V semiconductors,” *Rev. Mod. Phys.*, vol. 78, p. 809, 2006.
- [13] J. Nitta, T. Akazaki, H. Takayanagi, and T. Enoki, “Gate control of spin-orbit interaction in an inverted $\text{In}_{0.53}\text{Ga}_{0.47}\text{As}/\text{In}_{0.52}\text{Al}_{0.48}\text{As}$ heterostructures,” *Phys. Rev. B*, vol. 78, p. 1335, 1977.

- [14] Y. K. Kato, R. C. Myers, A. C. Gossard, and D. D. Awschalom, "Observation of the spin hall effect in semiconductors," *Science*, vol. 306, p. 1910, 2004.
- [15] B. A. Bernevig, T. L. Hughes, and S. C. Zhang, "Quantum spin hall effect and topological phase transition in HgTe quantum wells," *Science*, vol. 314, p. 1757, 2006.
- [16] M. König, S. W. C. Brüne, A. Roth, H. Buhmann, L. W. Molenkamp, X. L. Qi, and S. C. Zhang, "Quantum spin hall insulator state in HgTe quantum wells," *Science*, vol. 318, p. 766, 2007.
- [17] S. A. Wolf, D. D. Awschalom, R. A. Buhrman, J. M. Daughton, S. von Molnár, M. L. Roukes, A. Y. Chtchelkanova, and D. M. Treger, "Spintronics: A spin-based electronics vision for the future," *Science*, vol. 294, p. 1488, 2001.
- [18] D. D. Awschalom and M. E. Flatté, "Challenges for semiconductor spintronics," *Nat. Phys.*, vol. 3, p. 153, 2007.
- [19] C. Liu, T. L. Hughes, X.-L. Qi, K. Wang, and S.-C. Zhang, "Quantum spin hall effect in inverted type-II semiconductors," *Phys. Rev. Lett.*, vol. 100, p. 236601, 2008.
- [20] K. v. Klitzing, G. Dorda, and M. Pepper, "New method for high-accuracy determination of the fine-structure constant based on quantized hall resistance," *Phys. Rev. Lett.*, vol. 45, p. 494, 1980.
- [21] D. C. Tsui, H. L. Stormer, and A. C. Gossard, "Two-dimensional magnetotransport in the extreme quantum limit," *Phys. Rev. Lett.*, vol. 48, p. 1559, 1982.
- [22] R. B. Laughlin, "Anomalous quantum hall effect: An incompressible quantum fluid with fractionally charged excitations," *Phys. Rev. Lett.*, vol. 50, p. 1395, 1983.
- [23] M. Z. Hasan and C. L. Kane, "Topological insulators," *Rev. Mod. Phys.*, vol. 82, p. 3045, 2010.
- [24] X.-L. Qi and S.-C. Zhang, "Topological insulators and superconductors," *Rev. Mod. Phys.*, vol. 83, p. 1057, 2011.
- [25] Y. Ando, "Topological insulator materials," *J. Phys. Soc. Jpn.*, vol. 82, p. 102001, 2013.
- [26] J. D. Koralek, C. P. Weber, J. Orenstein, B. A. Bernevig, S.-C. Zhang, S. Mack, and D. D. Awschalom, "Emergence of the persistent spin helix in semiconductor quantum wells," *Nature*, vol. 458, p. 610, 2009.
- [27] D. Neumaier, M. Schlapps, U. Wurstbauer, J. Sadowski, M. Reinwald, W. Wegscheider, and D. Weiss, "Electron-electron interaction in one- and two-dimensional ferromagnetic (Ga,Mn)As," *Phys. Rev. B*, vol. 77, p. 041306, 2008.
- [28] U. Wurstbauer, C. Śliwa, D. Weiss, T. Dietl, and W. Wegscheider, "Hysteretic magnetoresistance and thermal bistability in a magnetic two-dimensional hole system," *Nat. Phys.*, vol. 6, p. 955, 2010.
- [29] S. Ohya, K. Takata, and M. Tanaka, "Nearly non-magnetic valence band of the ferromagnetic semiconductor GaMnAs," *Nat. Phys.*, vol. 7, p. 342, 2011.
- [30] Q. Wang, X. Liu, H.-J. Zhang, N. Samarth, S.-C. Zhang, and C.-X. Liu, "Quantum anomalous hall effect in magnetically doped InAs/GaSb quantum wells," *arXiv preprint*, p. arXiv:1311.4113v1, 2013.

- [31] A. L. Gazoto, M. J. S. P. Brasil, F. Iikawa, J. A. Brum, E. Ribeiro, Y. A. Danilov, O. V. Vikhrova, and B. N. Zvonkov, “Enhanced magneto-optical oscillations from two-dimensional hole-gases in the presence of Mn ions,” *Appl. Phys. Lett.*, vol. 98, p. 251901, 2011.
- [32] T. B. Kehoe, C. M. Townsley, A. Usher, M. Henini, and G. Hill, “Exchange-enhanced energy shifts in the polarized photoluminescence of a two-dimensional hole system in the integer quantum hall regime,” *Phys. Rev. B*, vol. 68, p. 045325, 2003.
- [33] P. Hawrylak and M. Korkusinski, *Single Quantum Dots: Fundamentals, Applications, and New Concepts*, vol. 90 of *Topics in Applied Physics*. Berlin: Springer-Verlag, 2003.
- [34] A. Wojs and P. Hawrylak, “Charging and infrared spectroscopy of self-assembled quantum dots in a magnetic field,” *Phys. Rev. B*, vol. 53, p. 10841, 1996.
- [35] S. Tarucha, D. G. Austing, T. Honda, R. J. van der Hage, and L. P. Kouwenhoven, “Shell filling and spin effects in a few electron quantum dot,” *Phys. Rev. Lett.*, vol. 77, p. 3613, 1996.
- [36] A. Ghosal, A. D. Güçlü, C. J. Umrigar, D. Ullmo, and H. U. Baranger, “Correlation-induced inhomogeneity in circular quantum dots,” *Nat. Phys.*, vol. 2, p. 336, 2006.
- [37] S. S. N. G. Stoltz, M. T. Rakher, L. A. Coldren, P. M. Petroff, and D. Bouwmeester, “High-frequency single-photon source with polarization control,” *Nat. Photon.*, vol. 1, p. 704, 2007.
- [38] J. A. Brum and P. Hawrylak, “Coupled quantum dots as quantum exclusive-OR gate,” *Superl. and Microstr.*, vol. 22, p. 431, 1997.
- [39] D. Loss and D. P. DiVincenzo, “Quantum computation with quantum dots,” *Phys. Rev. A*, vol. 57, p. 120, 1998.
- [40] D. Heiss, V. Jovanov, M. Bichler, G. Abstreiter, and J. J. Finley, “Charge and spin readout scheme for single self-assembled quantum dots,” *Phys. Rev. B*, vol. 77, p. 235442, 2008.
- [41] P. M. Koenraad and M. E. Flatté, “Single dopants in semiconductors,” *Nat. Mater.*, vol. 10, p. 91, 2011.
- [42] S. Jamet, H. Boukari, and L. Besombes, “Spin dynamics of a Mn atom in a semiconductor quantum dot under resonant optical excitation,” *Phys. Rev. B*, vol. 87, p. 245306, 2013.
- [43] M. Ciorga, A. S. Sachrajda, P. Hawrylak, C. Gould, P. Zawadzki, S. Jullian, Y. Feng, and Z. Wasilewski, “Addition spectrum of a lateral dot from Coulomb and spin-blockade spectroscopy,” *Phys. Rev. B*, vol. 61, p. R16315, 2000.
- [44] P. M. Petroff, *Electronic properties of self-assembled quantum dots*, in *Single Quantum Dots: Fundamentals, Applications, and New Concepts*, *Topics in Applied Physics*, vol. 90 of *Topics in Applied Physics*. Berlin: Springer-Verlag, 2003.
- [45] S. T. Ochsenbein, Y. Feng, K. M. Whitaker, E. Badaeva, W. K. Liu, X. Li, and D. R. Gamelin, “Charge-controlled magnetism in colloidal doped semiconductor nanocrystals,” *Nat. Nanotechnol.*, vol. 4, p. 681, 2009.
- [46] D. A. Bussian, S. A. Crooker, M. Yin, M. Brynda, A. L. Efros, and V. I. Klimov, “Tunable magnetic exchange interactions in manganese-doped inverted core-shell ZnSe-CdSe nanocrystals,” *Nat. Mater.*, vol. 8, p. 35, 2009.

- [47] D. Goldhaber-Gordon, H. Shtrikman, D. Mahalu, D. Abusch-Magder, U. Meirav, and M. A. Kastner, "Kondo effect in a single-electron transistor," *Nature*, vol. 391, p. 156, 1998.
- [48] L. Kouwenhoven and L. Glazman, "Revival of the kondo effect," *Phys. World*, p. 33, 2001.
- [49] N. A. J. M. Kleemans, J. van Bree, A. O. Govorov, J. G. Keizer, G. J. Hamhuis, R. Nötzel, A. Y. Silov, and P. M. Koenraad, "Many-body exciton states in self-assembled quantum dots coupled to a fermi sea," *Nat. Phys.*, vol. 6, p. 547, 2010.
- [50] P. Recher, E. V. Sukhorukov, and D. Loss, "Quantum dot as spin filter and spin memory," *Phys. Rev. Lett.*, vol. 85, p. 1962, 2000.
- [51] P. Hawrylak, *The Physics of Diluted Magnetic Semiconductors*. Springer Series in Materials Science, Berlin: Springer-Verlag, 2011.
- [52] R. M. Abolfath, P. Hawrylak, and I. Žutić, "Tailoring magnetism in quantum dots," *Phys. Rev. Lett.*, vol. 98, p. 207203, 2007.
- [53] U. C. Mendes, M. Korkusinski, and P. Hawrylak, "Electron-electron interaction mediated indirect coupling of electron and magnetic ion or nuclear spins in self-assembled quantum dots." Submitted to *Phys. Rev. B*.
- [54] E. Vernek, F. Qu, F. M. Souza, J. C. Egues, and E. V. Anda, "Kondo screening regimes of a quantum dot with a single Mn ion," *Phys. Rev. B*, vol. 83, p. 205422, 2011.
- [55] U. C. Mendes, M. Korkusinsk, A. H. Trojnar, and P. Hawrylak, "Optical properties of charged quantum dots doped with a single magnetic impurity," *Phys. Rev. B*, vol. 88, p. 115306, 2013.
- [56] L. Besombes, Y. Leger, L. Maingault, D. Ferrand, H. Mariette, and J. Cibert, "Probing the spin state of a single magnetic ion in an individual quantum dot," *Phys. Rev. Lett.*, vol. 93, p. 207403, 2004.
- [57] Y. Leger, L. Besombes, J. Fernández-Rossier, L. Maingault, and H. Mariette, "Electrical control of a single Mn atom in a quantum dot," *Phys. Rev. Lett.*, vol. 97, p. 107401, 2006.
- [58] A. H. Trojnar, M. Korkusinski, U. C. Mendes, M. Goryca, M. Koperski, T. Smolenski, P. Kossacki, P. Wojnar, and P. Hawrylak, "Fine structure of a biexciton in a single quantum dot with a magnetic impurity," *Phys. Rev. B*, vol. 87, p. 205311, 2013.
- [59] A. O. Govorov, "Optical probing of the spin state of a single magnetic impurity in a self-assembled quantum dot," *Phys. Rev. B*, vol. 70, p. 035321, 2004.
- [60] J. Fernandez-Rossier, "Single-exciton spectroscopy of semimagnetic quantum dots," *Phys. Rev. B*, vol. 73, p. 045301, 2006.
- [61] A. Kudelski, A. Lemaitre, A. Miard, P. Voisin, T. C. M. Graham, R. J. Warburton, and O. Krebs, "Optically probing the fine structure of a single Mn atom in an InAs quantum dot," *Phys. Rev. Lett.*, vol. 99, p. 247209, 2007.
- [62] A. H. Trojnar, M. Korkusinski, E. S. Kadantsev, P. Hawrylak, M. Goryca, T. Kazimierzczuk, P. Kossacki, P. Wojnar, and M. Potemski, "Quantum interference in Exciton-Mn spin interactions in a CdTe semiconductor quantum dot," *Phys. Rev. Lett.*, vol. 107, p. 207403, 2011.

- [63] A. Wojs and P. Hawrylak, "Theory of photoluminescence from modulation-doped self-assembled quantum dots in a magnetic field," *Phys. Rev. B*, vol. 55, p. 13066, 1997.
- [64] D. Dalacu, M. E. Reimer, S. Frederick, D. Kim, J. Lapointe, P. J. Poole, G. C. Aers, R. L. Williams, W. R. McKinnon, M. Korkusinski, and P. Hawrylak, "Directed self-assembly of single quantum dots for telecommunication wavelength optical devices," *Laser & Photon. Rev.*, vol. 4, p. 283, 2010.
- [65] R. M. Martin, *Electronic Structure: Basic Theory and Practical Methods*. Cambridge: Cambridge University Press, 2004.
- [66] P. Hohenberg and W. Kohn, "Inhomogeneous electron gas," *Phys. Rev.*, vol. 136, p. 864, 1964.
- [67] W. Kohn and L. J. Sham, "Self-consistent equations including exchange and correlation effects," *Phys. Rev.*, vol. 140, p. 1133, 1965.
- [68] A. Wensauer, M. Korkusinski, and P. Hawrylak, "Configuration Interaction method for Fock-Darwin states," *Solid State Commun.*, vol. 130, p. 115, 2004.
- [69] E. Engel and R. M. Dreizler, *Density functional Theory: An Advanced Course*. Theoretical and Mathematical Physics, Berlin: Springer, 2011.
- [70] K. Capelle, "A bird's-eye view of density functional theory," *Arxiv Preprint*, pp. cond-mat/0211443v5, 2006.
- [71] U. von Barth and L. Hedin, "A local exchange-correlation potential for the spin polarized case: I," *J. Phys. C*, vol. 5, p. 1629, 1972.
- [72] O. Gunnarsson and B. I. Lundqvist, "Exchange and correlation in atoms, molecules, and solids by the spin-density-functional formalism," *Phys. Rev. B*, vol. 13, p. 4274, 1976.
- [73] J. Kohanoff, *Electronic Structure Calculations for Solids and Molecules: Theory and Computational Methods*. Cambridge: Cambridge University Press, 2006.
- [74] F. C. Alcaraz and K. Capelle, "Density functional formulations for quantum chains," *Phys. Rev. B*, vol. 76, p. 035109, 2007.
- [75] W. Kohn, "Nobel lecture: Electronic structure of matter - wave functions and density functionals," *Rev. Mod. Phys.*, vol. 71, p. 1253, 1999.
- [76] H. S. Vosko, L. Wilk, and M. Nusair, "Accurate spin-dependent electron liquid correlation energies for local spin density calculations: a critical analysis," *Can. J. Phys.*, vol. 58, pp. 1200–1211, 1980.
- [77] J. P. Perdew and Y. Wang, "Accurate and simple analytic representation of the electron-gas correlation energy," *Phys. Rev. B*, vol. 45, p. 13244, 1992.
- [78] F. Qu and P. Hawrylak, "Magnetic exchange interactions in quantum dots containing electrons and magnetic ions," *Phys. Rev. Lett.*, vol. 95, p. 217206, 2005.
- [79] LAPACK: Linear Algebra Package: Documentation available in <http://www.netlib.org/lapack/>.
- [80] A. Wensauer, M. Korkusinski, and P. Hawrylak, "Theory of the spin-singlet filling factor $\nu = 2$ quantum hall droplet," *Phys. Rev. B*, vol. 67, p. 035325, 2003.

- [81] J. Gaj and J. Kossut, eds., *The Physics of Diluted Magnetic Semiconductors*. Springer Series in Materials Science, Berlin: Springer-Verlag, 2011.
- [82] K. Olejník, M. H. S. Owen, V. Novák, J. Mašek, A. C. Irvine, J. Wunderlich, and T. Jungwirth, “Enhanced annealing, high Curie temperature, and low-voltage gating in (Ga,Mn)As: A surface oxide control study,” *Phys. Rev. B*, vol. 78, p. 054403, 2008.
- [83] L. Chen, S. Yan, P. F. Xu, J. Lu, W. Z. Wang, J. J. Deng, X. Qian, Y. Ji, and J. H. Zhao, “Low-temperature magnetotransport behaviors of heavily Mn-doped (Ga,Mn)As films with high ferromagnetic transition temperature,” *Appl. Phys. Lett.*, vol. 95, p. 182505, 2009.
- [84] D. Chiba, M. Sawicki, Y. Nishitani, Y. Nakatani, F. Matsukura, and H. Ohno, “Magnetization vector manipulation by electric fields,” *Nature*, vol. 455, p. 515, 2008.
- [85] P. Nemeč, E. Rozkotová, N. Tesarová, F. Trojánek, E. D. Ranieri, K. Olejník, J. Zemen, V. Novák, M. Cukr, P. Malý, and T. Jungwirth, “Experimental observation of the optical spin transfer torque,” *Nat. Phys.*, vol. 8, p. 411, 2012.
- [86] N. Tesařová, P. Nemeč, E. Rozkotová, J. Zemen, T. Janda, F. T. D. Butkovičová, K. Olejník, V. Novák, P. Malý, and T. Jungwirth, “Experimental observation of the optical spin-orbit torque,” *Nat. Photon.*, vol. 7, p. 492, 2013.
- [87] K. M. Yu, T. Wojtowicz, W. Walukiewicz, X. Liu, and J. K. Furdyna, *Spintronics*, vol. 82 of *Semiconductor and Semimetals*. Amsterdam: Elsevier, 2008.
- [88] M. Wang, K. W. Edmonds, B. L. Gallagher, A. W. Rushforth, O. Makarovskiy, A. Patané, R. P. Campion, C. T. Foxon, V. Novak, and T. Jungwirth, “High Curie temperatures at low compensation in the ferromagnetic semiconductor (Ga,Mn)As,” *Phys. Rev. B*, vol. 87, p. 121301(R), 2013.
- [89] P. Nemeč, V. Novák, N. Tesarová, E. Rozkotová, H. Reichlová, D. B. F. Trojánek, K. Olejník, P. M. R. Campion, B. L. Gallagher, J. Sinova, and T. Jungwirth, “The essential role of carefully optimized synthesis for elucidating intrinsic material properties of (Ga,Mn)As,” *Nat. Commun.*, vol. 4, p. 1422, 2013.
- [90] A. K. Bhattarjee and C. B. á la Guillaume, “Model for the Mn acceptor in GaAs,” *Solid State Commun.*, vol. 113, p. 17, 2000.
- [91] T. Jungwirth, J. Sinova, A. H. MacDonald, B. L. Gallagher, V. Novák, K. W. Edmonds, A. W. Rushforth, R. P. Campion, C. T. Foxon, L. Eaves, E. Olejník, J. Mašek, S.-R. E. Y. J. Wunderlich, C. Gould, L. W. Molenkamp, T. Dietl, and H. Ohno, “Character of states near the Fermi level in (Ga,Mn)As: Impurity to valence band crossover,” *Phys. Rev. B*, vol. 76, p. 125206, 2007.
- [92] M. Abolfath, T. Jungwirth, J. Brum, and A. H. MacDonald, “Theory of magnetic anisotropy in $\text{III}_{1-x}\text{Mn}_x\text{V}$ ferromagnets,” *Phys. Rev. B*, vol. 63, p. 054418, 2001.
- [93] T. Dietl, “A ten-year perspective on dilute magnetic semiconductors and oxides,” *Nat. Mater.*, vol. 9, p. 965, 2010.
- [94] T. Jungwirth, J. Wunderlich, V. Novák, K. Olejník, B. L. Gallagher, R. P. Campion, K. W. Edmonds, A. W. Rushforth, A. J. Ferguson, and P. Nemeč, “Spin-dependent phenomena and device concepts explored in (Ga,Mn)As,” *arXiv:1310.1944v1*, 2013.

- [95] T. Dietl and H. Ohno, "Dilute ferromagnetic semiconductors: physics and spintronic structures," *Rev. Mod. Phys.*, vol. 86, p. 187, 2013.
- [96] N. Samarth, "Ferromagnetic semiconductors: Battle of the bands," *Nat. Mater.*, vol. 11, p. 360, 2012.
- [97] M. Dobrowolska, K. Tivakornsasithorn, X. Liu, J. K. Furdyna, M. Berciu, K. M. Yu, and W. Walukiewicz, "Controlling the Curie temperature in (Ga,Mn)As through location of the fermi level within the impurity band," *Nat. Mater.*, vol. 11, p. 444, 2012.
- [98] B. C. Chapler, S. Mack, L. Ju, T. W. Elson, B. W. Boudouris, E. Namdas, J. D. Yuen, A. J. Heeger, N. Samarth, M. D. Ventra, R. A. Segalman, D. D. Awschalom, F. Wang, and D. N. Basov, "Infrared conductivity of hole accumulation and depletion layers in (Ga,Mn)As- and (Ga,Be)As-based electric field-effect devices," *Phys. Rev. B*, vol. 86, p. 165302, 2012.
- [99] M. P. Marder, *Condensed Matter Physics*. New York: John Wiley & Sons, Inc., 2000.
- [100] G. Bastard, *Wave Mechanics Applied to Semiconductor Heterostructures*. Monographies de physique, Paris: Les Editions de Physique, 1992.
- [101] T. Dietl, H. Ohno, and F. Matsukura, "Hole-mediated ferromagnetism in tetrahedrally coordinated semiconductors," *Phys. Rev. B*, vol. 63, p. 195205, 2001.
- [102] N. W. Ashcroft and N. D. Mermin, *Solid State Physics*. Saunders College, Philadelphia, 1976.
- [103] L. Besombes, Y. Leger, L. Maingault, D. Ferrand, H. Mariette, and J. Cibert, "Carrier-induced spin splitting of an individual magnetic atom embedded in a quantum dot," *Phys. Rev. B*, vol. 71, p. 161307, 2005.
- [104] M. H. Degani and M. Z. Maialle, "Numerical calculations of the quantum states in semiconductor nanostructures," *J. Comput. Theor. Nanosci.*, vol. 7, p. 454, 2010.
- [105] G. A. Farias, M. H. Degani, J. A. K. Freire, J. C. e Silva, and R. Ferreira, "Impurities and geometrical effects on the electron energy spectrum of quantum rings," *Phys. Rev. B*, vol. 77, p. 085316, 2008.
- [106] M. H. Degani, M. Z. Maialle, G. Medeiros-Ribeiro, and E. Ribeiro, "Two-dimensional magnetoexcitons in type-II semiconductor quantum dots," *Phys. Rev. B*, vol. 78, p. 075322, 2008.
- [107] P. L. DeVries, *A First Course in Computational Physics*. New York: Wiley, 1st ed., 1993.
- [108] H. Munekata, H. Ohno, S. von Molnar, A. Segmüller, L. L. Chang, and L. Esaki, "Diluted magnetic III-V semiconductors," *Phys. Rev. Lett.*, vol. 63, p. 1849, 1989.
- [109] S. Knott, T. C. Hirschmann, U. Wurstbauer, W. Hansen, and W. Wegscheider, "Magnetoresistance effects and phase coherent transport phenomena in a magnetic nonplanar two-dimensional hole system," *Phys. Rev. B*, vol. 84, p. 205302, 2011.
- [110] S. V. Zaitsev and B. N. Zvonkov, "Circularly polarized photoluminescence of insulating InGaAs/GaAs heterostructures with a ferromagnetic Mn δ -layer in the barrier," *Phys. Status Solidi B*, vol. 248, p. 1526, 2010.

- [111] V. L. Korenev, I. A. Akimov, S. V. Zaitsev, V. F. Sapega, L. Langer, D. R. Yakovlev, Y. A. Danilov, and M. Bayer, “Dynamic spin polarization by orientation-dependent separation in a ferromagnet-semiconductor hybrid,” *Nat. Commun.*, vol. 3, p. 959, 2012.
- [112] M. A. G. Balanta, M. J. S. P. Brasil, F. Iikawa, U. C. Mendes, J. A. Brum, M. Z. Maialle, Y. A. Danilov, O. V. Vikhrova, and B. N. Zvonkov, “Compensation effect on the CW spin-polarization degree of Mn-based structures,” *J. Phys. D: Appl. Phys.*, vol. 46, p. 215103, 2013.
- [113] J. Kunc, K. Kowalik, F. J. Teran, P. Plochocka, B. A. Piot, D. K. Maude, M. Potemski, V. Kolkovsky, G. Karczewski, and T. Wojtowicz, “Enhancement of the spin gap in fully occupied two-dimensional landau levels,” *Phys. Rev. B*, vol. 82, p. 115438, 2010.
- [114] T. Uenoyama and L. J. Sham, “Many-body theory of magneto-optical spectra in doped quantum wells,” *Phys. Rev. B*, vol. 39, p. 11044, 1989.
- [115] S. Katayama and T. Ando, “Magnetic oscillation of luminescence energy in modulation-doped quantum wells,” *Solid State Commun.*, vol. 70, p. 91, 1989.
- [116] P. Hawrylak and M. Potemski, “Theory of photoluminescence from an interacting two-dimensional electron gas in strong magnetic fields,” *Phys. Rev. B*, vol. 56, p. 12386, 1997.
- [117] S. Takeyama, G. Karczewski, T. Wojtowicz, J. Kossut, H. Kunimatsu, K. Uchida, and N. Miura, “Zeeman-gap anomaly in photoluminescence from a two-dimensional electron gas in CdTe/(Cd,Mg)Te quantum wells,” *Phys. Rev. B*, vol. 59, p. 7327, 1999.
- [118] Y. V. Ponomarev, A. Usher, P. J. Rodgers, B. L. Gallagher, M. Henini, and G. Hill, “Millikelvin magneto-optical studies of two-dimensional hole systems,” *Phys. Rev. B*, vol. 54, p. 13891, 1996.
- [119] B. A. Aronzon, M. A. Pankov, V. V. Rylkov, E. Z. Meilikhov, A. S. Lagutin, E. M. Pashaev, M. A. Chuev, V. V. Kvardakov, I. A. Likhachev, O. V. Vihrova, A. V. Lashkul, E. Lahderanta, A. S. Vedeneev, and P. Kervalishvili, “Ferromagnetism of low-dimensional Mn-doped III-V semiconductor structures in the vicinity of the insulator-metal transition,” *J. Appl. Phys.*, vol. 107, p. 023905, 2010.
- [120] U. Wurstbauer, M. Soda, R. Jakiela, D. Schuh, D. Weiss, J. Zweck, and W. Wegscheider, “Coexistence of ferromagnetism and quantum hall effect in Mn modulation-doped two-dimensional hole systems,” *J. Cryst. Growth*, vol. 311, p. 2160, 2009.
- [121] U. Gupta and A. K. Rajagopal, “Density functional formalism at finite temperatures with some applications,” *Physics Reports*, vol. 87, pp. 259–311, 1982.
- [122] J. M. Luttinger and W. Kohn, “Motion of electrons and holes in perturbed periodic fields,” *Phys. Rev.*, vol. 97, p. 869, 1955.
- [123] S.-R. E. Yang, D. A. Broido, and L. J. Sham, “Holes at GaAs-Al_xGa_{1-x}As heterojunctions in magnetic fields,” *Phys. Rev. B*, vol. 32, p. 6630, 1985.
- [124] L. G. Rego, P. Hawrylak, and J. A. Brum, “Electronic structure of holes in modulation doped *p*-Si_{1-x}Ge_x/Si strained quantum wells in a magnetic field,” *Solid State Commun.*, vol. 105, p. 139, 1998.

- [125] O. V. Volkov, "Self-consistent calculation of Landau levels of a quasi-two-dimensional hole gas at a GaAs/AlGaAs p-type heterojunction," *Phys. Solid State*, vol. 40, p. 1019, 1998.
- [126] T. Wimbauer, K. Oettinger, A. L. Efros, B. K. Meyer, and H. Brugger, "Zeeman splitting of the excitonic recombination in $\text{In}_x\text{Ga}_{1-x}\text{As}/\text{GaAs}$ single quantum wells," *Phys. Rev. B*, vol. 50, p. 8889, 1994.
- [127] G. Bastard and J. A. Brum, "Electronic states in semiconductor heterostructures," *IEEE Journal of Quantum Electronics*, vol. 22, p. 1625, 1986.
- [128] D. A. H. Mace, D. C. Rogers, K. J. Monserrat, J. N. Tohill, and S. T. Davey, "Sub-band energies of highly strained InGaAs-GaAs quantum wells," *Semicond. Sci. Technol.*, vol. 3, p. 597, 1988.
- [129] I. Vurgaftman, J. R. Meyer, and L. R. Ram-Mohan, "Band parameters for III-V compound semiconductors and their alloys," *J. Appl. Phys.*, vol. 89, p. 5815, 2001.
- [130] D. J. Arent, K. Deneffe, C. V. Hoof, J. D. Boeck, and G. Borghs, "Strain effects and band offsets in GaAs/InGaAs strained layered quantum structures," *J. Appl. Phys.*, vol. 66, p. 1739, 1989.
- [131] S. L. Chuang, *Physics of Optoelectronic Devices*. New York: John Wiley & Sons. Inc., 1995.
- [132] M. Poggio, R. C. Myers, N. P. Stern, A. C. Gossard, and D. D. Awschalom, "Structural, electrical, and magneto-optical characterization of paramagnetic GaMnAs quantum wells," *Phys. Rev. B*, vol. 72, p. 235313, 2005.
- [133] A. M. Nazmulla, S. Sugaharaa, and M. Tanak, "Mbe growth, structural, and transport properties of Mn δ -doped GaAs layers," *J. Cryst. Growth*, vol. 251, p. 303, 2003.
- [134] J. F. Sampaio, S. L. S. Freire, and E. S. Alves, "The effect of the surface Fermi level pinning on the properties of δ -doped system," *J. Appl. Phys.*, vol. 81, p. 530, 1997.
- [135] T. Ando and Y. Uemura, "Theory of quantum transport in a two-dimensional electron system under magnetic fields. I. characteristics of level broadening and transport under strong fields," *J. Phys. Soc. Jpn.*, vol. 36, p. 959, 1974.
- [136] B. E. Larson, K. C. Hass, H. Ehrenreich, and A. E. Carlsson, "Theory of exchange interactions and chemical trends in diluted magnetic semiconductors," *Phys. Rev. B*, vol. 37, p. 4137, 1988.
- [137] P. Kacman, "Spin interactions in diluted magnetic semiconductors and magnetic semiconductor structures," *Semicond. Sci. Technol.*, vol. 16, p. R25, 2001.
- [138] K. Asano and T. Ando, "Photoluminescence in integer quantum hall systems," *Phys. Rev. B*, vol. 65, p. 115330, 2002.
- [139] G. E. W. Bauer and T. Ando, "Theory of band gap renormalisation in modulation-doped quantum wells," *J. Phys. C: Solid State Phys.*, vol. 19, p. 1537, 1986.
- [140] P. A. Bobbert, H. Wieldraaijer, R. van der Weide, M. Kemerink, P. M. Koenraad, and J. H. Wolter, "Exchange-correlation energy of a hole gas including valence band coupling," *Phys. Rev. B*, vol. 56, p. 3664, 1997.

- [141] J. Okabayashi, A. Kimura, O. Rader, T. Mizokawa, A. Fujimori, T. Hayashi, and M. Tanaka, "Core-level photoemission study of $\text{Ga}_{1-x}\text{Mn}_x\text{As}$," *Phys. Rev. B*, vol. 58, p. R4211, 1998.
- [142] R. Kotlyar, T. L. Reinecke, M. Bayer, and A. Forchel, "Zeeman spin splittings in semiconductor nanostructures," *Phys. Rev. B*, vol. 63, p. 085310, 2001.
- [143] T. Dietl, D. D. Awschalom, M. Kaminska, and H. Ohno, eds., *Semiconductors and Semimetal: Spintronics*, vol. 82. Elsevier, 2008.
- [144] M. J. S. P. Brasil private communication.
- [145] N. T. T. Nguyen and F. M. Peeters, "Correlated many-electron states in a quantum dot containing a single magnetic impurity," *Phys. Rev. B*, vol. 76, p. 045315, 2007.
- [146] J. Kondo, "Resistance minimum in dilute magnetic alloys," *Prog. Theor. Phys.*, vol. 32, p. 34, 1964.
- [147] A. C. Hewson, *The Kondo Problem to Heavy Fermions*. Cambridge: Cambridge University Press, 1993.
- [148] V. Madhavan, W. Chen, T. Jamneala, M. F. Crommie, and N. S. Wingreen, "Tunneling into a single magnetic atom: Spectroscopic evidence of the kondo resonance," *Science*, vol. 280, p. 567, 1998.
- [149] J. Li, W.-D. Schneider, R. Berndt, and B. Delley, "Kondo scattering observed at a single magnetic impurity," *Phys. Rev. Lett.*, vol. 80, p. 2893, 1998.
- [150] D. Jacob, M. Soriano, and J. J. Palacios, "Kondo effect and spin quenching in high-spin molecules on metal substrates," *Phys. Rev. B*, vol. 134417, p. 2013, 88.
- [151] G. Balasubramanian, I. Y. Chan, R. Kolesov, M. Al-Hmoud, J. Tisler, C. Shin, C. Kim, A. Wojcik, P. R. Hemmer, A. Krueger, T. Hanke, A. Leitenstorfer, R. Bratschitsch, F. Jelezko, and J. Wrachtrup, "Nanoscale imaging magnetometry with diamond spins under ambient conditions," *Nature*, vol. 455, p. 648, 2008.
- [152] H. J. Mamin, M. Kim, M. H. Sherwood, C. T. Rettner, K. Ohno, D. D. Awschalom, and D. Rugar, "Nanoscale nuclear magnetic resonance with a nitrogen-vacancy spin sensor," *Science*, vol. 339, p. 557, 2013.
- [153] N. T. T. Nguyen and F. M. Peeters, "Cyclotron resonance of a magnetic quantum dot," *Phys. Rev. B*, vol. 78, p. 245311, 2008.
- [154] T. Machida, S. Ishizuka, T. Yamazaki, S. Komiyama, K. Muraki, and Y. Hirayama, "Spin polarization of fractional quantum hall edge channels studied by dynamic nuclear polarization," *Phys. Rev. B*, vol. 65, p. 233304, 2002.
- [155] M. H. Fauzi, S. Watanabe, and Y. Hirayama, "Microscopic characteristics of dynamic nuclear polarization and selective nuclear depolarization at the $\nu = 2/3$ spin phase transition," *Appl. Phys. Lett.*, vol. 101, p. 162105, 2012.
- [156] K. Akiba, T. Yuge, S. Kanasugi, K. Nagase, and Y. Hirayama, "Optically induced nuclear spin polarization in a single GaAs/AlGaAs quantum well probed by a resistance detection method in the fractional quantum hall regime," *Phys. Rev. B*, vol. 87, p. 235309, 2013.

- [157] A. O. Govorov and A. V. Kalameitsev, "Optical properties of a semiconductor quantum dot with a single magnetic impurity: photoinduced spin orientation," *Phys. Rev. B*, vol. 71, p. 035338, 2005.
- [158] P. Hawrylak, "Far infrared absorption by screened D-states in qwells in a strong magnetic field," *Solid State Commun.*, vol. 88, p. 475, 1993.
- [159] P. Hawrylak, M. Grabowski, and J. J. Quinn, "Tunneling in a periodic array of semi-magnetic quantum dots," *Phys. Rev. B*, vol. 44, p. 13082, 1991.
- [160] S. Loth, K. von Bergmann, M. Ternes, A. F. Otte, C. P. Lutz, and A. J. Heinrich, "Controlling the state of quantum spins with electric currents," *Nat. Phys.*, vol. 6, p. 340, 2010.
- [161] F. Henneberger and O. Benson, eds., *Semiconductor Quantum Bits*. Singapore: Pan Stanford Publishing, 2008.
- [162] C.-Y. Hsieh, Y. Shim, M. Korkusinski, and P. Hawrylak, "Physics of lateral triple quantum-dot molecules with controlled electron numbers," *Rep. Prog. Phys.*, vol. 75, p. 114501, 2012.
- [163] G. Kioseoglou, M. Yasar, C. H. Li, M. Korkusinski, M. Diaz-Avila, A. T. Hanbicki, P. Hawrylak, A. Petrou, and B. T. Jonker, "Intershell exchange and sequential electrically injected spin populations of InAs quantum dot shell states," *Phys. Rev. Lett.*, vol. 101, p. 227203, 2008.
- [164] A. Hundt, J. Puls, and F. Henneberger, "Spin properties of self-organized diluted magnetic $\text{Cd}_{1-x}\text{Mn}_x\text{Se}$ quantum dots," *Phys. Rev. B*, vol. 69, p. 121309, 2004.
- [165] M. Goryca, T. Kazimierzczuk, M. Nawrocki, A. Golnik, J. A. Gaj, P. Kossacki, P. Wojnar, and G. Karczewski, "Optical manipulation of a single Mn spin in a CdTe-based quantum dot," *Phys. Rev. Lett.*, vol. 103, p. 087401, 2009.
- [166] C. L. Gall, R. S. Kolodka, C. L. Cao, H. Boukari, H. Mariette, J. Fernandez-Rossier, and L. Besombes, "Optical initialization, readout, and dynamics of a Mn spin in a quantum dot," *Phys. Rev. B*, vol. 81, p. 245315, 2010.
- [167] L. Besombes, C. L. Cao, S. Jamet, H. Boukari, and J. Fernandez-Rossier, "Optical control of the spin state of two Mn atoms in a quantum dot," *Phys. Rev. B*, vol. 86, p. 165306, 2012.
- [168] A. L. Efros, M. Rosen, and E. I. Rashba, "Paramagnetic ion-doped nanocrystal as a voltage-controlled spin filter," *Phys. Rev. Lett.*, vol. 87, p. 206601, 2001.
- [169] F. Qu and P. Hawrylak, "Theory of electron mediated Mn-Mn interactions in quantum dots," *Phys. Rev. Lett.*, vol. 96, p. 157201, 2006.
- [170] D. E. Reiter, T. Kuhn, and V. M. Axt, "All-optical spin manipulation of a single manganese atom in a quantum dot," *Phys. Rev. Lett.*, vol. 102, p. 177403, 2009.
- [171] R. Oszwaldowski, I. Zutic, and A. G. Petukhov, "Magnetism in closed-shell quantum dots: Emergence of magnetic bipolarons," *Phys. Rev. Lett.*, vol. 106, p. 177201, 2011.
- [172] J. Fernandez-Rossier and R. Aguado, "Single-electron transport in electrically tunable nanomagnets," *Phys. Rev. Lett.*, vol. 98, p. 106805, 2007.

- [173] S.-J. Cheng and P. Hawrylak, "Controlling magnetism of semi-magnetic quantum dots with odd-even exciton numbers," *Europhys. Lett.*, vol. 81, p. 37005, 2008.
- [174] A. H. Trojnar, M. Korkusinski, M. Potemski, and P. Hawrylak, "Theory of optical properties of II-VI semiconductor quantum dots containing a single magnetic ion in a strong magnetic field," *Phys. Rev. B*, vol. 85, p. 165415, 2012.
- [175] G. A. Narvaez and P. Hawrylak, "Effects of electron-electron interactions on excitonic absorption in charged self-assembled quantum dots," *Phys. Rev. B*, vol. 61, p. 13753, 2000.
- [176] M. Ediger, K. Karrai, A. Badolato, P. M. Petroff, and R. J. Warburton, "Controlled charging of the same single quantum dot from +6e to -8e: emission, shell filling and configuration interactions," *Phys. Stat. Sol. (c)*, vol. 3, p. 3806, 2006.
- [177] P. Hawrylak, "Single-electron capacitance spectroscopy of few-electron artificial atoms in a magnetic field: Theory and experiment," *Phys. Rev. Lett.*, vol. 71, p. 3347, 1993.
- [178] E. S. Kadantsev, M. Zielinski, M. Korkusinski, and P. Hawrylak, "Ab initio calculation of band edges modified by (001) biaxial strain in group IIIA-VA and group IIB-VIA semiconductors: Application to quasiparticle energy levels of strained InAs/InP quantum dot," *J. Appl. Phys.*, vol. 107, p. 104315, 2010.
- [179] Y. Leger, L. Besombes, L. Maingault, D. Ferrand, and H. Mariette, "Hole spin anisotropy in single Mn-doped quantum dots," *Phys. Rev. B*, vol. 72, p. 241309, 2005.
- [180] Y. Leger, L. Besombes, L. Maingault, D. Ferrand, and H. Mariette, "Geometrical effects on the optical properties of quantum dots doped with a single magnetic atom," *Phys. Rev. Lett.*, vol. 95, p. 047403, 2005.
- [181] K. L. Liu, A. H. MacDonald, J. M. Daams, S. H. Vosko, and D. D. Koelling, "Spin density functional theory of the temperature-dependent spin susceptibility: Pd and Pt," *J. Magn. Magn. Mater.*, vol. 12, pp. 43-47, 1979.
- [182] N. D. Mermim, "Thermal properties of the inhomogeneous electron gas," *Phys. Rev.*, vol. 137, p. 1441, 1965.